Synthesis Design and Full Cell Development of Ni-rich Cathodes for Lithium-ion Batteries

by

Ethan Thomas Williams

UNIVERSITY OF BIRMINGHAM

A thesis submitted to the University of Birmingham for the degree of DOCTOR OF PHILOSOPHY

School of Metallurgy and Materials

College of Engineering and Physical Sciences

University of Birmingham

March 2025

Abstract

The growing demand for electric vehicles (EVs) and grid storage solutions has driven the need for lithium-ion batteries (LIBs) with higher energy densities, that can endure longer lifetimes. Nickel-rich layered oxide cathodes, such as $LiNi_{0.9}Mn_{0.05}Co_{0.05}O_2$ (NMC90-5-5), are promising candidates for high-energy LIBs, due to their high specific capacity and limited cobalt content, but their practical application is hindered by capacity fade, structural instability, and poor cycle life. This thesis explores practical large batch synthesis and doping strategies to enhance the electrochemical performance and stability of Ni-rich NMC cathodes, with a focus on firing conditions, bulk-surface engineering, and full-cell optimisation.

First, the role of boron-based fluxes (boric acid and borax) in the synthesis of NMC90-5-5, introduced to optimise firing conditions, was investigated. Boric acid reduced bulk cation mixing and surface lithium residues, improving initial capacity and charge transfer kinetics but leading to capacity fade due to an irreversible phase transition at 4.1 V. Conversely, borax-doped cathodes exhibited superior long-term stability, with 75% capacity retention after 200 cycles, highlighting the importance of the boron-based fluxes in tailoring electrochemical performance.

To further improve the structural resilience and rate capability of Ni-rich cathodes, boron (B) and tin-boron (Sn-B) co-doping strategies were implemented. Sn-B co-doped cathodes demonstrated reduced cation mixing, lattice stabilisation, and higher reversibility of the H2-H3 phase transition. This material also delivered superior rate performance across a wide temperature range (-5°C to 45°C), due to enhanced lithium-ion diffusivity and reduced interfacial resistances, resulting in faster kinetics.

Furthermore, post-mortem analyses confirmed that doping stabilised the oxidation states of transition metals, reduced residual lithium compounds and mitigated surface degradation caused by electrolyte decomposition. These findings highlight the synergistic role of Sn-B co-doping in improving the structural and electrochemical resilience of Ni-rich NMC cathodes at low and high temperatures, demonstrating the potential of tailored doping strategies for improving the performance of lithium-ion batteries under extreme conditions.

Finally, full-cell studies incorporating pristine and doped NMC 90-5-5 cathodes with graphite anodes were conducted to assess practical battery performance. Full-cells containing the Sn-B co-doped cathodes exhibited superior rate capability in both coin and pouch cells, with improved lithium transport and reduced polarization. A higher N/P ratio was also identified for optimised high-rate performance, by reducing overpotentials at the graphite to prevent plating and lowering the polarisation at the cathode to limit time spent at the high voltage phase transition. High-mass-loading pouch cells (~4.5 mA h cm^{-2}) demonstrated the potential of Sn-B doping for commercial-scale LIB applications by maintaining long-term stability and mitigating degradation under fast rate cycling.

Acknowledgements

First and foremost, I would like to thank my supervisor Professor Emma Kendrick, without whom this work would not be possible. I am deeply grateful for the endless guidance, support, and time you have devoted to this project and my personal development over the last few years. Your patience, encouragement, and commitment to excellence have pushed me to become a better scientist, and I will carry your teachings with me throughout my career and beyond.

I would like to express my sincere gratitude to my co-supervisor, Professor Peter Slater, for his constant support throughout this project. His dedication, timely and insightful feedback been truly invaluable. His enthusiasm and encouragement have not only shaped several aspects of this work but have also reinforced my own passion for research.

To the Energy Materials Group, members past and present, I owe my perpetual thanks for harbouring an environment of welcoming and innovation, it has been a pleasure to be a part of this group during my time in Birmingham, and the experience has been all the more special because of it. In particular, I wish to acknowledge Dr David Burnett for his guidance and mentorship during my studies, from synthesis to full-cells, your knowledge and support has been unparallel. I am also grateful to Ben Pye, the true backbone of the group, you have gone above and beyond to keep this research ship afloat, without you there is no EMG. I am also grateful for the support and kindness of Dr Rob Sommerville and Dr Carl Reynolds, you have helped me immeasurably and I have had the pleasure of sharing many the Staff House visits with, which I will always treasure.

To those who occupied that welcomed oasis, we fondly call the Retirement Office; Sam, Halima, Giar, and Issy, I could not have done it without you, and I am eternally fortunate I never had to. I am grateful to call you friends, and immensely proud to have shared this journey with you all. The magnitude of relief I feel in the submission of this thesis is only matched by the nostalgia that is now setting on the end of this chapter.

To my parents, you have helped me in more ways than I can ever hope to thank you enough for, you have been the cornerstones of normality and reassurance in an everchanging world. Thank you for all the years of love and support, without your selfless generosity this journey would have had no end.

Table of Contents

List of Figures

List of Tables

Publications

This thesis comprises of the three following papers, which have either been published or submitted for publication:

- Williams, E.; Burnett, D., Slater, P., Kendrick, E., Investigation of Firing Conditions and Boron Fluxes for the Optimised Synthesis of $LiNi_{0.9}Mn_{0.05}Co_{0.05}O_2$ for High Energy Density Li-ion Batteries. *ChemElectroChem*, **2025,** 12, e202400677
- Williams, E.; Burnett, D.; Swallow, J.; Parmenter, R.; Lima da Silva; W., Weatherup, R.; Slater, P.; Kendrick, E., Improved Cycle Life and Li-Ion Transport Parameters at Low Temperature in Doped Ni-Rich NMC Cathodes. (10.26434/chemrxiv-2025-940p9-v2*).*
- Williams, E.; Burnett, D.; Chen, Y.; Slater. P; Kendrick, E., Balancing kinetics and stoichiometry in Li-ion full cells with co-doped NMC9½½. *Journal of Power Sources,* **2025**, 659, 238415

In addition, the following paper was published as a co-author during the period of the PhD study:

- Chen, Y.; Lakhdar, Y.; Chen, Y.; Kishore, B.; Choi, J.; Williams, E.; Spathara, D.; Jackowska, R.; Kendrick, E., Accurate voltage prediction for lithium and sodium-ion full-cell development, *Next Energy,* **2024**, 5, 100166.

Abbreviations

BX	Borax Anhydrous, $Na_2[B_4O_5(OH)_4]$
CAM	Cathode Active Material
CC-CV	Constant Current-Constant Voltage
CEI	Cathode Electrolyte Interface
CSTR	Continuous Stirred Tank Reactor
DMC	Dimethyl Carbonate
EC	Ethyl Carbonate
ECM	Electric Circuit Model
EDS	Energy Dispersive Spectroscopy
EIS	Electrochemical Impedance Spectroscopy
EMC	Ethyl Methyl Carbonate
GITT	Galvanostatic Intermittent Titration Technique
HB	Boric Acid, H_3BO_3
LIB	Lithium-ion Battery
NMP	N-Methyl-2-Pyrrolidine
N/P	Negative electrode: Positive electrode area capacity
pCAM	Precursor Cathode Active Material
PVDF	Polyvinylidene Fluoride
SEI	Solid Electrolyte Interphase
SEM	Scanning Electron Microscopy
SHE	Standard Electrode Potential
TM	Transition Metal
VC	Vinylene Carbonate
XAS	X-ray Absorption Spectroscopy
XPS	X-ray Photoelectric Spectroscopy
XRD	X-ray Diffraction

Chapter 1 Introduction

1.1 Motivation and wider context

In an era of colossal industrial and technological expansion, the persistent increase of global energy demand, coupled with the ongoing exhaustion of fossil fuels, has catalysed the drive towards sustainable energy sources. With their ability to generate power with minimal or no depletion of fossil fuel-based energy source and thus negating the further addition of greenhouse gas emissions into the atmosphere, renewable energy technologies such as wind, solar, nuclear, hydro, and geothermal energy sources have been introduced to society.[1] However, the specific conditions of weather and geography cause limitations on the reliable and continuous use of some of these technologies. Therefore, the need to establish efficient and dependable energy storage systems as part of the electrical grid can help address the intermittency issues of renewable sources, as well as relieving unexpected demand surges.[2]

Electrochemical systems (such as batteries and fuel cells) enable the conversion of chemical energy into electrical electricity, facilitating stored energy to be repurposed as electricity.[3] They are therefore key contenders in the management of renewable resources. With societies' increasing reliance on portable technology, the ability to store energy at high density and efficiency will be decisive. Over the last three decades, lithium ion batteries (LIBs) have been established as the preferred technology to meet such demands. Hence, since 1991, LIBs have found applications in various consumer electronics and have facilitated the mass commercialization of battery electric vehicles (BEVs), hybrid electric vehicles (HEVs), and plug-in hybrid electric vehicles (PHEVs).

Despite the growing adoption of EVs in mainstream society, a permanent shift towards widespread electrification requires LIBs with longer lifetimes and higher energy outputs at high rates to deliver improved power capabilities over longer distances.[4] Improvements at the cathode, which is often the limiting electrode for the overall energy density and cycling performance in a battery, will prove decisive in advancing this technology.

Specifically; a driving range of 300 miles, specific capacity >200 mAh g^{-1}, cut-off voltage >4.4 V, energy density of 750 Wh Kg^{-1}, is needed from the cathode to ensure feasible adoption of EVs.[5] The energy density of a material is the product of both its specific capacity and the working voltage, and whilst many cathode materials have reached the extent of their specific capacity, pushing the limits of their electrochemical potential is still being explored.[6] Higher working voltages introduce new challenges regarding both cathode and electrolyte degradation and must be tackled to exploit the high energy density of these materials that will deliver battery packs with lower cost and weight. The discovery of new cathode materials as well as the optimisation of current high performing options has therefore received extensive research efforts. The scale-up of these materials is less understood but equally as important for achieving cathode commercialisation. A comprehensive understanding of how the structure and properties of these cathodes can be controlled and optimised by various synthetic methods, and how these synthesis techniques can be scaled most efficiently and cost-effectively, is now greatly desirable.

1.2 Lithium-ion battery working principles

A lithium-ion battery is an electrochemical cell that consists of a positive and negative electrode, divided by a porous separator which enables their contact through an

electrolyte containing lithium ions. The electrodes are coated onto metallic current collectors typically made of aluminium and copper for the cathode and anode respectively, which are chosen for their excellent electrical conductivity. These foils also enable the completion of the external circuit, facilitating the passage of electrons from the active material to the current collector and the subsequent conduction of electricity to the other electrode.[7] To balance the flow of electrons, charged ions migrate through the electrolyte solution.

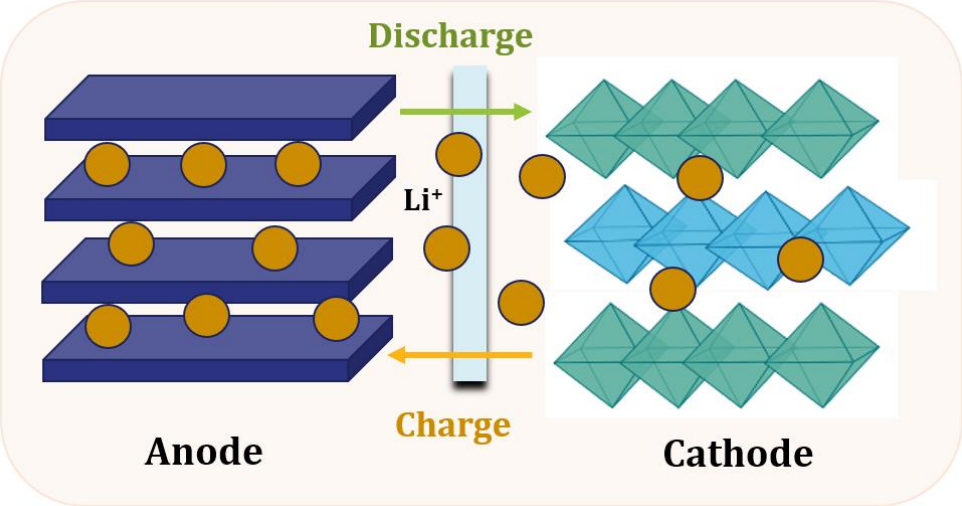

Figure 1.1: Schematic of the basic components and working principles of a lithium-ion battery. Note, the anode and cathode labels here are based on the situation under discharge of the battery.

Batteries store energy by utilizing electrochemical potentials to drive redox reactions between the anode and cathode, whilst the battery voltage (cell potential) is determined by the difference in electrochemical potentials between the two electrodes. The electrochemical potential is a total of the chemical and electrical potentials:

$$\bar{\mu}_i = \mu_i + z_i F \Phi_i \tag{1.1}$$

the chemical potential (μ_i) is a measure of the material's capability to cause a reaction, in this case the propensity to intercalate Li^+, and is determined by the chemical composition of the electrode. The electric potential ($z_i F \Phi_i$) refers to the energy per unit charge due to the electric field created by electron movement in the external circuit, where z_i is the valency, F is the Faraday constant (C mol^{-1}), and Φ_i is the local electrostatic potential (V).

The standard electrode potential (E^o) is a measure of the electrochemical potential of a half-cell reaction to occur at the electrode relative to a reference, typically the standard hydrogen electrode (SHE), as these potentials cannot be measured in isolation. The energy available for electrical work in a redox reaction is quantified by Gibbs free energy, which is determined by the cell potential and the number of available electrons, and is related to the standard electrode potential by Equation 1.2.[6,8]

$$-zFE = \Delta G \tag{1.2}$$

When a system is under equilibrium, the standard Gibbs free energy is described as:

$$\Delta G^0 = -RTln(K_{eq}) \tag{1.3}$$

Where R is the universal gas constant (8.315 J K^{-1} mol^{-1}), T is the temperature (K), and K is the equilibrium reaction constant. Otherwise, the electrode potential under nonstandard conditions can be described as:

$$\Delta G = \Delta G^0 + RTln\frac{[Ox]}{[Red]} \tag{1.4}$$

When combining these equations, they can be rearranged for the Nernst Equation:

$$E_{cell} = E^0_{cell} - \frac{RT}{nF} ln\frac{[Ox]}{[Red]} \tag{1.5}$$

From which the thermodynamic favourability of a reaction can be determined based on the standard electrode potential of the half-cell reaction. In lithium-ion batteries, Li^+/Li vs SHE is -3.04 V.

In the operation of lithium-ion batteries, Li^+ is transferred from the cathode to the anode during charge, in which an energy input (applied current) is required to overcome the non-spontaneous reactions arising from the positive ΔG value. In the discharge process, the reaction is reversed which proceeds in a spontaneous manner ($\Delta G < 0$) due to the large difference in chemical potential between the anode and cathode.

The capacity of an electrode material is another important characteristic used in electrochemistry to characterise the performance of the cathode or anode. Capacity is a measure of stored charge in a cell at an applied current. The theoretical specific capacity of a material can be calculated using Faraday's Law of electrolysis, which states that the amount of substance deposited or liberated at an electrode is directly proportional to the quantity of charge (Q) passed through the electrolyte. This can also be expressed in terms of moles of electrons (n) transferred during the reaction at the electrode using Faradays constant (F = 96485 C mol^{-1}), which is the charge of one mole of electrons.

$$Q = nF$$

Since each Li^+ ion transfers one electron, n also directly relates to the number of transferred Li^+, which is determined by the accessible redox states of the elements in the electrode active material that are stable within the operating voltage window. The measured capacity of an electrode is typically presented as the specific capacity (mA h g^{-1}), which is normalised by the mass of the active material within the electrode.

1.3 Towards high energy cathodes

The energy density of a cell is determined by the capacity and operating voltage limits of the individual electrodes which must be balanced and paired appropriately to exploit the full potential curves of each material. At the negative electrode side, the performance of graphite is already close to the limits of its specific capacity, whilst its operating voltage has been pushed as close to 0 V to extend the energy density of the cell without incurring detrimental Li plating. Therefore, the advances in high energy Li-ion batteries are closely aligned with improving performance in the cathode. The specific transition metal (TM) ions present in the cathode material structure will contribute directly to the capacity and operating voltage of the cell depending on their redox activity. Therefore the cathode performance can be optimised based on the structural and compositional design.[9] Additionally, expanding the voltage limits requires consideration of the electrolyte stability range, outside which decomposition can occur due to oxidation or reduction depending on high or low voltage.

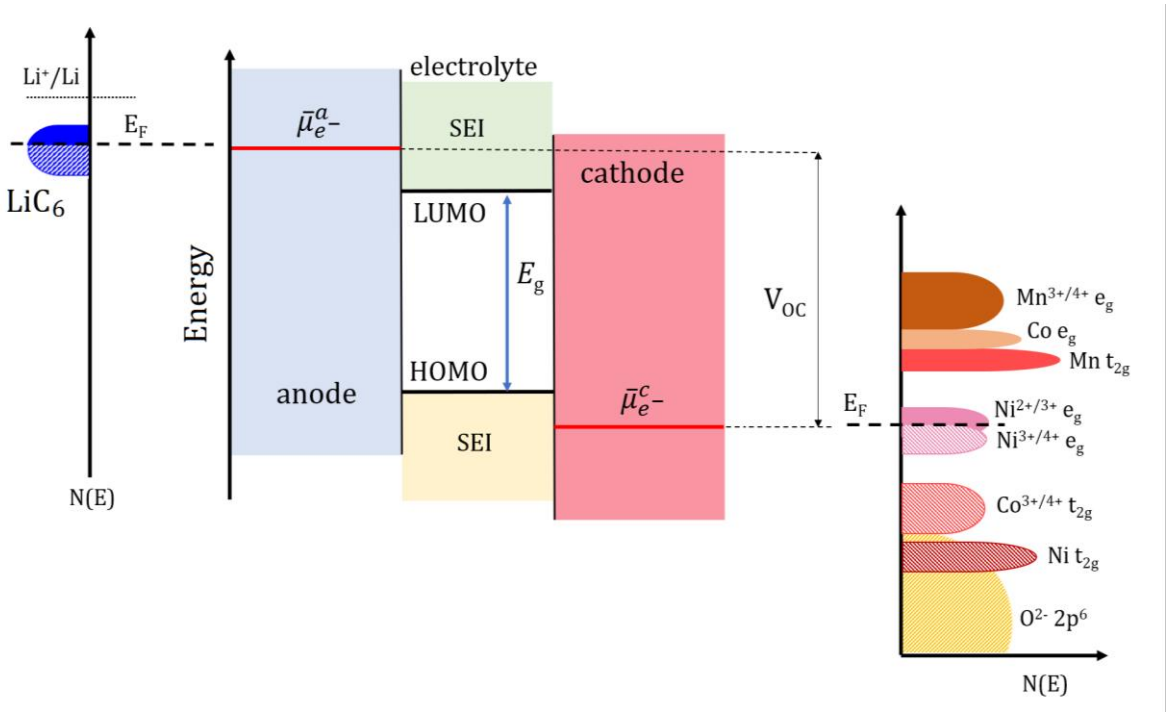

Figure 1.2: Energy diagram of the electrolyte stability range with respect to the HOMO and LUMO bands of the cathode and anode. Adapted with permission [10]. Copyright 2010, American Chemical Society.

1.3.1 Cathode Material Development

Since the first commercial Li-ion battery in 1991, which utilised $LiCoO_2$ (LCO) as the positive electrode, the general trend in cathode development has been towards cheaper/safer materials that can deliver higher energy densities. The polyanion type $LiFePO_4$ (LFP) and spinel type $LiMn_2O_4$ (LMO) cathode materials deliver both low cost and high safety, whilst also removing the need for Co and thus avoiding the ethical issues surrounding artisanal mining. However, LMO displays a limited cycling performance due to Mn dissolution in the electrolyte and Jahn-Teller induced phase transitions, whilst LFP suffers from poor conductivity and lower specific capacity and operating voltages.[5,7,11,12] On the flip side, $LiNiO_2$ (LNO) which is isostructural to LCO, attracted early attention due to its higher capacity and operating voltage. However, LNO suffers considerable

downsides arising from the difficult control of its Li/Ni stoichiometry during synthesis and its considerable structural instability during cycling.[13,14] Instead, it was found that the partial substitution of Ni with other transition metals could afford improved stability (long cycle life and safety), whilst not forfeiting significantly on the overall energy density.

The layered ternary Ni oxide cathodes $LiNi_xCo_yM_zO_2$ (M = Mn, Al), offer high capacity (>200 mA h g^{-1}) at high operating voltages ≥4.3 V. The presence of Co in the structure acts to suppress the unfavourable Li/Ni mixing whilst increasing electronic and ionic conductivity.[15,16] The role of Mn has been shown to provide improved structural and thermal stability due to the strong Mn – O bonds, whilst stabilizing both capacity and voltage during cycling.[17] Additionally, the substitution of Mn for Al can also inhibit cation mixing whilst still maintaining cycling stability.[18] However, the safety and lifetime advantages of ternary cathode containing Mn rather than Al has cumulated in NMC materials being the dominant choice for long-range EV applications.[19] Initially, the stoichiometric ratio of the transition metals was kept equal at $LiNi_{0.33}Mn_{0.33}Co_{0.33}O_2$ (NMC-111), however the need for cheaper and higher energy batteries has dictated the push for increasingly higher Ni contents (Ni ≥0.8). This is also beneficial as Co still plays a role in faster capacity and structural degradation by excessively triggering irreversible lattice oxygen redox and the release of oxygen, and Mn is typically electrochemically inactive in NMC, remaining as Mn^{4+}, and limits conductivity.[20] Despite this, the Ni-rich NMC cathode materials still encounter a range of challenges that are detrimental to their structural and thermal stability, resulting in considerable capacity degradation.

The layered transition metal oxides (such as LCO, LNO, and NMC) belong to the *R-3m* space group, adopting the α-$NaFeO_2$ structure, where the Li and TM atoms reside in

different layers in the 3a and 3b sites respectively, whilst the oxygen atoms occupy the 6c sites in a cubic close-packed (ccp) array. Both the Li and TM ions occupy an octahedral (O_h) coordination, with the TM ions forming edge sharing TMO_6 octahedra and the Li ions situated in the O_h sites in the interstitial spaces between the TM – O slabs.[21,22] The oxygen sublattice adopts a typical O3-type structure, displaying ABCABC stacking in this case corresponding to O-Li-O-TM-O layers in the [001] direction.[23] The ccp structure also creates interstitial vacancies in tetrahedral (T_d) sites between adjacent Li O_h sites in the Li layer. These T_d vacancies act as intermediate sites for Li^+ to hop between vacant O_h sites, enabling the diffusion of Li^+ along the Li layer. The introduction of additional ions into the NMC crystal structure, such as cation doping, typically results in substitution into the TM sites. However, incorporation into the Li sites may occur for larger ions of the alkali metals which also are of the same valence, whilst ions with smaller radius than Li may occupy the Td interstitial sites. The possible doping scenarios are displayed in Figure 1.3.

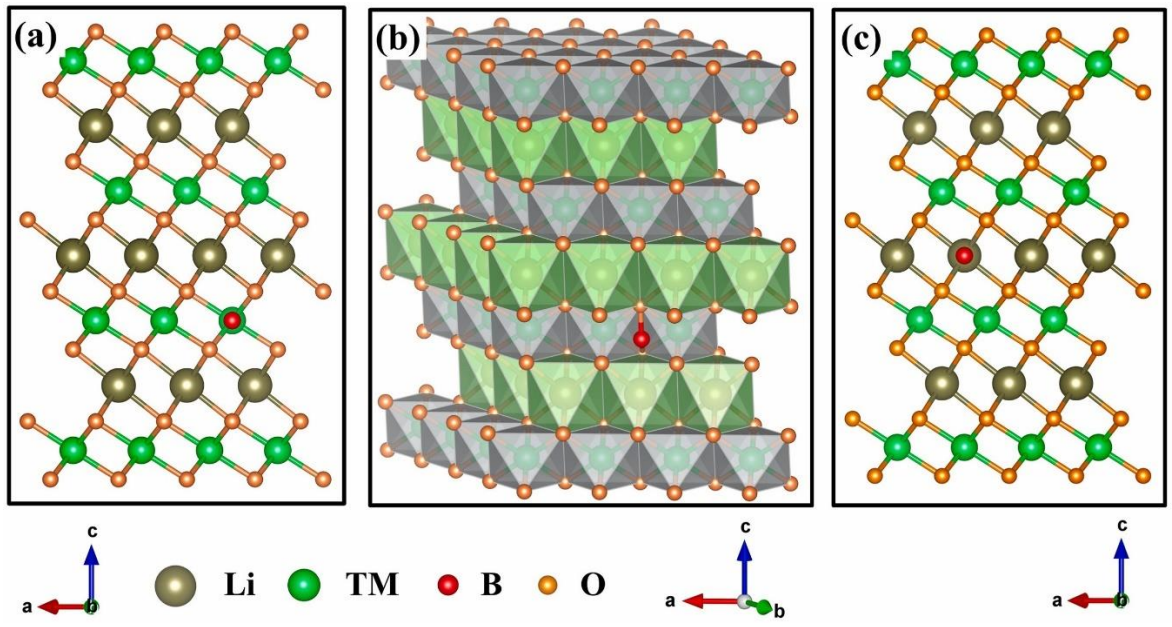

Figure 1.3: Possible substitution sites of doped cations in the NMC crystal structure: transition metal ion site (a), oxygen tetrahedral gap sites (b), and Li ion sites (c). Reproduced with permission.[24] Copyright 2020, Elsevier.

1.3.2 High Voltage Cathode Materials

Li-rich layered oxides and disordered rock salts

When seeking out the upper-bound of specific capacities and energy densities for cathodes, Li-rich oxides ($Li_{1+x}TM_{1-x}O_2$) are some of the most promising materials, exhibiting capacities up to 300 mA h g^{-1}. Unlike the stoichiometric Li cathodes, the Li-rich materials utilise both transition metal and oxygen redox, which can be accessed in the extended voltage ranges (2.0 – 4.8 V) typically used.[25,26] Despite considerable advancements in Li-rich materials, poor cycling performance remains a significant challenge when these cathodes are charged to high voltages.[27] This arises due to the continuous evolution of oxygen gas which initiates the migration of TM's to Li sites and consequently, the unfavourable layered to spinel phase transformation which increases charge transfer resistance as well as capacity fade.[28] Voltage decay and capacity loss is also inherent to the structural collapse that follows oxygen loss in these cathodes. Cathode research has more recently begun to target Li-rich disordered rock-salt oxides (DRX) as a means to achieve even higher energy densities, stabilised at higher operating voltages, whilst also utilising more abundant and less expensive metals.[29] In particular, it is this disordered structure that has overcome the limited Li-ion conductivity in the TM oxides, shifting from poor mobility in the 0-TM channel towards the creation of a 3-dimensional diffusion pathway, although this still tends to be lower than the layered oxide cathode. The electronic conductivity can be accelerated additionally by implementing a carbon coating during synthesis.[30]

Polyanionic materials

Polyanionic olivine materials ($LMPO_4$) consist of edge-sharing MO_6 octahedra and PO_4 tetrahedra, and are characterised by high thermodynamic stability as a result of their strong covalent P – O bonds. However, the PO_4^{3-} anion in $LiFePO_4$ is associated with low 3d orbital redox energies, resulting in lower operating potentials and energy densities.[31] To capitalise on these stable cathode materials, the basic olivine structure can be modified to obtain more promising higher-voltage cathodes. Unlike LFP, the high operating voltage (4.7 V) of $LiCoPO_4$ (LCP) renders it a consideration for 5 V cathode materials, providing its low electronic conductivity can be optimised. One approach to enhancing the olivine conductivity is by doping Co into the 4c sites of Ni during the hydrothermal synthesis of $LiNi_{0.5}Co_{0.5}PO_4$ (LNCP), which has been explored to achieve a range of particle morphologies and architectures. [32] Specifically, higher conductivity arises due to the presence of Co-$3d_{yz}$ orbital that provides electronic states across the Fermi level.

1.3.3 Synthesis Methods

The synthesis method and the associated parameters chosen to elucidate the final cathode material is of great importance, and can dramatically influence particle size, particle morphology, porosity, cation mixing, surface elemental distribution, and surface impurities/residues. Each of these factors, if not controlled, can negatively impact the electrochemical performance of the final product. Some of the common synthesis routes to cathode materials include co-precipitation, sol-gel, hydrothermal/solvothermal, combustion, and most commonly solid-state.[5,32–35] Efforts have also been made to further control solid state synthesis by use of eutectic molten-salts.[36,37] Despite the plethora of synthesis approaches and the large amount of literature that investigates their

accompanying performance enhancement, the scale-up of these techniques and subsequent industrial adoption is still largely unexplored.

Table 2.1: A summary of the advantages and disadvantages of the synthesis methods proposed for high-voltage cathodes.

Synthesis method	**Advantages**	**Disadvantages**
Co-precipitation	Accurate stoichiometry, spherical particles, industrial size reactors exist, morphology engineering from control of conditions which can be automated.	Requires additional separation/drying steps, large quantities of water needed with scale-up, time-consuming.
Eutectic molten salt	Inexpensive, simple procedure, targets lower temperatures, can avoid milling, uniform mixing.	Little control of resulting particles.
Sol-gel	Low reaction temperatures, made simple and cost-effective when combined with combustion, homogenous mixing gives narrow particle size distribution, polymerising agents can control porosity.	Expensive raw materials, many-step preparation process, presence of residual water possible, large quantity of solvents and organic materials.
Spray pyrolysis	Single-step method, very fast production, uniform particle size and composition.	Difficult to control/determine temperature within larger furnace, low yields, some separation steps needed.
Ceramic/solid-state synthesis	Simple preparation, easy to scale-up, low additional costs.	Batch inconsistencies, impurities common, poor morphological control, lengthy and energy consumptive.
Hydrothermal/ solvothermal	High phase purity, uniform product control, cheap material costs.	Difficult to scale up, low yield, high equipment costs.

Coprecipitation

Designing synthesis methods that provide facile control of conditions will be essential when scaling up these methods to industrial level. One approach that satisfies this requirement is the co-precipitation method, in which TM salts are dissolved in a homogeneous solution in the correct stoichiometry. This is then fed into an aqueous

medium along with the lithium salt, a reaction follows and the final TM precursor is precipitated out. The formation of the precipitate adheres to nucleation-growth aggregation followed by Ostwald ripening.[38] Whilst the reaction is relatively easy to control and provides atomic mixing, allowing for homogeneity in the resulting oxide, a rise in local concentration upon addition of the precipitant can disturb the stoichiometry balance.[39] The choice of initial TM salt has also proved important during coprecipitation synthesis, with hydroxides requiring a nitrogen atmosphere to prevent the oxidation of Mn^{2+} and Co^{2+}, and so carbonates and sulphates are preferred, in which the TM's exist solely in the +2 state.[38]

During co-precipitation reactions of Ni-rich cathodes, NaOH typically acts as the precipitating agent, whilst NH_3 plays the role of a chelating agent. The careful control of NH_3 concentration in the synthesis can enable the preferential growth of desired crystal facets in the NMC material, which provide a more open structure for enhanced Li^+ transport .[35] Other factors, including temperature, pH, and feed rate, also influence particle architecture. A gradual pH increase during synthesis can create a Ni valence gradient, strengthening interfacial bonding. Moreover, stirring and precipitation rates affect morphology, whilst the choice of raw material can also significantly impact morphology, such as the use of AlOH in $LiNi_{0.8}Co_{0.15}Al_{0.05}O_2$ (NCA) which catalyses the continuous nucleation of $Al(OH)_3$.[40]

Whilst the route to the transition metal (TM) precursor can take many synthetic approaches, the elucidation of the final cathode material usually requires a high temperature calcination step after the addition of a lithium source at the desired stoichiometry. On an industrial scale, a blend of the TM and Li precursor are continuously fed through a rotary furnace at high temperature.[41] It is desirable when producing

cathode materials on this scale to perform this at a high throughput, utilising large loads at short firing times, as is the case with NMC-111. However, when moving to higher Ni contents (to achieve higher energy densities), the process gets increasingly difficult due to the low thermodynamic stability of Li in the Ni-rich NMC, resulting in the formation of soluble base impurities (Li_2CO_3 and LiOH) on the surface. Additionally, LiOH is preferred to Li_2CO_3 as the lithium source during synthesis as it facilitates the formation of Ni-rich NMC at lower temperature due to the lower melting point and increased solubility of the Li salt. The reduced temperature limits changes in the Ni oxidation state which can be detrimental to the crystal structure.[42,43]

1.4 Challenges for Ni-Rich Cathodes

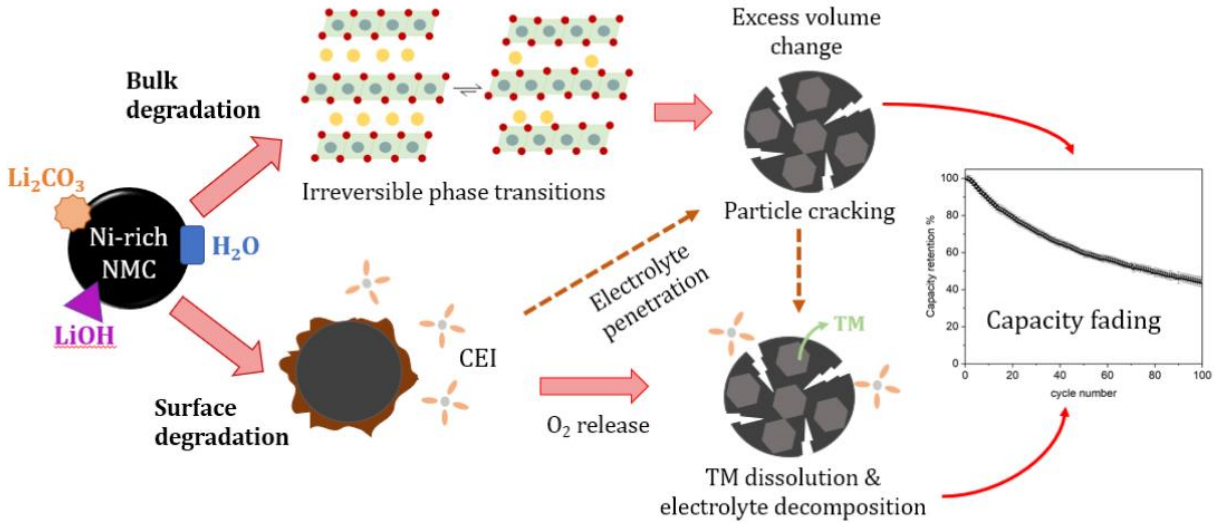

Figure 1.4: Schematic showing the failure mechanisms in Ni-rich cathode materials. Adapted from [44] with permission under a Creative Commons license.

1.4.1 Lithium Residuals and Surface Instability

Layered oxide cathodes with higher Ni contents contain a larger proportion of Ni^{3+} due to the stoichiometric balance of charge. These cations display considerable chemical instability in air with a high propensity to be reduced to Ni^{2+} in air.

The high firing temperatures (>750°C) required for the formation of Ni-rich NMC materials is accompanied by considerable Li volatilization as the melting point of LiOH (462 °C) is exceeded. To alleviate this Li loss during firing, an excess of the lithium source is typically added, around 5 – 10 mol%, to ensure as close a 1:1 stoichiometric ratio of Li and Ni is achieved in the calcined active material. However, this can lead to the formation of residual lithium in an enriched surface coating on the active material particles. The prevalence of lithium residues, which arise from reaction of the excess lithium with H_2O and CO_2 in the air during firing, cannot be overstated. The effect of these residues is detrimental to both the cathodes atomic structure, as well as the bulk cathode slurry properties.

Residual $LiOH/Li_2CO_3$ remaining after synthesis are moisture absorbing which can propagate the decomposition of the $LiPF_6$ in the electrolyte, resulting in corrosive HF generation. This can be understood on a theoretical basis, in which oxygen exposure on the cathode surface (especially the active Ni-exposed facets) brings down the Fermi level to that of the electrolyte, instigating decomposition. Furthermore, the insulating Li_2CO_3 that prevails on the surface is reported to increase first cycle losses in NCA, as well as accelerating Ni and Co dissolution.[40]

The degradation mechanism arising from the occurrence of lithium residuals on the cathode surface depends on the following processes:

- Adsorption of H_2O and CO_2 species from the atmosphere.
- Loss of Li^+ from the active material surface to form an uneven coating layer of $LiOH/Li_2CO_3$ impurities.
- Interaction of this impurity layer with the de-lithiated layer near the surface.

The irreversible breakdown of the lithium residual components, accompanied by the spontaneous reduction of Ni^{3+} and release of oxygen at the cathode surface results in impedance growth and deterioration of the rate performance.[45,46]

If the formation of these lithium residuals is not controlled in the synthesis of the cathode active material, additional issues can occur during the preparation of the electrode coatings. The residual species can instigate slurry gelation by the dehydrofluorination of the PVDF binder, which can induce uneven surface formation when coating.[47] The gelation acts to increase the viscosity of the slurry which if not counteracted by undesirable increased solvent contents, can encourage thickness variation during cathode coating.[48] In some cases the gelation causes the slurry to become solid, in which it is no longer pourable and prevents the coating of the slurry.

1.4.2 Cation Mixing and Structural Disorder

NMC cathode materials are characterised with the α-$NaFeO_2$ crystal structure, in which alternating Li and transition metal (TM) layers are arranged along the (111) plane. However, the size similarity of Ni^{2+} (69 pm) and Li^+ (76 pm) cations in the structure of Ni-rich layered cathode materials results in their partial mixing between the 3b sites at the Li layer and the 3a sites of the TM later.[49] This cation mixing can occur during the high temperature synthesis of the active material and deteriorate further under

electrochemical operation of the cathode in a cell.[50] In the former, the conditions are typically non-equilibrium and so cationic ordering during the synthesis of Ni-rich NMC is largely dictated by kinetic factors.[51] In the latter, the exchange is catalysed by the extraction of Li^+ during the charge process which causes the migration of Ni^{2+} and the simultaneous loss of lattice oxygen from the TM octahedra, driven by the low energy barrier of migration.

Cation mixing can also be influenced by super-exchange interactions, which is an indirect magnetic interaction between cations arising in transition metal oxides for cations with unpaired spins. When Ni ions occupy lithium sites (antisite defects), they exhibit an opposite magnetic moment to those in the transition metal (TM) layer. This facilitates the formation of a 180° linear super-exchange chain involving Ni^{2+}, Ni^{3+}, and Mn^{4+} through a strong σ-bond interaction between Ni^{2+} and O^{2-}. Due to the presence of this σ bond, the 180° super-exchange interaction is significantly stronger than the 90° interaction, enhancing the tendency for cation mixing. Among these interactions, Ni^{2+}–O–Ni^{2+} exhibits the strongest super-exchange, providing substantial driving force for Li/Ni intermixing. In contrast, Ni^{2+}–O–Co^{3+} interactions are weaker due to the absence of unpaired electrons in Co^{3+}, which helps suppress cation mixing.[52,53]

The Li/Ni disordering has several consequences for the structure of the NMC material:[49,53–55]

- The Ni^{2+} at the 3b sites can inhibit the transport of Li^+ between layers due to the strong electrostatic forces between the two ions.
- The Ni^{2+} occupying the Li layer are prone to oxidation at deeper states of charge (higher voltage), generating Ni^{4+} which initiates a considerable shrinkage of the octahedral shell in the Li layer.

- The increasing Ni migration and oxygen loss initiates the onset of the surface structure rearrangement from layered to the electrochemically inactive disordered rock salt structure.
- The oxygen vacancies formed in the TM and Li layers provide more diffusion pathways for further Ni^{2+} migration from the TM octahedra to the Li octahedral sites via these vacancies, which is driven by the local structure distortion from the O defects.

1.4.3 Capacity Fading Mechanisms

The capacity fade observed in layered metal oxide cathode materials is often associated with irreversible phase transitions caused by repeated lithium insertion cycles. The phase changes are accompanied by oxygen evolution as a result of the formation of MO – OM peroxide bonds, which instil severe volume changes.[56] Both cation mixing and oxygen evolution accelerate TM dissolution from the cathode. The dissolved TM^{2+} species are responsible for the irreversible Li^{+} consumption from the cathode and, thus, the reduction in the cathode/anode capacity ratio. The disturbance of this, not only deteriorates the performance of the cell, but can result in safety issues relating to overcharging.[56] The occurrence of both Jahn-Teller (JT) active (low-spin Ni^{3+}, Co^{2+}, high spin Mn^{3+}) and inactive (low-spin Co^{3+}, Ni^{2+}, Mn^{4+}) ions in Ni-rich NMC, can result in distortions of the octahedral TM-O complex upon Li extraction to accommodate charge compensation (e.g. Ni^{2+} to Ni^{3+}).[40] The Jahn-Teller effect is also accompanied by a series of phase transitions with further de-lithiation between different hexagonal (H) phases at higher voltages. Initially, NMC exhibits the O3 structure, characterised by an ABC-type stacking of the layered oxygen ions, also labelled the H1 phase due to the hexagonal

symmetry of the Li and TM in the O_h sites. Upon lithium extraction, the $Li_x[NMC]O_2$ structure initially undergoes a solid-solution reaction between 1.0 > x > 0.8, at which point a phase transition occurs from hexagonal to monoclinic (H1 → M). After further de-lithiation to ~ $Li_{0.4}[NMC]O_2$, a second transition from monoclinic to hexagonal phase (M → H2) occurs, which remains between 0.4 > x > 0.25, after which a final hexagonal to hexagonal (H2 → H3) transition is triggered as the remaining accessible lithium is extracted.[57] Over the cause of the H polymorph transitions, the *a*-axis decreases continuously due to the contraction in NiO_6 octahedra that accompanies the oxidation of Ni^{3+} to Ni^{4+} that compensates for the Li^+ removal. In contrast, the *c*-axis initially increases gradually during the H1 → M → H2 transitions, arising from enhanced O – O electrostatic repulsions as Li^+ is removed from the interlayer. However, subsequent shrinkage occurs during further de-lithiation in the H2 phase, followed by significant contraction of the Li layer during the H2 → H3, likely due the increased Ni – O covalency, which reduces the O – O electrostatic repulsions.[13,58] The main structural crystallographic changes between the different H polymorphs for the Ni-rich NMC material are summarised in Figure 1.4.

For NMC materials with different Ni contents, the H1→ M and M → H2 phase transitions typically occur at consistent potentials around 3.6 V and 4.0 V vs Li^+/Li respectively. The H2 → H3 is usually initiated above 4.2 V vs Li^+/Li with poor reversibility during the subsequent lithiation process, however high Ni contents can result in this transition at premature potential regions.[14,59,60] Additionally, repeat charge-discharge cycles cause the build-up of localised mechanical stress as a result of the continuous large anisotropic volume changes, which can generate microcracks within the secondary cathode particles.[61] These microcracks allow for the electrolyte penetration, exposing the highly reactive Ni^{4+} ions in the inner primary particles to parasitic reactions, resulting in capacity fading and voltage polarization.[62] Elsewhere, the increased proportion of Ni^{4+}

can also accelerates transition metal dissolution, triggering oxidative side reactions with the electrolyte. Since the electrolyte stability window typically ranges from 1.3 to 4.3 V, high-voltage operation exacerbates these issues, particularly when the cathode's lowest unoccupied molecular orbital (LUMO) is lower than the highest occupied molecular orbital (HOMO) of the electrolyte. This mismatch can drive continuous cathode electrolyte interphase (CEI) growth, increasing impedance and further degrading capacity and cycle life.[63]

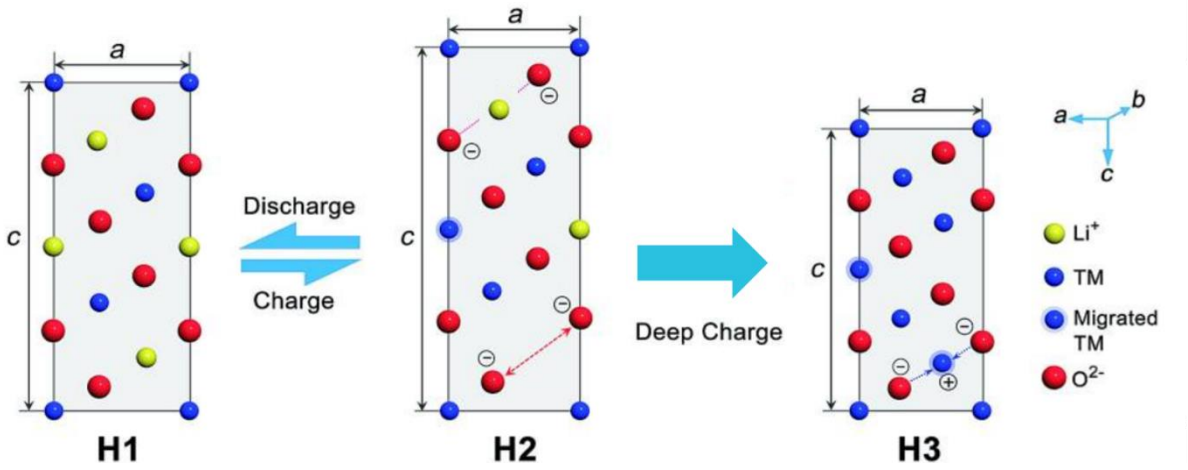

Figure 1.5: Crystal structures associated with layered Ni-rich cathodes the various hexagonal phase transitions which occur during (de-)lithiation. Reproduced with permission under a Creative Commons Licence.[64]

1.5 Mitigation Strategies for Ni-Rich Cathodes

1.5.1 Bulk Doping and Surface Coatings

Among the most common methods applied to stabilise the cycle life of Ni-rich cathode materials are bulk cation substitution (or doping) and coating of the active material surface. Bulk doping involves substituting or introducing foreign elements into the crystal structure of the cathode material. This approach helps to stabilize the layered

structure, reinforce primary particle structure, reduce cation mixing, and improve electrochemical performance via enhancing Li^+ diffusivity. Common dopants include Al, Mg, Ti, and W, which enhance cycle life, thermal stability, and structural integrity by mitigating phase transitions and oxygen release at high voltages.[14,64–66] Despite its potential, theoretical studies indicate that doping efficiency is low due to the formation of electrochemically inert compounds on the particle surface, reducing its effectiveness.[67]

Surface coating forms a protective layer on the cathode particle surface to minimize side reactions with the electrolyte and prevent structural degradation. Materials such as metal oxides (Al_2O_3, ZrO_2), phosphates, and fluorides are commonly used as coatings.[68–72] These coatings improve interfacial stability, suppress electrolyte decomposition, and enhance long-term cycling performance. However, these approaches have limitations, including low Li-ion conductivity, which reduces specific capacity, and non-uniform coatings that fail to provide sufficient protection. Simultaneous application of both doping and coating modifications could provide synergistic effects to stabilise the cathode performance, however the industrial application of both methods remains challenging due to the moisture sensitivity of Ni-rich precursors and the presence of excess residual lithium sources.[67,73]

1.5.2 Cathode Electrolyte Interface Stabilisation

As cathode materials are pushed towards higher operating voltages in order to achieve the desired higher energy densities, the task of finding stable electrolytes to facilitate these cells becomes increasingly difficult. These high-voltage materials are severely prone to detrimental side reactions at the active interfaces, including the decomposition

of the electrolyte and corrosion of the electrode. Similar to the solid electrolyte interface (SEI) that forms on the anode at low voltages, the prevalence of a cathode electrolyte interface (CEI) is triggered at high voltages.[74] Failure to stabilise the CEI risks continuous electrolyte decomposition and poor compatibility between the electrode-electrolyte interface, which will cause a surge in the resistance.

Electrolyte additives are one way in which CEI stability can be promoted at high voltages. These additives are deployed to alter the interfacial chemistry and provide the electrolyte with protection from oxidation, with the end goal of promoting better cycling life and reduced irreversible capacities.[75] It is important that any additive used will undergo sacrificial decomposition before that of any bulk electrolyte component, and if successful will provide an interphase that is both an effective barrier to side reactions, whilst also facilitating facile Li ion transport. Selection of electrolyte additives have thus far been prone to an unconvincing selection process, with most researchers adopting a trial and error approach. However, lithium bis(oxalato) borate (LiBOB) has emerged as one of the most common additives in recent years, and has been used in various studies to stabilise high-voltage cathodes.[28,76–78] LIBOB is specifically a film-forming agent that shows favourable effects of reducing impedance and transition metal dissolution. The difluoro derivative, LiDFOB, also shows these desirable properties whilst displaying better protection towards corrosion of the Al current collector, when employing lithium bis(fluorosulfonyl)imide (LiFSI) as the electrolyte salt.[76] This would be desirable when moving away from $LiPF_6$ towards salts that do not face contamination from hydrogen fluoride and consequential unwanted side reactions. Furthermore, the formation of a fully fluorinated CEI has shown to be robust against oxygen release and consequential phase degradation in Li-rich NMC cathodes, when using a LiDFOB additive.[28]

1.6 Anode Materials

Graphite is the most widely used negative electrode material for lithium-ion batteries, owing to its high theoretical capacity of 372 mA h g^{-1}, low operating voltage down to 0.1 – 0.05 V vs Li^+/Li, and low toxicity. When paired opposite a cathode material, Li^+ reversibly intercalates between the graphite layers during charge and discharge. The mechanism of intercalation during the electrochemical reactions proceeds *via* the formation of staged structures with varying amounts of Li existing between the interlayer graphite spacing.[79] This is evident in the multiple potential plateaus of the charge-discharge profile of graphite, which represent the phase transition between the different Li-intercalated graphite structures. The complete intercalation of graphite can also lead to the formation of Li plating and dendrites on the surface of the electrode. These dendrites build up overtime with continuous electrochemical cycling of the graphite, and in some cases their protrusion can destroy the thermal stability of the SEI layer, as well as react violently with the electrolyte, and even pierce the separator thus initiating a short circuit.[80,81]

As well as intercalation hosts like graphite, the spinel structure of lithium titanate or LTO ($Li_4Ti_5O_{12}$) is an insertion type anode which operates at slightly higher voltages around 1.55 V vs Li^+/Li and therefore can avoid Li plating. LTO can afford high safety and long cycle life performance due to displaying minimal volume changes during Li insertion/extraction and the absence of an SEI formation. However, the theoretical capacity (175 mA h g^{-1}) is much lower than graphite, as is the ionic and electrical conductivity of LTO in its de-lithiated state due to the empty 3d orbitals of Ti^{4+} and its large band gap (~2 eV),[82] ultimately resulting in their poor rate performance.[83–85] Whilst

$Li_4Ti_5O_{12}$ is inherently an insulating material, with an electronic conductivity around 10^{-13} S cm^{-2}, even slight lithiation can significantly enhance its conductivity, reportedly reaching 10^1 S cm^{-2} in the rock salt Li_7 phase.[86–88] Furthermore, the $LiTi_2O_4$ spinel structure is superconducting below a critical temperature of ~13 K, with the enhanced conductivity arising from an electronic conduction path formed by edge-sharing TiO_6 octahedrons with LiO_4 tetrahedrons supplying the accommodating charge reservoir.[89,90]

Alloying anodes (such as Si, Al, Sn, Sb) are another set of anode materials that have also been explored as a drop-in alternative to the intercalation materials. Of these elements, Si anodes have gained the most attraction due to its exceptionally high theoretical specific capacity (3579 mA h g^{-1} based on $Li_{15}Si_4$) and wide resource availability in the Earth's crust. However, all alloy materials suffer from heavy volume changes during cycling, and in fact is most excessive for Si which can reach up to 300% expansion, compared to ~10% for graphite.[91,92] The continuous volume changes lead to severe particle fragmentation and pulverisation, which also propagates to cracks in the strongly bonded SEI layer, allowing electrolyte penetration. This can have the detrimental effect of forming a new SEI around individual particles, electrically isolating the pulverised particles, thus reducing conductivity and limiting the cycle life.[93]

1.7 Summary and Future Directions

The energy density of a lithium-ion battery can be manipulated and optimised by considered selection of the cathode and anode materials. At the cathode, the presence of transition metals capable of multiple redox reactions to accommodate a larger proportion of Li^+ intercalation will enable higher capacities, whilst improved rate

performances can be achieved by crystal structures intrinsic of rapid electronic and ionic conductivity. Additionally, cathodes with higher reduction potentials (most positive) and anodes with the lowest reduction potentials (most negative) should be selected to maximise the operating voltage window, without compromising the stability of the electrolyte. The performance parameters of the cathode must also be balanced by low criticality of its constituting transition metals. Therefore, the optimisation of cobalt-low or cobalt-free cathode materials, which minimise the need for the critical and expensive metal which suffers from considerable supply risk, is of significant importance.

Ni-rich layered oxides, such as NMC ($Ni \geq 0.8$), are considered the most appropriate cathode material for achieving higher energy density Li-ion batteries to satisfy the driving range requirements for BEVs. However, the severe structural and thermal instability synonymous with the high Ni which manifests in irreversible phase transitions, Li/Ni disorder, and highly reactive particle surfaces, result in considerable capacity degradation during practical operation.

The particular synthetic method of the cathode is not only an optimisation strategy, but is key to the particular scalability of the material. Co-precipitation can be easily adapted to large scale production with use of a CSTR (continuous stirred tank reactor), as well as delivering high yields, cost efficiency, and careful design of the cathode structure and morphologies, although careful selection of reaction conditions and precursors is critical for achieving optimal material properties.

Both bulk doping and surface coatings offer effective strategies to enhance the cycle life and stability of Ni-rich cathodes, yet each method comes with inherent limitations, such as low doping efficiency and reduced Li-ion conductivity in coatings. A combination of both approaches could yield synergistic benefits, but industrial application remains

challenging due to the sensitivity of Ni-rich materials to moisture and residual lithium sources. The push towards higher operating voltages for increased energy density introduces greater instability of the CEI, which require the use of electrolyte additives to mitigate degradation from detrimental side reactions and further capacity fade.

A holistic approach is essential for designing next-generation Ni-rich cathodes, considering material supply, synthesis methods, and scalable, sustainable production. Critical raw materials used during synthesis and modification must be carefully selected to ensure long-term availability and reduced dependence on geopolitically sensitive resources. Synthesis methods should balance performance enhancement with cost-effectiveness and environmental impact, favouring techniques that minimize waste and energy consumption. Scale-up must prioritize reproducibility and sustainability, ensuring that lab-scale innovations translate efficiently to industrial production without compromising material quality or electrochemical performance. Integrating these factors will be key to developing high-performance, commercially viable Ni-rich cathodes for future energy storage systems.

1.8 Thesis Objectives

This project focuses on understanding the performance and limitations of the Ni-rich layered material, $LiNi_{0.9}Mn_{0.05}Co_{0.05}O_2$ (NMC 90-5-5), as a cathode for Li-ion batteries. The material was chosen as it is the most likely successor to the current NMC811 technology utilised for high energy density EV applications. As discussed, the increased Ni content encourages more severe crystal structure degradation and surface reactivity, accumulating in rapid capacity fading.

The specific objectives of this thesis are:

- Develop and optimize the synthesis and processing conditions of Ni-rich NMC cathodes, exploring strategies to reduce costs during the firing process, whilst stabilising the detrimental cation mixing in the bulk and lithium residual compounds at the surface.
- Enhance the stability and cycle life of Ni-rich NMC cathodes through advanced doping strategies to suppress the excessive crystal structure degradation caused by irreversible phase transitions at high voltages.
- Characterise the influence and mechanism of doping on the reaction kinetics and thermodynamics in Ni-rich NMC cathodes.
- Evaluate the practical application of Ni-rich NMC cathodes in full-cell configurations, optimizing electrode and cell design for performance in power cells and towards high-energy lithium-ion battery applications.

1.9 Layout of Thesis

The research objectives are subsequently investigated in the following chapters:

Synthesis Development: Chapter 3 establishes the coprecipitation method for the synthesis of the transition metal hydroxide precursor and explores the subsequent firing conditions used for the calcination of a stable Ni-rich active cathode material (NMC 90-5-5). Boron containing flux additives were introduced during sintering to enable lower firing temperatures and shorter firing times. The effect of the firing conditions on the bulk

and surface structure of the cathode materials was studied alongside the changes in electrochemical performance.

Dopants: Chapter 4 further explores the surface and bulk stabilisation of NMC 90-5-5 by the introduction of boron and dual tin-boron doping strategies to extend the cycle lifetime of the cathode. The mechanism of the doping stabilisation towards the capacity degradation was studied by comprehensive characterisation for comparison of the pristine and cycled cathode materials. The influence of doping on the reaction kinetics are also extensively explored under different temperatures.

Full Cell Optimization: In Chapter 5, the doped cathode materials from Chapter 4 are then validated in full cells against graphite to test their practical application. The study evaluates the effects of cathode doping and electrode capacity balance variations on the stoichiometry, rate capability, and long-term stability across coin and pouch full-cells. Finally, the cell design was adjusted for high-energy applications with high mass loading electrodes to study the performance limitations in these full-cells.

Chapter 2 Experimental Methods

This chapter details the materials and experimental methods used in the synthesis, characterisation, and electrochemical testing of the cathode materials used throughout this PhD research.

2.1 Materials Preparation

2.1.1 Co-precipitation synthesis

The Ni-rich NMC materials made in this work were produced by the co-precipitation method, which is a common technique used in the industrial production of cathode active materials (CAM). The widespread adoption of this method arises from its advantages of providing a homogenous atomic mixing, control of particle size and morphology, and ease of process scalability.[94,95]

The co-precipitation reaction itself more specifically refers to the synthesis of the precursor cathode active material (pCAM), which in this work is the mixed transition metal hydroxide, $Ni_{0.9}Mn_{0.05}Co_{0.05}(OH)_2$, which is subsequently mixed with a lithium source and calcined to produce the lithiated transition metal oxide.

Synthesis of the pCAM relies on a chemical reaction between a mixed metal salt solution and a precipitating agent in the presence of a chelating agent. The reaction mechanism follows a process of nucleation of transition metal hydroxides, growth of these nuclei into the formation of primary particles, and aggregation of sufficiently sized primary particles into larger secondary particles.[96] An aqueous solution of mixed metal salts (2 mol L^{-1}) in this case $NiSO_4.6H_2O$, $CoSO_4.7H_2O$, and $MnSO_4.H_2O$, is prepared in the desired stoichiometric ratio, and separately a solution (2 mol L^{-1}) of NaOH and NH_4OH is prepared at a suitable concentration ratio between the precipitating and chelating agents

respectively. The two solutions are fed into the reactor vessel by peristaltic pump which is kept at a constant internal temperature (typically between 50 – 80°C) under a flowing N_2 atmosphere, which is employed to prevent undesirable oxidation of Mn^{2+}.[97] A pH probe is also inserted into the vessel to maintain the desired pH (usually between 10 – 11), with the feed rate of the $NaOH/NH_4OH$ solution varied during the reaction to counter any deviation registered. The formation of the hydroxide precursor follows a two-step process, in which TM ions in solution are first complexed with the ammonium ions, which slows down the nucleation rate. Following this, the TM ions are gradually released and react with the hydroxide ions to form precipitates.[98] The procession of the complex-precipitation mechanism can be described by the following reaction sequence:

$$TM^{2+} + xNH_4OH\ (aq)\ \rightarrow [TM(NH_3)_n]^{2+}\ (aq) + xH_2O \tag{2.6}$$

$$[TM(NH_3)_n]^{2+}\ (aq) + yOH^- \rightarrow TM(OH)_2\ (s) + nNH_3.H_2O\ (aq) \tag{2.7}$$

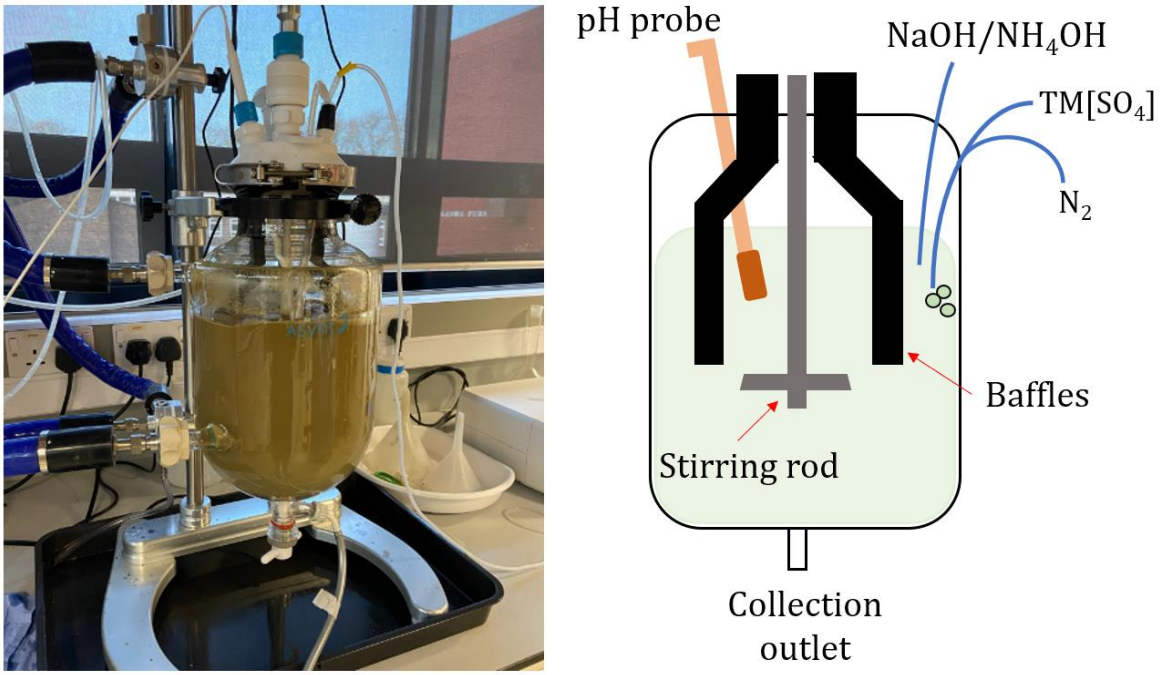

Figure 2.1: CSTR (5 L) rig used for the coprecipitation synthesis of the $Ni_{0.9}Mn_{0.05}Co_{0.05}(OH)_2$

After stopping the feed of both reactant solutions, the mixed solution was continued to stir vigorously for another 24 h whilst kept under a N_2 atmosphere to encourage further particle growth and sphericity. The precipitate hydroxide pCAM is then filtered under vacuum and washed with copious amounts of deionised water to achieve a close to neutral pH, by removing any unwanted ions, such as unreacted metal salts and residual anions that can affect the precursor crystallinity. The filtered material was then dried in a vacuum oven at 120°C to for 12 h to enable sufficient removal of the residual process water.

In this work, LiOH monohydrate (≥99.9%, Sigma-Aldrich) was used as the lithiating agent during the calcination, which was first ball milled at 300 rpm for 2 h and subsequently and dried under vacuum at 120°C. The LiOH was combined with the pCAM in a molar ratio of TM/Li = 1: x (x = 1.05 – 1.10) and mixed in a ball mill at 200 rpm for

30 min to give a homogenous mixture. The mixed powders were compressed into round bottom rectangular alumina crucibles (Almath) by hand and fired in a tube furnace (Carbolite) either in air or under flowing oxygen. In the latter, the tube was initially allowed to purge for 2 h at an oxygen flow rate of 0.5 L min^{-1} prior to starting the first temperature ramp. The firing process followed a two-hold step procedure, in which the temperature was first brought to a lower hold temperature (T1: 450 – 550 °C) at a rate of 2 °C min^{-1} and held for 5 h, before ramping to the second temperature (T2: 750 °C) at the same rate and holding for 5 – 15 h. The furnace was then cooled to 80 °C at a rate of 1 °C min^{-1}, before transferring directly to an argon filled glovebox to minimise exposure to air and moisture. The active cathode powder was ground with pestle and mortar if required and sieved through a 105 μm mesh sieve prior to use.

2.1.2 Electrode Preparation

The cathode coatings were prepared using the synthesised NMC active material along with a poly(vinylidene fluoride) (PVDF, Solef 5130, Solvay) binder, carbon black (C65, Imerys) conductive additive, synthetic graphite (KS6L, Imerys), with n-methyl-2-pyrollidone (NMP) solvent. LFP, C65, and KS6L was mixed into a PVDF solution (8 wt% in NMP) at a 90: 5: 2: 3 wt% ratio for the desired electrode formulation with a targeted solids total of 42 wt.% in the slurry. The mixing of the active material, conductive carbons, and binder solution was performed in a sealed jar with a Thinky ARE-250 Planetary Mixer. The precise mixing procedure of the cathode ink had the following steps:

1. The carbons were added into half of the desired PVDF solution and then mixed at 1400 rpm for 5 mins.

2. NMC was added to the thick slurry, followed by the remaining PVDF solution then mixed at 1400 rpm for 3 mins.

3. NMP was added to reach the target solids content, then mixed again at 1400 rpm for 3 mins, followed by a degassing step at 1600 rpm for 2 mins.

The well mixed cathode inks were then coated onto aluminium foil (16 μm) using a doctor blade with an automated drawdown device. The coatings were initially dried on a hot plate at 60 °C, and then transferred to a vacuum oven set at 120 °C for 24 h. Once dried, the electrodes were calendared at 80 °C to a desired thickness as to obtain an electrode porosity of 30% by adjusting the gap between the heated rollers of the calendaring press (MSK-HRP-01, MTI Corporation, USA).

To calculate the electrode porosity, the electrode density (ρ_f) was first calculated from the material densities of the electrode components using Equation 2.3, in which m and ρ represent the wt.% and density of the specific component in the electrode formulation.

$$\rho_f = \frac{1}{\left(\frac{m_{NMC}}{\rho_{NMC}}\right)+\left(\frac{m_{PVDF}}{\rho_{PVDF}}\right)+\left(\frac{m_{C65}}{\rho_{C65}}\right)+\left(\frac{m_{KS-6L.}}{\rho_{KS-6L}}\right)} \quad (2.8)$$

The true density of the electrode (ρ_{el}) is calculated using the relationship between the electrode mass (m_{el}), thickness (Th_{el}), and area (A_{el}) as given in Equation 2.4. The volume fraction (ε) is then calculated by dividing the different electrode densities, from which the electrode porosity (ε_{ac}) is yielded by rearranging Equation 2.5, and finally converted from a fraction to a percentage.

$$\rho_{el} = \frac{m_{el}}{Th_{el} \times A_{el})} \quad (2.9)$$

$$\varepsilon = \frac{\rho_{el}}{\rho_f} = 1 - \varepsilon_{ac} \tag{2.10}$$

All steps involved in the electrode preparation process was carried out in a dry room (Munters) which had a maximum dew point of −40 °C.

2.1.3 Cell Assembly

Coin Cells

To perform the electrochemical characterisation of the synthesised active cathode materials, half-cell testing was performed in two-electrode coin cells (CR2032). The electrodes were punched at a 14.8 mm diameter using a high precision electrode cutter (EL-Cut, EL-CELL). As seen in Figure 2.2, the stainless-steel casing housed the working electrode coating and the Li metal counter electrode, separated by a 16 µm PP/PE/PP trilayer microporous membrane (Celgard H1609) which was wetted with 70 µL of 1 M $LiPF_6$ in a 30: 70 wt.% mix of ethyl carbonate (EC) and ethyl methyl carbonate (EMC) with 2 wt.% additive of vinylene carbonate (VC). Once assembled, coin cells were sealed using a hydraulic crimper (MSK-110, MTI Corporation) by applying a pressure of 1000 psi.

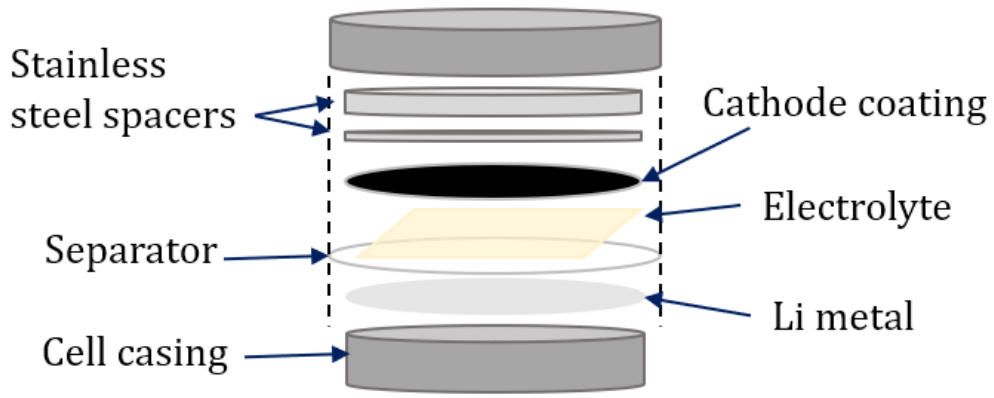

Figure 2.2: Schematic of the coin cell parts and assembly for half-cell testing.

Pouch Cells

For the full-cell testing in Chapter 5, single-layer pouch cells were also assembled from cathode and anode coatings which were punched out to the desired geometry using a swing arm cutting press (Global Cutting Technologies). The coatings were positioned under the cutting die so that the part of the electrode coating still occupied around a third of the tag, leaving the remaining space to be uncoated so that the tabs could be attached. Similar to the coin cells, the cutting die for the anode coating was designed to punch a larger area compared to the cathode to prevent misalignment and possible lithium plating at the edges of the negative electrode.[99] The tabs were welded onto the exposed current collector tags using an ultrasonic metal welder (Cambridge Energy Solutions). For the cathode electrodes coated onto aluminium foil, an aluminium tab was also used, whilst a nickel tab was employed for the anode materials coated onto copper foil. The electrode stacking was performed using the fold method described in Figure 2.3, in which the electrodes were wrapped in sufficient separator and divided by a single layer of the separator (2325, Celgard) material, ensuring the tabs are not covered by the separator. The electrode stack was then placed between two layers of pouch bag material and heat sealed at three of the edges so that the electrolyte could be pipetted directly onto the separator via the one exposed edge, before heat sealing the pouch closed. The pouch was left for a couple of hours to allow the electrolyte to soak, following which the pouch was cut open and resealed under vacuum.

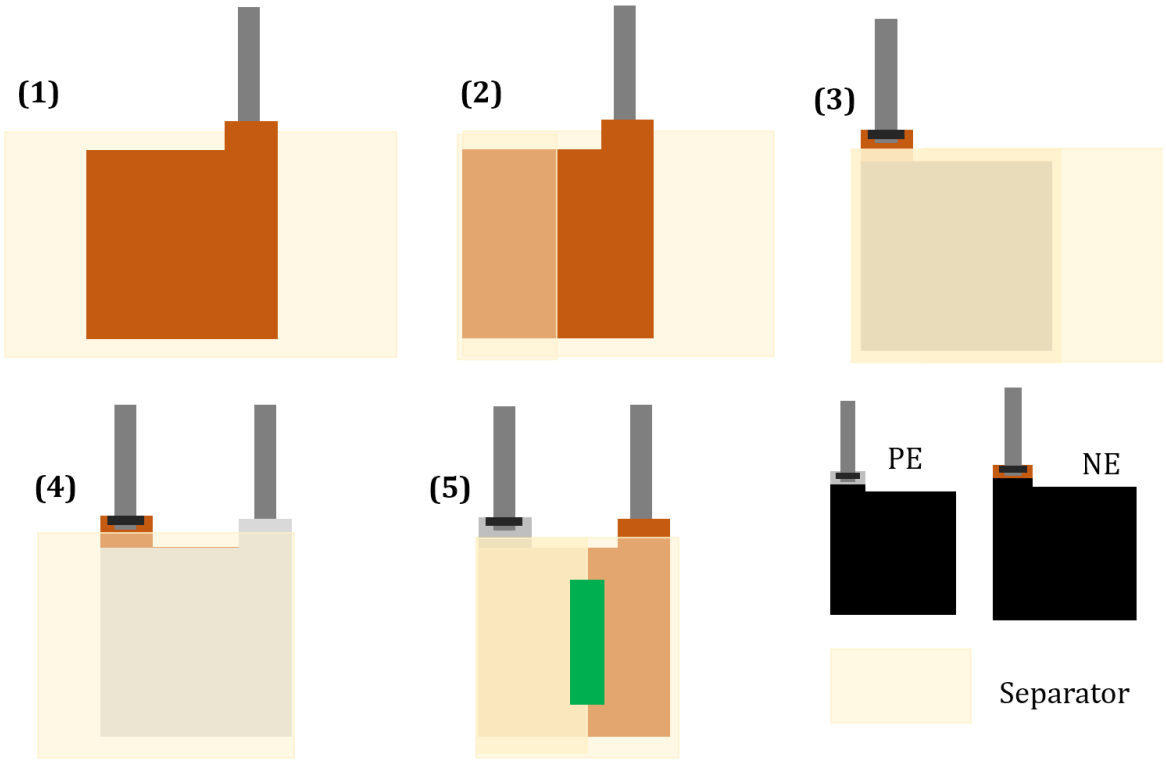

Figure 2.3: Assembly of the electrode stack used in full pouch cells, consisting of the negative electrode (NE) coated on copper foil, positive electrode (PE) coated on aluminium foil, and separator.

Three-electrode Cells

In the conventional two-electrode set-up, the measured voltage profile of a full-cell is a representation of the overall cell performance, which may mask the identity of the limiting electrode. The introduction of a third 'reference' electrode into full-cell configurations enables the isolation of the potential profiles of both the anode and cathode. This is especially important for monitoring and preventing cell degradation, particularly from lithium-metal deposition (Li plating) which can occur in graphite when the potentials drops below 0 V vs Li/Li^+. The onset of this plating results in larger impedances in the cell as well as accelerating potential safety issues if dendritic structures are formed.[100,101] Implementing a reference electrode can decouple the electrode voltages and thus guide cell design to mitigate possible degradation mechanisms. Lithium metal is often used as the reference electrode because it provides a

stable and well-defined potential. However, some disadvantages pertaining to galvanic corrosion and possible side reactions have led to the exploration of alternative reference electrodes, such as LFP and LTO.[100,102] The two-phase behaviour of these materials which corresponds to extended plateaus in their voltage profiles is favoured due to the resulting stable potential, low polarizability, and fewer side reactions it provides over this window.[103]

Three-electrode configured PAT-Cells (EL-Cell) were also used in Chapter 5 to elucidate the voltage profiles of each electrode in the assembly of NMC-graphite full-cells at different electrode capacity balances. For cell assembly, the positive and negative electrode coatings were transferred to an argon filled glovebox, where discs of 18 mm diameter were punched out. The cell stack was assembled as displayed in Figure 2.4, in which the electrodes are inserted into the insulation sleeve (ECC1-00-0210-V/X) which included a PP fibre and PE membrane separator (FS-5P), and a lithium metal reference ring, all contained in a PP sleeve.

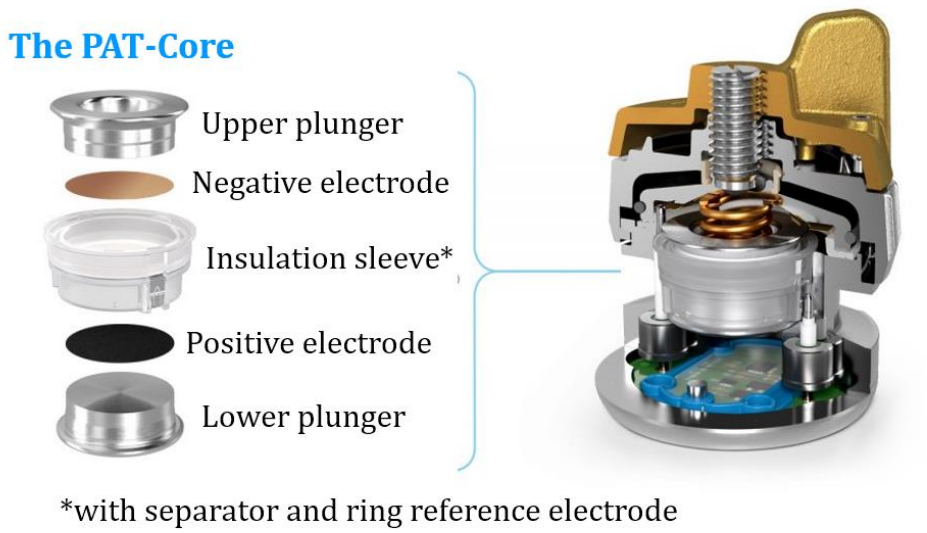

Figure 2.4: Three-electrode cell set-up in a PAT cell (EL-Cell) for full-cell testing.

2.2 Physical Characterisation

2.2.1 Powder X-ray Diffraction (XRD)

X-ray diffraction (XRD) is a powerful analytical technique used to determine the crystalline structure of materials. Diffraction occurs due to the wavelength of these electromagnetic waves (0.1 – 100 Å) being of the same order of magnitude as the interlayer spacings of the crystal lattice (~0.5 – 5 Å). Diffraction patterns can be collected based on the constructive interference of X-rays scattered by the electron cloud around atoms in a periodic arrangement of a crystalline material, as described by Bragg's law:

$$n\lambda = 2d\ sin\,\theta \tag{2.11}$$

Where n is the order of diffraction, λ is the wavelength of the X-ray source, d is the inter-planar spacing, and θ is the angle of incidence (or diffraction).[104]

The measurement is performed in an X-ray diffractometer, in which X-rays emitted from the source are directed at the sample stage and then the diffracted X-rays are collected at the detector. The angle of incidence and detector angles are varied so that a one-dimensional diffraction pattern can be collected in the desired 2θ range.

Each crystal structure has a distinct set of interplanar spacings and symmetry elements, which result in a characteristic set of diffraction peaks at specific angles. Therefore, the precise crystalline phases present in a material can be identified from the specific diffraction pattern. Variations in atomic positions, unit cell dimensions, and symmetry lead to shifts in peak positions, intensities, and widths, providing insights into structural properties such as lattice strain, defects, and crystallite size. The latter can also be obtained using the Scherrer equation:

$$D = \frac{K\lambda}{\beta\ cos\,\theta} \tag{2.12}$$

which relates the Bragg broadening (β) of a peak, taken as the FWHM corrected for instrumental broadening, the Bragg angle of the peak (θ), the wavelength of the X-ray (λ), and the shape factor (K), typically taken as 0.9, to the crystallite size (D).

The structural properties of the synthesised active materials characterised by XRD in this work was performed using an X-ray diffractometer (AXRD Benchtop, Proto) with a Cu $K\boldsymbol{\alpha}$ source, λ = 1.5406 Å. Diffraction data was collected in a 2θ range of 15 – 70° at a scan rate of 1° min^{-1}. To collect higher resolution data for Rietveld refinements, a larger 2θ range of 15 – 90° was scanned at a slower rate of 0.25° min^{-1}.

Structural Refinements

The identification of crystalline phases can be performed by indexing the peaks in a measured XRD pattern by assigning the peak positions to a set of Miller indices (*hkl*), which arise from a specific set of lattice planes. Rietveld refinement employs a non-linear least squares method to fit a structural modal to the experimental data. The technique enables optimisation of the calculated pattern fit by simultaneously refining multiple parameters such as; lattice parameters, peak profile parameters, atomic site occupancies, and thermal parameters. The background is typically modelled with a Chebyshev polynomial, and it is important to have this well-established along with the lattice parameters and peak profiles before refining the atomic structure model. The quality of the fit can be assessed by a number of parameters, such as the profile factor (R_p), weighted profile factor (R_{wp}), and the overall 'goodness of fit' (χ^2), whilst the plot of the difference between the calculated and experimental profiles allows for a visual comparison.

All of the refinements presented in this work were conducted in the GSAS software and visualised using the EXPGUI interface.[105,106] The structure was refined from an initial phase based on NMC 811 material with α-$NaFeO_2$ structure type and space group R-3m (ICSD_CollCode169367).[107]

2.2.2 X-ray Photoelectron Spectroscopy (XPS)

XPS is a strong tool for conducting surface analysis on a material to identify the constituent elements present at the surface and interfaces, and elucidate key information about these elements, such as their oxidation state and chemical environment.

In XPS measurements, a sample is irradiated by an X-ray source at a sufficient energy (hν) to initiate the excitation of a core electron by the emission of a photoelectron *via* the photoelectric effect. The kinetic energy (E_{KE}) of the emitted electron is measured, from which the binding energy (E_{BE}) can be determined from rearranging the following expression:

$$h\nu = E_{BE} + E_{KE} + \Phi_{spec} \quad (2.13)$$

which states that the energy of the X-ray is completely transferred to the core electron and is equal to the sum of its binding energy and resulting kinetic energy when emitted, plus the work function of the spectrometer (Φ_{spec}). The binding energy of an electron is a measure of how strongly bound to an atom or orbital and thus is influenced by its chemical environment. In the case of C 1s, the binding energy is strongly influenced by the electronegativity of neighbouring elements, with a more electronegative adjacent atom resulting in an increase in E_{BE}. In this way, XPS can be used to identify and distinguish between specific functional groups such as C−O, C=O, and CF_2 which appear

at increasing binding energies in an XPS spectra. For transition metals, oxidation state has the most significant effect on the binding energy, which increases with the valence state, as electrons become more difficult to remove from atoms with a larger positive charge.[108]

Due to the low inelastic mean free path of the emitted electrons, XPS is a surface-sensitive technique, with the maximum sampling depth typically limited to around 10 nm when using an Al Kα X-ray source, as employed in this project. To analyse deeper layers of the sample, depth profiling can be performed using argon ion milling, in which the sample is sputtered for a short period of time, and then XPS is collected again. However, some caution should be applied when interpreting the results after depth profiling as the cations in transition metal oxides may be reduced as a result of preferential oxygen sputtering.[109]

XPS experiments in Chapter 3 were performed using an ultra-high vacuum spectrometer (Escalab 250XI, Thermo Fischer Scientific, UK) using a monochromatic Al-K*α* source (1486.74 eV) and a flood gun for charge neutralization. Depth profiling was performed on the electrode samples using Ar^+ sputtering. The XPS experiments in Chapter 4 were performed on a different ultra-high vacuum spectrometer (Versaprobe III, PHI) however utilised the same X-ray source and use of a flood gun. CasaXPS software was used for the analysis of the XPS data, in which the spectra were fitted using Voight (mixed Gaussian-Lorentzian) functions and Shirley backgrounds. The binding energies were scaled to the adventitious C 1s peak, which was set at 284.8 eV.

2.2.3 X-ray Absorption Spectroscopy (XAS)

X-ray absorption spectroscopy (XAS) is a powerful technique used to study the local electronic and structural environment of elements in a material. It relies on the interaction of X-ray photons by core electrons of an atom (K, L, or M shell), causing excitation to unoccupied states or ionization, and leaving a core level hole. The absorption edges arise from these specific electron excitations at X-ray energies characteristic to the element. The edge energy is also dependent on the atomic number, increasing for heavier elements.

In the transmission mode, the transmitted intensity is measured at different X-ray energies while scanning across an element absorption edge, from which the X-ray absorption coefficient, μ(E), is determined based on the Beer-Lambert law. Near the absorption edge, changes in μ(E) reflect electronic transitions, and so provide information on the oxidation state and chemical bonding. In the extended X-ray absorption fine structure (EXAFS) region, oscillations in μ(E) result from interference effects due to scattering of the emitted photoelectron waves by neighbouring atoms, giving structural information regarding local environment, such as interatomic distances and coordination number. Spectra collected from XAS measurements contains both the X-ray Absorption Near Edge Structure (XANES) and EXAFS as depicted in Figure 2.5.

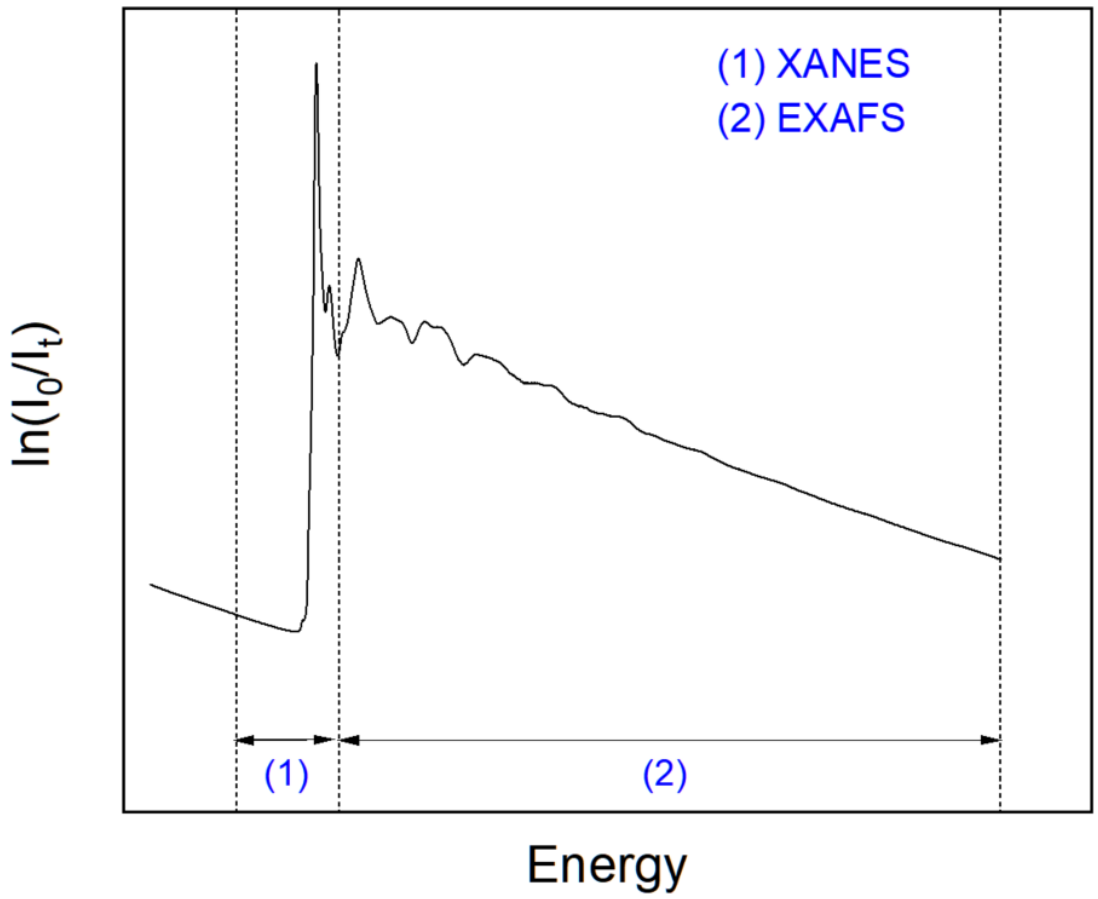

Figure 2.5: The defined XANES and EXAFS regions with the X-ray absorption spectrum.

For the cathode material XAS samples, pellets of 13 mm diameter were prepared by grinding the cathode active powder or reference material with PVP (Sigma Aldrich) until a homogenous colour, and then pressed at a pressure of 5 tons using a manual press. The required amount of the material was calculated using the XAFSmass software, based on the molecular weight and optimised for the desired edges. In the case of the $LiNi_{0.9}Mn_{0.05}Co_{0.05}O_2$ samples, this equated to ~7 mg for the Ni edge and ~20 mg for the Co and Mn edges. The pellets were arranged into a sample rack holder, and Kapton tape was placed between the samples to help with rigidity without completely covering them. The sample rack was then placed in an aluminium foil bag and sealed under vacuum.

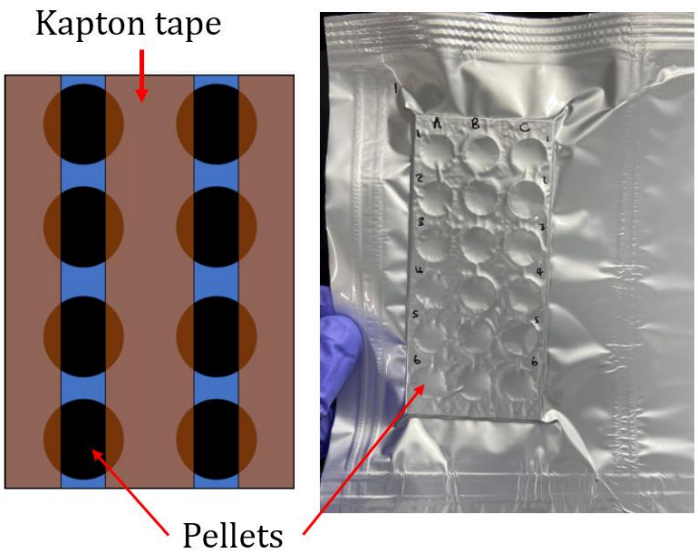

Figure 2.6: Sample rack used to mount active material pellets (13 mm diameter) or electrode discs (12 mm diameter) for XAS measurements.

The XAS data was collected at beamline B18 at the Diamond Light Source (UK) and measured at the Ni, Co, and Mn K-edges. X-ray absorption near-edge structure (XANES) spectra and Extended X-ray absorption fine structure (EXAFS) spectra were collected in transmission. The Ni, Co, and Mn K-edge spectra were aligned and calibrated using a reference foil that was collected simultaneously during each measurement. Data analysis was carried out using the Athena software.[110]

2.2.4 Scanning Electron Microscopy

The surface morphology of a material can be investigated with scanning electron microscopy (SEM) by scanning the surface of a solid sample with a focused electron beam. The interaction of the beam with atoms at the surface results in the ejection of back-scattered and secondary electrons which are collected at a detector and transformed into a three-dimensional image which contains detailed surface characteristics of the specimen.

The morphology of the cathode materials investigated in this project consist of primary particles which agglomerate into larger secondary particles of pseudo-spherical shape. The general shape and size of the secondary particles is established during the synthesis of the precursor material, which in the case of this project was largely determined by the experimental inputs for the coprecipitation method. The primary particle size is typically influenced by the following calcination step, in which the temperature, heating rate, and holding times can directly influence the particle growth and extent of sintering. The observed particle morphology and size will impact the specific electrochemical properties of the electrode material, whether through influencing the packing efficiency of the secondary particles in the electrode, or the exact diffusion length of the Li^+ through the primary particles.

The morphology of the cathode materials was observed using a Zeiss EVO10 field emission electron microscope, operated at an accelerating voltage of 15 keV and a probing current of 50 pA. The sample stage was brought up to a working distance between 9 – 10 mm, from which the focus and stigmation were gradually adjusted to sharpen the image. The microscope was also coupled with an energy-dispersive spectroscopy (EDS) detector which was utilised for elemental analysis of the materials. The cathode materials were sputter-coated with gold nanoparticles to provide a conductive surface which helps prevent the charging typically observed in these poor electrical conductors.

2.3 Electrochemical Testing

Testing of half- and full-cells under galvanostatic charge-discharge cycles, along with the galvanostatic intermittent titration technique (GITT) tests were performed on a Bio-

Logic BCS 805 series battery test system. Electrochemical impedance spectroscopy (EIS) measurements and galvanostatic cycling of three-electrode EL-Cells were conducted using a Bio-Logic VMP3 system.

2.3.1 Galvanostatic Cycling

The standard cell testing employed in this work was galvanostatic cycling, in which cells are subject to charge and discharge using a constant current from which the voltage response is observed. The constant current used in each cell test was determined from the active material mass based on the desired current rate chosen for the particular charge and discharge operation. In this work the current rate used refers to a gravimetric current density or specific current (mA g^{-1}), from which the required current is calculated from the active mass of the cathode material in the electrode using:

$$I = I_m \times (f_A \times (m_{elec} - m_{cc})) \quad (2.14)$$

Where I is the current (mA), I_m is the specific current (mA g^{-1}), m_{elec} and m_{cc} are the mass of the electrode coating and the current collector (both in g), and f_A is the fraction of the active mass in the electrode, typically 90% in this work.

In the cases where a C-rate was used, the required charge and discharge currents were calculated based on the practical specific capacity of the active material (Q/ mA h g^{-1}), which was taken as the discharge capacity at the end of the second formation cycle when tested in a half-cell. The product of this specific capacity, the active mass in the electrode, and the desired C-rate gives the required applied current for the cycle. The C-rate refers to the specific current required to discharge the battery in one hour.

Upon assembly, cells were left to rest at their OCV for 8 hours to allow for complete electrolyte wetting of the separator and electrodes in the cell before starting any

electrochemical testing. The standard formation protocol used for all cells in this work, constituted two cycles in which the cell was charged to the upper voltage limit at a constant current (CC) density of 10 mA g^{-1}, proceeded by a constant voltage (CV) step for the duration at which the current relaxed back to a tenth of the value applied in the cc step. The cell was then allowed to rest for 15 min, followed by a CC discharge step at 10 mA g^{-1} to the lower voltage limit, after which the full CC-CV-CC cycle was repeated.

2.3.2 Differential Capacity

Differential capacity analysis can be applied to the voltage profiles collected during the galvanostatic charge and discharge of a cell to elucidate further understanding of the particular lithiation equilibria and phase transitions occurring at the electrode. When the derivative of the galvanostatic capacity response (dQ/dV) is plotted, peaks appear in place of the plateau regions in the voltage-capacity profiles due to dV tending to zero. The physical representation of the voltage plateaus denotes a two-phase region which can be associated with phase transitions that occur due to a distinct change in lithiation equilibria. Sloping regions instead relate to solid solution behaviour, where the variation of lithiation is constant and no discrete phases arise.[111]

The particular peaks in the dQ/dV of electrode materials measured in half-cells have been well characterised to known structural phase transitions. Therefore, observed changes in the position, intensity, and shape of these identified peaks with increasing cycles can be used as a tool for identifying degradation mechanisms over the lifetime of a battery.[112]

2.3.3 Potentiostatic Electrochemical Impedance Spectroscopy

Electrochemical impedance spectroscopy (EIS) is a common technique used to measure the dynamics of electrochemical processes in a battery. EIS operates by the perturbation

of an electrochemical system at equilibrium or steady state through the application of a sinusoidal signal across a broad frequency range. The system's response, in the form of a corresponding sinusoidal signal, is then monitored to analyse its impedance characteristics. When performed in the potentiostatic mode (PEIS), as was utilised for the tests in this project, the impedance response (AC current) to an applied AC voltage is measured.[113] The application of the voltage under AC conditions, Ohms law (R = V/I) can be expressed as an impedance, Z(ω) , which is described as the resistance that disturbs the current flow in a circuit after applying the AC voltage.

$$Z(\omega) = \frac{V(\omega)}{I(\omega)} = \frac{V_m \, sin(\omega t)}{I_m \, sin(\omega t - \phi)} \quad (2.15)$$

Where ω is the angular frequency ($2\pi f$) of the AC voltage, which results in a phase difference (ϕ) between the applied voltage V(ω) and measured current I(ω), relating to the time constant of the process at the specific frequency. The impedance can also be expressed in terms of imaginary numbers by using the complex function $j = \sqrt{-1}$ and the application of Euler's formula which is simplified to:

$$Z(\omega) = Z_0 \, cos(\phi) + Z_0 \, sin(\phi) j \quad (2.16)$$

Which is divided into the real ($Z_0 \cos(\phi)$) and imaginary ($Z_0 \sin(\phi)$) parts which relate to the resistance (Z'_{real}) and the combination of the capacitance and inductance (Z''_{img}) respectively. The data collected during EIS is typically presented in a Nyquist plot, which plots $-Z''_{img}$ on the y-axis against Z'_{real} on the x-axis.

The characterisation of the complex processes occurring within lithium-ion batteries by EIS is possible as the different physical, electrical, and electrochemical phenomena operate on distinct time scales. As a result, the impedance contributions from these processes manifest in different frequency regions of the impedance spectrum, allowing

them to be decoupled and individually examined. By fitting the EIS data to an Equivalent Circuit Model (ECM), these processes can be represented using common electrical components such as resistors, capacitors, and inductors. These elements are arranged in specific configurations in a circuit to simulate charge transfer resistance, double-layer capacitance, electrolyte resistance, and diffusion-related processes. The fitting model is used to return numerical values for the circuit elements to aid quantification of the reaction processes contributing to battery performance and degradation.

The EIS data collected in this project was typically fitted with the ECM depicted in Figure 2.7, which contains resistors (R) and constant phase elements (CPE). The single R element connected in series is used to represent the electronic (or Ohmic) resistance of the cell. When the R is placed in parallel with a capacitor, which describes the double layer capacitance which forms due to charge separation at the electrode-electrolyte interface, the transient interfacial behaviour in a battery can be represented. This RC loop is physically represented by a perfect semi-circle in the Nyquist plot, however in practice the collected data typically displays a flattened or depressed arc due to the dispersion effect. This effect represents the deviation away from ideal capacitance behaviour due to the changing porosity and surface roughness of the electrode interface as a result of the evolving passivation surface films.[114] As a result, the capacitors are replaced with CPEs, to which no physical interpretation can be assigned, however the value of its associated exponent denotes the extent of the deviation from ideal capacitance (equal to 1) towards a true resistor (equal to 0).[115,116] The other main feature in the Nyquist plot in Figure 2.7 is the ~45° tail in the low frequency region which is characteristic of the solid-state diffusion processes within a cell. This is typically modelled by a Warburg element, however in this work only the mid-to-high frequency regions (i.e. the distorted semi-circles) were modelled, and so the Warburg element was not included in the ECM.

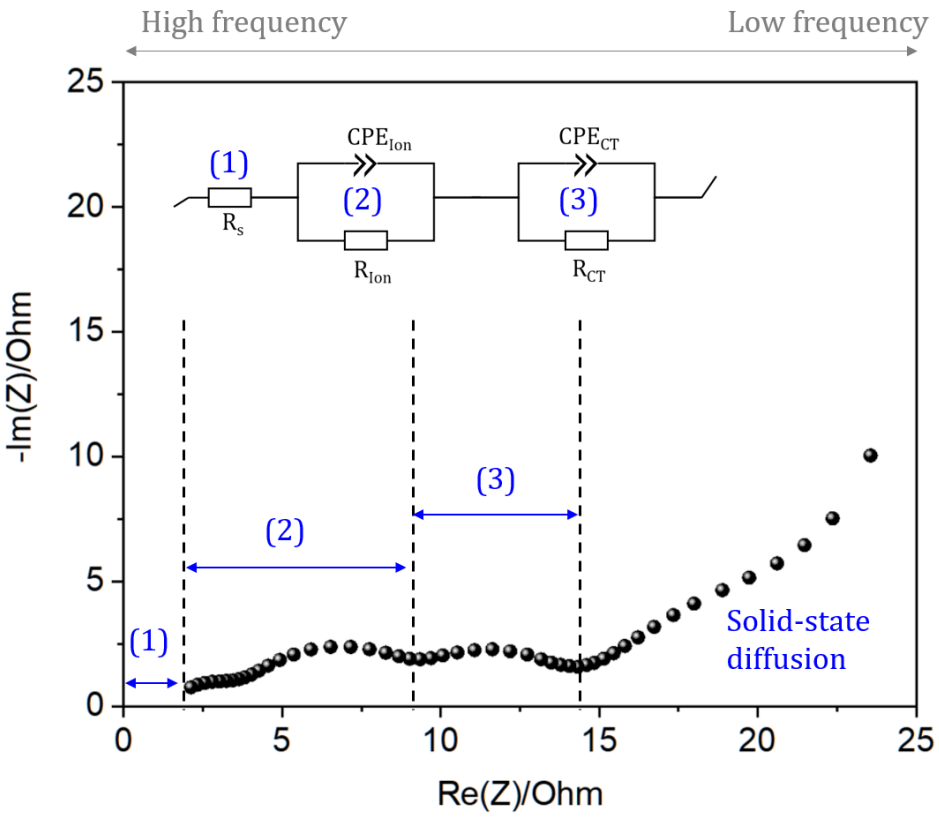

Figure 2.7: Nyquist plot displaying the typical EIS response for a lithium-ion cathode half-cell and the corresponding equivalent circuit model which could be used to fit the data. Adapted from [117] *with permission under a Creative Commons license.*

PEIS was performed in coin half-cells in Chapter 3 and Chapter 4, and on full-cells in both coin and pouch formats in Chapter 5. The measurements were recorded after formation, usually at various points within the 4.3 – 2.5 V potential window. A low current rate was used to charge or discharge the cell to the desired voltage, and then was left to rest at OCV for at least 30 min prior to the PEIS test which scanned a frequency range between 100 kHz and 10 mHz, with an amplitude of 10 mV.

2.3.4 Galvanostatic Intermittent Titration Technique

The solid-state lithium ion diffusion coefficients (D_{Li}) can be determined by galvanostatic intermittent titration technique (GITT), based on the method proposed by Weppner and Huggins.[118] During the GITT measurement, the system is systematically perturbed by the

application of a constant current pulse for a short time, and then is allowed to relax for a longer period of time so that the system can reach a near steady state as it tends to the equilibrium voltage. The voltage is monitored over the duration of the technique in both the transient (V_t) and steady state regions (V_s). The overall voltage changes in these regions, as shown in Figure 2.8, are extracted to calculate the apparent diffusion coefficients at different lithium stoichiometries, whilst the ohmic (IR) drops can also be decoupled.

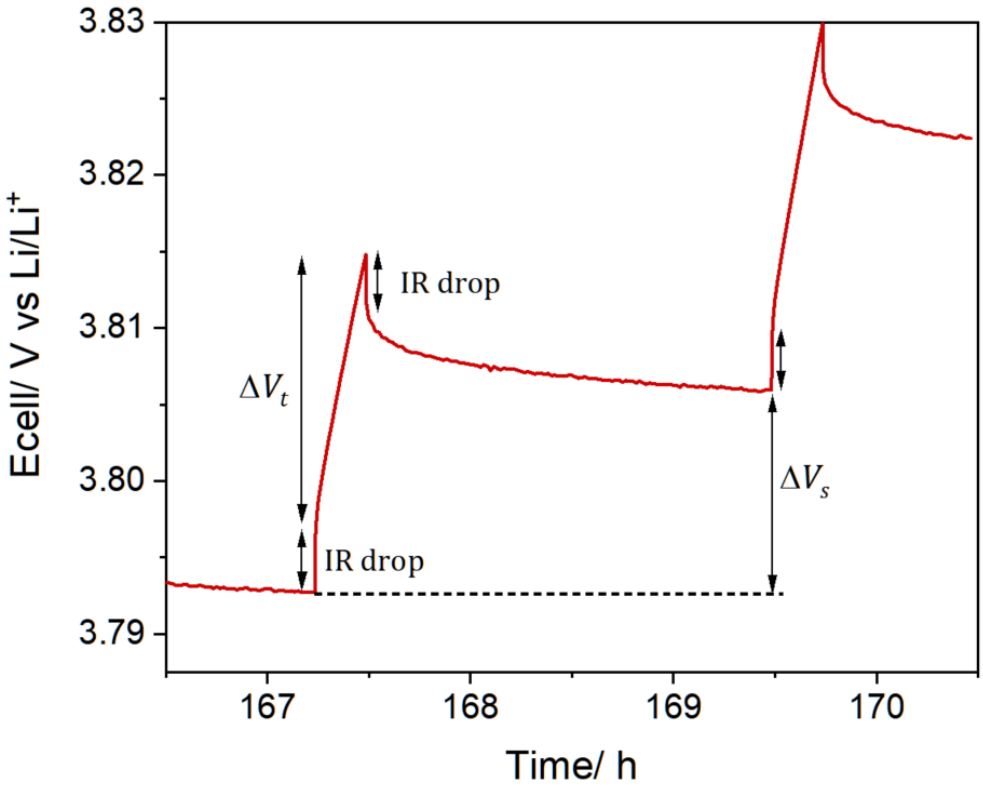

Figure 2.8: Section of the recorded GITT data showing a single current pulse (transient) and subsequent voltage relaxation (steady-state) as well as the associated IR drops. Adapted from [119] *with permission under a Creative Commons license.*

The calculation of the diffusion coefficients in the model for GITT developed by Weppner *et al.* relies on several simplifying assumptions around electrochemical charge transport and system dimensions. These assumptions include one-dimensional diffusion in a dense electrode, governed by Fick's laws within a thin film near the electrode/electrolyte

interface, treating the medium as semi-infinite. Concentration variations in the electrolyte, phase transformations, and volume or porosity changes are considered negligible. Additionally, the diffusion coefficient is assumed constant during each pulse and relaxation period, while overpotentials at the electrode/electrolyte interface and electrochemical double-layer capacitance are ignored.[120] These simplifications enable apparent diffusion coefficients to be extracted using the following equation:

$$D_{Li+} = \frac{4}{\pi}\left(\frac{iV_m}{nFS}\right)^2 \left(\frac{dV_s/d\delta}{dV_t/dt^{0.5}}\right)^2 \quad (2.17)$$

Where i is the applied pulse current (A), V_m is the molar volume of the active materials (m^3 mol^{-1}) based on their molecular weight and true density, n is the number of transferred electrons (1), F is the Faraday constant (C mol^{-1}), and S is the electrode active surface area (m^2) as described in Equation 2.13. The gradient $dV_s/d\delta$ refers to the derivative of the OCV with respect to the calculated lithium concentration in the electrode, $dV_t/dt^{0.5}$ is the slope of the linearized plot of the transient voltage within the duration of the current pulse, which holds if short time intervals are used ($t \gg L^2/D_{Li+}$).[120–122]

$$S = \frac{\varepsilon_{act} V_{elec}}{V_{particle}} SA_{particle} \quad (2.18)$$

Where ε_{act} is the active material volume fraction, V_{elec} is the volume of the electrode disc, $V_{particle}$ is the volume of the active material particle, and $SA_{particle}$ is the surface area of the particle, which is assumed to be spherical.

Chapter 3: Investigation of Firing Conditions and Boron Fluxes for the Optimised Synthesis of $LiNi_{0.9}Mn_{0.05}Co_{0.05}O_2$ for High Energy Density Li-ion Batteries

This work has been published in ChemElectroChem, 2025, **12**, e202400677 (Ethan Williams, David Burnett, Peter Slater, Emma Kendrick)

DOI: celc.202400677R1

Submitted: 24/02/2025

Accepted: 09/03/2025

Author contribution: E.W. and E.K. conceived and designed the research. E.W. performed the experiments, characterisation, electrochemical testing, and data analysis. D.B. helped with design of the coprecipitation rig. All authors provided comments and revisions of the manuscript.

The authors acknowledge use of the Cambridge XPS System, part of Sir Henry Royce Institute - Cambridge Equipment, EPSRC grant EP/P024947/1. The XPS data was collected at the Maxwell Centre, University of Cambridge, by Dr Carmen M. Fernandez-Posada.

3.1 Introduction

Lithium-ion batteries (LIBs) have played a pivotal role in the transition to an electrified society, becoming the dominant energy storage technology for a wide range of applications, from portable electronics to hybrid and electric vehicles, due to their high energy density.[123] The synthesis of Ni-rich layered oxides, especially those for which Ni ≥ 0.8 is a challenging hurdle that must be overcome for the realization of batteries with greater energy density. The main source of their problems is associated with the high Ni content, which promotes a more reactive surface oxygen, making these materials more sensitive to air and moisture.[124,125] The larger proportion of Ni^{3+} in the bulk of Ni-rich cathodes contributes also to its highly unstable nature and weak bond with oxygen. This leads to oxygen release, the accompanying reduction of Ni^{3+} to Ni^{2+}, and the formation of oxygen defects during the firing process.[126,127] It is therefore necessary to use an oxygen-rich environment during synthesis whilst a long hold at high temperatures (750 - 900°C) are traditionally employed to ensure the formation of a well-ordered layered structure, leading to higher manufacturing costs.

In traditional ceramics manufacturing, mineralisers or flux agents can be added during calcination to reduce the temperature and firing time to produce the active materials.[128] This produces significant energy and cost savings when producing ceramics. Due to their strong fluxing properties, one class of traditionally used mineralisers are boron compounds such as boric acid and borax.[129–131] Mass transfer in solid-state synthesis is predominantly controlled by grain boundary migration. Growth proceeds by Ostwald ripening, in which larger grains consume smaller grains by minimising surface energy.[132] During the coprecipitation synthesis stage, particles with desirable primary and secondary structures are produced.[133] Care must be taken during the sintering stage to maintain or improve these.

Using flux agents or mineralisers, can promote interface atomic diffusion at temperatures below the melting point of LiOH.[134] This has encouraged the use of some lithium-based fluxes in the synthesis of single-crystal cathode materials, including Ni-rich (≤80mol% Ni) layered oxides, which are added in excess quantities to promote growth in molten salt.[135–139] However, this method requires additional washing and post-heat treatment steps, adding further cost and time during large-scale production.

The introduction of some boron additives (such as B_2O_3 and H_3BO_3) during calcination have previously revealed improved structural and electrochemical properties in Ni-rich lithium-ion cathode materials due to the presence of strong B—O bonds.[60,140,141] The introduction of boron additives have also been demonstrated to be desirable in their tendency to promote the formation of rod-like crystallites, which can mitigate microcracking by relieving internal particle strain.[142,143] However, their influence on optimising the calcination step during the synthesis of Ni-rich materials has not previously been studied. In this work, two boron-containing flux agents, boric acid (H_3BO_3) and borax ($Na_2[B_4O_5(OH)_4]$), were added as mineralisers (extra ions) during the firing step reduce the temperature and time needed to produce higher Ni content polycrystalline $LiNi_{0.9}Mn_{0.05}Co_{0.05}O_2$ and their role in stabilising the cathode structure and electrochemical performance is evaluated.

3.2 Experimental

3.2.1 Synthesis of $LiNi_{0.9}Mn_{0.05}Co_{0.05}O_2$ (NMC 90-5-5)

The NMC 90-5-5 materials were synthesised *via* a hydroxide coprecipitation in a 5 L continuously stirred tank reactor. An aqueous metal solution was prepared from stoichiometric amounts of $NiSO_4.6H_2O$, $CoSO_4.7H_2O$, and $MnSO_4.H_2O$ and pumped into the reactor. Separately, aqueous solutions of NaOH (2 mol L^{-1}) and NH_4OH (2 mol L^{-1}) were

mixed before being fed into the reactor to act as precipitating agent and chelating agent. The reaction solution was maintained at pH 11 and temperature of 80 °C throughout the duration of the coprecipitation. The solution was allowed to age for 12 h before filtration and aqueous washing. After the filtrate was dried under vacuum at 120 °C overnight, >200 g of the transition metal hydroxide precursor, $Ni_{0.9}Mn_{0.05}Co_{0.05}(OH)_2$ was collected and ground into a fine powder.

For the baseline material, $Ni_{0.9}Mn_{0.05}Co_{0.05}(OH)_2$ (4.00 g) was mixed with a 5 mol % excess of pre-milled LiOH (1.08 g) in a planetary mill at 300 rpm for 30 mins. The mixed powders were then fired in a box furnace under air, in a two-step firing procedure, holding first at a lower temperature (T1 = 500 °C) for 5 h and then up to the higher temperature (T2 = 750 °C) for a further 15 h.

In the modified firing reaction, 0.5 mol % of either boric acid (H_3BO_3, HB) or borax anhydrous, ($Na_2[B_4O_5(OH)_4]$, BX) were added as a mineraliser to the precursor material along with the LiOH. The powders were milled as previous and then fired in a box furnace under air, or in a tube furnace if under a flowing oxygen atmosphere, at 0.5 L min^{-1}, in a two-step firing procedure, holding first at a lower temperature (T1 = 400, 450, 500 °C) for 5 h and then up to the higher temperature (T2 = 700, 750 °C) for a further 5 h.

3.2.2 Materials Characterisation

Powder XRD of the materials was collected on a laboratory diffractometer using a Cu K$\boldsymbol{\alpha}$ source, in a 2$\boldsymbol{\theta}$ range of 15 – 70° at a scan rate of 1° min^{-1}. To collect higher resolution data for Rietveld refinements, the diffraction spectra of the selected materials were measured again in a 2$\boldsymbol{\theta}$ range of 15 – 90° at a scan rate of 0.25° min^{-1}. The morphology of the prepared cathode powders and electrodes were imaged using a Zeiss EVO10 scanning

electron microscope using an accelerating voltage of 15 kV and a probing current of 50 pA. The elemental distribution of the particles was analysed with the energy dispersive X-ray (EDX) spectrometer attached to the SEM. The cross-sections of the electrodes were prepared using a microtome blade.

The surface chemistry of the cathode materials was characterised using Fourier-transform infrared spectroscopy (FTIR) and X-ray photoelectron spectroscopy (XPS). The FTIR measurements were recorded on Thermo Scientific FTIR iS50 for 16 scans in the range of 4000 – 400 cm^{-1}. XPS was performed on an ultrahigh-vacuum Escalab 250XI spectrometer (Thermo Fisher Scientific) with the samples transferred to the instrument under argon to avoid air exposure. The instrument was operating in constant analyser energy mode, using a monochromatic Al-Kα source (1486.74 eV) and a flood gun for charge neutralization. Survey scans were acquired using pass energy of 100 eV, 900 **µ**m spot size, 0.5 eV step size, and dwell of 50 ms. For narrow scans the number of scans was 50, using pass energy of 30 eV, step size of 0.05 eV, dwell time of 2500 ms, with spectra from two different areas of the samples collected and the results averaged. Depth profiling was performed on the electrodes using Ar^+ sputtering, with spectra recorded after 60 s and 120 s exposure. The energetic position of the C 1s emission line (284.8 eV) was chosen to calibrate the energy scale of the spectra. Fitting was performed in CasaXPS using Voight-type line shape LA(1.53, 243) and a Shirley background.

3.2.3 Electrochemical Testing

The positive electrodes were fabricated based on a formulation consisting of 92% active material, 3% PVDF (Solef 5130, Solvay), 3% carbon black (Super 65, Imerys), and 2% synthetic graphite (KS6L, Imerys) by weight, mixed together to form a homogenous slurry and coated onto aluminium foil. Electrodes were dried overnight at 120°C and

assembled into CR2032-type coin cells using 1 M $LiPF_6$ in EC/EMC (3:7 by volume) + 2 wt.% VC for the electrolyte solution and Li metal as the counter electrode. The half-cells underwent two formation cycles between at 10 mA g^{-1} between 4.3 – 2.5 V. The short-term cycle life tests were performed at a 1C charge/discharge rate with a slower C/5 rate used every 10^{th} cycle to assess the capacity recovery.

The long-term cycle life tests were performed at a C/2 charge/discharge rate over 200 cycles. The rate capability tests were conducted using 3 cycles with charge/discharge rates varying between C/5 and 5C. The rated capacity of 1C used in these tests to determine the different rates was based on the discharge capacity of the second formation cycle measured at 10 mA g^{-1}. Electrochemical impedance spectroscopy (EIS) was measured between 100 kHz and 10 mHz with an amplitude of 10 mV. Galvanostatic intermittent titration technique (GITT) measurements were recorded by applying C/10 pulses for 20 min followed by a 2 h rest to allow a quasi-steady-state equilibrium to be reached.

3.3 Results and Discussion

3.3.1 Mineraliser Firing Study

The powder XRD patterns of the cathode active materials mineralised with boric acid (HB) and borax (BX) at different furnace conditions are displayed in Figure 3.1. It is observed that the shortening of the high temperature hold from 15 hours to 5 hours has no discernible effect on the NMC structure, with the diffraction patterns of the shorter fired fluxed materials retaining the characteristic peaks of the α-$NaFeO_2$ hexagonal structure in the $R\bar{3}m$ space group, with no impurity peaks observed. The splitting of the (006)/(102) and (108)/(110) peaks in NMC materials are traditionally reported in the literature as an indication for a highly ordered layered structure.[144–146] In both sets of

peaks, the splitting is stronger for the NMC materials fired with HB compared to BX, suggesting the borax introduces more disorder into the cathode structure. It can also be observed that the HB cathodes show a smaller intensity ratio of the $(I_{006} + I_{102})/I_{101}$ peaks at each firing condition, which suggests the boric acid favours a higher degree of hexagonal ordering.[144].

Table 3.1*: The (003) and (104) peak intensity ratios from the XRD diffraction patterns of the different NMC 90-5-5 fired with boric acid (HB), borax (BX), or no mineraliser.*

Sample	**T1/** ℃	**t/ h**	**T2/** ℃	**t/ h**	**Atmos.**	**(003)/(104) ratio**
NMC	500	5	750	15	Air	1.17
HB01, BX01	400	5	750	5	Air	1.18, 0.90
HB02, BX02	450	5	750	5	Air	1.20, 0.98
HB03, BX03	450	5	750	5	O_2	1.14, 1.07
HB04, BX04	450	5	700	5	Air	0.95, 0.87
HB05, BX05	500	5	700	5	Air	1.09, 0.92

The ratio of the (003) and (104) peak intensities have frequently used as an indication of the extent of cation mixing that occurs between the similarly sized Li^+ and Ni^{2+} cations, with a value <1.2 often set as the benchmark for undesirable mixing. The peak ratios along exhibited by the HB and BX cathode materials at different firing conditions are reported in Table 3.1. The calculated lattice parameters can also be found in Table A.1. The samples fired with BX all display a lower (003)/(104) peak intensity ratio and a higher calculated occupancy of Ni on the Li sites, indicating a greater degree of cation mixing. Additionally, the calculated *a*-parameter and unit cell volume are larger in the BX samples at all of the tested firing conditions. This could indicate some of the Na^+ from the

borax becomes incorporated in the lithium layer of the BX samples, but instead contradicts previous suggestions that the larger Na^+ acts to prevent cation mixing by providing steric hinderance.[147]

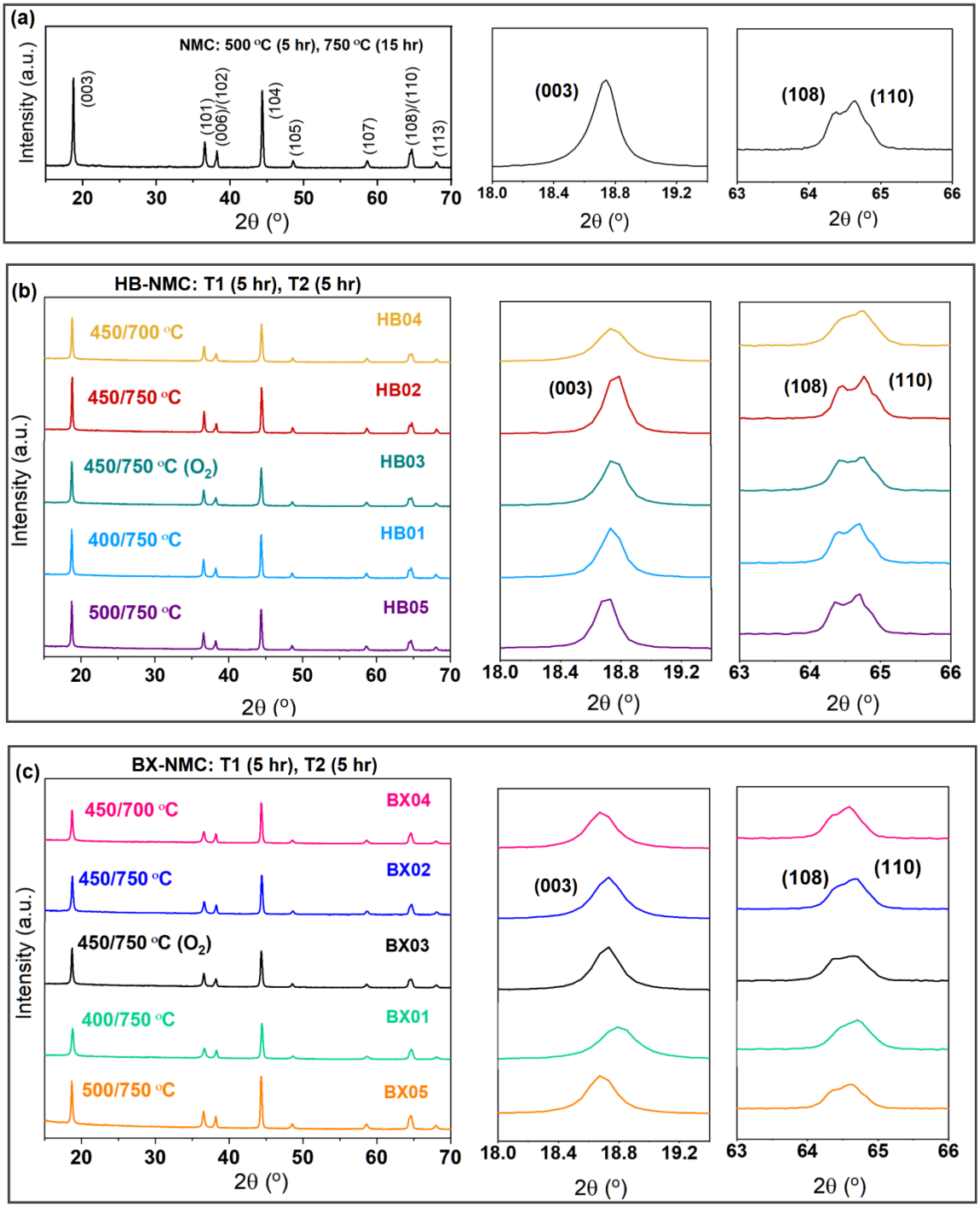

Figure 3.1: XRD patterns (λ= 1.5418 Å) of NMC 90-5-5 prepared: with no mineraliser the standard holding time at 750°C (a), and with the addition of boric acid (b) or borax (c) at 0.5 mol% boron, using a lower hold temperature of 400, 450, or 500°C followed by a shortened holding time of 5 h at 750°C.

The effect of the firing conditions on the lattice parameters are compared in Figure 3.2:.2. When the higher hold temperature (T2) is kept at 750°C, the *a* and *c* parameters in both fluxed materials are at their largest and smallest values respectively at a T1 of 450°C. Firing at this T1 but reducing T2 from 750°C to 700°C results in a shrinking of the *a*-axis and *c*-axis for both HB and BX. Furthermore, these samples show the largest occupancy of Ni in the Li sites, suggesting a T2 of 750°C is required to provide enough thermal energy to promote structural ordering and reduce cation mixing.

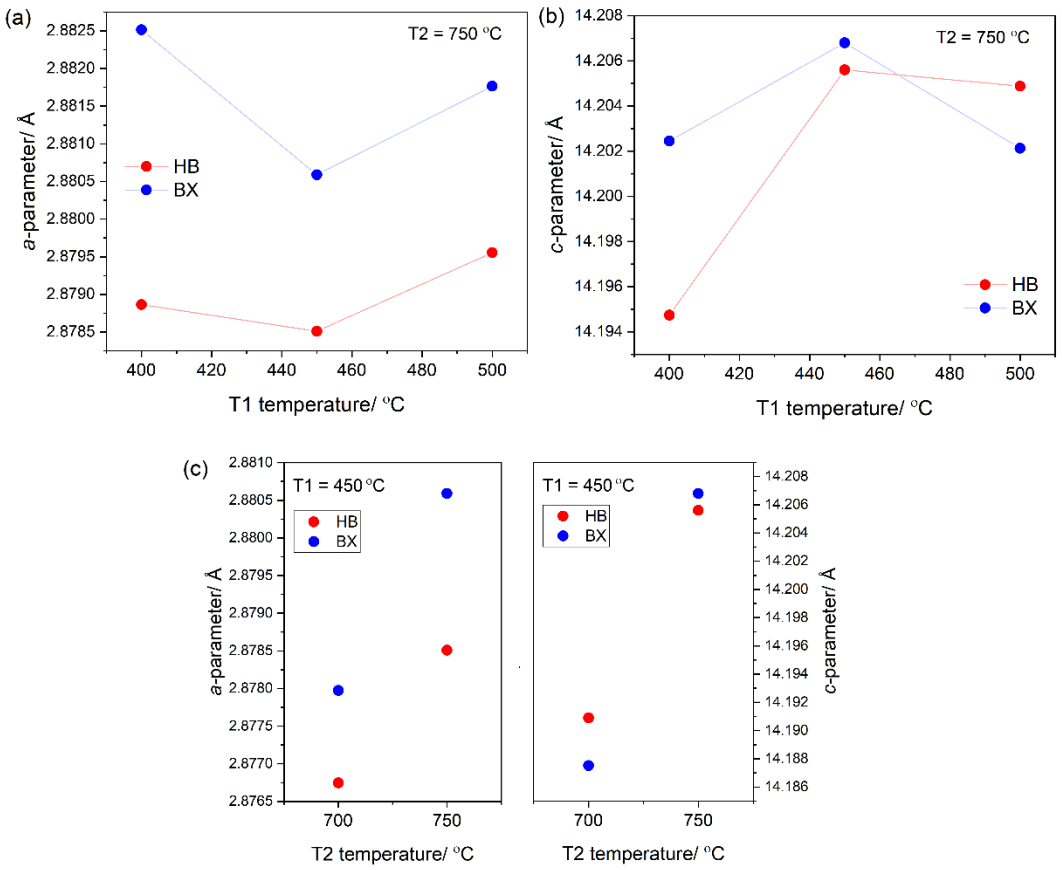

Figure 3.2: Lattice parameters for NMC 90-5-5 samples fired with HB and BX at various lower hold temperatures, T1 (a, b) and higher hold temperatures, T2 (c).

The optimised firing temperatures to minimise cation mixing is also determined as a T1 at 450 °C and T2 at 750 °C. The calcination reaction at these temperatures was also repeated under an atmosphere of flowing oxygen. It is well reported that an oxygen environment can accelerate the oxidation of Ni^{2+} to Ni^{3+}, therefore limiting the Ni^{2+}/Li^{+} mixing and also promoting a higher rate of lithium intercalation *via* the formation of cation vacancies.[148] The effect of the oxygen environment on the (003): (104) was found to show opposing changes for the different mineralisers, with the peak ratio decreasing with HB and increasing with BX compared to when fired in air at the same temperature and duration.

It is noted that the firing temperature and atmosphere used in the calcination synthesis will strongly influence the final structural ordering of the cathode material. Low temperatures may be insufficient in promoting full site ordering, whilst increasing the temperature too high may incur Li disorder on the 3a sites and TM deficiency on the 3b sites.[149] Therefore, care should be taken when interpreting the absolute values of the refined lattice parameters between samples prepared under different firing conditions. The effect of the different boron mineraliser can instead be inferred from the general trends in lattice parameters when comparing between the HB and BX samples, with borax resulting in larger *a*-parameter and lattice volume, as well as a higher proportion of cation mixing.

To examine the effect of firing conditions on the electrochemical behaviour of the mineralised NMC 90-5-5 materials, galvanostatic charge-discharge testing was performed. The first two formation cycles of each material are shown in Figure 3.3**.** The shape of the reversible capacity curves agrees with Ni-rich NMC materials found in the literature. The average initial reversible capacities of the NMC materials ranged from

213.7 mA h g^{-1} for HB02 and 189.9 mA h g^{-1} for BX05, with corresponding coulombic efficiencies of 95.1% and 88.7%. The first cycle loss, which accounts for the irreversible consumption of lithium ions in the first de-lithiation step which cannot then be reinserted back into the layered oxide structure, is found to be lowest in BX02 (a loss of 9.5 mA h g^{-1}).

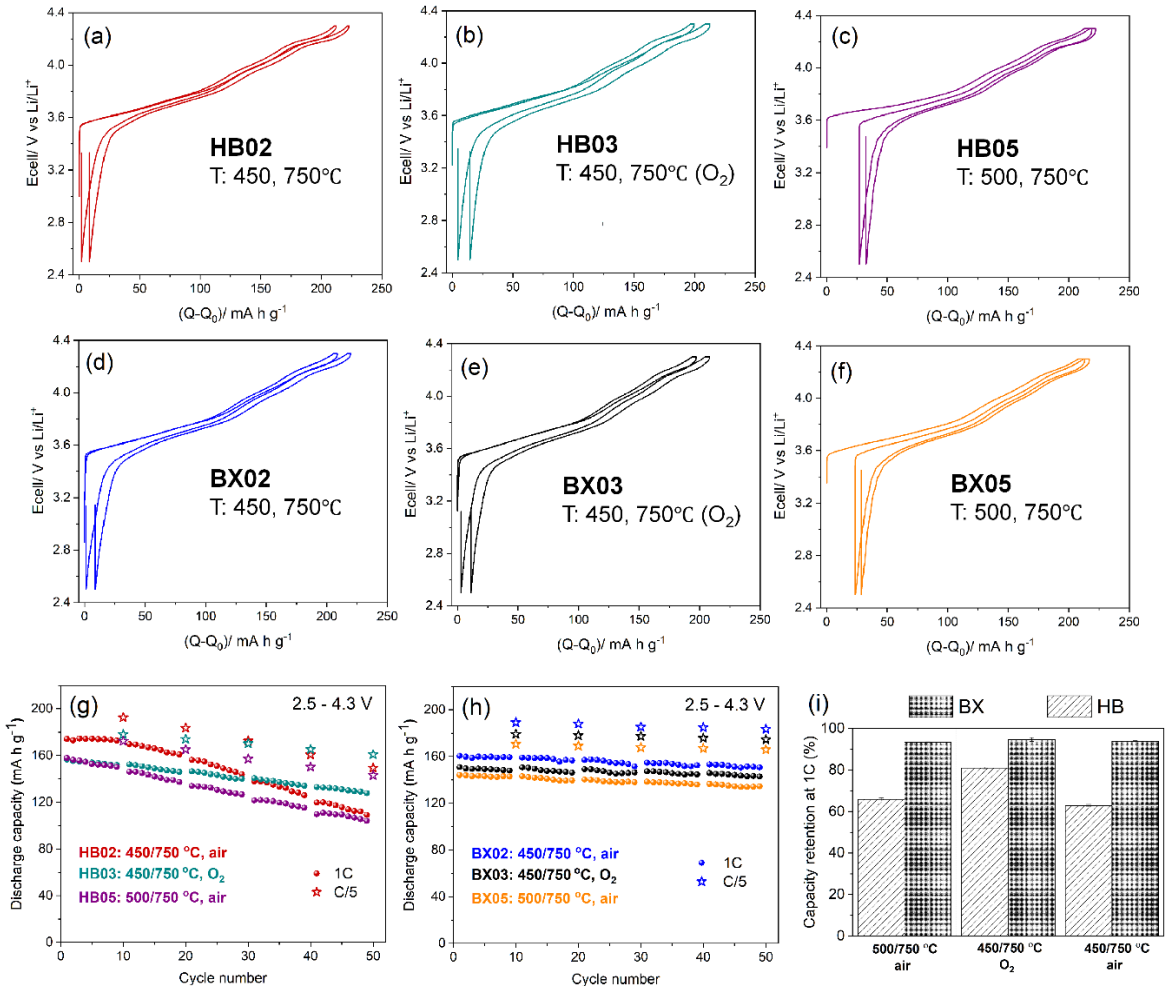

Figure 3.3: (a) – (f) The first and second charge-discharge profiles of the NMC 90-5-5 prepared with boric acid (HB) or borax (BX) in different furnace conditions, in the voltage range of 2.5 – 4.3 V vs Li/Li+ at a specific current of 10 mA g^{-1}. (h) – (i) Cycling performance of the boron fluxed NMC 90.5.5 materials at 1C and C/5 between 4.3 – 2.5 V vs Li/Li+ and the capacity retention after 50 cycles at 1C (j).

The reversible capacities and first cycle losses of all the tested NMC materials are further summarised in Figure A.1. At each of the different furnace conditions, those fired with boric acid display slightly higher reversible capacities, whilst using borax resulted in

lower first-cycle losses. Furthermore, both parameters were optimised with a lower first hold temperature of 450 °C compared to 500 °C and in the absence of a flowing oxygen environment. The higher capacities also align with the higher peak ratio of (003)/(104) measured in the materials with a T1 of 450 °C, which agrees with this measure reflecting a lower proportion of Ni^{2+}/Li^{+} cation mixing.

Whilst the initial capacities of the HB05 and BX05 materials are lower than the expected capacity of NMC 90-5-5, the irreversible capacity losses are still relatively low at 14.3% and 11.3%, respectively, which is at the lower end of the 12 – 30% loss outlined for all layered oxides by Whittingham.[150]

The short-term lifetime of the materials was determined by symmetric 1C charge-discharge cycling, with the depreciation of the resulting discharge capacities shown in Figure 3.3(h-j). In the first 10 cycles, the discharge capacity of HB02 is considerably higher than the other NMC materials, delivering a 1C capacity of 172.9 mA h g^{-1} at its 10th cycle. However, the material experiences significant capacity fade following this cycle and falls to a discharge capacity lower than BX05 (initially the lowest capacity material) after the 33rd cycle. The poor capacity retention was also present in the capacity delivered at the intermittent slower C/5 cycles, suggesting irreversible degradation in the HB materials. Conversely, the cycle stability of the BX cathodes is substantially higher than those fired with HB, displaying capacity retentions between 93.3 – 94.7% after 50 cycles. This variation in capacity stabilisation between the materials fired with HB or BX can be better understood by the dQ/dV plots displayed in Figure A.2. The high voltage peak that is observed around 4.2 V vs Li/Li+ during the de-lithiation process is largely attributed to the H2 to H3 phase transition in layered oxide cathodes, which is associated with

irreversible structure change, resulting in severe capacity fade.[59,60] In each of the BX materials, the H2-H3 phase transition is not reached within the tested voltage range during the 1C cycling. This could be explained by the incorporation of Na^+ into the Li layer as suggested by the expansion of the *a*-axis and unit cell volume in these materials. Such partial occupancy or substitution at the Li sites may help to stabilise the MO_6 octahedral framework by reducing oxygen mobility, thus delaying the detrimental lattice collapse.[151]

Firing in an oxygen atmosphere delivers the highest capacity retention for both mineralisers, however, the more palpable effect is observed for the HB flux, with the capacity retention increasing from 62.9% to 81.0% at the 450°C low-temperature hold.

3.3.2 Role of Boron Mineraliser on the Bulk and Surface Stability

To further understand the effect of the mineraliser on the bulk structure of the NMC 90-5-5 materials, higher resolution PXRD patterns (Figure 3.4) were acquired, and subsequent Rietveld refinements performed and modelled with the $R\bar{3}m$ phase. The results of the fitting are tabulated in Table 3., which shows a slight increase in both the *c*-axis and the lattice volume for the materials fired with small amounts of boric acid or borax. The slight expansion of the unit cell could suggest a small incorporation of the boron into the bulk during the calcination process. The degree of layered ordering can be assessed by the c/a ratio of the lattice parameters, and indicates the deviation away from the value of $\sqrt{24}$ or 4.899, which is representative of the *fcc* NiO rock-salt structure.[152] The c/a value determined for the pristine and fluxed NMC materials are: 4.931 (NMC02), 4.935 (HB02), and 4.932 (BX02), indicating the addition of boric acid results in the highest order of layered structure. To determine the extent of Ni^{2+}/Li^+ mixing from the refinement of the diffraction patterns, the $(Li_{1-x}Ni_x)_{3a}(Li_xNi_{0.9-x}Mn_{0.05}Co_{0.05})_{3b}$ structural model was used, similar to that previously adopted in the literature.[153,154]

Table 3.2: Lattice parameters and cation exchange of Ni^{2+} into the 3a sites of NMC 90-5-5 samples synthesised in air at a T1 = 450 °C and T2 = 750 °C.

Sample	*a*/ Å	c/ Å	Volume/ $Å^3$	Ni in Li site/ %	Rwp/ %
NMC02	2.87851(6)	14.1962(3)	101.868(4)	8.31(1)	3.5
HB02	2.87851(2)	14.2056(2)	101.936(2)	6.76(5)	3.4
BX02	2.88059(5)	14.2058(4)	102.085(4)	11.1(1)	3.1

In this model, the Mn and Co occupancy fractions were kept constant at 0.05 in accordance with the NMC 90-5-5 chemical composition, whilst the additional Li atom is introduced into the transition metal layer on the 3b sites and a Ni atom in the Li layer on the 3a sites. The fraction of the Ni (3b) and Li (3a) atoms were then constrained to fluctuate with respect to the Li (3b) and Ni (3a) by equal and opposite proportions, to compensate for cation mixing in both layers. The results of the refinement show the boron mineralisers act in opposing effects on the cation mixing of the synthesised NMC, with an increase in the Ni^{2+}/Li^{+} site exchange observed with the borax, whilst the use of boric acid acts to stabilise the cation migration. One of the physical effects of Li^{+} moving into the 3b sites, is a widening of the transition metal layer due to the larger ionic radius of Li^{+} compared to Ni^{2+}, which is accompanied by an increase in the c-axis. However, the increase of the *c* parameter in HB02 with respect to NMC02 despite the lower proportion of Ni^{2+}/Li^{+} exchange, could provide further evidence of minor bulk penetration of the boron mineralisers. An increase along the *a*-axis is also observed for BX02, which corresponds to an increase in the Li layer spacing. The *a* parameter in HB02 is instead unchanged compared to NMC02, which suggests the increase seen for BX02 is due to the

incorporation of some Na^+ from the borax into the lithium layer, consistent with the larger ionic radius of Na^+ compared to Li^+ (1.02 Å and 0.76 Å).[155]

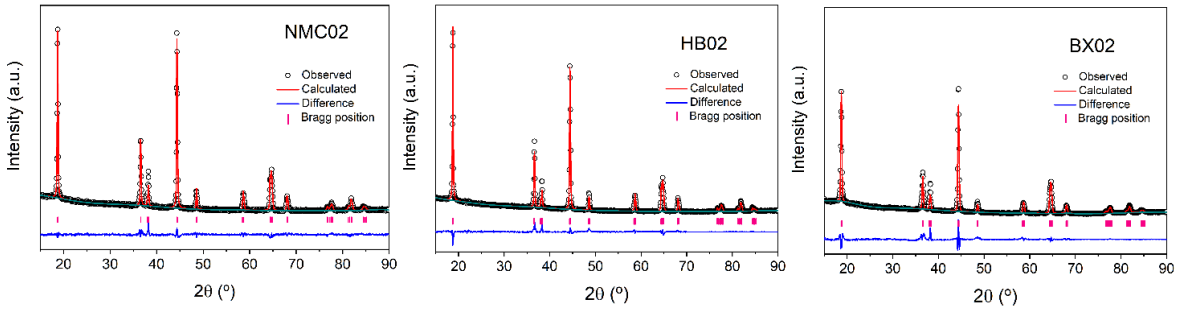

Figure 3.4: Observed, calculated and difference profiles from Rietveld refinements using powder XRD data for NMC02 (a) HB02 (b) and BX02 (c).

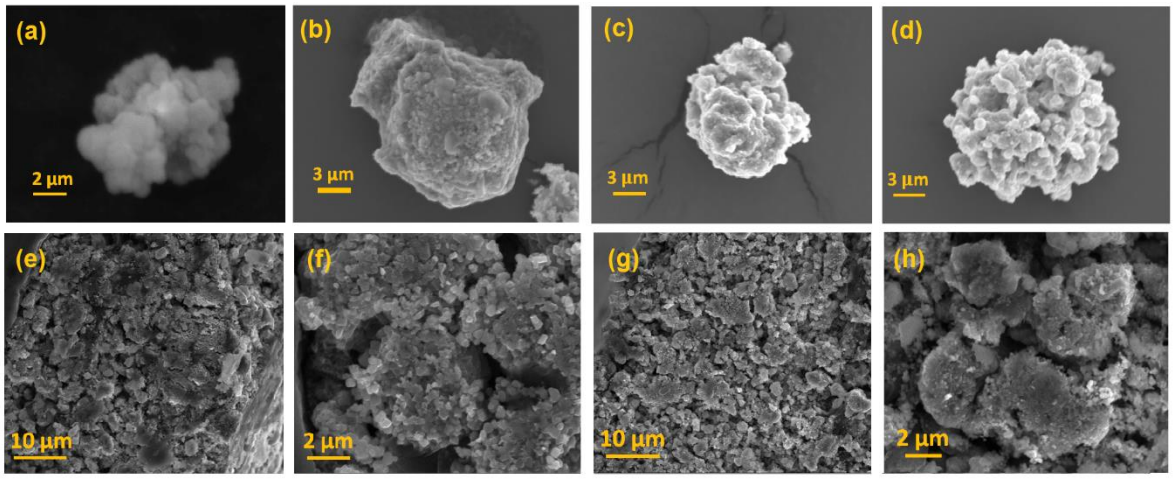

Figure 3.5: SEM images of the hydroxide precursor powder (a), and the active material powders of NMC02 (b), HB02 (c), and BX02 (d). SEM images of the electrode cross-sections of HB02 (e – f) and BX02 (g – h).

The particle morphologies of the hydroxide precursor and active materials calcined at 450/750°C with HB, BX, or no flux are compared in Figure 3.5. The precursor material morphology consists of 1 µm sized globules, which are agglomerated into irregular clusters of sizes <5 µm. After firing, additional particle growth appears due to particle fusing at temperature, which is especially prevalent in materials fired with the boron mineralisers. The surface of the particles is smooth and shows no unprecipitated impurities, suggesting the washing stage successfully removed these species. The

secondary particle morphology of all the active cathode materials shows irregular polycrystalline particles measuring at a size <10 μm. The cathode materials prepared with the different boron fluxes show a similar particle size distribution as observed in Figure A.3, with D50 values of 7.1 $\pm$ 0.1 μm and 8.2 $\pm$ 0.2 μm for HB02 and BX02 respectively. Additionally, BX02 displays a larger tail at higher particle sizes, suggesting the material fired with borax has a greater tendency to agglomerate. However, the size of the secondary particles can largely be expected to remain unchanged from the precursor, and instead the effect of the flux on morphology and size is better understood by the change in the primary particles. The average crystallite sizes calculated from the Scherrer equation using the FWHM of the most intense diffraction peaks are displayed in Table 3.3 The addition of either the boric acid and borax demonstrates different effects on the crystallite size of the NMC 90-5-5 primary particles. The FWHM of the (003) peak is smallest for HB02, which can be indicative of good crystallinity, as well as larger grain size.[138] When comparing both the d(003) and d(104) values of HB02 to NMC02, the HB appears to promote elongation of the primary particles, which coincides with previous reports of preferential (003) faceting by the addition of boron into the lattice of Ni-rich cathodes.[141,156] With the addition of BX, peak broadening and consistent decrease in the crystallite size is observed, suggesting this flux inhibits excessive grain growth which can occur when the sintering aid segregates at the grain boundaries. This is also evident in the morphology of the HB02 and BX02 primary particles in Figure 3.5e-h, obtained from the cross-sectional SEM.

In addition to crystallite size effects, peak broadening may also arise from lattice microstrain or compositional inhomogeneity induced by boron incorporation in the structure or non-uniform boron solubility at the grain boundaries. These factors can

coexist, manifesting in local lattice distortions and collectively influence the observed FWHM, complicating direct interpretation using the Scherrer equation alone.[157]

Table 3.3: Crystallite size calculated from the broadening of the 003 and 104 peaks according to the Scherrer equation for NMC 90-5-5 samples synthesised in air at a T1 = 450 ℃ and T2 = 750 ℃.

Sample	NMC02	HB02	BX02
d(003) / nm	44 ± 2	52 ± 4	37 ± 2
d(104)/ nm	48 ± 1	48 ± 2	40 ± 2

The complex kinetics which govern the solution nucleation-growth of a ternary transition metal precursor, along with the increased possibility of TM oxyhydroxides formation in a hydroxide coprecipitation, means attaining a desired TM stoichiometry is challenging.[97] The elemental compositions of the cathode materials were evaluated by EDS analysis, in which four different point scan measurements were taken on a particle of each cathode. The stoichiometric ratio of the transition metals calculated from the elemental wt.% of the Ni, Co, and Mn in the EDS measurements are shown in Table 3.4 and show good agreement with the intended 0.9: 0.05: 0.05 NMC composition. The addition of the boric acid and borax are shown to have no significant change on the resulting transition metal make-up after the calcination step.

Table 3.4: Elemental ratio of the transition metals in the NMC materials measured from EDS analysis.

Sample	Ni	Mn	Co
Precursor	0.908 ± 0.004	0.043 ± 0.003	0.049 ± 0.004
NMC02	0.902 ± 0.002	0.046 ± 0.003	0.052 ± 0.003
HB02	0.903 ± 0.005	0.046 ± 0.002	0.051 ± 0.003
BX02	0.906 ± 0.005	0.043 ± 0.005	0.051 ± 0.009

To investigate how the different boron mineralisers altered the surface of the cathode materials, FTIR spectra of the active material powders were initially collected, as shown in Figure 3.6. The presence of Li_2CO_3 in both powder samples is identified by the absorption peaks at 1411 cm^{-1} and 1392 cm^{-1} in HB02 and BX02, which is assigned to the asymmetric stretching vibration of CO_3^{2-}, as well as those at 864 cm^{-1} and 867 cm^{-1} which agree with the carbonate out-plane vibration. A peak is also observed around 2350 cm^{-1}, which is distinctive of the asymmetric stretching of CO_2. The larger intensity of this peak in the HB02 material could suggest a greater amount of CO_2 is absorbed onto the particle surface, which can subsequently react to form further hydroxyl and carbonate residuals.[158]

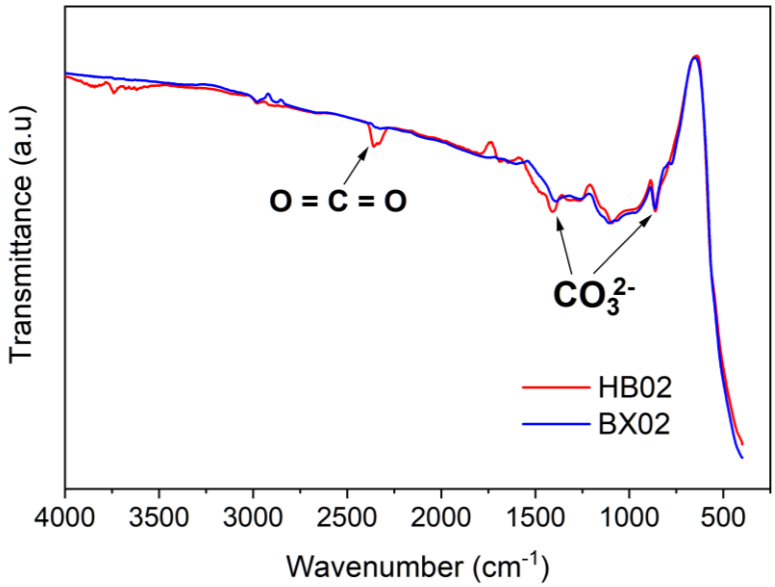

Figure 3.6: The FTIR spectra of the boric acid and borax fluxed NMC 90.5.5 powder materials.

To better understand the surface and near-surface stability and composition, the electrodes were characterised by X-ray photoelectron spectroscopy (XPS). Unlike with the FTIR measurements, the XPS instrument allowed for inert transfer so that the surfaces could be analysed as close to the pristine composition of the electrodes as made

in the dry room, without exposure to ambient moisture. Depth profiling was also performed on the electrodes, in which an argon ion beam was used to etch away at the samples and used to examine the change in composition below the surface. The carbon 1*s* and oxygen 1*s* XPS spectra can identify surface residuals in the two boron mineralised electrodes, which are displayed in Figure 3.7, with the associated time exposed to the Ar^+ beam indicated. The O 1s profiles show two distinct peaks in both electrodes at binding energies of ~531.9 eV and ~529.6 eV, which are typically assigned to the Li-O residuals (such as LiOH and Li_2CO_3) and the transition metal bound oxygen within the crystal lattice.[159,160] The surface of the electrodes are both dominated by the residual species, with the peak fitting revealing a larger proportion of these residuals present in BX02 based on the RSF weighted peak area. After the initial 60 s sputtering time, a larger proportion of the residuals are still present in BX02 compared to HB02, however the relative atomic contents of the residual Li-O species in the O 1*s* spectra are reduced to 34 – 37% after a total of 120 s etching time.

Inspection of the C 1*s* spectra show similar profiles for both electrodes, compromising of three peaks attributed to C – C (284.8 eV), C – O (~285.6 eV), and Li_2CO_3 (~289.8 eV) which are in close agreement with those reported in the literature.[161,162] The calculated amount of lithium residuals and relative composition in the C 1*s* spectra are almost equal on the surfaces of the two electrodes, with a slightly larger value present in the BX02 after etching. Given the discrepancy between the much larger proportion of Li-O species in the O 1s spectra of BX02 compared to HB02, but their roughly equal proportion of carbon containing residuals, the Li-O peak is predominantly due to the presence of LiOH.

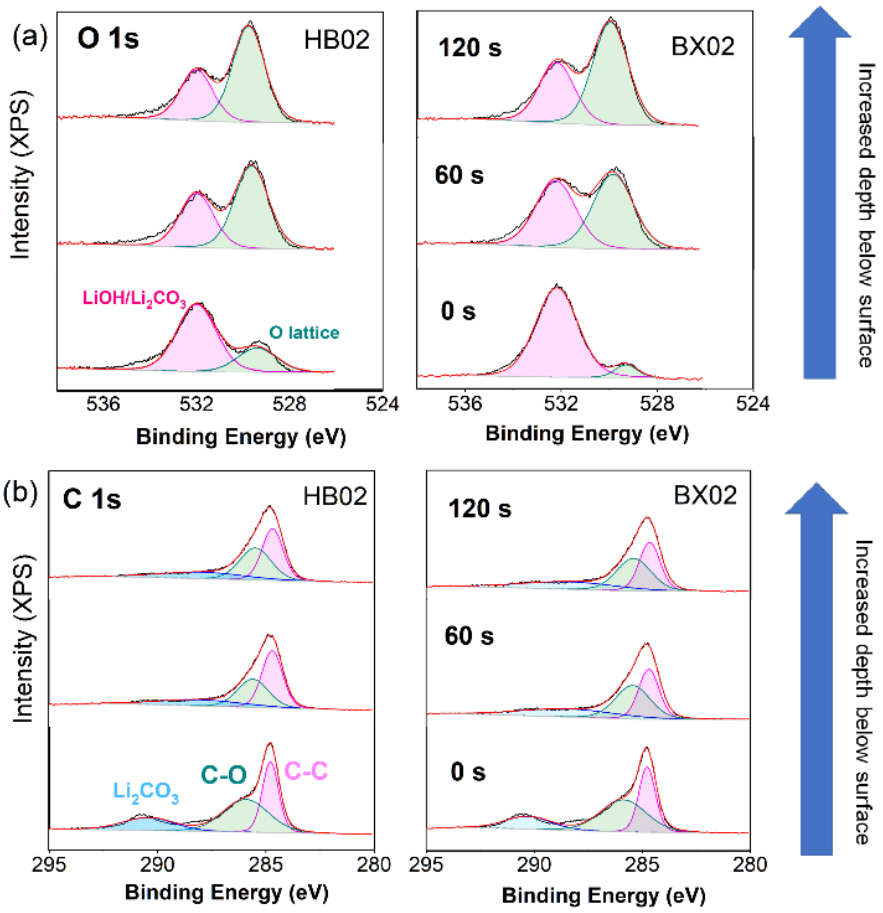

Figure 3.7: Depth profiling measurements for the O 1s (a) and C 1s (b) XPS spectra of the HB02 and BX02 electrodes recorded as prepared and after 60 s and 120 s of etching.

The depth profiling studies also reveals the presence of boron in both materials at and below the surfaces, represented by the single peak located at ~192 eV in the B 1s spectra in Figure 3.8, which agrees with previously studied boron doped or coated cathode materials.[160,163] The XPS analysis reveals that the boron penetration is greater in the BX02 material, showing 88% and 52% of the amount of the surface boron after 60 s and 120 s of etching, compared to 41% and 35% in the HB02 material. In accordance with the chemical composition of borax ($Na_2B_4O_7$), the Na 1s spectra was also recorded for BX02, in which a single peak could be fitted at a binding energy of 1071.5 eV. The relative amount of sodium calculated from the peak fitting remained constant at the surface and at each of the subsequent etched levels. These results indicate that both the boric acid

and borax mineralisers are capable of diffusion both onto the surface and into the near-surface edge region of the NMC particles during the calcination process.

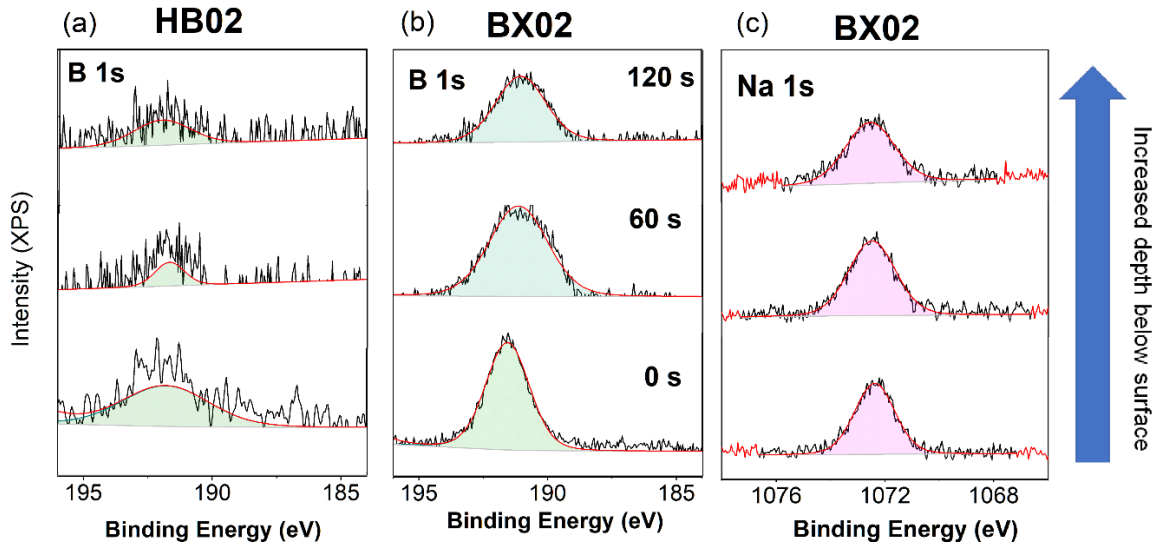

Figure 3.8: Depth profiles of the B 1s XPS spectra of the HB02 (a) and BX02 (b) electrodes and the Na 1s spectra of the BX02 electrode (c) recorded at the surface and after 60 s and 120 s of Ar^+ ion etching.

The oxidation states of the transition metals in the cathode active material can also be determined by XPS analysis due to the difference in binding energies exerted by differently charged metal ions. In particular, the valence of the Ni in the NMC can give an indication of the effect the mineraliser species has on stabilising the cation mixing by minimising the Ni^{2+} proportion. However, for the electrodes containing PVDF binder, the fluorine Auger spectral lines can show strong overlap with the Ni 2p photoelectron peaks when XPS is conducted under Al Kα X-ray excitation. It has since been shown by Bondarchuk that the use of a Mg Kα can be effective in shifting the fluorine Auger peaks away from the Ni 2p spectra to lower binding energies, due to the independence of their kinetic energy on the change in excitation energy.[164] Additionally, it is known that NiO and other transition metal oxides are readily reduced by argon ion sputtering and so the oxidation states of the Ni in NMC are likely altered by the etching process.[109,165,166] Therefore the Ni 2p XPS spectra of the HB02 and BX02 surface of the active material

powders were also recorded and are compared in Figure 3.9, showing the characteristic $2p_{3/2}$ and $2p_{1/2}$ peaks with their associated satellite peaks. The envelope of the $2p_{3/2}$ main peak in each material is centred around ~855 eV which lies between the binding energies of the same peak reported in the literature for NiO (854 eV) and Ni_2O_3 (856 eV), suggesting a mixture of the Ni^{2+} and Ni^{3+} species are present on the surface.[167] The main peaks and satellite peaks of the $2p_{3/2}$ and $2p_{1/2}$ were therefore each fitted with two peaks to account for both of these cation species, with the area of the $2p_{1/2}$ constrained to be half that of the $2p_{3/2}$ in accordance with the spin-orbit coupling of the Ni 2p peak.

The positions of the fitted Ni^{2+} and Ni^{3+} peaks in the $2p_{3/2}$ on the surface were found at 855.2 eV and 856.6 eV for HB02 and BX02 alike. The Ni^{2+} fraction at the surface corresponding to $Ni^{2+}/(Ni^{2+} + Ni^{3+})$ was calculated from the RSF corrected peak areas, yielding values of 57.1% and 44.0% for HB02 and BX02. Based on this fitting, a larger proportion of the Ni^{2+} species is accounted for in the HB02 electrode at the surface, which suggests a greater surface instability of the HB02 electrode to air and moisture due to an increased proportion of Ni^{3+} to Ni^{2+} reduction, which weakens the Ni – O bond and encourages the presence of more active oxygen species that catalyse residual lithium species formation. However, this does not corroborate with the analysis of the O 1s and C 1s XPS spectra which showed a smaller proportion of the peaks attributed to the surface residual species on the HB02 electrode. This may be caused by the acidic nature of boric acid which has been reported to reduce the amount of lithium residuals by an acid-base neutralization.[168,169]

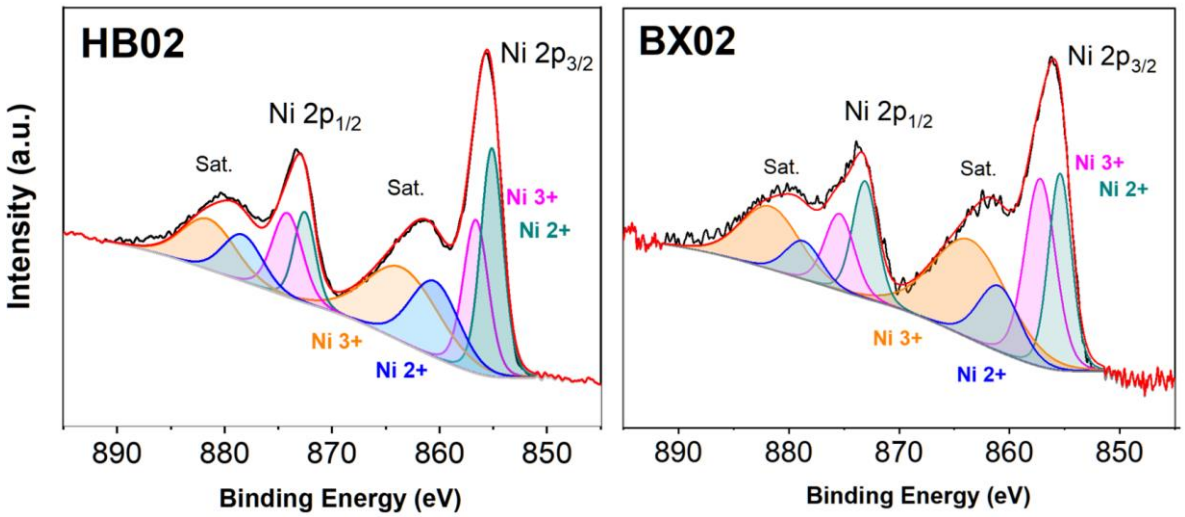

Figure 3.9: The Ni 2p XPS spectra taken at the surface of HB02 and BX02, showing the fitted $Ni^{2+}$and Ni^{3+} components in each peak.

3.3.3 Role of Boron Mineraliser on Electrochemical Performance

The long-term cycling performance of the HB and BX cathode materials was further assessed over 200 cycles at a constant discharge rate of C/2, where 1C = 1.25 mA h. Beyond the previously observed 50 cycles, the capacity of HB02 continues to fade rapidly eventually reaching a plateau around 43 mA h g^{-1} after 180 cycles. Despite the greater extent of Li^{+}/Ni^{2+} cation mixing elucidated from the XRD refinements, the BX02 material shows a superior lifetime, retaining 75% of the initial first cycle capacity compared to just 23% retained in HB02 after 200 cycles. This is further illustrated by the point of 80% 'State of Health' (SOH), a common metric for battery performance, shown in Figure 3.10, which is reached after 156 cycles and 34 cycles in BX02 and HB02 respectively. The IR drop experienced between charge and discharge cycles relates to the instantaneous fall in voltage, and is largely induced by the change in internal resistances arising from the cell components.[6] The evolution of the IR drop in each cathode closely follows the trend of capacity fade, with HB02 showing a significant increase from 7.4 mV in the first cycle

to 110 mV at the 200th cycle. The IR drop in BX02 displays a steadier growth over the cycling range from 11 mV to 30 mV in the final cycle.

To understand the capacity fade, the differential capacity (dQ/dV) plots can be inspected, which are also presented in Figure 3.10. The position of the H2-H3 oxidation peak is initially found at 4.24 V vs Li/Li+ in HB02 and at 4.28 V vs Li/Li+ in BX02, with the earlier onset of the transition producing a more intense peak for HB02 compared to the more suppressed form in the case of BX02. The more severe drop off in intensity of this peak is also noticeable in the HB02 material between the 1st and 50th cycle, which coincides with more severe capacity fade observed for this cathode.

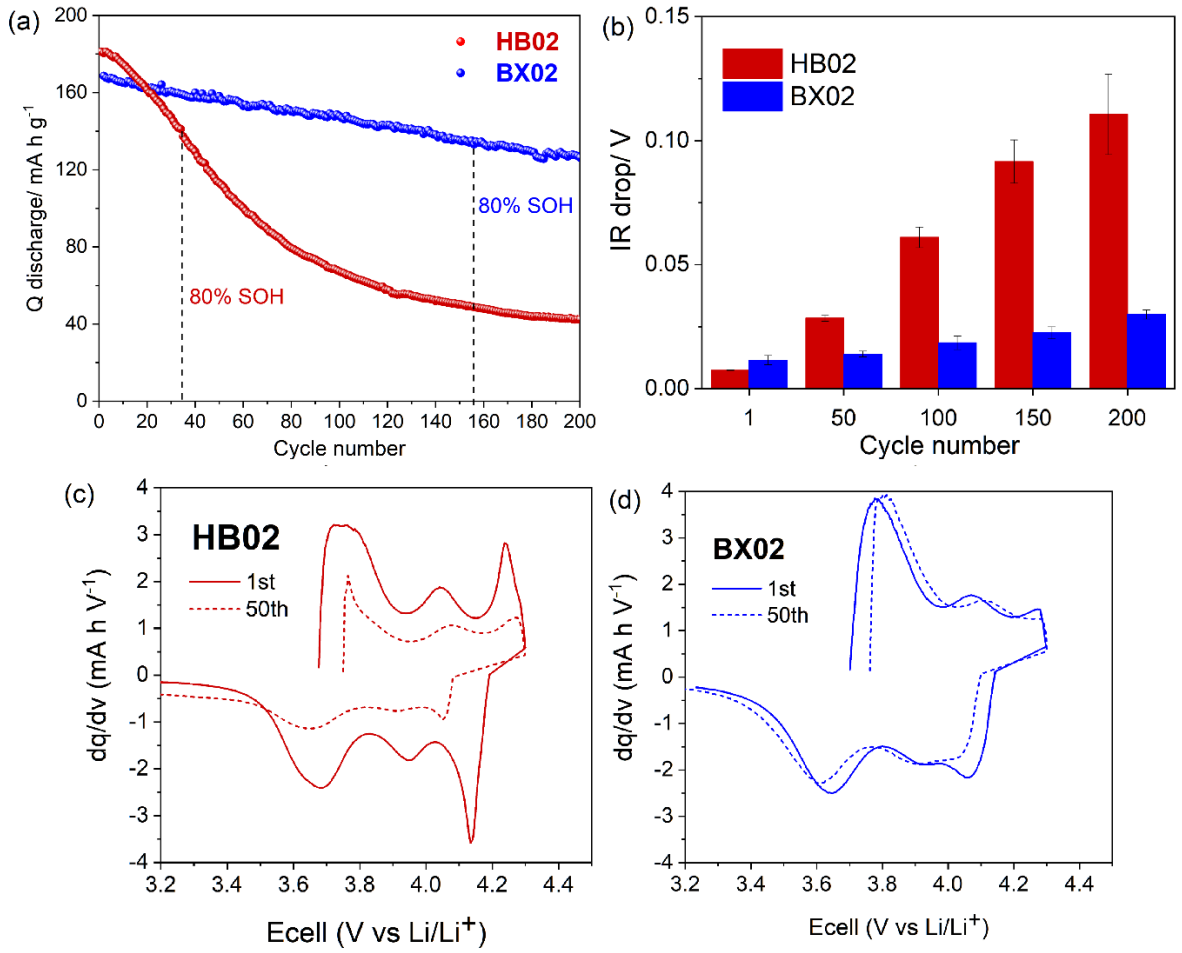

Figure 3.10: Cycling performance of HB02 and BX02 cycled in the voltage range of 2.5 – 4.3 V vs Li/Li+ at a rate of C/2 (a), the resulting IR drops recorded at the upper voltage limit at various cycles (b), and the differential capacity plots of the 1st and 50th cycle for HB02 (c), and BX02 (d).

The faster degradation of the capacity in HB02 compared with BX02 can also be understood in the context of the XPS results, with the greater extent of bulk penetration of the B and Na in the BX02 providing a form of structural stabilisation. When considering the much larger ionic radius of sodium (102 pm) compared to boron (23 pm), the incorporation of Na into the Li layer in BX02 would result in a widening of the transport channel. This is supported by the previous XRD refinement which revealed a larger value of the lattice parameter *a* in BX02, as well as previous reports of Na substitution into the Li layer of different NMC compositions.[170,171] Therefore, the greater structural stability in BX02 could arise due to the Na^+ acting as pillar ions which can act to screen the $O^{2-} - O^{2-}$ repulsions between the interlayers.[147] This pillaring protects the large anisotropic strain brought about by the H2 to H3 phase transition, that ultimately prevents substantial capacity fade.[172] However, it is also evident the comparison of the voltage profiles and dQ/dV plots in Figure A.5, that the choice of flux effects the overpotentials. When cycled at a lower specific current of 20 mA g^{-1}, the H2-H3 peak is present in both cathode materials at around 4.2 V. During the faster rate cycle at 200 mA g^{-1}, there is a visible shift in the charge peaks to higher voltages resulting from the increased overpotential at the beginning of charge. BX02 displays a larger overpotential than HB02 at this rate, suggesting the lithium concentration at the surface of the BX material is more impeded.[173] This causes the upper potential limit to be reached premature of the H2-H3 phase transition, thus the peak is absent from the dQ/dV plot of BX02 at the faster rate.

To further investigate the voltage shift of the H2-H3 peak in the BX02 material, additional half-cells were constructed and cycled between 2.5 – 4.4 V. The initial charge-discharge profiles recorded at 10 mA g^{-1} are displayed in Figure A.6, yielding reversible capacities of 203.4 and 199.8 mA h g^{-1} in the two formation cycles. The BX02 cells cycled to 4.4 V vs Li/Li+ demonstrated a first cycle coulombic efficiency of 87.8%, lower than the 95.6%

previously recorded for the cells formed in a potential window of 2.5 – 4.3 V. Figure A. also displays the cycling performance of BX02 recorded at a charge and discharge rate of 1C at the different upper voltage limits. Initially, the BX02 cells cycled to 4.4 V vs Li/Li+ deliver a higher discharge capacity of 160.4 mA h g^{-1} compared to 155.2 mA h g^{-1} at 4.3 V. However, the higher cut-off voltage results in faster decay of this capacity, displaying a capacity retention of 79.4% after 50 cycles, whilst 93.2% of the capacity is retained at the 4.3 V vs Li/Li+ cut-off. The increased capacity fade in the 4.4 V vs Li/Li+ cells can be understood by the differential capacity plots, which now shows the complete peak for the H2-H3 transition in the 1st cycle at 1C. However, the intensity of the peak is reduced significantly after 50 cycles, indicating the borax acts to delay the onset of the irreversible H2-H3 phase transition beyond the standard operating potential limits of Ni-rich NMC materials.

The rate capabilities of the two boron fluxed materials assessed at different C rates are shown in Figure 3.11. The HB02 delivered higher capacities at each of the discharge rates tested between C/5 and 5C. The resulting discharge capacities are most apparent at the faster C rates, with an initial capacity of 145 mA h g^{-1} recorded at 5C for HB02 compared to 115 mA h g^{-1} in BX02. Compared to existing work, the 5C capacity achieved in HB02 is slightly higher than the average for NMC 811 of 137.1 mA h g^{-1} calculated by Savina and Abakumov from over 100 publications.[174] Some capacity fade can be observed in BX02 at the 5C rate over the 3 cycles recorded. However, both electrodes show excellent recovery after the fast charging, recuperating 99.5% and 98.7% of the C/5 rate capacity when returning to this rate for HB02 and BX02, respectively. The XPS results show that the boron and sodium form a larger interface in the borax fluxed material compared to boric acid. Here we note that the kinetics across the surface are affected by the different interfaces formed by each mineraliser, with the boric acid promoting faster kinetics. The

better rate performance and overall higher initial capacity in HB02 could be ascribed to the smaller proportion of the residual Li – O species seen in the O 1s spectra compared with BX02, indicating that boric acid is more effective in converting the lithium residuals into a conductive Li_3BO_3 surface layer that facilitates increased Li ion mobility.[160]

The reaction kinetics of the cathodes during the electrochemical charge and discharge process can also be examined by electrochemical impedance spectroscopy, EIS, in which the obtained Nyquist plots were fitted to an equivalent circuit model as seen in Figure 3.11. The EIS testing was performed in cells after formation, with measurements taken at every 10% 'state of charge' (SOC). It can be seen in the Nyquist plots, that both materials show a larger semi-circle at a higher frequency cantered around 2.5 kHz and a second smaller semi-circle at a lower frequency around 16 Hz, and as such a modified Randles cell containing two sets of parallel resistor-CPE loops connected in series was used to fit the impedances. The semi-circle at 16 Hz appears initially supressed in both materials at the lower voltage region, but grows more prominent at increasing SOC. The series resistance (R_s) is generally related to the electrolyte resistance in the cell, which remains fairly constant with values below 4 Ω in both cathodes at each SOC. Fitting of the semi-circle features with the two R/CPE loops allows for deconvolution of the resistances relating to the electrode/electrolyte surface interface (R_{SE}) and the charge transfer between the active material and the interface. The R_{SE} did not vary significantly within the SOC range, however the R_{CT} values display a parabolic-type shape. The nature of the varying charge transfer values has been attributed to the gradual oxidation of Ni during the de-lithiation process, which accompanies the removal of electrons. The initial removal of lithium results in a growing mixture of $Ni^{3+/4+}$ as well as a growing surrounding conductive network of electrons, which couples with the reducing R_{CT} values. The increasing R_{CT} values at the high SOC has subsequently been attributed to a

breakdown of this electron network with further oxidation to a single Ni^{4+} state.[175] The charge transfer resistances were lower in HB02 for the majority of the SOC range, except at the very upper voltage limit, where BX02 demonstrated a lower R_{CT} value.

The apparent lithium ion diffusion coefficients of HB02 and BX02 were calculated using the galvanostatic intermittent titration technique (GITT) method. The shape of the diffusion profiles (Figure A.7) are largely similar at low SOC in both the de-lithiation (charge) and lithiation (discharge) curves for the two cathode materials. However, a more pronounced peak at the high SOC region (above 4.15 V vs Li/Li+) is observed for the HB02 cathode. This feature aligns with the more sloping tip of the voltage profile (Figure 3.3) observed in the corresponding upper voltage limit of the HB02 compared with that of the BX02 electrode. The values of the calculated apparent diffusion coefficients for both cathodes are recorded within the range of 7×10^{-14} cm2 s-1 and 3×10^{-11} $cm^2\ s^{-1}$, with an average value during de-lithiation measured to be 2.7×10^{-11} $cm^2\ s^{-1}$ in HB02 and 3.8×10^{-11} $cm^2\ s^{-1}$ in BX02. This suggests that the diffusion of lithium ions in and out of the layered structure proceeds at a faster rate in the BX02 electrode for the majority of the voltage range, except between 4.15 – 4.25 V vs Li/Li+, in which the rate of solid-state lithium transport through the active material is higher in the HB02 electrode.

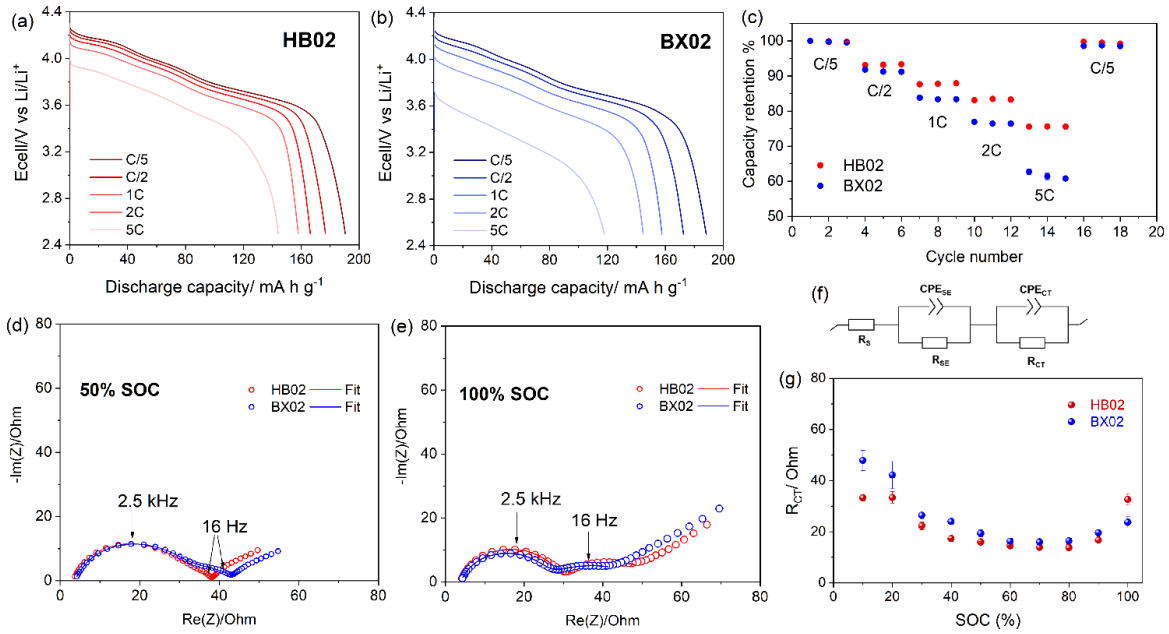

Figure 3.11: Discharge profiles of HB02 (a) and BX02 (b) half cells and their rate performance (c) measured at symmetric charge and discharge rates of C/5, C/2, 1C, 2C, 5C between 2.5 and 4.3 V. Nyquist plots of HB02 and BX02 recorded after formation at 50% SOC (d) and 100% SOC (e). Fitted charge transfer resistances as a function of SOC (g) and the equivalent circuit model used for fitting the EIS data (f).

3.4 Conclusion

Ni-rich NMC ($LiNi_{0.9}Mn_{0.05}Co_{0.05}O_2$) has been successfully synthesised by large-scale (>200 g) hydroxide coprecipitation and under simplified firing conditions of low temperatures and short calcination time in air atmosphere. Following initial screening by XRD and subsequently by electrochemical testing, the optimised firing conditions for the low and high-temperature holds were found to be 450°C and 750°C respectively. Of the two boron-based fluxes investigated at these conditions, boric acid is more effective in limiting the amount of bulk cation mixing between the similarly sized Li^+ and Ni^{2+} as determined from the XRD patterns and refinements, whilst also reducing the amount of residual lithium species on the surface. These properties, along with the smaller observed over potentials, are the key factors in the higher initial capacity, better rate capability, and lower charge transfer resistance displayed in the HB02 cathode. However, this

material shows significant capacity fade due to the severe irreversibility of the H2 – H3 phase transition. The materials synthesised with borax flux additions result in a slightly lower capacity at slow and fast rates but exhibit a superior cycle life performance, demonstrating a final capacity retention of 74.9% after 200 cycles at C/2. The role of the borax flux in subduing the capacity degradation in the Ni-rich NMC cathode is attributed to the more significant proportion of boron and additionally sodium penetration from the flux into and below the surface of the particles. The presence of these ions results in a slight expansion of the lattice parameters, as well as larger overpotentials at the faster rate, which delays the high voltage (4.1 V vs Li/Li^+) phase transition, reducing the detrimental volume changes during cycling in the voltage range of 4.3 – 2.5 V. This work highlights the importance of optimising both the bulk and surface of NMC 90-5-5, as small changes in the surface resistance can significantly affect the observed overpotentials and resulting cycle life.

Chapter 4: Improved Cycle Life and Li-Ion Transport Parameters at Low Temperature in Doped Ni-Rich NMC Cathodes

This work has been formatted into a paper and will be submitted to *Journal of Materials Chemistry A* (Ethan Williams, David Burnett, Jack Swallow, Ryan Parmenter, Wilgner Lima da Silva, Peter Slater, and Emma Kendrick).

Author contributions: E.W. and E.K. conceived and designed the research. E.W. conducted the experiments, performed the data analysis, and drafted the manuscript. J.S. collected the XPS data and provided guidance with the analysis, R.P. helped collect the XAS data and provided guidance with the analysis, W.L.S. collected the *Ex-situ* XRD data. E.K., P.S., and D.B. reviewed and edited the manuscript.

4.1 Introduction

One of the most significant challenges in adopting Ni-rich NMC cathode materials in next-generation EVs is their poor long-term cycle life.[176] The origin of the declining capacity with increasing cycles has been attributed to structural degradation from cationic mixing disorder, irreversible phase transitions, microcrack evolution, and oxygen release,[145,177,178] and surface instabilities due to residual lithium compounds, electrolyte decomposition, and transition metal dissolution.[62,179–181] To overcome these failure mechanisms, several strategies have been explored by researchers, such as bulk doping,[182–184] surface coatings,[73,160,185] electrolyte additives,[78,186,187] and core-shell designed particles.[188,189] Of these methods, bulk doping can be incorporated during the standard synthesis process and easily scaled for increasing batch sizes. The role of a dopant when incorporated in the bulk structure has been previously attributed to providing strong M – O bonds, a pillaring effect to prevent detrimental phase transitions, and to expand the transition metal slab, thus improving lithium ion transport. Their inclusion has often contributed to extending the cycle life but at the expense of initial capacity due to their electrochemical/redox inactivity during the charge and discharge processes. When selecting a dopant, it is also important to consider elements of low cost, low criticality, and a robust supply chain so as not to impose additional economic and sustainable challenges when scaling-up the materials synthesis of the cathode active material.

Boron has emerged as a promising element for the doping and modification of Ni-rich NMC to enhance the electrochemical performance, either by promoting favourable radially aligned microstructures or a surface coating on primary crystallites, improving the cycle life.[190] The higher bond dissociation energy of B – O (806 kJ mol^{-1}) compared with Ni – O (392 kJ mol^{-1}), Mn – O (402 kJ mol^{-1}), and Co – O (368 kJ mol^{-1}) is also key to

improving the structural stability of the layered oxides.[168] Sn-doping of NMC cathodes has also been identified as having a similarly stabilising effect on the structure due to the strong Sn – O bond (548 kJ mol^{-1}) as well as the tendency of Sn^{4+} to remain isovalent and not adopt the tetrahedral coordination.[191,192] In addition, the low cost and low toxic nature of Sn makes it a preferable choice of cation dopant for application in lithium-ion cathode applications.[193] However, to the best of our knowledge, the combination of boron and tin as dopants in the NMC system has not yet been studied. The impact of operating temperature also has significant impact on the performance of lithium-ion batteries and is an important factor when assessing the practical application of cathode materials for electric vehicles (EVs). At elevated temperatures, electrolyte and active material decomposition can occur, whilst detrimental side reactions and changes at the SEI have also been reported, which all contribute to capacity degradation.[194] Low operating temperatures similarly introduce performance issues resulting from increased charge transfer resistance and reduced transport of lithium ions through electrodes and across the electrolyte, contributing to lower power and energy output.[195,196] Several studies have investigated the lifetime of NMC cells tested at various temperatures, usually with a focus on characterising the electrolyte degradation and implementing surface modifications to alleviate this.[197–200] However, far fewer studies have focused on the interplay between bulk and surface modifications that stabilise cycle life whilst enabling improved performance in a range of temperatures. More recently, a study by Ren et al. highlighted the promising performance of a Nb^{5+} doped $LiNi_{0.83}Co_{0.12}Mn_{0.05}O_2$ cathode across a wide temperature range, in which the improved kinetics was attributed to a lowering of the dissolution activation energy calculated from the EIS.[201]

To this end, we have investigated and studied how single and multi-element doping of boron or boron and tin into the crystal lattice of NMC 90-5-5 can be employed in the

synthesis to improve the cycle life and understand their role in influencing the reaction kinetics of the cathode when tested in half-cells at room (25°C), elevated (45°C), and low (-5°C) temperatures.

4.2 Experimental

4.2.1 Synthesis of Doped NMC 90-5-5

The $[Ni_{0.9}Mn_{0.05}Co_{0.05}](OH)_2$ precursor was initially synthesised by a hydroxide coprecipitation method, in which a 2 mol L^{-1} aqueous transition metal solution was first prepared from stoichiometric amounts of $NiSO_4.6H_2O$, $MnSO_4.H_2O$, and $CoSO_4.7H_2O$. The solution was then pumped into a 5 L CSTR reactor along with a pre-mixed solution of NH_4OH (4 mol L^{-1}) and NaOH (10 mol L^{-1}) at a controlled rate to maintain a pH of 10.8. The reaction was maintained at 50 °C under a flowing N_2 atmosphere for 8 hours, after which it was left to age for 2 days at temperature. The powder precursor material was after vacuum filtration and washing, before drying under vacuum at 120 °C overnight. The baseline NMC material was prepared by mixing 40 g of the precursor material with a 7.5% molar excess of LiOH on a roller mill for one day and subsequently fired in a tube furnace with a flowing oxygen feed at a rate of 0.5 L min^{-1}, initially ramping to 450°C at a rate of 1°C min^{-1} for a 5 hr hold and then to 750°C to hold for 9 hrs. The doped materials in this study were prepared based on the target formula of $Li([Ni_{0.9}Mn_{0.05}Co_{0.05}]_{1-x-y}B_xSn_y)O_2$. In both cases, a target of doping 2.5% of the transition metal sites was used, where x = 0.025, y = 0 for B25 and x = y = 0.0125 for SB25. The required metal oxides (B_2O_3 and SnO_2) were first ball milled for 3 hrs at 400 rpm before being mixed with the precursor powder and LiOH on the roller mill and fired at the same conditions as the baseline NMC.

4.2.2 Materials Characterisation

Powder X-ray diffraction measurements were performed on a Proto AXRD Benchtop instrument with a Cu Kα source, in a 2θ range of 15 – 90° at a scan rate of 1° min^{-1}. The particle morphology of the powdered cathode material was investigated using a Zeiss EVO10 scanning electron microscope using an accelerating voltage of 15 kV and a probing current of 50 pA. The elemental composition and valence of the surface of the particle surfaces were determined by X-ray photoelectron spectroscopy (XPS). The XPS measurements were all performed using a PHI Versaprobe III XPS system using a monochromatic Al-Kα source at 1486.74 eV. Fitting of the XPS spectra was performed in CasaXPS, with the binding energies of each sample calibrated to the adventitious C1s peak at 284.8 eV, and a Shirley background was used to fit each spectra.

X-ray absorption spectroscopy (XAS) data were collected at beamline B18 at the Diamond Light Source, UK, and measured at the Ni, Co, and Mn K-edges.[202] The cathode powder materials were ground and diluted with PVP and pressed into 13 mm pellets that were then secured in Kapton tape. Reference samples (>99%) were also purchased (Sigma Aldrich) and measured to aid with the calibration of the XANES oxidation state. All samples were prepared in a dry room (dew point −45°C). X-ray absorption near-edge structure (XANES) spectra and Extended X-ray absorption fine structure (EXAFS) spectra were collected in transmission mode. The Ni, Co, and Mn K-edge spectra were aligned and calibrated using a reference foil that was collected simultaneously during each measurement. Data analysis was carried out using the Athena software.[110]

Degradation studies were also performed and characterised by ex-situ XPS and XAS experiments, in which spectra were collected on both the as-made electrodes and on electrodes after electrochemical cycling. Half-cells were constructed in the two electrode

Swagelok cells and cycled 200 times between 4.3 – 2.5 V with a charge specific current of 100 mA g^{-1} and discharge specific current of 200 mA g^{-1}. The cells were disassembled in a glovebox, and the electrode disc was washed in DMC to remove the residual electrolyte before sealing under the glovebox atmosphere. For ex-situ XRD measurements, for investigation of the 1st cycle, cells were disassembled and cleaned as stated above following an initial rest at OCV for 6 hrs and subsequent cc-cv charging to 4.3 V at 10 mA g^{-1} or after the following cc discharge to 2.5 V at the same specific current. Ex-situ XRD was collected on a Bruker D8 Advance diffractometer (Cu Kα1,2) between 15°-90° 2θ (step size 0.0189 and 253.3 s per step). Electrodes were loaded onto a domed sample holder (Anton Paar) in an argon atmosphere inside an argon filled glovebox. For investigation of the 1st cycle, cells were disassembled and cleaned as stated above following an initial rest at OCV for 6 hrs and subsequent cc-cv charging to 4.3 V at 10 mA g^{-1} or after the following cc discharge to 2.5 V at the same specific current. Ex-situ XRD was also performed on electrodes extracted from cells at the same voltage cut-offs following asymmetric cycling with cells charged/discharged at 200/500 mA g^{-1}.

4.2.3 Electrochemical Testing

Electrode coatings were prepared by mixing the cathode active material, PVDF binder solution, carbon black, and synthetic graphite in a 90: 5: 3: 2 wt.% ratio into a homogeneous slurry which was then coated onto an aluminium current collector. Electrodes were dried overnight at 120°C and assembled into CR2032-type coin cells using 1 M $LiPF_6$ in EC/EMC (3:7 by volume) + 2 wt.% VC for the electrolyte solution with a Celgard separator and a lithium metal counter electrode. All tested half-cells underwent the same formation process following an 8 hr rest to allow for complete electrolyte

wetting, using two galvanostatic charge/discharge cycles at an applied specific current of 10 mA g^{-1} at a voltage range of 4.3 – 2.5 V.

Rate capability was tested using a constant charging specific current of 20 mA g^{-1} and a variable discharge specific current of either 20, 50, 100, 200, 500, 1000, and 2000 mA g^{-1} for 5 cycles at each rate. Electrochemical impedance spectroscopy (EIS) was performed at various voltage points after a 30 min rest in a frequency range between 100 kHz and 10 mHz at an amplitude of 10 mV. The evaluation of the exchange specific current (J_0) requires an estimation of the particles electrochemically active surface area (S) using Equation 1, for which a spherical geometry is assumed.

$$S = \frac{v_{act} \times A \times L \times S_p}{V_p} \quad (1)$$

Where v_{act} is the active material volume fraction in the electrode, A is the geometric area of the electrode disc, L is the electrode thickness, S_p is the surface area of a sphere using the measured particle diameter from the particle size analysis, and V_p is the volume of the same sphere. The exchange specific current can then be calculated from this value of S by a linearized form of the Butler-Volmer equation as shown in Equation 2.

$$J_0 = \frac{RT}{R_{CT} SF} \quad (2)$$

with R as the ideal gas constant, T as the testing temperature (in K), and F as the Faraday constant.[203] The exchange current densities are also presented at varying lithium stoichiometries (x_{Li}) which can be calculated at different SOC by the relationships in Equation 3 and Equation 4

$$x_{Li} = \frac{1 - \frac{Q}{Q_{max}}}{C_{s(\max)}} \quad (3)$$

$$C_{s(\max)} = \frac{GSM}{M_w \times L \times v_{act}} \quad (4)$$

where Q is the capacity at a particular SOC, Q_{max} is the discharge capacity at 100% SOC, and $C_{s(\max)}$ is the maximum lithium concentration in an electrode, calculated from its areal loading, GSM (in g m^{-2}), molecular weight of the active material, M_w, the electrode thickness, L, and the active material volume fraction, v_{act}. Note a stoichiometry of x_{Li} = 0 is never achieved in these cathode materials due to the inability to remove all the lithium from the layered structure as this is prevented by thermodynamics and structure collapse. Galvanostatic intermittent titration technique (GITT) tests were performed by applying transient current pulses at a rate of C/15 for 15 mins followed by a 2 hr relaxation period. Diffusion coefficients were calculated based on the Weppner and Huggins method using Equation 5, in which the SAND equation is applied to fit the individual current pulses, as described in previous work.[121]

$$D_{\mathrm{Li+}} = \frac{4}{\pi}\left(\frac{iV_m}{nFS}\right)^2 \left(\frac{dV_s/d\delta}{dV_s/dt^{0.5}}\right)^2 \quad (5)$$

In order to investigate the effect of temperature extremes, the electrochemical testing described above was also performed at temperatures of 45 °C and −5 °C, in which cells were placed inside an environmental test chamber (ECO HTLC135, Temperature Applied Sciences Ltd) after undergoing formation at room temperature. Before the start of each test at a new temperature, a 3 hr rest step was instigated to allow for thermal acclimatisation.

4.3 Results and Discussion

4.3.1 Optimised Doping

Single cation doping of boron and tin was initially studied at dopant concentrations of 1.0, 2.5, and 5.0 mol%, relating to x = 0.01, 0.025, and 0.05 for $Li(Ni_{0.9}Mn_{0.05}Co_{0.05})_{1-x}M_xO_2$ where M is B or Sn. Each of the doped cathodes (where B10 and Sn10 refer to the 1.0 mol% doped NMC etc.) retain the layered α-$NaFeO_2$ structure with the *R*-3*m* space group as displayed in Figure B.1a. However, additional small peaks are observed for Sn50 at 2θ of 18, 35, and 43°, which closely matches those found in the XRD pattern of Li_2SnO_3. This formation of the Li_2SnO_3 phase is consistent with previous Sn doping studies at higher dopant concentrations, possibly arising from the segregation of the excess Sn and subsequent reaction with Li at the particle surface.[204]

The electrochemical properties extracted from the initial charge-discharge cycles of the single doped NMC cathodes are summarised in Table B.1. The first-cycle discharge capacities are comparable for Sn10 and Sn25, as well as for B10 and B25 (around 201–202 mA h g^{-1}), but the 2.5 mol% doped cathodes show higher capacities in the second cycle. Increasing the dopant concentration to 5.0 mol% results in the lowest discharge capacities for both the boron- and tin-doped series, although Sn50 still performs better than B50. The intermediate cycle life of the doped materials was assessed over 100 cycles at a specific current of 200 mA g^{-1}, resulting discharge capacities are presented in Figure B1b. Between both boron and tin samples, B25 delivers the both the highest capacity and best cycle life over the full cycle window, ranging from an initial discharge capacity of 183.9 mA h g^{-1} to 163.8 mA h g^{-1} at the 100th cycle, with a retention of 89.0%. B10, Sn10 and Sn25 initially display similar discharge capacities in the first few cycles, however this degrades significantly in the Sn10 sample, displaying a capacity retention of 50.1% after 100 cycles, compared to 79.2% for Sn25 and 74.3% for B10. The fast rate cycling capacities delivered by Sn50 and B50 are lower than the rest of the doped samples, however to demonstrate relatively stable cycling, retaining 79.2% and 83.3% of capacity

in the 100th cycle. Following these results, it was determined that B25 demonstrated the optimal performance of the doped materials, whilst this doping concentration also yielded the best performance in the Sn series, in particular displaying the highest FCE (96.3%) amongst all the samples. B25 and SB25, in which B and Sn are both doped at 0.125 mol% to obtain a balance between cycle life and kinetics, were therefore selected for further study.

The XRD patterns in Figure 4.1 show retention of the layered α-$NaFeO_2$-type rock-salt structure is observed for the synthesis of the boron doped (B25) and tin-boron doped (SB25) NMC-90-5-5 materials. No additional peaks are present for the doped material, indicating the phase purity and supporting the incorporation of the doped cations into the bulk material. The doping is also evident from the shift in the (003) diffraction peak to lower angles compared to the pristine NMC, often attributed to an expansion in the *c* lattice parameter.[72,139] Furthermore, the peak broadening is increased in the doped materials which is usually indicative of lower crystallinity or compositional heterogeneity, but can also infer a smaller primary particle size and an increased number of grain boundaries within the secondary particles.[205] An increase in Li vacancies, possibly incurred by a doping imbalance, would introduce additional microstrain and local lattice disorder, resulting in broader peaks.[206] This broadening is typically anisotropic, in which a broader (003) reflection suggests greater interlayer disorder, whilst broadening of the (101) and (104) peaks are associated with in-plane strain and cation disorder. The increased broadening of the (003) peak in B25 compared to SB25 could therefore be attributed to the higher concentration of boron in the sample, occupying the interstitial sites between layers rather than the tin which is more likely to enter the TM layer.

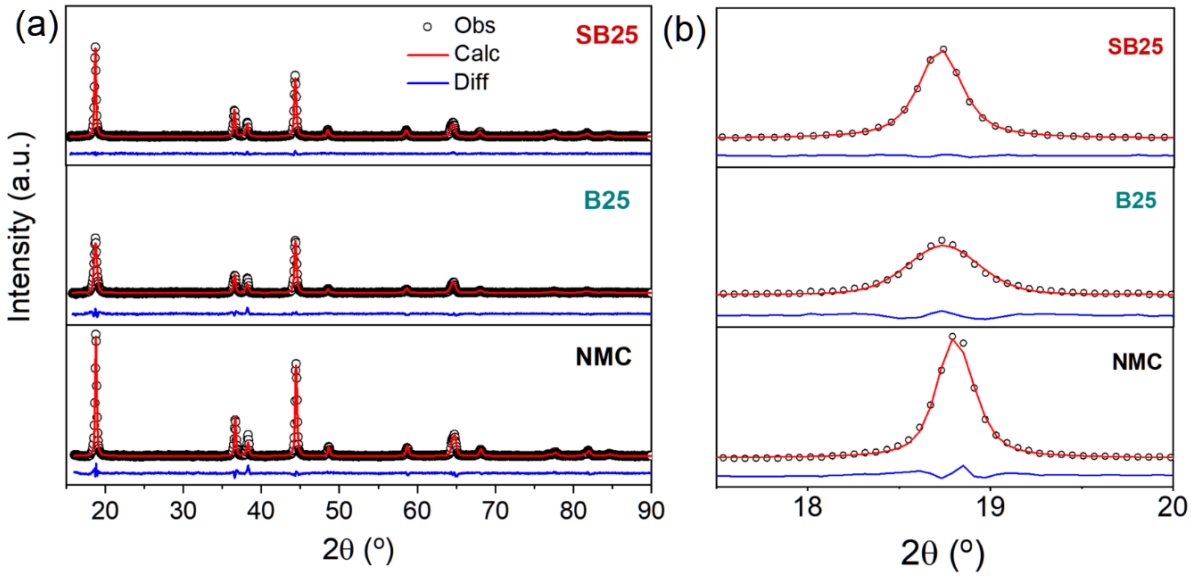

Figure 4.1: Observed, calculated, and difference profiles from Rietveld refinements using powder XRD data for the baseline and doped NMC 90-5-5 materials (a), and the inset of the (003) peak (b).

Rietveld refinements were also performed using the XRD data to elucidate further information about the influence of doping on the NMC lattice parameters, which are presented in Table 4.. The lattice parameters *a* and *c*, and the lattice volume all increase for the doped materials, further supporting the successful incorporation of the cations into the crystal lattice. The calculated *c* parameter is greater in SB25 which is consistent with the presence of the larger Sn^{4+} cation in the layered structure. The cation mixing between Ni^{2+} and Li^{+} in NMC is typically assessed by the intensity ratio of the (003) to (104) peaks, where a value lower than 1.2 is usually associated with a considerable extent of mixing. Sn doping into layered oxide cathode structures can increase the ionicity of the TM – O bond, which can minimise TM ion migration and therefore reduce cation mixing.[44] The values of the peak intensity ratios were calculated as 1.32, 1.05, and 1.47 for NMC, B25, and SB25 respectively, which would indicate that SB25 demonstrates the lowest proportion of cation mixing. However, the calculated Ni on the Li site from the Rietveld refinement is slightly larger in SB25 than for the pristine NMC. This could suggest the presence of some Sn in the Li layer, which has previously been observed in Li-rich NMC

due to the similar ionic radius of Sn^{4+} (0.71 Å) and Li^{+} (0.76 Å).[207] The larger value of I(003)/(104) in SB25 could therefore be due to the higher scattering factor of Sn compared to Ni and thus a larger contribution to the peak intensity at this site.

Table 4.1: The lattice parameters of the pristine and doped NMC 90-5-5 materials are calculated from Rietveld refinement.

Sample	a/ Å	c/ Å	Volume/ Å^3	Density/ g cm^{-3}	Ni on Li	Rwp %
NMC	2.87556(9)	14.1860(6)	101.586(6)	4.709	0.028(2)	5.29
B25	2.8811(1)	14.205(1)	102.11(1)	4.874	0.082(1)	5.02
SB25	2.88103(7)	14.2140(4)	102.174(4)	4.883	0.067(1)	2.01

Scanning electron microscopy (SEM) was used to assess the morphology of the precursor material before firing and the subsequent active materials of the pristine and doped NMC 90-5-5 materials, which are shown in Figure 4.2. The precursor morphology consists of sharp platelets that have agglomerated into quasi-spherical secondary particles. The SEM images of the cathode active materials reveal that these platelets are fused into denser cuboidal primary particles that are packed into denser secondary particles. Bulk doping with either boron or tin and boron shows no significant observable change in the particle morphology of the NMC material. Particle size analysis of the cathode materials revealed a smaller median (D50) particle size in the doped materials of 4.19 μm and 5.48 μm for SB25 and B25, compared with 5.96 μm in NMC.

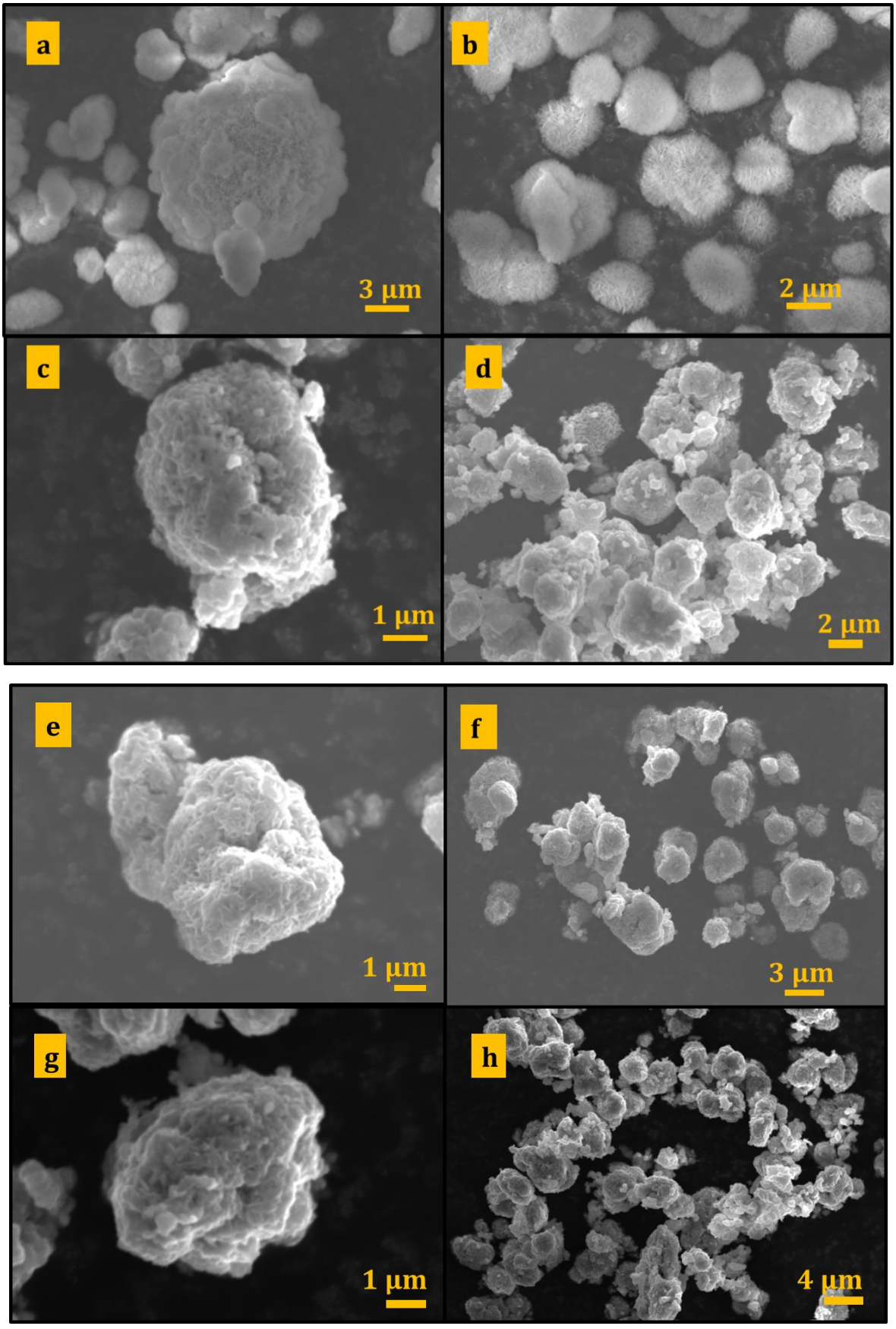

Figure 4.2: SEM images of the precursor (a, b) cathode material collected after coprecipitation and the fired pristine NMC (c, d) and doped B25 (e, f) and SB25 (g, h) cathode active materials.

The elemental ratio of the transition metals was determined by EDS, using an average of four different point scans on individual particles. The TM ratios calculated from the measured elemental wt% are displayed in Table 4.2 and are fairly consistent with the intended 0.90: 0.05: 0.05 ratio of Ni, Mn, Co for the NMC precursor and undoped baseline. The doped materials display a similar NMC ratio from the pristine material, in keeping with the $Li(Ni_{0.9}Mn_{0.05}Co_{0.05})_{1-x}M_xO_2$ intended stoichiometry. However, the small variation observed could arise from regions of inhomogeneity caused by the inclusion of tin or boron in the TM later. The low atomic mass of boron makes it difficult to detect under EDS due to the low energy of its characteristic X-rays, however the much heavier tin can be registered by EDS, displaying a NMC/Sn molar ratio of 0.988: 0.012. Elemental mapping was performed for SB25 (Figure B.2) on different particles of the CAM and demonstrates a uniform distribution of the tin at the surface of the NMC, along with the Ni, Mn, and Co.

Table 4.2: Elemental molar fraction ratios of the transition metals in the NMC precursor, undoped, and doped materials measured from EDS analysis.

Sample	Ni	Mn	Co	Sn
Precursor	0.905± 0.002	0.042± 0.002	0.054± 0.003	
NMC	0.909 ± 0.004	0.047 ± 0.003	0.044 ± 0.002	
B25	0.913 ± 0.003	0.041 ± 0.004	0.046 ± 0.001	
SB25	0.904 ± 0.004	0.046 ± 0.005	0.049 ± 0.003	0.011 ± 0.003

XPS was conducted on the active powder materials to investigate the effect on the chemical valence and surface composition in the pristine and doped NMC cathodes. The high-resolution XPS spectra of multiple elements are displayed in Figure 4.3. The spectra of Ni 2p for each cathode displays the characteristic spin-orbit doublet of the $2p_{3/2}$ and $2p_{1/2}$ core levels, which are centred respectively at 854.8 eV and 872.3 eV for the pristine NMC, with the associated shake-up satellite peaks at 861 eV and 879 eV. The Ni 2p peak positions in SB25 are consistent with the undoped material however the $2p_{3/2}$ and $2p_{1/2}$

are shifted to 855.5 eV and 872.7 eV for B25. The deconvolution of the Ni $2p_{3/2}$ and $2p_{1/2}$ was performed by peak fitting, resulting in relative proportions of Ni^{3+} of 13.3%, 26.6%, and 21.4% for the NMC, SB25, and B25 samples. This result suggests that doping with boron or with both tin and boron increases the average valence of the nickel at the near surface of the NMC particles.

The presence of Sn in SB25 is confirmed by the presence of the characteristic Sn $3d_{5/2}$ and $3d_{3/2}$ peaks in the XPS spectra, the positions of which appear at 485.3 eV and 493.9 eV, displaying a spin-orbit splitting of 8.6 eV. The recorded peak positions are at slightly lower binding energies than those previously attributed to Sn^{4+} doping in different NMC materials reported in the literature and for pristine SnO_2 spectra.[207–209]

The B25 and SB25 materials both show a single peak at 191.5 eV and 190.8 eV in their respective B 1s spectra. The relative intensity of this peak is greater for B25 than SB25 which agrees with the higher doping concentration of boron used in the singly B doped NMC. In both doped samples, the B 1s peak is located at a lower binding energy than that characteristic of B_2O_3 (193 – 194 eV) and instead is more aligned with the presence of lithium borate compounds.[143] This indicates some level of reaction between the B_2O_3 and the LiOH might have occurred during the calcination step, resulting in the formation of surface layer previously assigned to B^{3+} in Li_3BO_3 for the peak at 191.5 eV.[210] This is also supported by the Li 1s spectra of B25, in which the main peak at 55 eV appears with a higher intensity than the one in NMC and SB25, suggesting the presence of additional lithium compounds forming on the surface.

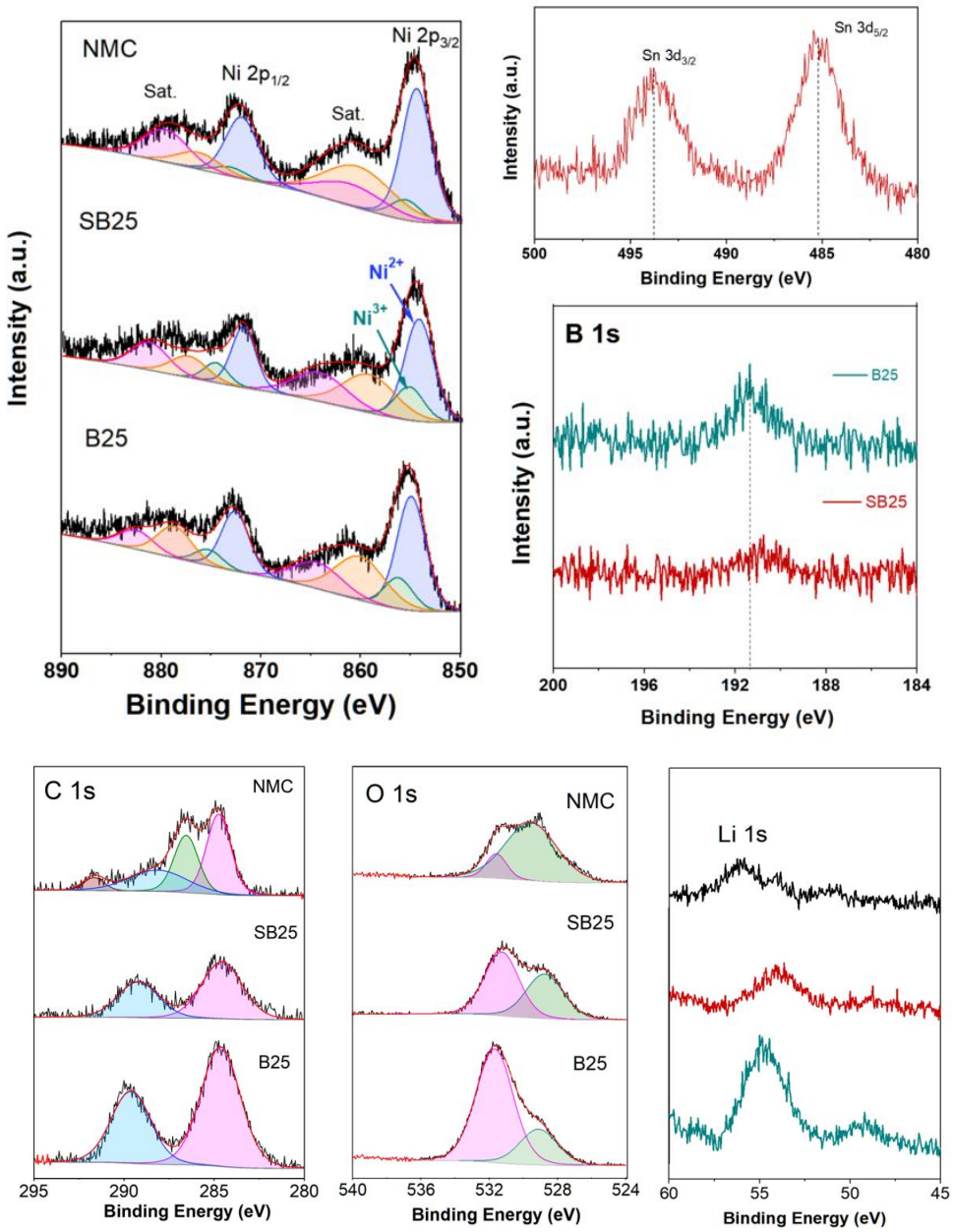

Figure 4.3: XPS spectra of the baseline and doped cathode powder materials, showing the Ni 2p, Sn 3d, B 1s, C 1s, and O 1s regions.

XAS analysis of powder samples

To further probe the structure and oxidation states of the NMC transition metals in the bulk materials, XANES measurements were carried out on the powders at the Ni, Co, and Mn K-edge. Standard Ni, Mn, and Co containing inorganic standards of known oxidation states were also measured as reference compounds, these being NiO, $Ni(CH_3CO_2)_2$,

$Mn(CH_3CO_2)_2$, Mn_2O_3, MnO_2, $Co(CH_3CO_2)_2$, Co_2O_3, and $LiCoO_2$. The values of the threshold energy (E_0) were measured following normalisation of the pre-edge and post-edge regions and are compared for the standards and samples at the different metal K-edges in Table B.2.

It is difficult to find a reliable standard consisting of purely Ni^{3+} or Ni^{4+} due to their instability towards reduction or disproportionation, and so a complete assessment of the Ni oxidation state could not be acquired.[211] The E_0 values determined from the position of the peak maximum (white line energy) at the Ni K-edge for the NMC and doped samples are all located at ~8352 eV, displaying a shift to higher energy compared to the nickel (II) acetate (8349.1 eV) and nickel (II) oxide (8350.4 eV) standards. This suggests the presence of both Ni^{2+} and Ni^{3+} in each of the cathodes.[212] The similar peak position between the cathodes indicates the valence of the Ni in the bulk is unchanged upon doping, contrary to the case at the surface as suggested by the XPS. Overall, the shape of the XANES spectra of the doped materials at the Ni K-edge closely mirror that of the pristine NMC, suggesting the bulk structure is preserved upon the addition of B and Sn.

Inspection of the Mn K-edge E_0 values reveals that all the cathode materials are at higher energies than the manganese (IV) oxide standard. The absorption peaks of the cathode materials in the Co K-edge were within <1 eV of the peak from the Co^{3+}, indicating Co is present in the trivalent state for each of the materials. These results agree with the theoretical oxidation states of Mn^{4+} and Co^{3+} in NMC, as well as the valence states and XANES curves seen in the literature for Ni-rich NMC cathodes.[213,214] The difference in edge energy determined from the white line positions in each of the metal K-edges are all less than 0.5 eV for NMC, B25, and SB25, which suggests doping does not result in a significant level of charge compensation.

The pre-edge region of the XANES can give information regarding the metal's coordination and environment. The presence of a small pre-edge peak in the Ni K-edge centred around 8335 eV can be observed in all of the cathode samples. This pre-edge feature is usually attributed to the hybridisation between electrons in the p orbitals of Ni and those in the nearby O p orbital.[215] The pre-edge peak is also observed in the Ni^{2+} standards at a similar energy of 8334.3 eV. Close inspection of the Mn pre-edge region revealed the presence of two peaks at 6541 eV and 6543 eV, which is consistent with the 1s to 3d electronic transitions associated with octahedral Mn^{4+} that has previously been reported in different NMC compositions.[214]

Data were also collected in the full EXAFS region for each of the materials to elucidate whether the introduction of the dopants resulted in changes in the local coordination environment of the NMC transition metal elements (Figure 4.4). The Ni EXAFS data show two main peaks for the cathode materials at distances of 1.47 Å and 2.52 Å relating to the scattering between Ni – O and Ni – TM nearest neighbour interactions. The position of these peaks in the pristine and doped NMC show close overlap, indicating that no distinct change in the bond lengths is observed upon B or Sn modification. However, the peak intensity of the Ni – TM environment slightly increases in B25 but decreases in SB25 relative to the baseline NMC, which can be correlated positively with changes in coordination number.[216] A similar trend is seen in the Mn spectra, which overall shows little variation between the baseline and doped NMC cathodes, suggesting the Mn environment is mainly retained. For Co however, the doped materials show lower populations in both the Co – O and Co – TM coordination, which is particularly emphasised for the Co – O bond in SB25, and could be attributed to a larger proportion of oxygen vacancies.

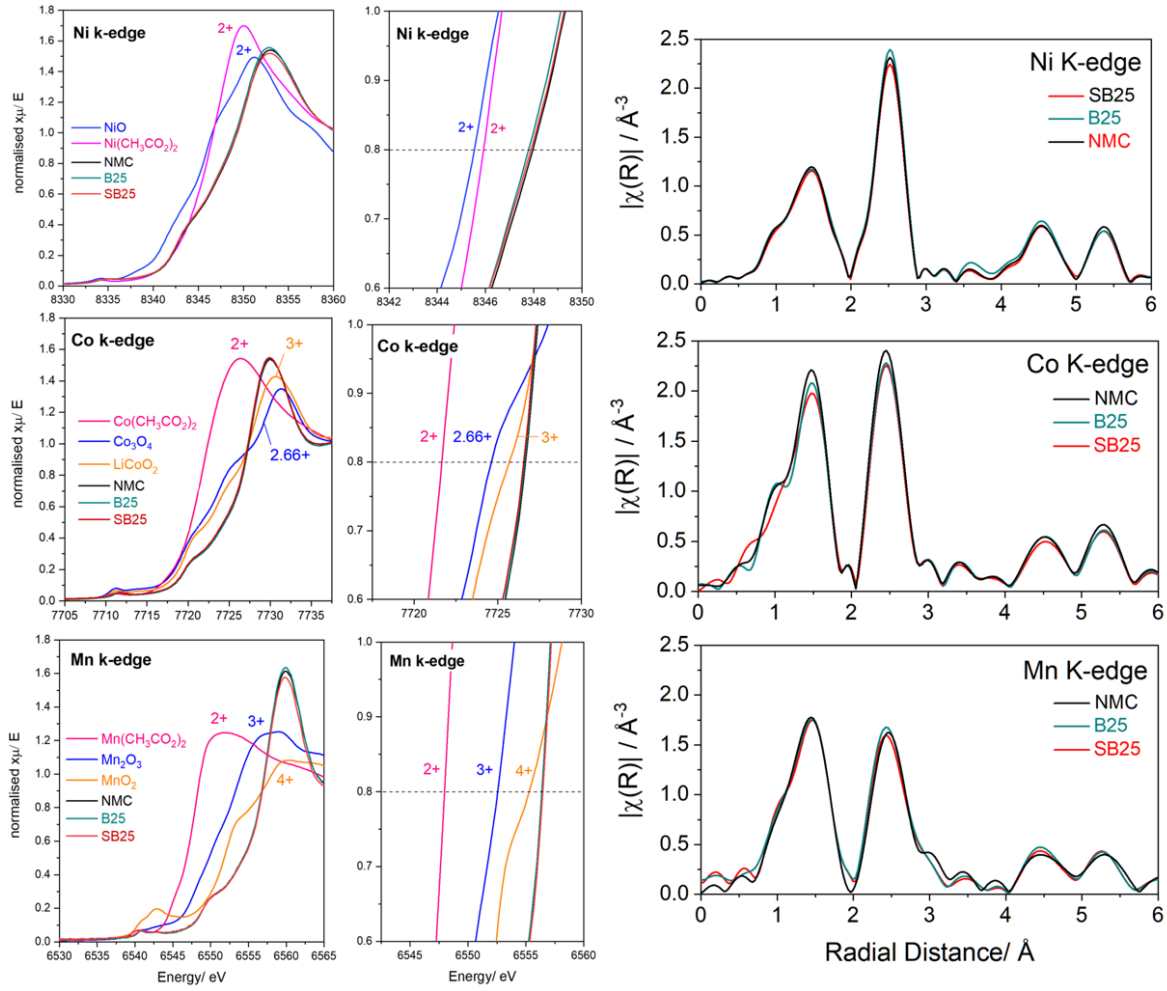

Figure 4.4: Normalised XANES spectra of the baseline and doped NMC cathode materials as well as the reference compounds at the Ni, Co, and Mn K-edges. EXAFS spectra of the cathode materials at the same metal edges.

Electrochemical Performance

The galvanostatic capacity profiles of the 1st and 2nd cycles recorded at a 10 mA g^{-1} rate within a voltage range of 4.3 – 2.5 V are shown in Figure B.3 from triplicate coin cell data for the pristine and doped materials. The recorded first cycle loss (FCL) was below 10 mA h g^{-1} for each material, whilst the Coulombic efficiencies (CE) were >98%, reflecting excellent structural stability during the creation of the CEI and decomposition of the electrolyte.[217] The SB25 material demonstrates the highest electrochemical reversibility in the half cells, with a FCL of 5.1 mA h g^{-1} and a FCE of 97.6%. The shape of the capacity

profile is largely unaffected by the bulk doping, however a slight increase in the polarization below 3.4 V is observed in B25, whilst the upper voltage sloping profile usually present in Ni-rich NMC materials above 4.2 V has been supressed. This is reflected in the lower discharge capacity of the doped B25 in the first cycle of 190.8 mA h g^{-1} compared to those of NMC (208.0 mA h g^{-1}) and the co-doped SB25 (210.2 mA h g^{-1}). The lower initial specific capacity of B25 is also consistent with the earlier diffraction results which suggests B25 demonstrates the largest proportion of cationic mixing, which can limit the amount of available Li^+ during charge and discharge.

The rate performance of the pristine and doped materials was assessed by asymmetric cycling with increasing discharge rates, using current densities between 20 – 2000 mA g^{-1} in a voltage range of 4.3 – 2.5 V. As displayed in Figure 4.5, SB25 delivers the highest specific discharge capacities over the five cycles recorded at each of the tested rates, demonstrating the largest increase at 500 and 1000 mA g^{-1} where larger initial capacities of 150 mA h g^{-1} and 134 mA h g^{-1} were obtained, compared with 137 mA h $g^{-1}$and 118 mA h g^{-1} in the pristine NMC. However, when the applied specific current was increased to 2000 mA g^{-1}, the capacity gain is less significant, with SB25 and pristine NMC delivering 105 mA h g^{-1} and 97 mA h g^{-1} respectively. The specific capacities of B25 were instead slightly lower than the pristine NMC at each of the discharge rates, delivering initial capacities of 131 mA h g^{-1} and 113 mA h g^{-1} at applied current densities of 500 and 1000 mA g^{-1}. However, B25 demonstrated a higher retention of its initial capacity at 20 mA g^{-1} than NMC at current densities up to 1000 mA g^{-1}, whilst SB25 delivered the highest capacity retention at all rates, demonstrating its superior rate performance. Following the fast discharge rates, recovery cycles were performed at 20 mA g^{-1}, yielding final capacity retentions of 91%, 95%, and 96% for NMC, B25, and SB25 respectively, illustrating the benefits of the doping.

The rate capabilities of the three cathode materials were also investigated at temperatures of 45 °C and −5 °C at current densities between 20 and 500 mA g^{-1} to probe the effect of doping on the Li-ion kinetics at non-ideal extreme conditions. The temperature varied rate performance of the different cathodes are shown in Figure 4.5, and largely reflect the trends observed at room temperature testing, with SB25 demonstrating higher discharge capacities for each rate when cycled at 45 °C or −5 °C. However, the rate capability of B25 relative to the pristine NMC is considerably better at 45 °C than at −5 °C, delivering higher specific capacities than NMC at current densities of 100 mA g^{-1} and above. The rate capacities obtained at 45 °C for each cathode are similar in magnitude to those recorded at room temperature, but in the case of the doped materials higher values were observed at the elevated temperature when cycled at the faster rates. The discharge capacities obtained at 500 mA g^{-1} were 133, 140, and 157 mA h g^{-1} for NMC, B25, and SB25, corresponding to 76%, 83%, and 83% of their initial 45 °C rate capacity (at 20 mA g^{-1}), compared to 71%, 73%, and 77% at room temperature. These results indicate that the doped materials are effective in enhancing the rate performance at room temperature and, more significantly, at elevated temperatures.

The specific capacities obtained from the rate capability tests performed at −5 °C were noticeably lower than those recorded at room temperature for both pristine and doped NMC. As seen at higher temperatures, SB25 shows the highest specific discharge capacities, delivering 149, 136, 124, 111, and 91 mA h g^{-1} at current densities of 20, 50, 100, 200, and 500 mA g^{-1} compared to 130, 117, 104, 92, and 73 mA h g^{-1} in the pristine NMC tested at the same rates. Contrasting to its rate performance at higher temperatures, the capacity delivered by B25 at −5 °C remained lower than that of the pristine material at faster rates. At 500 mA g^{-1}, B25 delivered only 42.4% of its initial rate capacity, compared to 56.2% for the pristine NMC. However, in the following recovery cycles at 20

mA g^{-1}, B25 and pristine NMC both recovered 98% of their initial rate capacity, while the SB25 showed an even higher 99% capacity return.

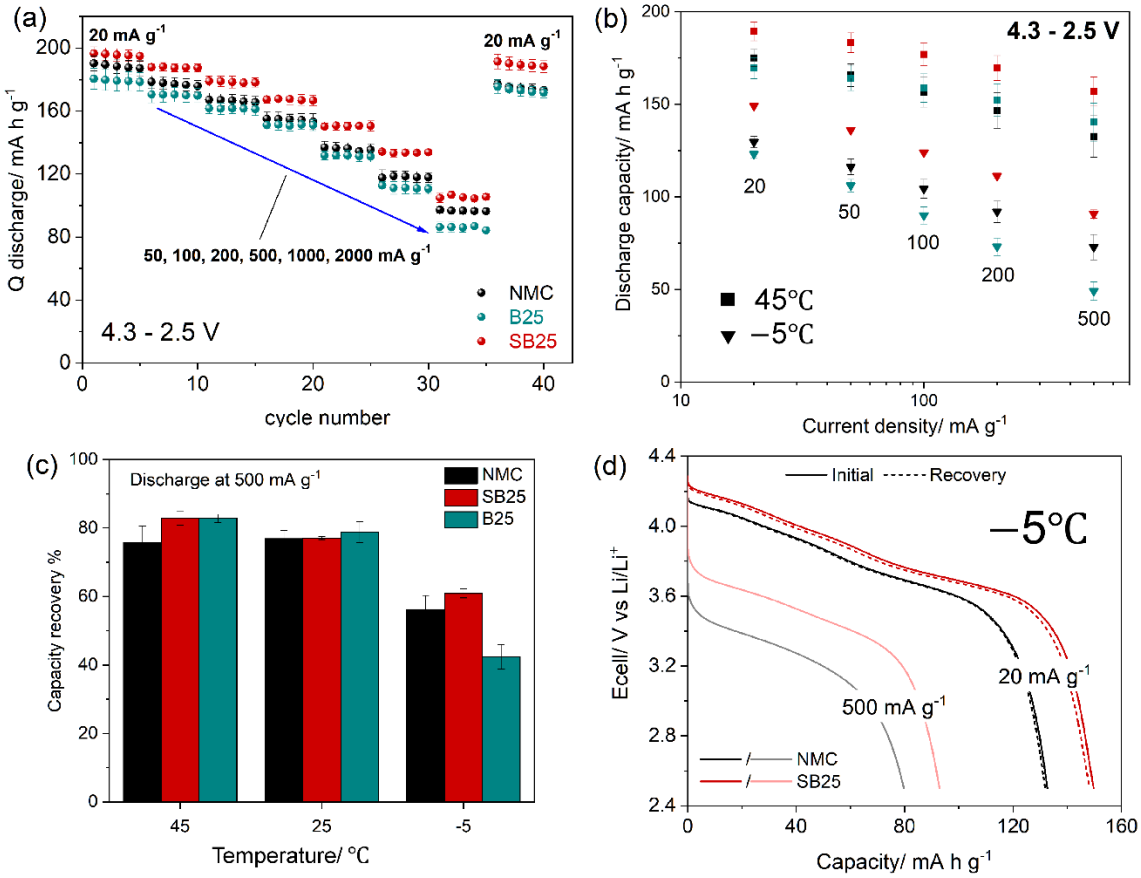

Figure 4.5: Rate capability of pristine and doped NMC materials at room temperature (a) and at 45°C and −5°C (b). Rate capacity recovery at 500 mA g^{-1} at different temperatures (c) and selected discharge profiles of the pristine and SB25 doped NMC at−5°C (d).

EIS measurements were performed on the pristine and doped materials to evaluate the effect of doping on the electrode-electrolyte interfacial resistances. The impedance spectra were collected on fresh cells after formation at room temperature at different states of charge (SOC) between 2.5 and 4.3 V. Figure 4.6 shows the fitted Nyquist plots of the three cathodes at 50% SOC which all share a small semi-circle at around 100 kHz, assigned to the cathode electrolyte interface (R_{SEI}), followed by a larger semi-circle centred at 0.5 kHz which is attributed to the charge transfer resistance (R_{CT}). In the pristine NMC material, the charge transfer semi-circle in the medium to low-frequency

region is split into two, with a further semi-circle appearing at 0.02 kHz. This additional semi-circle is subdued for B25 and disappears completely for SB25. The depression of this additional resistive process in the doped cathodes and their improved rate capability suggest the dopants act to provide further surface stabilisation by forming a conductive layer. The R_{CT} values at 50% SOC for NMC, B25, and SB25 are 10.34 Ω, 10.04 Ω, and 8.79 Ω, revealing the combined boron and tin doping is more effective in reducing the charge transfer resistance at the mid charge point. The ohmic resistance (RS) values in the B25 and SB25 at 50% SOC are 1.13 Ω and 1.42 Ω, which are lower than the 4.08 Ω calculated for the pristine NMC. The doped materials also showed smaller R_S values during the entire charge cycle, as listed in Table B3, suggesting that doping B^{3+} and Sn^{4+} into the NMC structure reduces the internal resistance of the electrolyte.

The temperature dependence of the impedance in the pristine and doped NMC cathodes was also studied by EIS measurements at 45 °C and −5 °C, for which the Nyquist plots at 50% SOC are shown in Figure 4.6. At 45 °C, the additional lower frequency semi-circle is no longer present in the impedance spectra of the pristine NMC. Instead, it displays an elongated semi-circle in the high frequency region followed by a second smaller semi-circle at 0.2 – 0.02 kHz. The shape of the Nyquist plots of B25 and SB25 are more consistent with those at room temperature, except for the smaller diameter of the semi-circles. The R_{CT} values of at 50% SOC are quite similar between the pristine NMC and the doped materials, being 5.9 Ω compared to 4.5 Ω and 5.5 Ω for B25 and SB25. However, at 100% SOC, the R_{CT} value for the pristine NMC increases considerably to 20.2 Ω, whereas no increase is observed in the doped cathodes, further highlighting the improvements on doping. Additionally, the SEI resistance measured in the cells at 45 °C is lower for B25 and SB25 over the complete SOC range.

The EIS responses of the cathodes recorded at −5 °C display much larger semi-circles in the Nyquist plots corresponding to greater impedance across the cell. The increased resistance at low temperatures is thought to be associated with slower ionic and electronic transport within the solid electrode, the electrolyte, and at the CEI, resulting in large overpotentials.[218,219] The Nyquist impedance of the pristine NMC at −5 °C recorded at 50% SOC again shows the distinct appearance of an additional semi-circle in the low frequency region, which is still absent in the spectra of the doped cathodes. This is further demonstrated in the Bode plots displayed in Figure B.4, which shows the two low frequency signals for NMC at ~10^{-1} Hz and ~10^{1} Hz are replaced by a single signal in this region in the doped samples. However, compared to the appearance at room temperature, the third semi-circle appears to be the dominant impedance process in the pristine NMC, which is supported by the fitting results, which returned R_{CT} values of 50.7 Ω and 136 Ω for the two larger semi-circles. The impedance profile of the single and multi-cation doped NMC cathodes at low temperatures are similar in shape, displaying a single charge transfer. However, the SB25 material demonstrates a considerable reduction in the charge transfer impedance, with an extracted R_{CT} value at 50% SOC of 86.5 Ω, compared to 172 Ω for B25 which is similar to the combined R_{CT} values in the pristine NMC. The stabilisation of the charge transfer resistance in SB25 is further demonstrated at higher SOC, in which it decreases slightly to 71.4 Ω when charged to the upper voltage limit. In the pristine NMC, the first R_{CT} process remains constant with increasing SOC at around 50 Ω, however the second R_{CT} process grows considerably to 356 Ω at 4.2 V and finally to 717 Ω when charged up to 4.3 V.

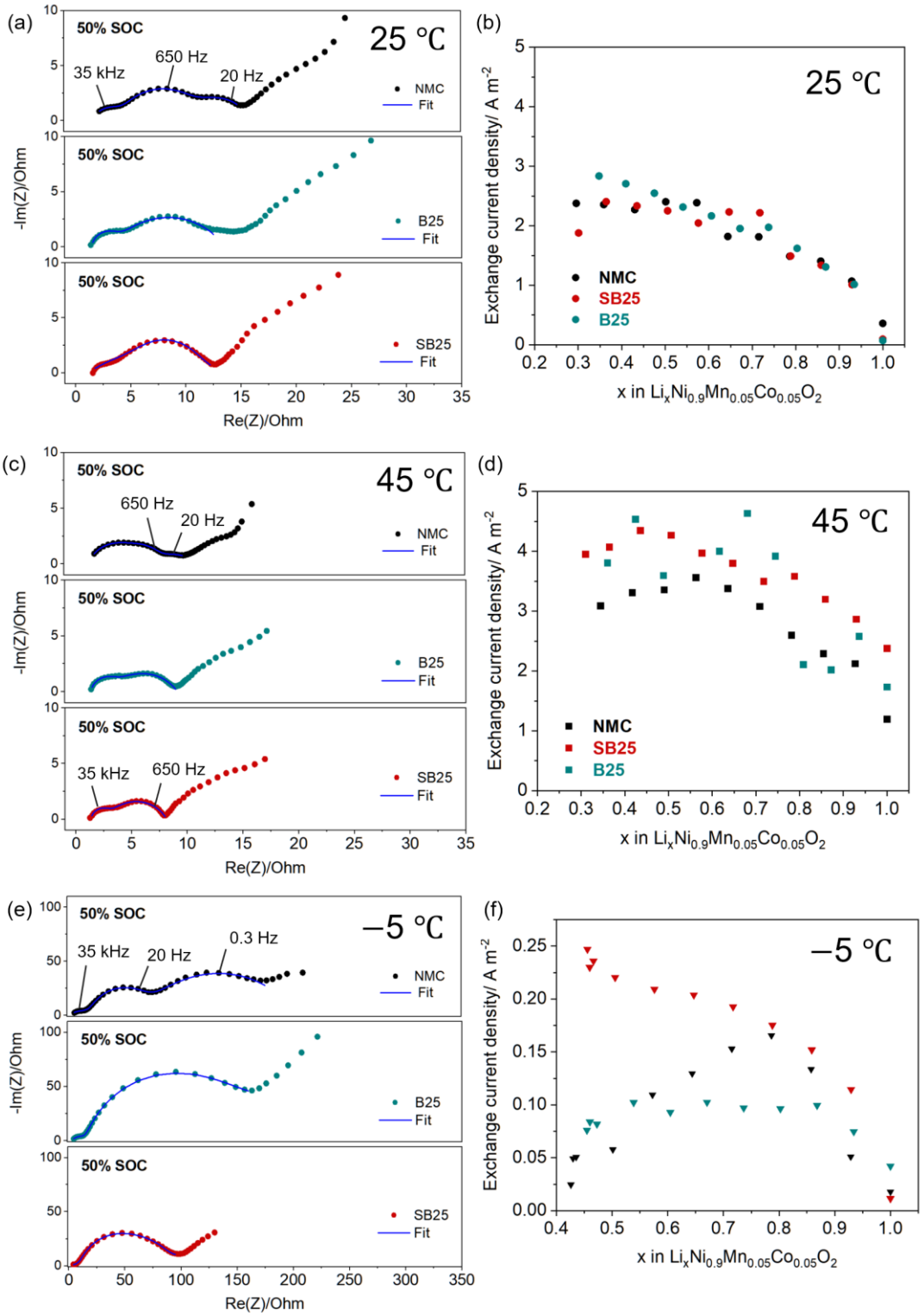

Figure 4.6: Nyquist plots from the EIS measurements at 50% SOC at various temperature (a, c, e) and the calculated exchange current densities as a function of Li stoichiometry during charge (b, d, f).

To further understand the reaction kinetics, the exchange current densities were calculated at each SOC according to the Butler-Volmer relationship from the R_{CT} values obtained from the EIS fitting and are then normalised by the active electrochemical surface area. Figure 4.6 displays the evolution of J_0 as a function of lithium stoichiometry in the pristine and doped NMC materials at the various temperatures. At room temperature, the exchange current densities of the baseline and doped materials all follow a parabolic-like trend as a function of delithiation, with values ranging from 1.0 A m^{-2} and 2.7 A m^{-2} which is consistent with values previously reported for Ni-rich NMC811 materials.[69,220]

At the elevated temperature of 45°C, the calculated values of J_0 in all the cathodes increase, with these values now in the range of 2.0 A m^{-2} and 5.6 A m^{-2}. The evolution of J_0 with decreasing lithium stoichiometry follows a similar curve as that observed at room temperature, however the exchange current densities are generally higher in the doped cathodes over the majority of the stoichiometry range. The average values of J_0 at 45°C are reported as 2.6, 3.6, and 3.5 A m^{-2} for NMC, SB25, and B25 respectively, suggesting improved kinetics in the doped materials at higher temperature. The exchange current densities drop significantly at −5°C in all cathodes to values below 0.3 A m^{-2}, whilst the smaller stoichiometry range reflects the lower amount of available lithium that can be extracted at the sub-zero temperature. The inset in Figure 4.6 reveals a larger variation in the behaviour of J_0 between the different cathode materials at −5°C, with the exchange current densities in the baseline NMC following an inverted V-shape, reaching a maximum of 0.166 A m^{-2} at 30% SOC. Conversely, the exchange specific current in B25 displays a plateau above 20% SOC at a value close to 0.1 A m^{-2} for the rest of charge window, whilst the evolution of J_0 at increasing SOC in SB25 is more consistent with the behaviour seen at higher temperatures. Notably, SB25 exhibits the highest values of J_0

across the full delithiation process at the low temperature conditions, displaying considerable improvement compared to the baseline NMC at higher SOC.

GITT measurements were performed in coin cells after the formation process to extract information on the diffusivity of lithium ions across the different NMC materials. Figure B.5 shows the effective diffusion coefficients for the pristine and doped NMC materials measured at different temperatures. At room temperature, the introduction of the boron and tin dopants does not have a significant effect on the shapes of the diffusion curves, whilst the diffusion profiles of each material measured at 45 °C are largely consistent with those at room temperature. However, at −5°C a larger variation in the effective diffusion coefficients is revealed across the complete charge and discharge cycle, displaying a considerable drop off towards the fully de-lithiated and lithiated states. The variation in the effective diffusion coefficients between the different cathode materials is also more obvious at this temperature, with SB25 demonstrating a larger D_{Li+} over the full voltage window, most notably when the cathode is charged between 3.8 V and 4.3 V. The average charge and discharge D_{Li+} values for each cathode at the different temperatures generally follow the trend of SB25 > B25 > NMC. Additionally, it was found that the cells tested at room temperature displayed the highest average charge/discharge D_{Li+} values of 1.50/1.57, 1.51/1.44, and 1.62/1.66 $\times 10^{-12}$ cm^{-2} s^{-1} for NMC, B25, and SB25 respectively. This result is counterintuitive as higher temperatures typically enhance the solid-state diffusion of Li^+ in the active material. Despite leading to faster kinetics, as seen in the EIS results, lithium-ion transport within the solid cathode material may be hindered due to structural changes arising at 45 °C, such as phase changes or cation mixing which reduce Li^+ mobility within the cathode structure.

4.3.2 Dopant Stabilisation

To assess the structural stability of the materials under battery operation, cycling tests were performed with a discharge rate of 200 mA g^{-1} (≈ 1C). As seen at the slower rate, the initial capacity of the NMC and SB25 are higher than those delivered by B25, however the capacity fade is much slower in the boron doped material over the 100 cycles. After 50 cycles the discharge capacity of NMC falls below B25, whilst that delivered by SB25 still remains the highest for the duration of the cycle test. The capacity retentions of the materials are tracked along with the discharge capacity in Figure 4.7, and are higher for both the doped materials with final values of 92.7% (B25) and 88.7 % (SB25) compared to 78% in the pristine NMC.

The effect of bulk cation doping on extending the cycle life can be further understood by assessment of the sequential dQ/dV plots, which track the evolution in phase transitions for the 1st, 50th, and 100th cycle in Figure 4.7. The NMC materials all show three peaks relating to the main phase transitions associated with the layered oxide materials during lithiation/de-lithiation. Inspection of the H2 – H3 peak in the pristine NMC reveals a large decline in intensity between the 1st and 100th cycle, reflecting the poor reversibility in continuously forming the H3 phase in the highly de-lithiated state. In contrast, the loss of the H3 phase is significantly negated in the SB25 sample, showing a higher retention of the high voltage peak over the cycle range, which reflects the higher capacity retention. This is also the case for B25, however the initial peak intensity is much smaller for this material, suggesting a smaller proportion of the H3 phase is formed originally which is reflected in the greater degree of Li/Ni mixing and lower capacity of this material, as these phase transitions are strongly related to the lithium stoichiometry.[178] The suppression of the H2 – H3 phase transition brought about by the singular boron doping will also reduce

the large contraction of the crystallographic *c*-axis, which is associated with this transition and contributes heavily to the formation of microcracks.[59]

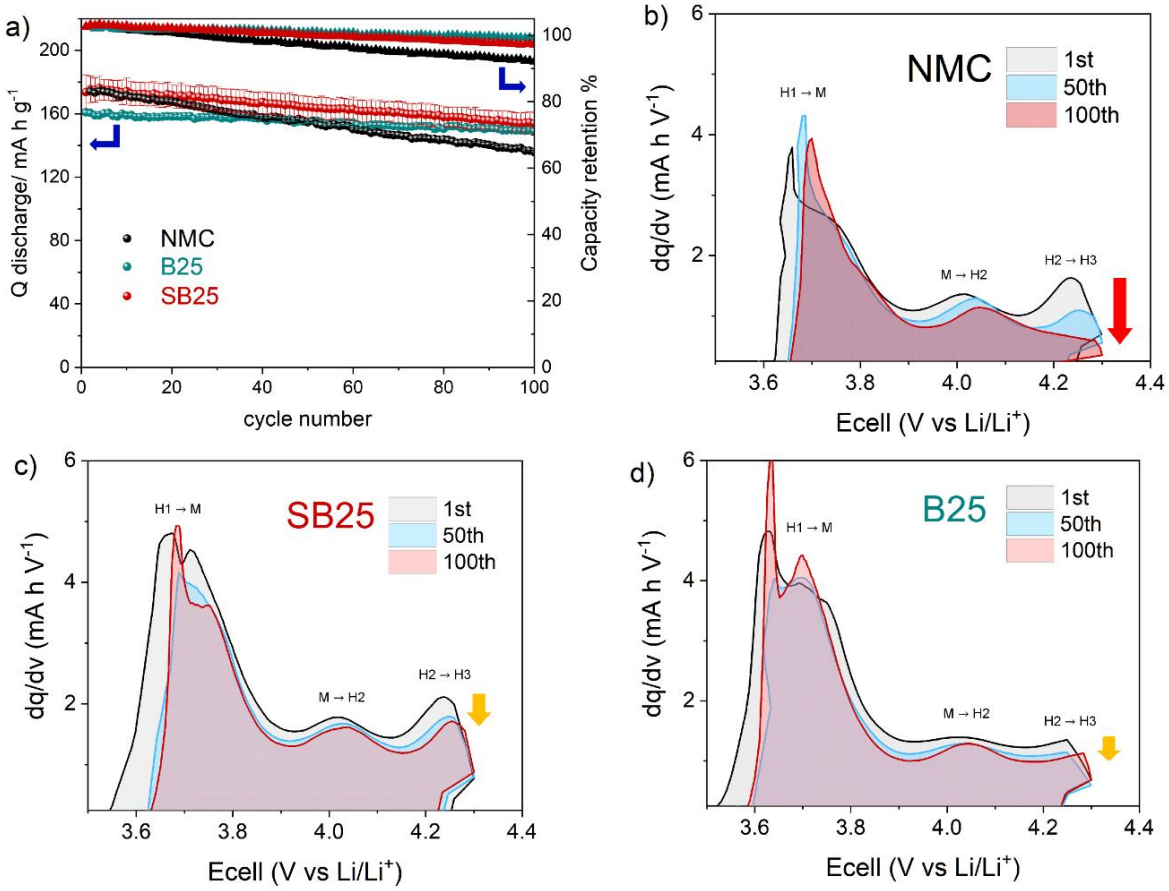

Figure 4.7: Cycle performance of NMC, B25, and SB25 measured between 4.3 – 2.5 V at 200 mA g-1 (a) and the corresponding dQ/dV curves of the 1st, 50th, and 100th charge cycle for pristine NMC (b), SB25 (c), B25 (d).

The superior performance of the cells containing the SB25 cathodes outlines the complimentary benefits of the boron and tin co-doping. Boron can partially occupy the interstitial sites, expanding the c-axis, thus facilitating improved Li^+ diffusion.[163,221] Simultaneously, the substitution of tin at the transition metal sites can enable strong Sn – O bonds which supress oxygen release and delay the H2 to H3 phase transition.[222,223] When co-doped, the SB25 material facilitates faster bulk Li^+ transport and lower

impedance, with this synergy resulting in improved rate capability and stability compared with the boron alone (B25), in line with prior co-doping studies.[224]

Ex-situ XRD

The evolution of the crystal structure upon electrochemical cycling was investigated by measuring the *ex-situ* XRD patterns of the pristine and doped NMC cathodes after being charged to 4.3 V or following the subsequent discharge to 2.5 V. Figure 4.8 compares the diffraction patterns of the as-made electrodes with those at the end of charge and discharge of the first cycle and at the same voltage points in cells after formation and an additional 20 cycles at 200/500 mA g^{-1}. Compared to the XRD of the active material powders, the diffraction patterns of each of the as made electrodes show additional peaks at 26.6° and 65.1°, which are attributed to the presence of graphite added in the electrode formulation and the aluminium foil respectively. During the first electrochemical cycle, additional low intensity peaks appear in the 2θ range between 20–25° which are consistent with previous ex-situ XRD studies of NMC materials and are related to superlattice peaks arising from cation ordering between Li and TM ions as well as the presence of an active monoclinic (C2/*m*) phase.[225–227] The splitting of the (108)/(110), which is indicative of a well layered structure, also remains consistent between the first cycle and in the cycled cells, suggesting the layered structure is largely unaffected by the fast rate cycling.

Rietveld refinements were also performed on the diffraction patterns from the *ex-situ* XRD studies to quantify the changes in structure following (de-)lithiation. The resulting variations in unit cell parameters upon each charge or discharge cycle are presented in Table B.6 and Figure 4.9. In all the cathodes, an increase in the *c*-parameter and decrease in the *a*-parameter is observed at the end of charge relative to its length in the pristine

electrode. The change in the *c*-axis is also reflected in the shift in the 2θ position of the (003) peak to lower angles and is indicative of a contraction in the interlayer spacing due to the removal of lithium from the Li layer, enabling an increase in electrostatic repulsions between oxygen in adjacent layers.[64] Conversely, the shrinking of the *a*-axis is a result of the increase in Ni oxidation state from the de-lithiation of the cathode, leading to stronger and shorter Ni – O bonds which reduces the average TM – TM interatomic distance. As the cathode materials undergo lithiation in the discharge, the *a* and *c* parameters respectively decrease and increase at the end of discharge, returning to values of similar size to those observed in the as made electrode coatings. The same trend is observed for both the initial formation cycle and the cycle proceeding the fast rate cycling, however the magnitude of the changes in lattice parameters vary for the different cathodes. The largest expansion in the *c*-axis is observed for SB25, which displays a ~0.128 Å increase at the end of the first charge cycle, compared to 0.095 Å and 0.074 Å in NMC and B25. These results are also consistent with the change in the (003) peak positions (Table B.6), with SB25 and NMC demonstrating a larger low angle shift than B25.

The *c*-axis variation can also be understood by the dQ/dV (Figure 4.9) which show the redox peak attributed to the H2-H3 transition is shifted to higher voltage in SB25 relative to the undoped NMC, whilst a broader incomplete peak is observed for B25. The absence of this defined peak along with displaying the smallest overall change in the *c*-parameter in the first cycle is consistent with a suppression of the H2-H3 phase transition in the single boron doped material.

Additionally, no distinct splitting of the (003) peak is observed in the *ex-situ* XRD of the cathodes at 4.3 V during the first formation cycle or after the fast rate cycling. Such peak splitting has previously been reported at this voltage for LNO and Ni-rich NMC due to the

co-existence of the H2 and H3 phases.[64,178,228] Instead, all the cathodes here display peak broadening in the collected XRD at the end of charge, which suggests a partial transition.[229] Following the phase transition the $(003)_{H3}$ peak is expected to be shifted back to a higher angle beyond that of its starting position due to the accompanying *c*-axis collapse. However, the (003) peaks in the cathodes at 4.3 V are still shifted to lower angles than in the as made electrodes, whilst the *c*-parameter is also larger, suggesting the average structure at this voltage most closely represents the H2 phase. Although the *ex-situ* XRD results do not detect the onset of the H2-H3 phase transition, likely due to the relaxation of the partially formed H3 lattice, the relative peak positions and *c*-parameter in each cathode can give an indication of the extent of the phase transition.

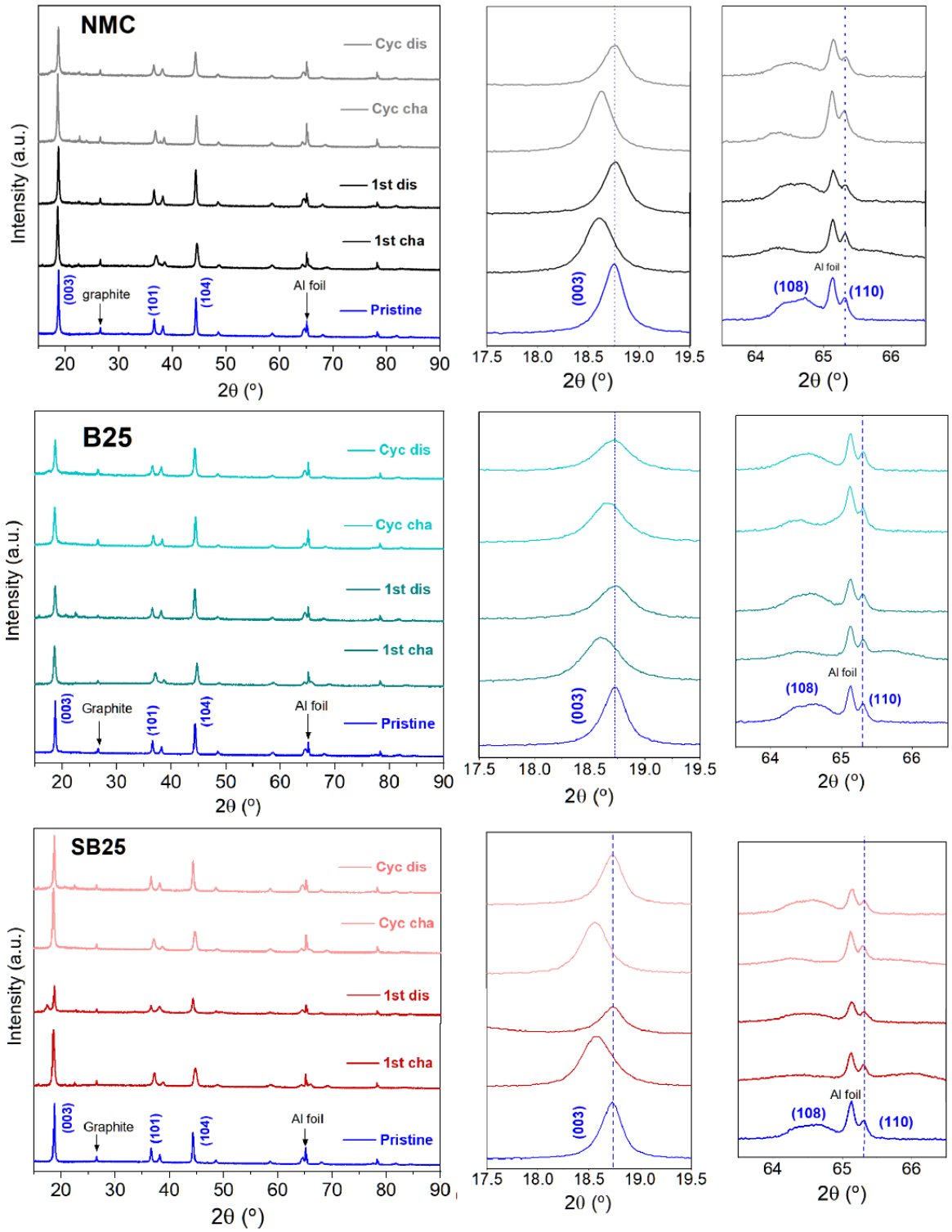

Figure 4.8: *Ex-situ XRD patterns collected on electrodes from cells cycled between 4.3 – 2.5 V at 10 mA g^{-1} during the first formation cycle and in after 20 cycles at a discharge rate of 500 mA g^{-1}.*

After the fast rate cycling, the expansion in the *c*-axis and contraction in the *a*-axis at the end of charge are smaller suggesting all cathodes show some irreversible structure change from the 20 cycles at 500 mA g^{-1}. Notably, the *c*-axis at the end of charge is almost unchanged for the undoped NMC material in the aged cell compared to the first cycle, whilst the *c*-axis in the doped materials display a smaller extension after cycling. However, the large reversible change in the *a*-parameter is still observed for the SB25 material after cycling.

The volume of the unit cell decreases during charge and increases during discharge as is consistent with the literature.[143,230,231] Between the end of charge and end of discharge in the first cycle, the doped materials show a larger volume change compared to the undoped NMC, with a 2.79% and 2.23% volume increase observed in SB25 and B25, whilst only a 1.25% decrease for NMC. After cycling, this volume change decreases slightly in NMC and SB25, but considerably in B25, which shows the lowest volume change of 0.74%.

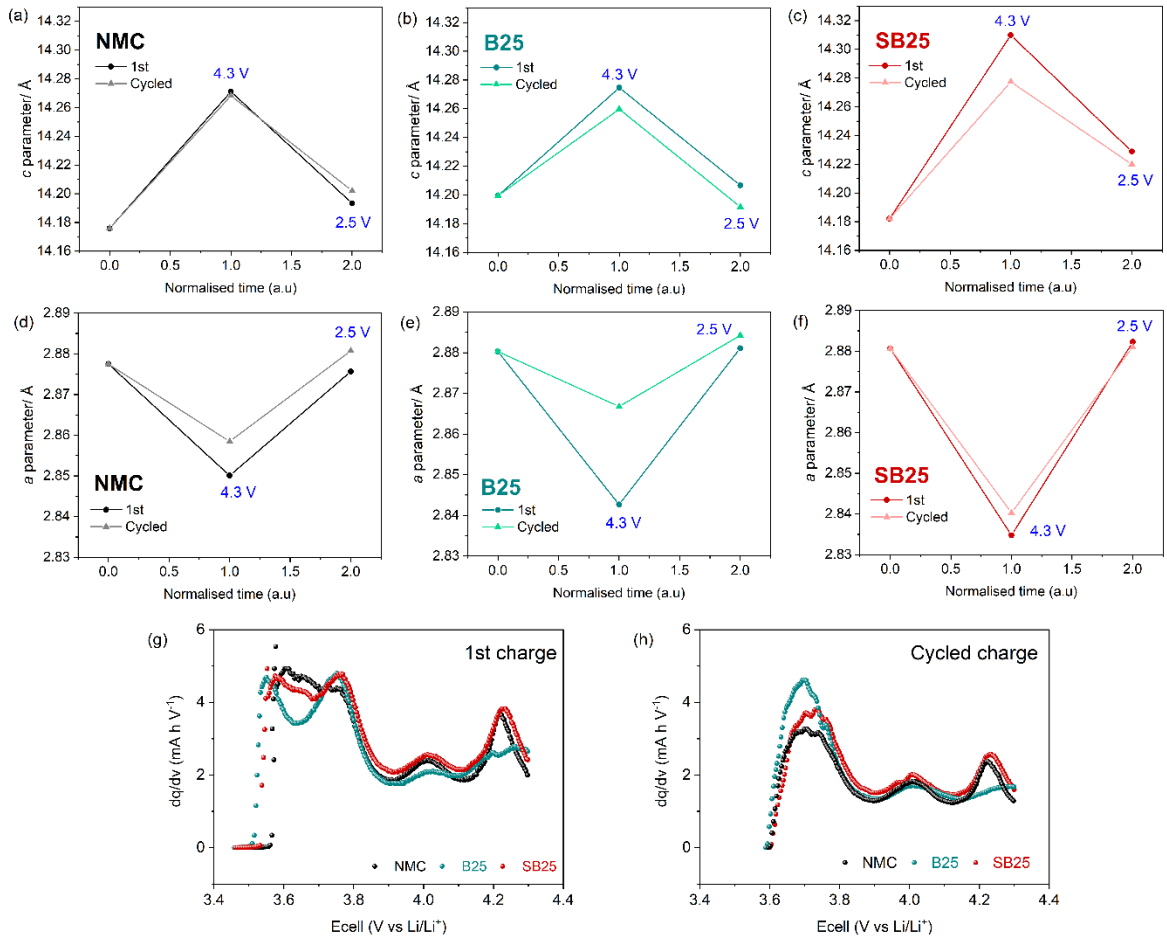

Figure 4.9: Changes of the unit cell parameters calculated from refinements of the ex-situ XRD patterns (a – f) collected on electrodes from cells cycled between 4.3 – 2.5 V at 10 mA g^{-1} during the first formation cycle and after 20 cycles at a discharge rate of 500 mA g^{-1}, and the corresponding dQ/dV plots of the charge cycle in each cell (g – h).

To investigate the effect of active material doping upon stabilising the electrode surface composition during cycling, XPS was used to characterise the as made NMC electrodes and the same electrodes after 200 cycles at a rate of 200 mA g^{-1}. Changes in the O 1s, F 1s, and C 1s spectra can be studied to investigate electrolyte decomposition and CEI evolution. Figure 4.10 shows the XPS spectra for the aforementioned core levels of the three pristine and cycled electrodes. Initially, the O 1s spectra show three peaks at 533.7 eV, 532.0 eV and 529.3 eV relating respectively to C – O – C from the oxidation of the conductive additive, C = O based surface residual lithium species and the lattice oxygen from the active material.[232] In all samples, the area of the C = O peak, most commonly

from lithium carbonate, is the dominating contribution in the spectra, highlighting the significant surface sensitivity of the Ni-rich electrodes even when prepared in a dry room. Post-mortem electrode analysis of the O 1s spectra confirms the formation of a substantial surface layer on the cathodes, reducing the relative proportion of the lattice oxygen to below 1% in each of the samples. Within the surface species, it is noted that the proportion of C – O – C is largest in the baseline NMC, which has previously been ascribed to an increase in polyether products from severe electrolyte decomposition.[159,232] The proportion of this peak in the O 1s spectra is slightly reduced for SB25; however, it is considerably lower in the B25 sample, which could suggest a lower level of electrolyte decomposition.

The C 1s spectra of the electrodes display multiple peaks which can be assigned to C = C (284.4 eV), C – C (284.9 eV), C – O (286.3 eV), C = O (287.8 eV), and C – F (290.4 eV). These environments are also resolved in the spectra of the cycled electrodes at the same binding energies, except for the C = O peak which is shifted to 288.7 eV in each cathode sample. Additionally, the cycled electrodes all show an increase in the peak intensity ratio C – O/C – C, which is associated with the decomposition of the electrolyte and subsequent build-up of CEI species.[233] The peak ratios are calculated as 1.98, 1.80, and 1.39 for NMC, SB25, and B25, respectively, which suggests the electrolyte decomposition is reduced for the doped materials. This result is also consistent with the trend in the electrochemical cycling performance of each material, in which B25 demonstrates the highest capacity retention.

Figure B.6 shows the Li 1s spectra of the pristine and aged electrodes. Prior to cycling, a single peak in the Li 1s spectra is present in each of the cathode electrodes at 55.2 eV which is present again at the same position in the cycled electrodes. However, an

additional peak can be detected in the cycled NMC baseline electrode, situated at a higher binding energy of 57.7 eV, which is not found for the doped cathodes. The occurrence of this second peak in the baseline NMC hints at the formation of a larger proportion of LiF and Li_2CO_3 from the irreversible consumption of active Li in the CEI, which by contrast is reduced in SB25 and B25, thus limiting the capacity fade.

The F 1s spectra of the electrodes prior to cycling shows very similar profiles, with two distinct fitted peaks at 688 eV and 685 eV (present in a consistent relative proportion across each of the cathodes) which are assigned to the C – F from the PVDF binder and LiF species. Following cycling, the peak shape becomes convoluted and the fitted peak positions shift to lower binding energies of about 686.4 eV and 684.3 eV. These peak positions reflect the additional presence of $Li_xPO_yF_z$ from the electrolyte decomposition (~686 eV) and transition metal fluorides from the reaction of surface migrated TM and the electrolyte (~684 eV) respectively.[234] After 200 cycles, the peak attributed to the Li-F and TM-F components is much weaker in B25 than for the undoped NMC cathode. For the Ni 2p spectra, the main $2p_{3/2}$ and $2p_{1/2}$ peaks appear at 855.5 eV and 873.0 eV in the as made electrodes of each cathode, but following cycling are shifted to higher binding energy, with the Ni $2p_{3/2}$ peak now located at 857.7 eV for the pristine NMC and at 858.5 eV in both SB25 and B25. This could suggest a larger proportion of Ni^{3+} is present in the cycled electrodes of the doped cathodes.

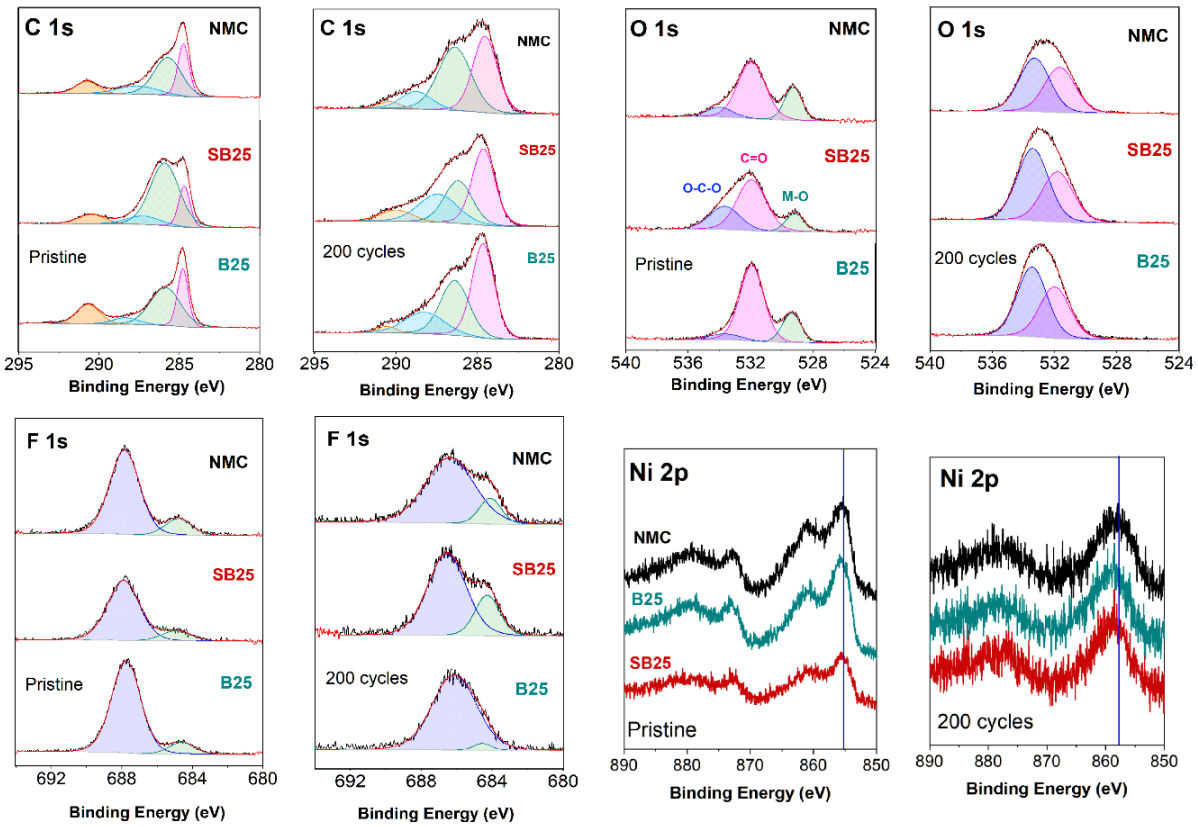

Figure 4.10: XPS collected on the pristine and cycled electrodes after 200 cycles at 200 mA g^{-1} for the C 1s, O 1s, F 1s, and Ni 2p spectra.

Ex-situ XAS

The variation in transition metal oxidation state after cycling was further studied by measuring XANES spectra of Ni, Mn, and Co K-edge on pristine electrodes and electrodes extracted from cells following 200 charge and discharge cycles, which are depicted in Figure 4.11. As seen previously in the powder samples (Figure 4.4), the white line position of all the electrode samples in the Ni K-edge are shifted to higher energies compared to the Ni^{2+} standards by the same gap present in the powders, suggesting no additional oxidation of the vacuum stored electrodes in the dry room. After 200 cycles, the white line energy of the pristine NMC at the Ni K-edge is shifted by 1.4 eV to a higher energy position, whereas a smaller shift of 1.1 eV is observed for B25, whilst no shift

occurs for SB25. The same trend is also displayed in both Co and Mn K-edge, where the positive energy shifts are 0.9 eV and 0.8 eV respectively for the baseline NMC, which are reduced to 0.3 eV and 0.5 eV for B25, whilst the maximum peak intensity positions for SB25 remain constant in the pre-cycled and cycled electrode. The larger energy shifts in the cycled baseline NMC indicates an increase in average oxidation states of the transition metals, whereas this is stabilised by the inclusion of boron in the structure, whilst the addition of tin appears to indicate complete retention of the TM valences. Therefore, after the 200th cycle the doped materials demonstrate a higher reversibility of the electrochemical active redox reactions, which is supported by the higher capacity retentions displayed in these cathodes.

Alongside the energy shift, changes in the loss of white line intensity are also observed in the Ni K-edge spectra for all cathodes, although the exact loss varies between the samples. Compared with the pristine NMC, the peak intensity loss is reduced for SB25, suggesting the co-doping stabilises the local structure environment of the Ni during cycling. The opposite effect is actually observed for B25, however the peak intensity in the cycled boron doped electrode is still higher than that displayed for the corresponding aged NMC electrode. The effect of doping on the peak intensity change after cycling in the Co and Mn K-edge is more aligned, with SB25 and B25 both acting to reduce the decay in peak intensity. Notably, the Mn K-edge spectra of SB25 before and after cycling can be overlaid almost identically, suggesting the structure and valence of Mn in SB25 is virtually unchanged after 200 charge and discharge cycles. Furthermore, the baseline NMC cathode shows a larger increase in intensity of the Mn pre-edge peak compared to the doped materials, which indicates a larger disorder in the octahedral coordination.[235]

The Ni EXAFS spectra of the cathodes presented in Figure 4.11 display small variation between the as made and cycled electrodes up to 3 Å, however beyond these distances in the region of multiple scattering peaks, there are considerable changes for the undoped NMC. Instead, the peaks in this region remain almost unchanged for SB25 after cycling, suggesting a greater stability of the transition metal structure in the outer coordination shells. Each cathode demonstrates a similar small loss of intensity at the Ni – TM peak, whilst no change in the radial distance is observed following cycling. The change in the peak intensity of the Ni – O shell reveals more variation between samples, with the intensity increasing for the NMC baseline, but decreasing in SB25 and remaining unchanged in B25. A small shift to smaller bond length is also observed for the Ni – O shell in the undoped NMC material after cycling, which is consistent with the higher average oxidation state of Ni observed in the XANES.

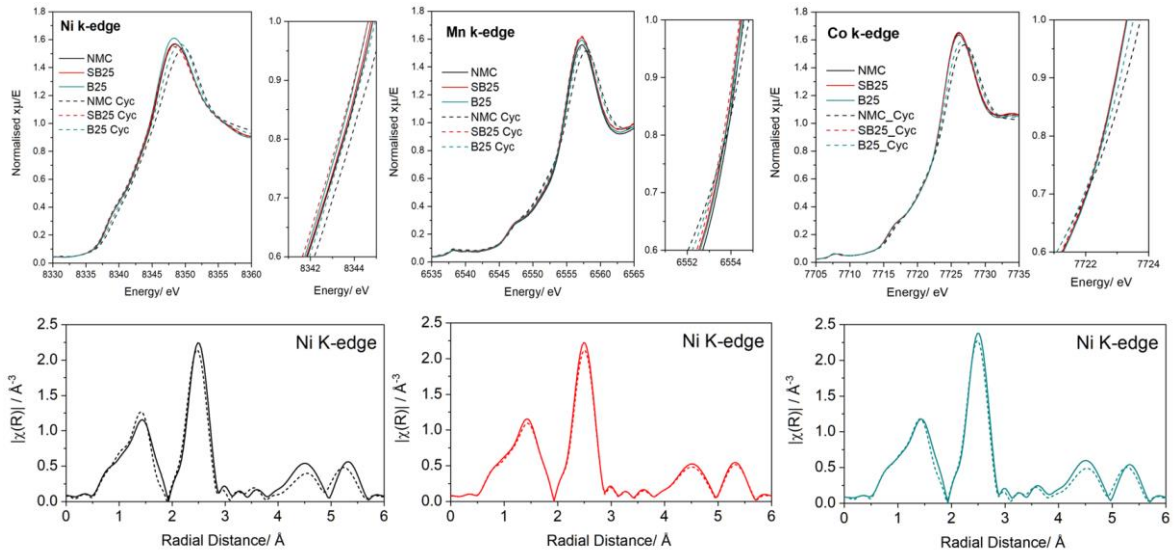

Figure 4.11: Normalised XANES spectra of the pristine and cycled electrode of NMC, SB25, and B25 at the Ni, Co, and Mn K-edge. EXAFS spectra of the cathode materials at the Ni K-edge.

4.4 Conclusions

This work demonstrates that boron (B25) and tin-boron (SB25) co-doping of Ni-rich NMC90-5-5 cathodes significantly enhance electrochemical performance and structural stability, particularly under extreme low and high temperature conditions. Both doped materials maintained the layered α-NaFeO2 structure. They exhibited improved lattice stability through reduced cation mixing and suppression of detrimental phase transitions such as H2–H3, which are linked to structural degradation during cycling.

The electrochemical performance and transport properties of the doped materials were assessed at elevated (45°C), room (25°C), and low (−5°C) temperatures to evaluate their effectiveness under practical conditions:

- **Room Temperature (25°C):** Sn-B co-doping (SB25) significantly outperformed both the pristine and single B-doped (B25) materials in terms of rate capability and capacity retention. In this respect, SB25 exhibited reduced charge-transfer impedance and a more stable cathode-electrolyte interphase (CEI), resulting in higher lithium-ion diffusivity and improved reversibility during cycling. B25, although showing a slightly lower initial capacity due to increased cation mixing, demonstrated excellent long-term capacity retention.
- **Elevated Temperature (45°C):** The doped materials exhibited superior rate performance compared to the pristine NMC, with SB25 delivering the highest capacities at all discharge rates. Both dopants reduced charge-transfer resistance with minimal degradation of the CEI. The B25 material showed notable capacity retention at high rates, suggesting that doping mitigates structural, and surface degradation typically exacerbated at elevated temperatures, perhaps due to a stabilising lithium borate surface layer.

- **Low Temperature (−5°C):** SB25 maintained superior rate performance at sub-ambient conditions, delivering significantly higher discharge capacities at faster rates than B25 and the pristine material. SB25's improved low-temperature performance is attributed to enhanced lithium-ion transport and reduced interfacial resistance. In contrast, B25 showed diminished performance at higher discharge rates but retained excellent capacity recovery, indicating effective structural stabilisation even at challenging temperatures.

Ex-situ analyses confirmed that the dopants stabilised the oxidation states of transition metals and mitigated surface degradation due to electrolyte decomposition across all temperatures. This stabilisation was more pronounced in the SB25 co-doped material, contributing to improved structural and electrochemical resilience.

In conclusion, Sn-B co-doping synergistically enhances the high-rate and temperature-dependent performance of Ni-rich NMC90-5-5 cathodes. The improved performance, particularly at low temperatures, underscores the potential of tailored doping strategies for advancing lithium-ion batteries for electric vehicles and other demanding applications. Further optimisation of the dopant ratios and investigation of their interactions with electrolytes could provide additional gains in performance and durability.

Chapter 5: Impact of Cell Balance in B and Sn Doped NMC 90-5-5 Li-ion Full Cells for High Power and High Energy Designs

This work has been published in *Journal of Power Sources,* **2025**, 659, 238415 (Ethan Williams, David Burnett, Yongxiu Chen, Peter Slater, and Emma Kendrick).

DOI: 10.1016/j.jpowsour.2025.238415

Submitted: 18/07/2025

Accepted: 14/09/2025

Author contributions: E.W. conceived and designed the research. E.W. conducted the experiments, performed the data analysis, and drafted the manuscript. Y.C. provided guidance and assistance with the GITT analysis. E.K. provided lead supervision and conceptualisation. E.K., P.S., and D.B. reviewed and edited the manuscript.

5.1 Introduction

The growing demand for sustainable energy usage, such as the electric vehicle and energy storage systems markets rely heavily on the use of lithium-ion batteries (LIB). To appease the larger adoption of these industries in society, ongoing improvements into LIB technology have been made to target higher power and energy densities. This requires development of the cathode and anode at both the material and electrode stage in order to target the desired application of the cell. At a materials level, the development of high voltage and high capacity cathodes such as Ni-rich $LiNi_{1-x-y}Mn_xCo_yO_2$ (NMC) materials coupled with a graphite anode have been adopted for high energy cells. In high power cells, different cell chemistries such as $LiFePO_4$ (LFP) cathode and niobium oxide anode materials that facilitate a fast and stable Li^+ diffusivity are required to enable fast charging capability.[236–238] Additionally, electrodes of low mass loadings and high porosities, containing active materials of small particle sizes and formulations with a high conductive carbon content are optimal in the design of high power cells, whilst the opposite is preferred when targeting higher energy densities.[239] Another important consideration in the cell design of LIB is the capacity balance between the negative and positive electrodes, known as the N/P ratio, which requires careful control to deliver high capacity, whilst preventing any Li plating occurring during the cell lifetime and limiting cathode degradation.[240,241] Full cells for high power and high energy applications have usually required material trade-offs, as materials that support rapid charge and discharge cycles may not store as much energy, and so achieving a balance between these two parameters is a significant design challenge. Additionally, new materials must not compromise battery lifetime, which is one of the challenges with silicon-based anodes, which demonstrate much higher capacities at appropriate operating voltages but suffer

from significant degradation induced by large volume changes and eventual particle pulverisation.[242,243]

The choice of the cathode and anode material, as well as their mass loadings and N/P ratio in which they are assembled, will also affect the thermodynamic and kinetic response during the full cell operation. A cell's overpotential is the sum of both the charge transfer and ohmic resistances, meaning the contributions from each electrode will be different and depend on the particular reaction stoichiometry, whilst the overall cell performance is typically limited by one of the electrodes.[121,244] Therefore, the cell design (power or energy) and test parameters (voltage range, C-rate) will change the magnitude of the overpotential and resulting stoichiometry in each electrode.

In previous work, it was demonstrated that Sn and B co-doping in $LiNi_{0.9}Mn_{0.05}Co_{0.05}O_2$ (NMC 90-5-5) reduces overpotentials and improves kinetics in the cathode performance, which could enable improved cell balancing at higher charge/discharge rates when integrated into full cells. While coin cells are commonly used in research due to their ease of assembly and reproducibility,[245] Larger-format single-layer pouch cells provide a more industrially relevant platform for assessing practical cell performance. Therefore, in this study, we investigate the impact of doping, cell balance (N/P ratio), and format (coin vs. pouch cells) on the electrochemical behaviour of full cells pairing pristine and doped NMC 90-5-5 cathodes with graphite anodes. We analyse how the material properties influence stoichiometry, rate capability, polarisation, and long-term cycle life using a range of electrochemical techniques, including galvanostatic cycling, electrochemical impedance spectroscopy (EIS), and galvanostatic intermittent titration technique (GITT). Additionally, we explore high-energy cell designs with high-mass-loading electrodes (~4.5 mA h cm^{-2}) in pouch cells to assess their viability for increasing energy density

while maintaining stable cycling. We provide key insights into optimising high Ni NMC full cells for both high-power and high-energy lithium-ion battery applications by examining the interplay between cathode kinetics, anode-cathode balancing, and polarisation effects.

5.2 Experimental

5.2.1 Electrode Materials

The cathode active materials synthesised in Chapter 4, those being the pristine (NMC) and doped (B25, SB25) NMC 90-5-5, were used in this work and thus the full details of the materials synthesis and electrode preparation can be found in that chapter.

A commercial graphite material (Targray, BFC-QC) was used for preparation of the negative electrode coatings, comprised of 95.25 wt.% active, 1.5 wt.% CMC (BVH8, Ashland), 2.25 wt.% SBR (BM-451B, Zeon), and 1 wt.% carbon black (C45, Timcal). The anode electrodes were coated onto 10 μm Cu foil. The cathode and anode coatings were calendared to the necessary thicknesses to obtain porosities of 30% and 40% respectively.

5.2.2 Cell Assembly

Coin cells were prepared using CR2032 cell parts, into which a separator (2325, Celgard) was placed between the disc punched electrodes and wetted with 90 μL of 1 M $LiPF_6$ in EC/EMC (30: 70, + 2 wt.% VC) electrolyte.

Single-layer pouch cells were assembled in two different size formats of active coating areas, referred hereafter as 3x3 pouch (9.0 cm^2 cathode, 9.61 cm^2 anode) and 5x7 pouch (35.0 cm^2 cathode, 36.21 cm^2 anode). Electrodes were punched out using a swing arm cutting press (Global Cutting Technologies), and the stack prepared so that the electrodes

were wrapped in sufficient separator and divided by a single layer of the separator (2325, Celgard) material. The stack was then placed between two layers of the pouch bag material and heat sealed at three of the edges so that the electrolyte could be pipetted directly onto the separator *via* the one exposed edge, before heat sealing the pouch closed. The electrolyte used was the same as described for the coin cells, of which 550 µL was added for the 3x3 pouch and 1950 µL added for the 5x7 pouch formats. The pouch was left for 1 or 2 hours depending on the chosen format to allow sufficient electrolyte wetting of the separator, before cutting open the pouch at one end and sealing again under vacuum.

The N/P ratio in the full cells were calculated based on the ratio of the negative and positive areal capacities. The cell balance was varied by using negative electrode coatings of different mass loading, achieved by changing the coating thickness. Detailed parameters of both electrodes used in the assembly of the coin and pouch full cells are given in Table 5..

Table 5.1: Electrode parameters of the positive (NMC, B25, SB25) and negative (graphite) coatings used in the assembly of coin and pouch full cells at different N/P ratios.

Format	Positive		Negative		N/P
	AM loading/ mg cm^{-2}	Areal capacity/ mA h cm^{-2})	AM loading/ mg cm^{-2}	Areal capacity/ mA h cm^{-2})	
Coin	55	1.14	32	1.15	1.0
			35	1.26	1.1
			39	1.37	1.2
Pouch	60	1.17	33	1.17	1.0
			41	1.41	1.2

Three-electrode cells (El-Cell PAT series) were assembled in a glovebox where electrode discs of 18 mm diameter were punched out and inserted into a pre-assembled insulation sleeve consisting of a PP/PE separator (FS-5P, EL-Cell) and lithium reference ring. The separator, was wetted with 120 µL of the standard electrolyte before sealing the cell stack with a stainless-steel plunger at either end.

5.2.3 Electrochemical Testing

Coin and Pouch Full-Cells

All cells were subject to an initial 8 h rest step at OCV followed by two cc-cv-cc formation cycles at a specific current of 10 mA g^{-1} (cv limit of 2 mA g^{-1}) between either 4.2 – 2.5 V or 4.3 – 2.5 V when stated. The rate capability of the cells was determined at a constant charge rate of 20 mA g^{-1} (or 100 mA g^{-1} where stated) and varying discharge rates between 20 and 500 mA g^{-1} for the coin and 3x3 pouch formats, with the range extended to 2000 mA g^{-1} in the 5x7 pouch cells to assess the high-power performance.

The lithium stoichiometry in the positive and negative electrodes was determined based on the evolution of the lithium concentration during charge and discharge from the capacity-voltage profiles, as calculated from Eq. (1) and Eq. (2).

$$C_{Li,x\%} = \frac{Q\ (mA\ h) \times 3.6}{F\ (C\ mol^{-1})} \quad (1)$$

$$Stoic = \frac{C_{Li,x\%} \times M_w}{GSM} \quad (2)$$

Where Q is the capacity in mA h, which is multiplied by 3.6 to convert to coulombs, and F is the Faraday constant, 96485.3 C mol^{-1}. $C_{Li,x\%}$ is the lithium concentration in the

electrode in mol m^{-3}, M_w is the molar mass of the active material in g mol^{-1}, and GSM is the gram per square meter mass loading of the electrode.

Electrochemical impedance spectroscopy (EIS) was performed on a VMP3 potentiostat (Biologic, France) during a C/10 charge and discharge cycle at specified points along the voltage profile following a 30 min rest. PEIS measurements were performed using a frequency range between 100 kHz and 10 mHz at an amplitude of 10 mV. Equivalent circuit model fitting of the data was performed with the ZFit function in the EC-Lab software.

Three-electrode Cells

Formation cycles were performed as described for the coin and pouch cell tests, using a cell operating voltage range of 4.3 – 2.5 V. Rate capability tests were performed using symmetric cycling to assess the limits of fast lithiation into each electrode, using rates of C/5, C/2, 1C, 2C, and 5C, where the 1C capacity was determined by BCD step at 20 mA g^{-1} following the formation cycles. Accelerated ageing was performed using a 2C cccv charge (0.1C cut off limit) and 2C cc discharge, after 100 cycles and 200 cycles a galvanostatic intermittent titration technique (GITT) cycle was employed as a reference performance test (RPT). GITT was performed using C/10 charge and discharge cycles in which the current was applied in pulses for 15 min followed by a 3 h rest period to allow the voltage to relax back to the OCV. Diffusion coefficients were calculated based on the Weppner and Huggins method using Eq. (3), in which the SAND equation is applied to fit the individual current pulses, as described in previous work.[121]

$$D_{\mathrm{Li+}} = \frac{4}{\pi}\left(\frac{iV_m}{nFS}\right)^2\left(\frac{dV_s/d\delta}{dV_s/dt^{0.5}}\right)^2 \quad (3)$$

The IR (voltage) drop was also extracted from GITT by measuring the instantaneous voltage change immediately following the start and end of the current pulse, and are used to investigate the kinetic overpotentials.

5.2.4 Post-mortem Characterisation

After cycling, the pouch cells were disassembled inside an argon-filled glovebox (H_2O, O_2 <0.1 ppm). Electrodes were separated from the stack and left to soak in dimethyl carbonate (DMC) (anhydrous, >99.0, Sigma Aldrich) for 30 mins before drying under vacuum at 80°C overnight. The morphology of the cycled electrodes was then viewed by SEM (EVO10, Zeiss) under an accelerating voltage of 15 kV.

5.3 Results and Discussion

5.3.1 Formation Stoichiometry

Half-cell testing

Initially, the individual stoichiometry of the positive and negative electrodes was investigated in half-cells to determine the amount of available lithium that can be extracted or inserted during the formation process. The measured capacities from the two formation cycles recorded at a specific current of 10 mA g^{-1} are displayed in Table 5.2**.** The graphite anode delivered a first cycle reversible capacity of 355 mA h g^{-1} and an initial coulombic efficiency (ICE) of 93.2%, which is close to the theoretical specific capacity of 372 mA h g^{-1}, whilst the ICE is within the expected benchmark range (90 – 96%) for commercial material.[246] The second cycle showed no change in the reversible capacity, whilst the CE increased to 99.3% suggesting a stable SEI had been formed on the graphite electrode in the first cycle and so did not consume anymore of the lithium

inventory. The reversible capacities and CE values for the cathode half cells are consistent with our previous work, with both values increasing for the dual doped SB25 material, but decreasing for the single doped B25 compared to the undoped NMC.

Table 5.2: Half-cell capacities (Q/ mA h g^{-1}) with the calculated stoichiometry range (x) and Coulombic efficiencies (CE) for the initial two formation cycles.

Electrode	1st Charge		1st Discharge		1st	2nd Charge		2nd Discharge		2nd CE
	Q	x	Q	x	CE%	Q	x	Q	x	%
NMC	216.6	0.211	208.0	0.969	96.0	206.4	0.216	204.0	0.961	99.3
B25	200.5	0.228	190.8	0.972	95.2	191.3	0.234	188.6	0.969	98.6
SB25	215.3	0.162	210.2	0.982	97.6	208.2	0.171	207.4	0.978	99.6
Graphite	381.2	0.802	355.2	0.077	93.2	359.1	0.870	356.5	0.085	99.3

The stoichiometry in the electrodes was calculated for each of the half-cells from the measured capacity over the two formation cycles, and the corresponding voltage curves are displayed in Figure 5.1. The calculated lithium stoichiometry values in the cathode and anode electrodes were determined from the half-cell formation cycle data. At the end of the first cycle, the stoichiometry in the cathode materials was found to be $Li_{0.969}$, $Li_{0.972}$, and $Li_{0.982}$ for NMC, B25, and SB25, respectively. After the second cycle, these values decreased to $Li_{0.961}$, $Li_{0.969}$, and $Li_{0.978,}$ indicating a reduction in lithium content upon cycling. Notably, the stoichiometry range in SB25 was considerably larger than that observed in the undoped NMC during each charge and discharge cycle. In the anode half-cell, the lithium stoichiometry in Li_xC_6 at the end of the first charge was determined to be $Li_{0.802}$, which increased to $Li_{0.870}$ following the second lithiation cycle. This shift is further supported by the differential capacity plot of the graphite anode (Figure C.1), where the charge peaks corresponding to graphite phase transitions during lithiation appear at lower voltages in the second cycle.

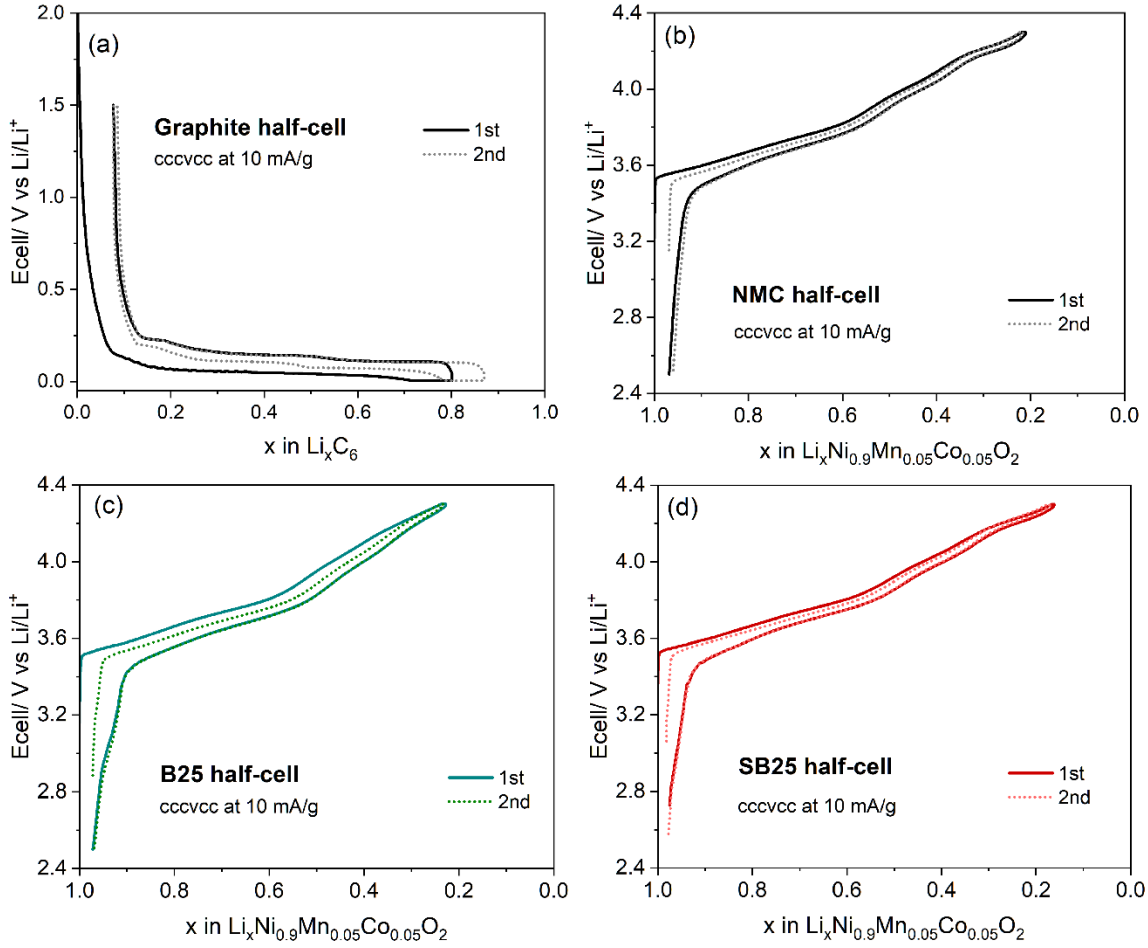

Figure 5.1: Half-cell formation voltage profiles of (a) commercial graphite anode at 15 mA/g at 0.005 - 1.5 V and (b - d) pristine and doped NMC 90-5-5 cathode materials at 10 mA/g at 4.3 - 2.5 V.

Full-cell testing

Having established the reversible capacities of the graphite material, the NMC, B25, and SB25 cathodes were paired with anodes of varying mass loadings to obtain full cells with N/P ratios of 1.0, 1.1, and 1.2 for coin cell tests. Figure 5.2 displays the voltage profiles for the formation cycles of these full cells tested at 10 mA g^{-1}. It is generally observed that the charge and discharge capacities in each cell decreases with increasing N/P, whilst the magnitude of the capacities follows a similar trend (SB25>NMC>B25) to that observed in the half-cells. However, the highest reversible areal capacity is found in the SB25 full cell assembled at N/P = 1.1, which delivers a reversible capacity of 1.11 mA h cm^{-2} at the end of the 2nd cycle. This cell also demonstrates the lowest first cycle loss, with an ICE of

91.4%, whilst the rest of the cells display ICE's between 86.4 – 90.1%. Typically, the ICE can be expected to decrease with increasing N/P ratio as the larger capacity excess at the anode means more lithium is consumed in the SEI formation. However, the contrary is observed in the undoped NMC cells, with the ICE increasing from 87.8% in the N/P 1.0 cell to 89.0% in the cell with a N/P ratio of 1.2. This could suggest the graphite in the cells with higher N/P ratio is not reaching such low voltages, which in turn reduces the amount of SEI formation.[247]

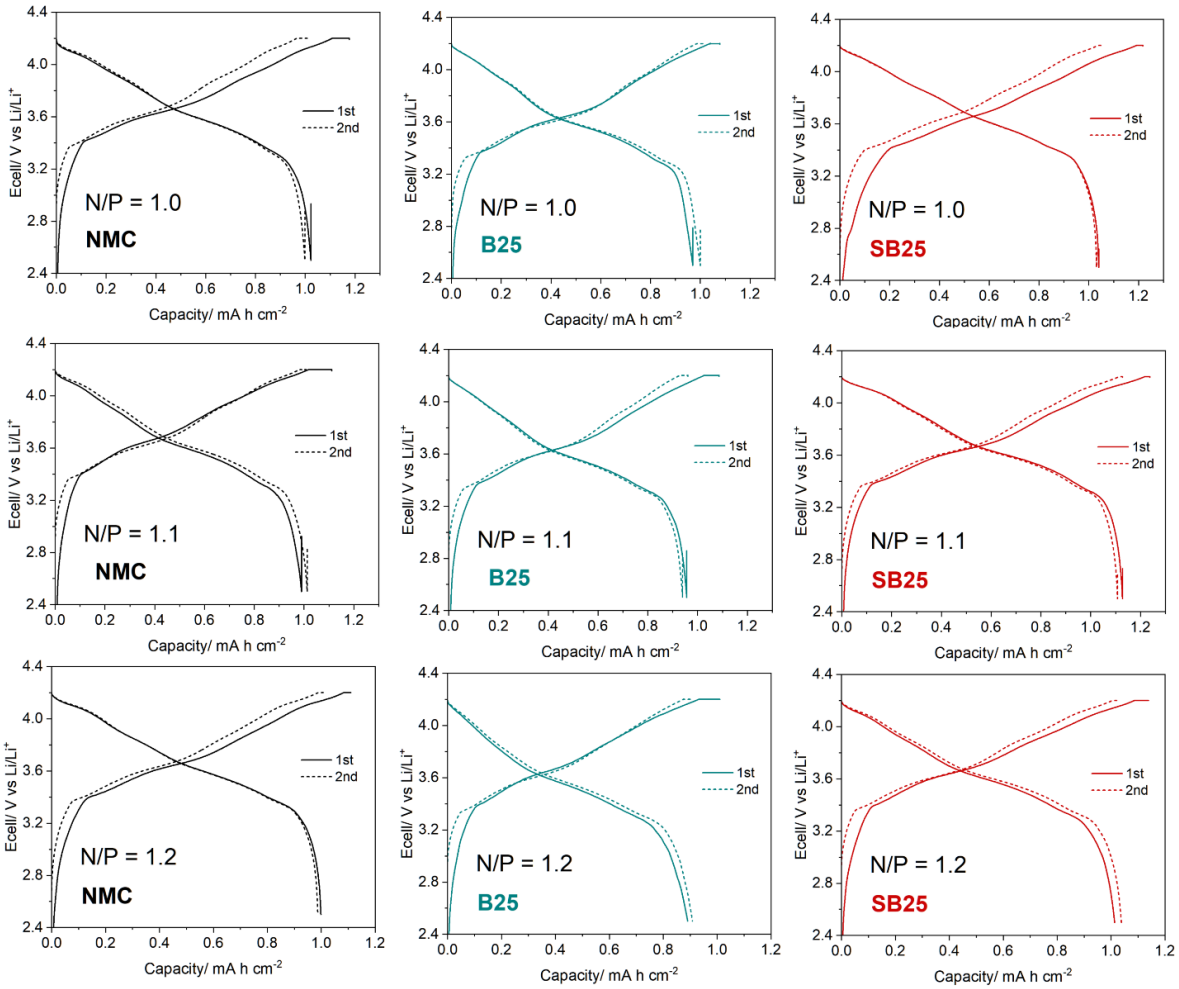

Figure 5.2: Formation voltage profiles from full cells assembled with a graphite anode and a pristine (NMC) or doped (B25, SB25) $LiNi_{0.9}Mn_{0.05}Co_{0.05}O_2$ cathode, cycled at 10 mA g^{-1} between 4.2 – 2.5 V.

The CE measured in all the cells after the 2nd formation cycle were between 98 – 100%, suggesting a stable SEI had be formed at the graphite electrode for all of the tested cell balances. Full cells were also assembled into the pouch format for the pristine and doped

cathodes with graphite at N/P ratios of 1.0 and 1.2, for which the results of the formation cycles are summarised in Figure C.2.

The lithium stoichiometry change at an electrode during charge and discharge indicates the thermodynamic boundary conditions and can be used to guide cell design to achieve high rate performance. The stoichiometry limits at the positive and negative electrodes were calculated in each of the tested full cells formats and are summarised in Figure 5.3 and Table C.2. In the coin cells, at the end of the charge cycles, the final value of Li_x in the B25 and SB25 cathode are higher than for NMC. The stoichiometry shift in the doped cathode suggests a lowering of the thermodynamic driving force for further lithium extraction, whilst the undoped NMC undergoes a deeper state of de-lithiation which can trigger unfavourable phase transitions. At higher N/P ratios, there is a general increase in the terminal Li_x in the cathode at the end of the 2nd charge, from $Li_{0.13}$, $Li_{0.29}$, and $Li_{0.22}$ for NMC, B25, and SB25 to $Li_{0.21}$, $Li_{0.34}$, and $Li_{0.27}$ as the cell balance is increased from an N/P of 1.0 to 1.2. Instead, the opposite effect is observed in the pouch cells with all the cathodes showing lower lithium stoichiometries at the higher N/P ratio, suggesting the excess graphite loadings in these cells afford further Li extraction. This shift in cathode stoichiometry is coupled with a decrease in the final Li stoichiometry in the graphite for the NMC and SB25 pouch cells at higher N/P, from $Li_{0.97}C_6$ and $Li_{0.98}C_6$ (N/P = 1.0) to $Li_{0.82}C_6$ and $Li_{0.88}C_6$ (N/P = 1.2), whilst the graphite in the B25 in fact shows a small increase from $Li_{0.91}C_6$ to $Li_{0.93}C_6$.

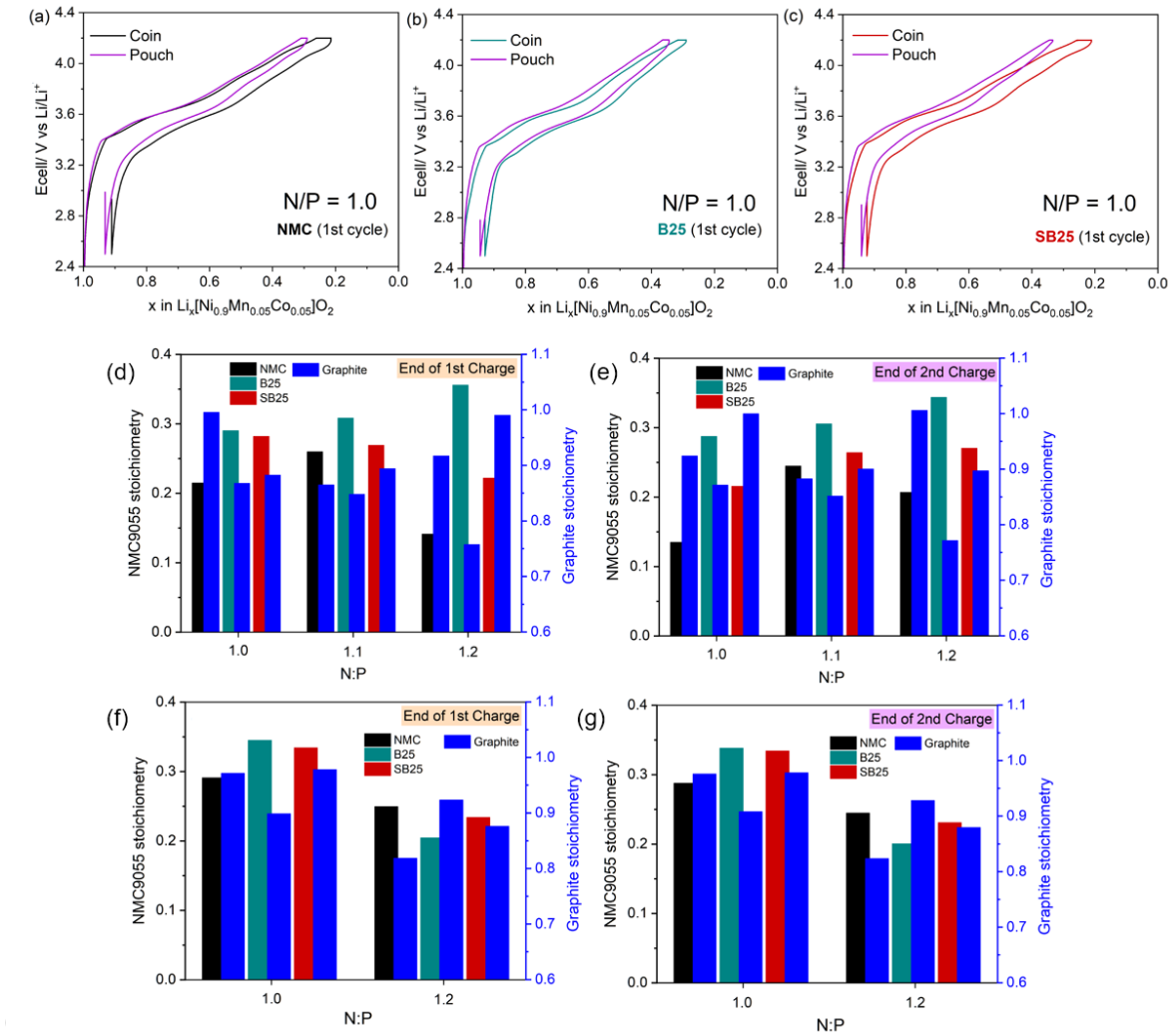

Figure 5.3: Full-cell voltage profiles plotted against the calculated stoichiometry at the cathode (a – c), and the terminal charge stoichiometries at either electrode for the formation cycles at 10 mA g^{-1} between 4.2 – 2.5 V in the coin cells (d – e) and pouch cells (f – g).

Three-electrode cells were constructed to better understand the change in stoichiometry within the different cells during formation by monitoring the individual potentials of both electrodes. The formation voltage profiles in Figure 5.4 show that the positive and negative terminal charge voltages are higher in the cells with an N/P of 1.2 for all cathode materials, suggesting a larger amount of lithium is being extracted from the cathode. In the cells with no excess anode capacity, the graphite voltage profiles display an overhanging potential at the end of the first charge cycle, with terminal voltages of 0.065, 0.052, and 0.046 V reached in the NMC, B25 and SB25 cells. The sloping voltage behaviour

could be indicative of an over-lithiation of the graphite due to electrode slippage from the cell balance, with the additional lithium becoming immobilised in the SEI.

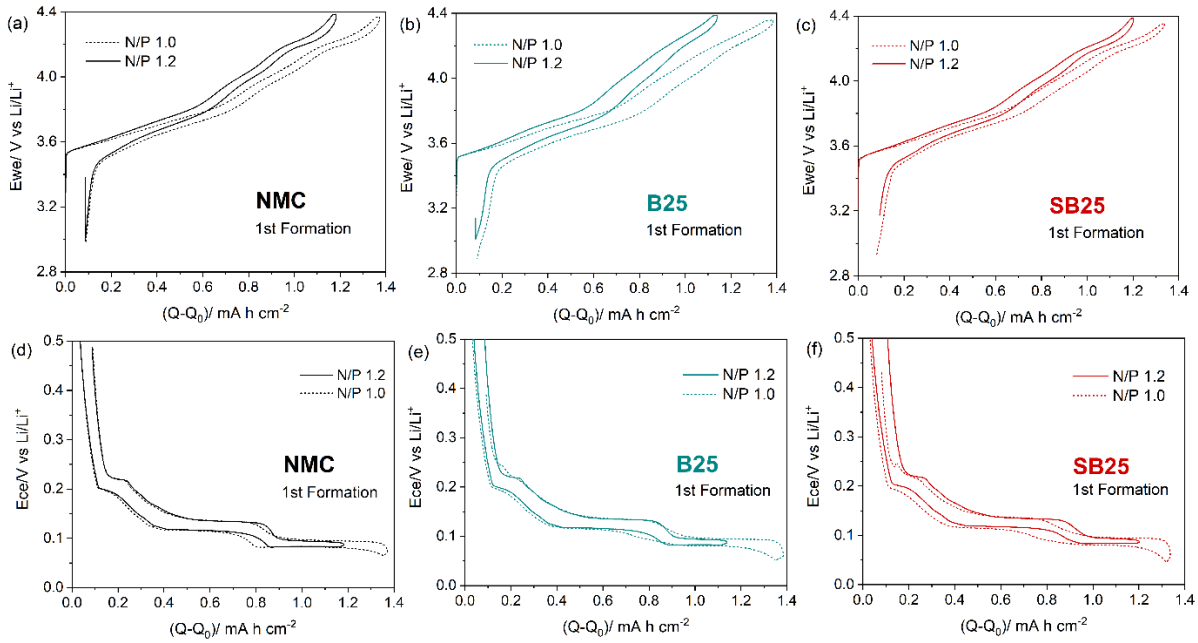

Figure 5.4: Three-electrode formation profiles of the decoupled cathode (a – c) and anode (d – f) electrodes in NMC 90-5-5||Graphite full cells at N/P ratios of 1.0 and 1.2 with pristine and doped cathodes.

5.3.2. Rate Capability and Kinetics

The full cell rate performance was assessed by asymmetric cycling, where the charge rate was kept constant at a specific current of 20 mA g^{-1} and the discharge rate varied between 20 and 500 mA g^{-1}. The corresponding rate capabilities of the coin and pouch cells are displayed in Figure 5.5**.** For the coin cells, the doped materials demonstrate better rate performance at increasing discharge rates across all of the tested N/P ratios, cycled between 4.2 – 2.5 V. At an applied specific current of 500 mA g^{-1}, the SB25 cell displays the highest capacity retention for the cell assembled at a N/P of 1.0, retaining 78.9% of its initial 1.18 mA h cm^{-2} capacity. With increasing N/P ratio, the capacity retention at faster rates in the SB25 full cell reduces. However, the loss in capacity retention is more

detrimental for the full cell containing the undoped NMC, with the capacity retention at 500 mA g^{-1} falling from 69.5% to 54.0% as the N/P ratio increases from 1.0 to 1.1 in the cells.

The full cell rate performance was also assessed in the 3x3 pouch formats cycled in the wider voltage range of 4.3 – 2.5 V. As demonstrated in the coin cells, the pouch cells containing the doped cathodes show improved rate capability across both tested N/P ratios. At faster rates, however, the capacity retention in the B25 cells is only marginally better than the NMC cells. In contrast, the SB25 displays considerable improvement, retaining 72.2% and 68.4% of its initial capacity at 500 mA g^{-1} for N/P ratios of 1.2 and 1.0 compared to 60.8% and 53.9% in NMC, respectively. The effect of the higher terminal charge voltage is evident in the sloping profiles of the capacity recovery in all cells at each rate. This is consistent with the increased irreversible structure change in the cathode afforded in this voltage range. Additionally, the final capacity recovery when cycled again at 20 mA g^{-1} is lower than those demonstrated in the coin cell tests up to 4.2 V only. However, these were still higher for the cells with the doped cathodes, with B25 demonstrating the highest fraction of recovered capacity, that being 91% and 96% for the NP-1.0 and NP-1.2 cells. The rate capability in the coin full cells with N/P = 1.0 was also tested up to an upper voltage limit of 4.3 V. The NMC cells demonstrate a considerably worse rate performance than the doped cathode cells at 100 – 500 mA g-1 rates. The capacity retention in B25 is the most stable to the higher voltage rate cycles, displaying similar capacity retentions of 78.7% and 76.6% when discharged at 500 mA g^{-1} for the 4.2 V and 4.3 V tests. The capacity fade at each rate in the 4.3 V tests is also more stable in SB25 and B25 in the coin format compared to the pouch cells, whilst the NMC cells display a sloping trend in the capacity retention in each cell format.

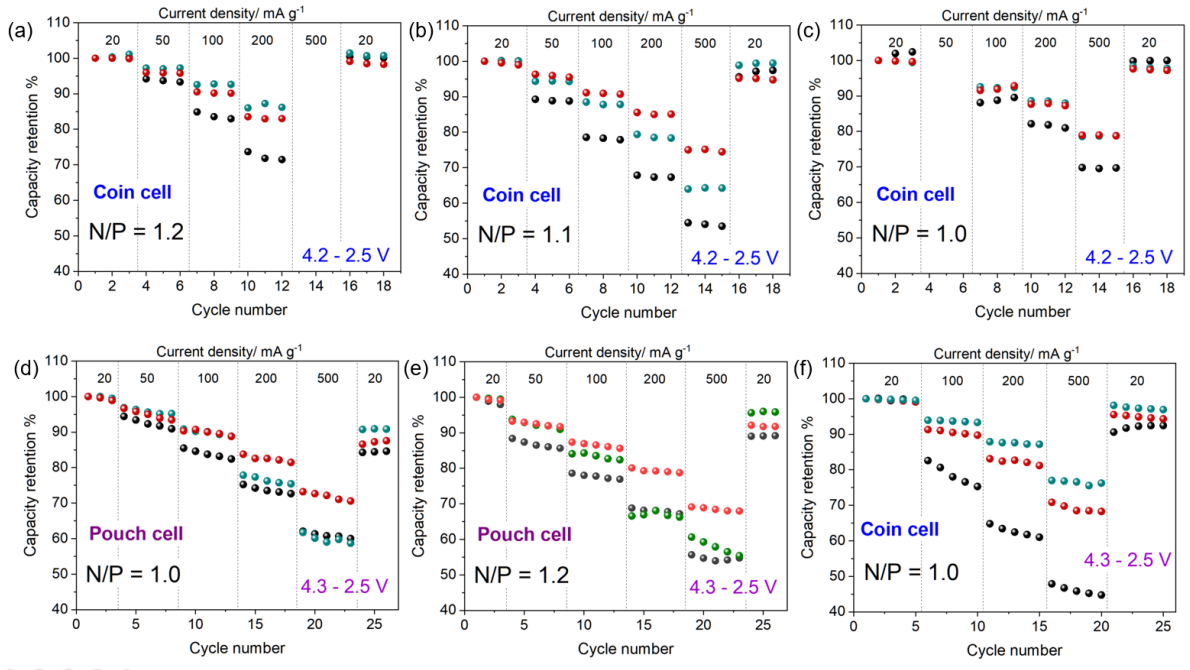

Figure 5.5: Rate capability of NMC 90-5-5||graphite full cells tested in (a – c) coin cells cycled between 4.2 – 2.5 V and in (d – e) pouch cells cycled between 4.3 – 2.5 V. The fixed low-rate charge cycle was performed at a specific current of 20 mA g^{-1}.

The full cell kinetics were also studied by EIS at different states of charge between 2.5 – 4.2 V when cycled at the low current rate of 20 mA g^{-1} as performed in the rate tests. Figure 5.6 shows the Nyquist plots for the NMC full cell at representative voltage points consisting of multiple semi-circle features. The smallest of these, which is located in the high frequency region between 10 and 250 kHz and is attributed to the series resistance in the cell, shows no observable change in size or shape over the charge cycle. As the cell approaches 3.5 V, the shape of the larger semi-circle appears now as a convolution of two smaller semi-circles, which both become smaller in radius as the cell is charged up to 4.0 V. Beyond this point, there is considerable growth in the response at the lower frequency, whilst the middle semi-circle remains constant in the EIS response taken at the upper voltage limit of 4.2 V. To compare the change in resistances across the different cells, the impedance spectra were fitted with the equivalent circuit model (Figure 5.6e). The ohmic series resistance (R_s) remained constant during the charge process in all cells and was

found to be lower in the full-cells containing the doped cathodes, with average values across this voltage range of 2.5, 1.1, and 1.5 Ω for NMC, B25, and SB25. The resistances from the solid electrolyte interphase (R_{SEI}) and charge transfer processes (R_{CT}), which typically occur on slower timescales and so are attributed to the larger perturbed semi-circles in the Nyquist plots, show the most variation upon charging of the full-cell and are presented in Figure 5.6c-d. The R_{CT} values follow a roughly U-shaped curve for the NMC and SB25 cells, with SB25 displaying the lowest resistance at all voltages. The same trend is not observed for the B25 cells, which display R_{CT} values in the range of 20 – 25 Ω in the potential window between 3.5 and 4.2 V, notably missing the spike in resistance at the top of charge. The absence of the impedance rise at the terminal cell voltage in B25 is consistent with the delay of the H2-H3 phase transition in the B25 doped cathode, which otherwise causes an increase in the charge transfer resistance due to the adverse structural instability that can promote side reactions.

The variation in R_{SEI} followed a less obvious trend across the different cells but generally showed an increase with SOC before decreasing again at the higher voltages. The voltage at which the decline in R_{CT} occurred followed B25 < SB25 < NMC, with the values of R_{CT1} found to be almost identical in B25 and SB25 between 3.5 and 4.2 V. The complete list of calculated impedance parameters from the equivalent circuit fitting model is collected in Table C.3.

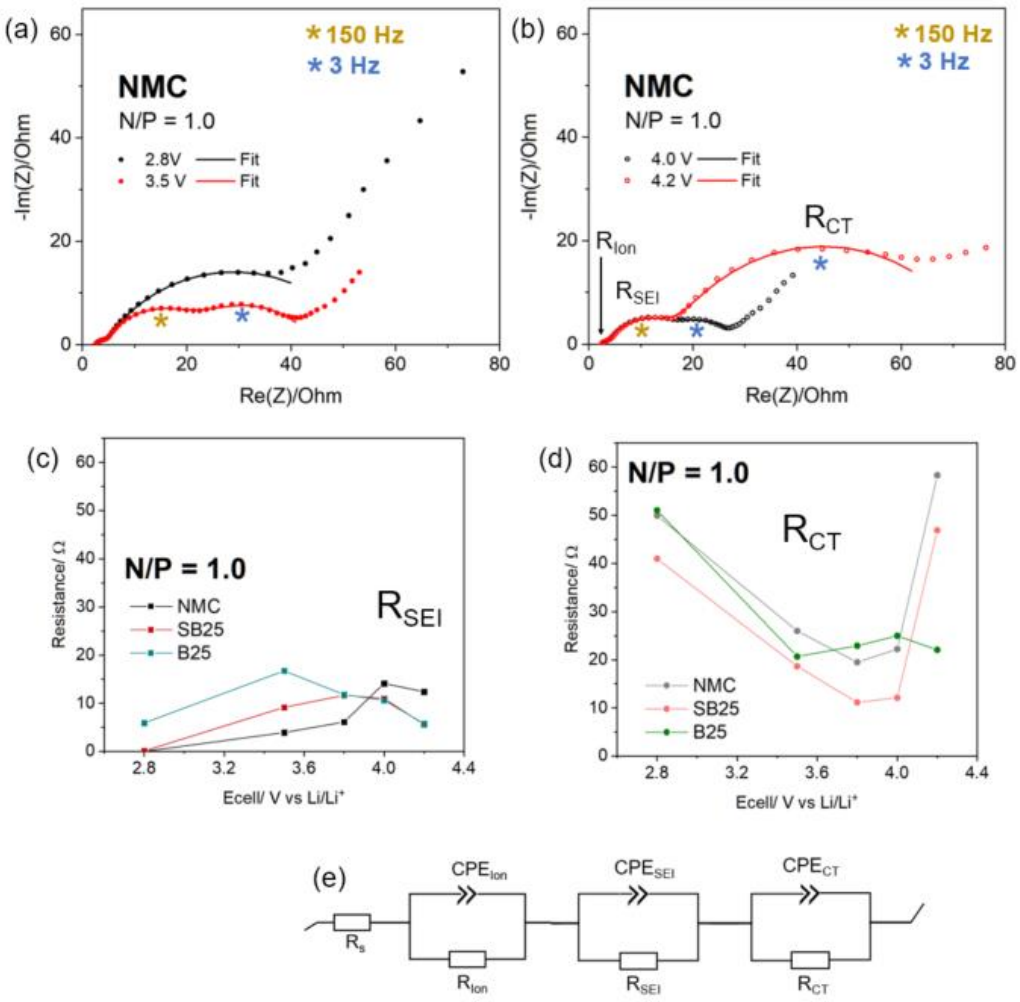

Figure 5.6: Nyquist plots from the EIS of the NMC full cell with N/P of 1.0 at different voltage points along a 20 mA g^{-1} charge cycle between 2.5 and 4.5 V (a – b) and the fitted solid electrolyte interphase (R_{SEI}) and charge transfer (R_{CT}) resistances calculated from the EIS data for the NMC, B25, and SB25 full cells.

Symmetrical rate tests were also performed in the three-electrode cells at rates between C/5 and 2C to understand the individual electrode limits at faster cycling rates with different cell balances. The discharge profiles displayed in Figure C.3 show a shift to lower average cathode and higher average anode voltages when cycled at higher C-rates, as expected from the larger overpotentials that arise with the increased internal resistance associated with faster transfer of Li ions within the electrodes.

NMC cells displayed minimal variation in voltage profiles between different N/P ratios. Notably, at lower N/P ratios, the graphite anode's voltage plateaus at 0.10 V and 0.14 V were prolonged and shortened, respectively. The lowest plateau is typically associated with lithium stripping before graphite delithiation, suggesting increased lithium plating in NP-1.0 cells during prior charging cycles.

In the undoped NMC cells, the lower N/P ratio significantly impacted the graphite voltage profiles at higher discharge rates, displaying larger initial overpotentials. Specifically, in the NMC cell with N/P of 1.0, nearly the entire 2C discharge curve remained above 0.2 V, whereas at the higher N/P ratio, this threshold was only surpassed after delivering 70% of the total capacity. This trend is reflected in the voltage shift (ΔV_N) between 50% depth of discharge (DOD) at C/5 and 2C discharge profiles. Lower N/P ratios corresponded to increased ΔV_N, rising to 0.123 V compared to 0.058 V in NP-1.2 cells. On the cathode side, a corresponding decrease in ΔV_P was observed for lower N/P ratios, with ΔV_P measuring 0.196 V and 0.229 V for cells with N/P at 1.0 and 1.2 respectively. However, the relative change at the positive electrode was smaller, especially considering the voltage ranges of both electrodes, suggesting that the graphite anode is the limiting factor in NMC cells at higher discharge rates.

This cell configuration can also be used to determine the limits of cell balance and C-rates on the onset of Li plating on the anode which is detrimental to full cell testing. When this occurs, the deposition of lithium metal onto the graphite becomes thermodynamically favourable which can lead to different types of dendritic growth depending on the testing conditions. Under fast charging rates, the Li deposition can favour dendrites of needle-like morphology.[248] The traditional dendritic region is highlighted by the pink region in Figure 5.7 for the 2C charge profiles of the NMC cells, which reaches a terminal anode

potential of 0.041 V and −0.022 V for cells with a N/P ratio of 1.2 and 1.0 respectively. However, once the cell voltage reaches the upper limit of 4.3 V, the individual potentials of both electrodes start to increase and continues to do so for the duration of the constant voltage hold, with the anode drifting back to a positive potential. It is also observed that the cells with a lower N/P ratio of 1.0 result in an extended CV region, accounting for 36.7% of the total charge capacity of the NMC full-cell, compared to just 15.0% in the cell with a higher N/P ratio. The formation of any dendritic features on the anode in this cell during the 2C cycles does not cause any imminent degradation, instead the cells display a high capacity recovery of >97% in the following C/5 cycles.

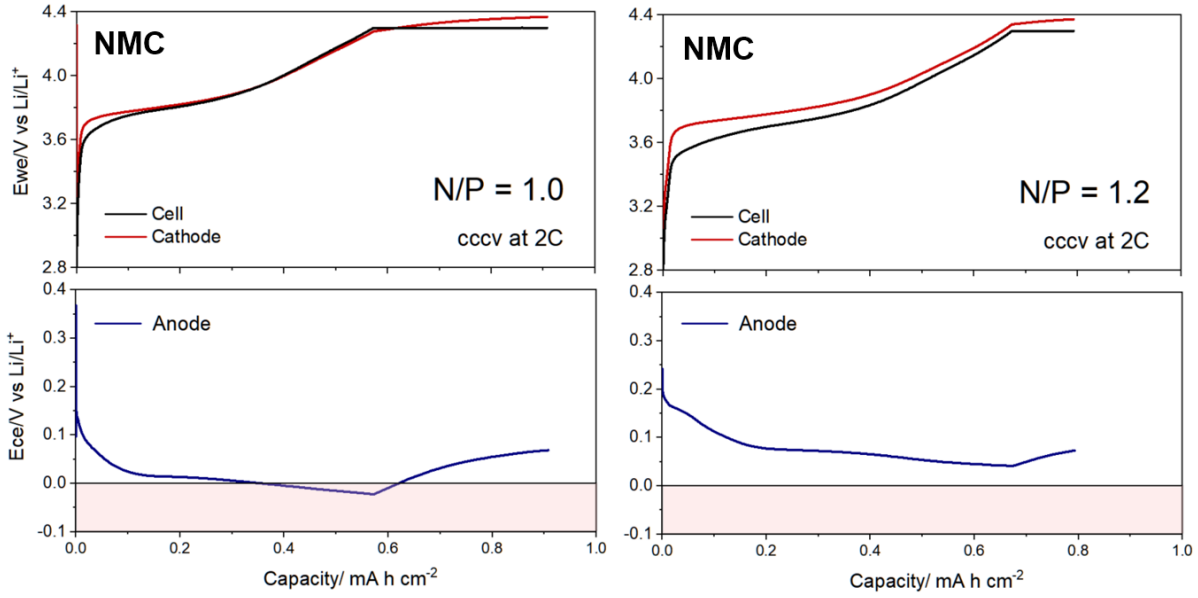

Figure 5.7: Individual charge profiles for the B25 three-electrode cells at different N/P ratios cycled at 2C in the controlled cell voltage window of 2.5 – 4.3 V.

5.3.3. Cycle Life and Degradation

The cycle life of the full cells assembled at different N/P ratios of 1.0 and 1.2 over 200 cycles using a symmetric charge-discharge current rate of 200 mA g^{-1} are compared in

Figure 5.8. In the coin cell format, the final capacity retention was greater for the cells comprised of the higher N/P ratio for all of the tested cathodes. The discharge capacities of these cell delivered at the 200th cycle was 0.475 mA h cm^{-2}, 0.660 mA h cm^{-2}, and 0.661 mA h cm^{-2} for NMC, B25, and SB25 full cells, correlating to capacity retentions of 76.9%, 86.7%, and 77.8% respectively. The full cells containing the doped cathode materials therefore demonstrate improved cycle life at a higher capacity. This trend is also observed for the cells assembled with a lower anode capacity excess (N/P = 1.1), with B25 delivering the highest 200th cycle capacity retention of 71.3% compared to 69.3% for SB25 and 66.9% for NMC. However, at this cell balance, B25 displays a similar final capacity as the NMC cell (0.470 and 0.441 mA h cm^{-2} respectively), whilst the SB25 delivers 0.601 mA h cm^{-2} at the end of the 200 cycles.

The dQ/dV plots calculated at representative cycles are displayed in Figure C.4 can give further insight on the degradation mechanisms in the full cells. For the cells with a higher N/P ratio, it is observed that the high voltage peak arising from the H2-H3 phase transition in the cathode, disappears after 50 cycles in the NMC cell, whereas the SB25 cell shows a much higher reversibility of this peak at the same cycle. In the B25 cell, the high voltage peak is not fully realised during the initial cycle, however the cell displays a high reversibility of the other redox peaks, including the retention of the peak at ~3.4 V which is attributed to the crystal structure changes in graphite as it is lithiated. This peak is not present in the dQ/dV plots after the 1st cycle in the other N/P 1.2 cells, suggesting that the structure of the graphite is irreversibly set during the initial lithiation cycle at 200 mA/g in these cells, but continues to undergo a reversible phase transition during the cycling in B25. By contrast, the B25 cell assembled at a lower N/P ratio of 1.1, in which the graphite peak is absent after the initial cycle, whilst the remaining redox peaks display irreversible losses in later cycles, which is reflected in the increased capacity degradation.

Figure 5.8 also shows the results of the pouch cell cycle performance, which were cycled at the same current rate (200 mA g^{-1}) as the coin cells, in the voltage range of 4.3 – 2.5 V.

For an N/P ratio of 1.2, the B25 cell exhibits the highest capacity retention at 78.5% after 200 cycles; however, the trend in pouch cells follows B25 ≈ NMC > SB25, differing from the trend observed in coin cells (B25 > SB25 ≈ NMC). Despite showing the lowest capacity retention of 63.3%, the SB25 cell still delivers the highest capacities over the 200 cycles, demonstrating a final capacity of 0.52 mA h cm^{-2}. When the N/P ratio is reduced to 1.0, capacity retention decreases significantly compared to coin cells assembled with an N/P of 1.1. Despite this, capacity degradation is less pronounced in the B25 cell, which retains 65% of its initial capacity, whereas NMC and SB25 display nearly identical degradation behaviour, with a final retention of 46%.

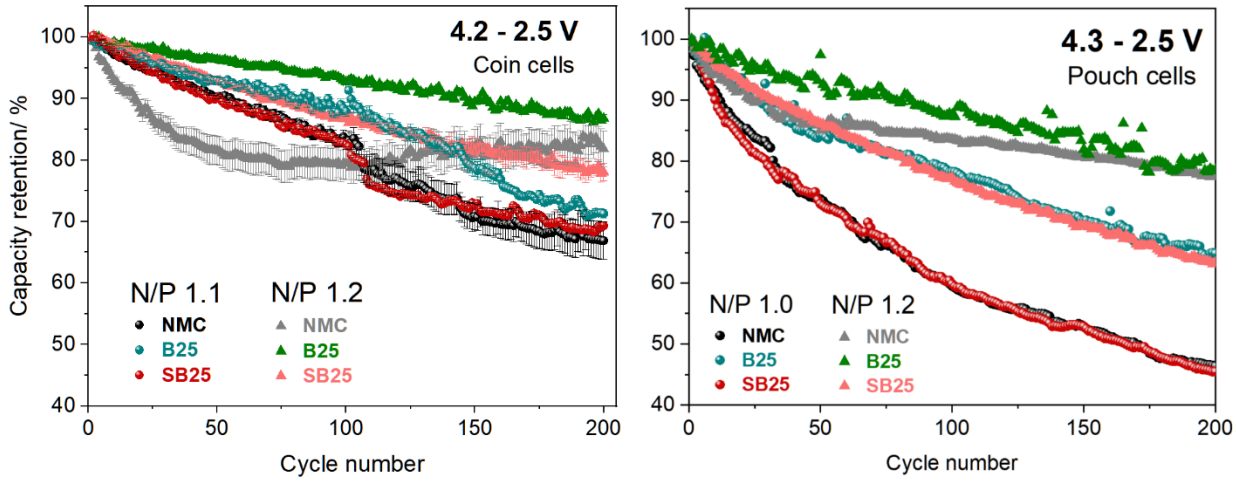

Figure 5.8: Cycle life performance of coin and pouch full cells at various N/P ratios cycled within a voltage range of 4.3 – 2.5 V at a 100/200 mA g^{-1} charge and discharge current rate.

The morphology of the aged electrodes from the pouch cells was studied under SEM to identify any physical changes in the electrodes which might contribute to the capacity fading mechanism. Given the largest disparity in capacity fade between the N/P 1.0 and N/P 1.2 cells, the cathodes from the NMC full cells are first compared to inspect any physical degradation. The SEM images in Figure 5.9 show that considerable electrode

cracking (50 – 100 μm long) could be observed along the positive electrode extracted from the NMC cells at both N/P ratios. Additionally, smaller cracks (~5 μm long) that appear to propagate through the secondary particles became visible upon higher magnification in the cathode from the N/P 1.0 cell. It is well studied that secondary particle cracking in polycrystalline NMC can accelerate degradation due to the increased exposed surface area, instigating slower kinetics from forced crystal restructuring, damaged Li transport channels, and electrical isolation.[249,250] The secondary particle cracking present in the N/P 1.0 cell but absent in the N/P 1.2 cell could, therefore, be a contributing factor in the much lower capacity retention of the former. This is also reflected in the dQ/dV plots displayed in Figure 5.9, which shows a more drastic change in the redox peak positions and magnitudes over the first 100 cycles for the N/P 1.0 cell.

Graphite undergoes irreversible volume expansion during cycling, which, upon releasing the induced stress, can result in cracking. This has been observed before in cycled pouch cells, whereby the cracks occur along the grain boundaries of the graphite particles and are propagated parallel to the current collector.[251] Post-mortem SEM studies showed no visible signs of cracking at the graphite electrode or particle level under the inspected magnification. However, the anodes extracted from both cells showed that the graphite particles possessed a 'fluffy' surface, which, upon closer inspection, appears to be a collection of sub-micron particles. The presence of these fine particles on the graphite surface after cycling has previously been attributed to the SEI growth on the primary particles from the electrolyte decomposition.[252,253]

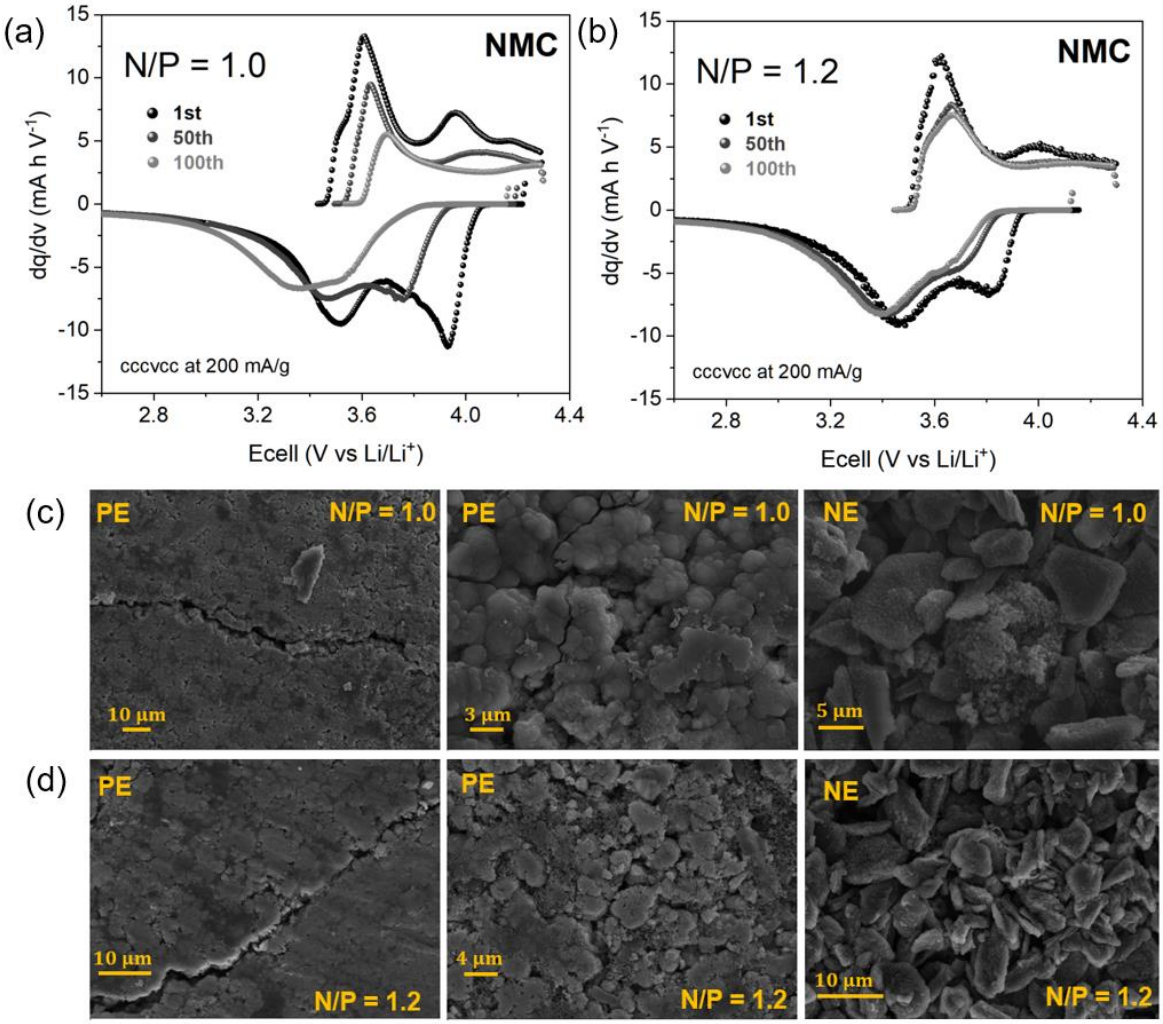

Figure 5.0.9: Differential capacity (dQ/dV) plots of the NMC pouch cells taken at progressive cycles during the charge-discharge cycling at 200 mA g^{-1}(a – b), and the SEM images of the aged NMC and graphite electrodes extracted from degraded pouch cells after 200 cycles at this cycling rate (c – d).

To probe and decouple the effect of cycling on the lithium diffusivity within the cathode and anode, the three-electrode cells were aged at a charge and discharge rate of 2C, and GITT measurements performed after the 100th and 200th cycle. Figure C.5 shows the evolution of the cycling capacity in these cells as well as the calculated diffusion coefficients within the cathode from the GITT analysis of the positive electrode OCV. The diffusion profiles of the cathodes in the uncycled full-cells are largely unaffected by the N/P ratio over the whole voltage range, however some variation in profile can be observed between the NMC and the doped cathodes. The NMC post-formation profiles

can be characterised by four small peaks in the charge process, whilst only the two higher voltage peaks at 4.2 and 4.0 V are resolved in the discharge process. Following the fast rate cycling, the high voltage peak during charge disappears with the diffusion coefficients decreasing rapidly beyond 4.2 V. This is consistent with the loss of this peak in the dQ/dV plots which coincides with the irreversible phase transition that occurs in NMC during cycling and consequently limits the available lithium diffusion pathways for the removal of the final lithium ions. This is also mirrored in the discharge process, where the initial spike in the diffusion coefficient is reduced after ageing due to the structural degradation in the cathode that limits re-intercalation of the lithium ions.

The high voltage peak in the diffusion coefficient during charge is not observed in the B25 cathode, even in the case of the GITT measured before cycling. As a result, the rate of decline in the diffusion coefficient in this voltage range remains constant with subsequent cycles. The charge and discharge diffusion profiles of B25 are largely unchanged by the 2C cycling. As the diffusion coefficient mainly relates to solid state movement in the crystal structure, this result would agree that the boron doping stabilises the bulk structure. However, some degradation in the diffusion coefficient can be observed in the NP-1.2 cell during the start of charge, with the peak at 3.8 V falling from 1.05×10^{-11} to 4.8×10^{-12} $cm^2\ s^{-1}$ after 100 cycles.

The diffusion profiles of the SB25 cathode before cycling closely resemble the ones for NMC. However, the average diffusion coefficients were larger in the Sn-B doped material over the voltage range of a complete cycle. The most notable difference is the shift in the maxima of D_{Li} during charge to a higher voltage in SB25, which in the NP-1.2 cell reaches 9.56×10^{-12} $cm^2\ s^{-1}$ at 3.78 V compared to 6.37×10^{-12} $cm^2\ s^{-1}$ at 3.65 V for the NMC cathode. However, after 100 cycles, the diffusion charge profile of SB25 is more consistent

with NMC with the D_{Li} maxima located around 3.62 V in both. The D_{Li} maxima during discharge is located at 4.2 V for both SB25 and NMC, with values of 9.91×10^{-12} and 1.12×10^{-11} cm^2 s^{-1} respectively, whilst the values of D_{Li} in the subsequent peak at 4.0 V are higher in SB25 and remain so for the following plateau. However, after these cells have undergone 100 cycles, the diffusion coefficients over this period fall to similar values as seen in the NMC.

The voltage IR drop (VIR) that occurs following the end of each current pulse can also be extracted from the GITT to investigate the kinetic overpotential. Figure C.6 displays the change in the VIR curves over charge and discharge at various degrees of cycling. These curves generally show a distorted U-type shape, with the voltage drops increasing at the terminal potentials of the charge and discharge processes. Before cycling, the plateau of the VIR curves during charge is lowest in the NMC cells and highest for the SB25 cells. However, above 4.2 V, the VIR in the undoped NMC display a sharp increase and becomes larger than those recorded in the doped cathode, suggesting the system becomes rate limited, which becomes more prominent in the aged cells. The shape of the VIR curves for the discharge process generally mirrors the charge profile, suggesting the electrode kinetics are initially reversible between the removal and re-insertion of Li ions in the cathode.

The N/P ratio was not found to have a large influence on the magnitude or evolution of VIR in the cathode during charging of the uncycled cells. However, when measured again after 100 cycles, the increase in VIR was greater for the NMC and B25 cells with N/P of 1.0, whilst the increase for SB25 remained consistent regardless of the cell balance. The B25 cells displayed the smallest increase in VIR with cycling, and after the full 200 cycles

at 2C displays the lowest values of VIR in both N/P cells for the majority of the charge and discharge regions.

5.3.4 Larger Format Power Cells

Based on the results from the rate and cycling tests in the 3x3 pouch cells, full cells with a N/P ratio of 1.15 were assembled in the larger 5x7 pouch format (30 mA h cells) for each of the three cathode materials. The results from the initial formation cycles are displayed in Figure 5.10a. All the cells demonstrate ICE values between 92 – 93% which are consistent with the smaller format pouch cells at the same cell balance. The 5x7 pouch cells displayed 2nd cycle discharge capacities between 0.9 – 1.05 mA h cm^{-2} which are consistent with the lower mass loadings of the positive and negative electrodes used in the 5x7 pouch cells to optimise the power performance. The gravimetric capacities based on the cathode active mass of NMC, B25, and SB25 were 202.5, 194.0, and 204.9 mA h g^{-1}, demonstrating the same trend observed for the half-cell capacities.

Figure 5.10c displays the results of the rate tests performed with the higher range of current densities between 100 – 2000 mA g^{-1} (~0.5 – 10C). The NMC and SB25 cells show very similar rate capability at each of the measured current rates, both retaining ~55% of the initial capacity when discharged at 2000 mA g^{-1}, equivalent to 0.51 and 0.53 mA h cm^{-2} respectively. For the B25 cell, the rate performance is much lower, especially at the faster rates which show degradation even over the 5 cycles. This contrasts the results previously seen for the B25 cell (N/P =1.2) in the 3x3 pouch format, which delivered more stable areal capacities at values similar or slightly larger than the NMC cell at the comparative rates (100 – 500 mA g^{-1}). However, all cells demonstrate similar capacity retentions between 89 – 90% in the recovery cycle at 100 mA g^{-1}. The gravimetric capacities of SB25 and B25 recorded at 500 mA g^{-1} of 139.6 and 106.6 mA h g^{-1} in the 5x7

cells were fairly consistent with the values of 131.0 and 103.6 mA h g^{-1} in the smaller pouch format, yet this was not the case for the NMC which yielded a higher capacity of 138.7 mA h g^{-1}, up from 105.4 mA h g^{-1} in the 3x3 pouch. The variation in rate performance is therefore unlikely to be due to the slightly lower cathode loadings (g cm^{-2}) in the larger pouch formats. Instead this could be attributed to the higher specific current used to charge the cells during the rate testing of the 5x7 pouch cells. The lower rate performance in the 5x7 pouch B25 cell could be being limited by the smaller stoichiometry window available as seen during the formation cycles. Therefore, at faster rates the cathode enters the stoichiometry associated with the slow kinetics before that of the other cells.

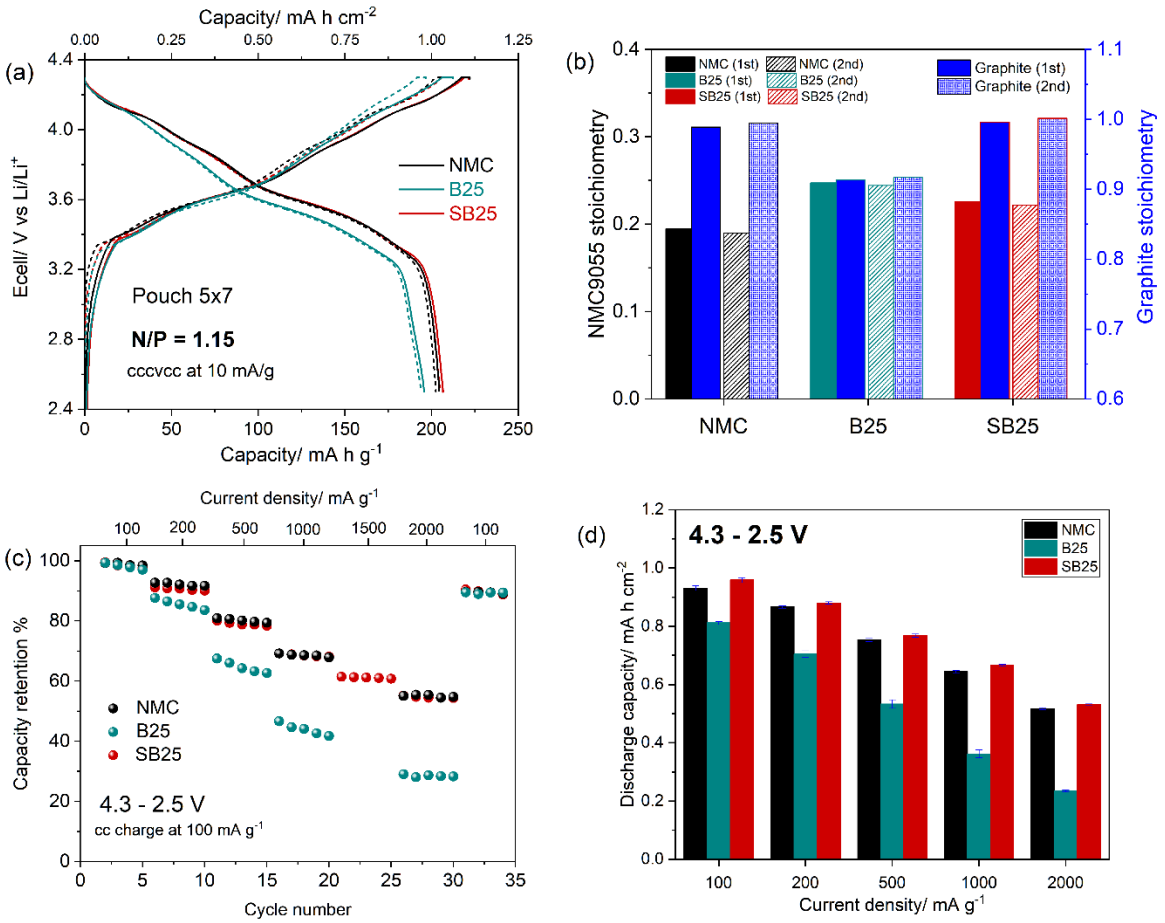

Figure 5.10: Electrochemical performance of 5x7 pouch cells; voltage profiles of the initial formation cycles recorded at 10 mA g^{-1} between 4.3 – 2.5 V (a), calculated lithium stoichiometries

in the cathode and anode at the end of the 1st and 2nd charge cycle (b), rate performance at varying discharge rates between 100 – 2000 mA g^{-1} (c – d)).

5.3.5. Design for an Energy Cell

Given the best performance was obtained for the SB25 system, this material was subsequently used to study the effect of higher mass loadings to increase the energy density of the NMC 90-5-5||Graphite full cells. In these studies, electrode coatings with higher mass loadings around 200 – 220 g m^{-2} were prepared to target larger cathode areal capacities of ~4.5 mA h cm^{-2}. Initially, the performance of the cathodes was tested in half-cells to assess the viability of the thick electrode coatings. The initial voltage curves from the formation cycles performed in coin and pouch formats are displayed in Figure 5.11a-b**.** The hysteresis in the capacity load curves is very low across both cell types, showing a high 1st CE of 97% in both formats. This is consistent with the performance of SB25 at lower mass loadings, suggesting the thicker electrode does not increase the irreversible consumption of lithium in the first cycle, consistent with that observed in other NMC materials.[254] The half-cells yielded a reversible capacity of 4.07 mA h cm^{-2} and 4.50 mA h cm^{-2} in the coin and pouch cells upon the second formation cycle. The deviation in areal capacity between the two cell formats is attributed to the slightly higher GSM of the cathode used in the pouch cells, as the corresponding gravimetric capacities are consistent between formats, being 200.8 and 205.5 mA h g^{-1} for the coin and pouch cells.

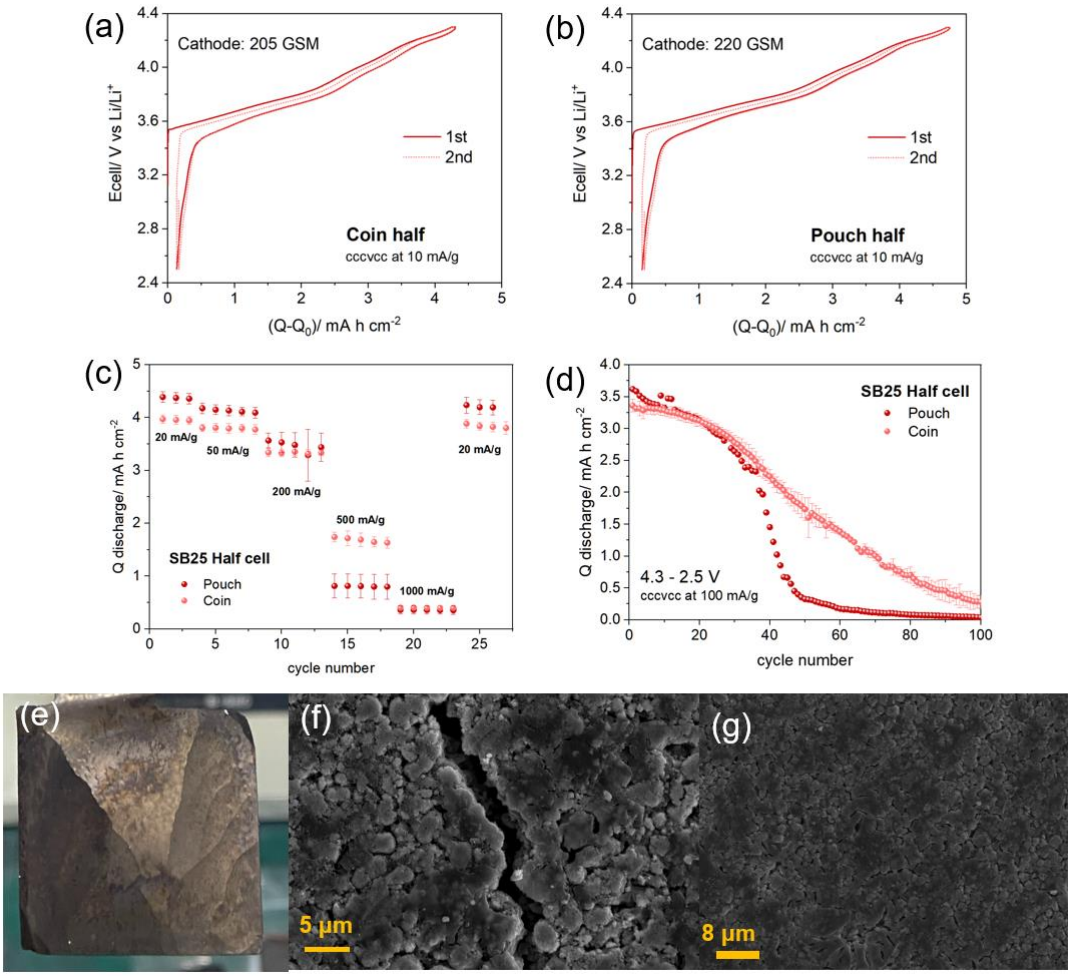

Figure 5.11: Electrochemical testing SB25 half-cells prepared in coin and pouch formats with electrodes at high mass loading cycled between 4.3 – 2.5 V; formation at 10 mA g^{-1} in coin (a) and pouch (b) cells, rate capability with constant charge rate of 20 mA g^{-1}(c), cycle life tests with symmetric 100 mA g^{-1} charge-discharge cycles (d), image of cycled SB25 cathode extracted from pouch half cell (e), and corresponding SEM images at different magnifications (f – g).

The rate performance of the high loading cathodes was also investigated to understand the limit of fast discharging. Figure 5.11c shows a substantial drop-off in capacity for both the coin and pouch cells at a rate of 500 mA g^{-1} (~2.5 C), delivering 43.8% and 18.5% of their initial discharge capacity at 0.1 C. The greater extent of degradation seen in the pouch cells compared with the coin cells is again likely due to the higher GSM of these electrodes, which accounts for the higher areal capacity at slower rates, but manifests in larger overpotentials arising from the increased ohmic resistance associated with more

limited diffusion of the Li^+ within the electrode pores.[255] Additionally, the pouch format can introduce further degradation factors from a thermal or mechanical standpoint, depending on the compression of the electrode stack, which, in contrast, is standardised in coin cells by the presence of the spring.[256] However, the high loading SB25 cathodes demonstrate high capacity recovery when the specific current is returned to 20 mA g^{-1}, regaining 97% and 96% of this capacity in the coin and pouch cells, respectively. The longer-term cyclability of the thick electrodes was studied under symmetric cycling at a specific current of 100 mA g^{-1}. Initially, the degradation rate progresses similarly in the coin and pouch cells, reaching the 80% capacity retention threshold after the 32nd and 26th cycles, respectively. However, the capacity degradation in the pouch cell increased significantly after this, as the capacity retention fell to 15% by the 45th cycle. Following the cycle tests, the pouch cell was discharged to 0% SOC and disassembled in a glovebox under argon atmosphere. The cycled cathode displayed considerable electrode cracking under visible inspection and in the SEM images; however, microcracking within the secondary particles was not directly observed. The macroscopic cracking throughout the electrode sheet likely arises from the higher susceptibility of thick electrodes to cracking during the drying process of the coating preparation, with these cracks propagating further between the active material and carbon-binder domains during cycling due to the increased mechanical stresses.[257,258]

Full cells of the thick SB25 electrodes were next paired with graphite coatings of appropriate coat weights and assembled in pouch cells for complete electrochemical characterisation. Two cells were prepared with N/P ratios of 1.25 and 1.0 with the specific electrode loadings described in Table 5.3, which also presents the initial areal

capacities from the formation cycles at 10 mA g^{-1}. Under the low current rate cycles, the cell with the higher N/P ratio delivers higher capacities at the end of each formation cycle but displays lower Coulombic efficiencies. This is most apparent in the first cycle losses, which were 0.55 mA h cm^{-2} for the N/P 1.25 cell compared to 0.27 mA h cm^{-2} in the N/P 1.0 cell, which is consistent with the increased cathode capacity facilitating a lower proportional consumption of the lithium inventory in the lower N/P cells. Additionally, the higher loadings of both electrodes used in the N/P 1.25 cell can enable excessive SEI formation or trapped lithium in the bulk material due to less uniform Li-ion diffusion.[259,260] Thicker electrodes also incur larger overpotentials which can shift the anode voltage to lower potential, enabling an increase in the SE formation. This is also consistent with the higher polarisation observed in the voltage profile of the N/P 1.25 cell in Figure 5.12**,** resulting in a shift in the terminal lithium stoichiometry in the cathode during discharge, between $Li_{0.23}$ to $Li_{0.92}$ in the first cycle and $Li_{0.22}$ to $Li_{0.89}$ in the second.

Table 5.3: Full cell parameters and formation results from the initial cycles at 10 mA g^{-1} between 4.3 – 2.5 V for the SB25-graphite pouch cells assembled with thick electrodes.

	Electrode loading/ g m^{-2}		Q discharge/ mA h cm^{-2}		Coulombic efficiency %	
N/P	Positive	Negative	1st	2nd	1st	2nd
1.25	230	165	4.54	4.46	89.2	97.2
1.0	210	119	4.01	3.95	93.7	98.5

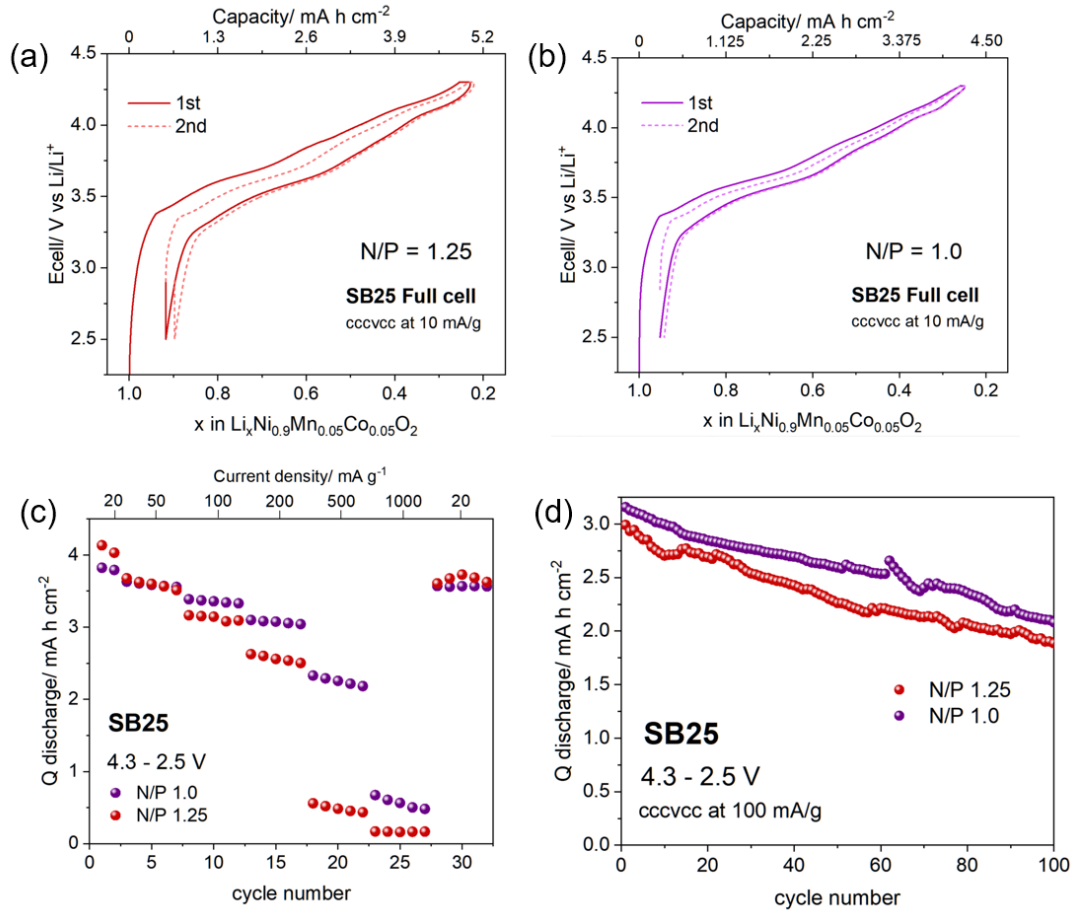

Figure 5.12c shows the resulting capacities from the galvanostatic cycling of the SB25 full cells at increasing discharge current rates. For the initial symmetric charge-discharge cycles at 20 mA g^{-1}, the N/P 1.25 cell still displays the higher capacity, however when the discharge specific current is increased to 50 mA g^{-1}, both cells show capacities of ~3.6 mA h cm^{-2}. At faster discharge rates the N/P 1.0 cell delivers higher capacities, which is consistent with the lower mass loadings of the electrodes in this full cell. The disparity in the discharge capacities increases significantly in the 500 mA g^{-1} cycles, for which the SB25 cells deliver an initial capacity of 0.56 mA h cm^{-2} and 2.33 mA h cm^{-2} at N/P ratios of 1.25 and 1.0, corresponding to capacity retentions of 13.5% and 60.9% respectively. However, the N/P 1.0 cell also displays some capacity fade in the following cycles at this rate with the discharge capacity falling to 2.18 mA h cm^{-2} in the 5th cycle. Following the

fast rate discharge steps, the full cells were cycled again at 20 mA g^{-1} in which the lower N/P (1.0) cell demonstrated a higher capacity recovery of 93% compared to 89% in the cell with an N/P of 1.25.

The lifetime of the high energy full-cells was also investigated under symmetric cycling at a specific current of 100 mA/g. The cycling results of the full-cells shown in Figure 5.12d display a more gradual decline in the discharge capacity compared to the half-cell pouch tests, suggesting the anode acts to limit the degradation of the high-energy cathodes. However, the cycle life is considerably worse than recorded previously for full-cells of lower loading electrodes, with the capacity retention here falling to 80% after 41 cycles in the N/P 1.2 cell and after 65 cycles in the lower N/P cell. After 100 cycles, the SB25 full cell with the lower N/P ratio still displayed the higher discharge capacities, which were 1.89 mA h cm^{-2} and 2.08 mA h cm^{-2} for the N/P 1.25 and 1.0 cells. However, the overall degradation between the two cells was more similar, demonstrating capacity retentions of 66% and 63% in the 100^{th} cycle.

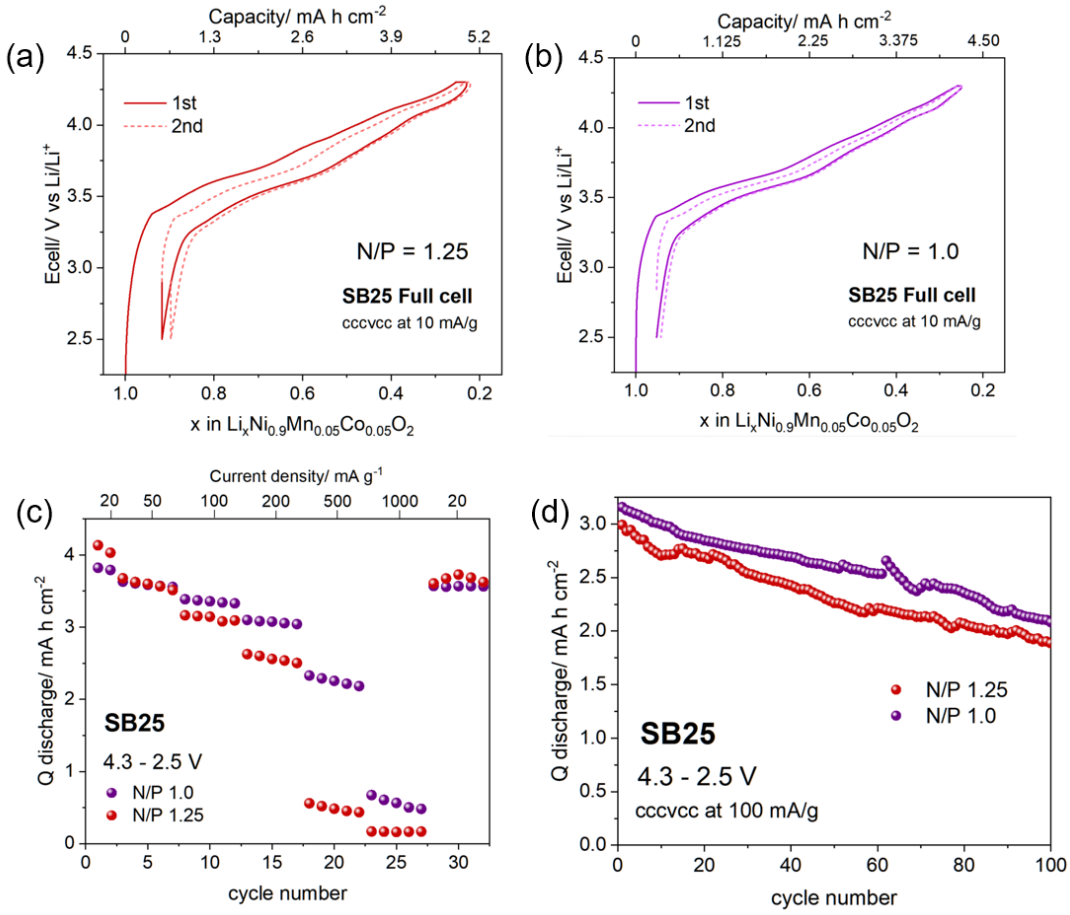

Figure 5.12: High loading SB25-graphite full-cell performance comparison at N/P of 1.25 and 1.0; formation capacity and stoichiometry (a – b), rate capability tests at a constant charge rate of 20 mA g^{-1} with increasing discharge current densities between 20 – 1000 (c), and cycle life tests at 100 mA g^{-1}.

Additional pouch cells with lower cathode loadings (190 GSM) were constructed to further explore the optimum electrode loading for high-energy Ni-rich full cells for both the SB25 and undoped NMC electrodes paired with graphite. The lower capacity balance of N/P = 1.0 was targeted in these cells so that the capacity of either electrode did not limit the cells. The reversible capacities recorded in the initial two formation cycles were 3.51 and 3.46 mA h cm^{-2} for NMC and 3.57 and 3.53 mA h cm^{-2} for SB25. Additionally, the SB25 full cell also demonstrated a higher 1st cycle efficiency of 92.1% compared to 90.7% in the NMC full cell, which is consistent with the values observed for the 1 mA h cm^{-2} pouch cells assembled at N/P 1.0 with lower mass loading electrodes (Figure C.2).

Similarly, the improved rate performance in the SB25 cells with thinner electrodes compared to NMC is also observed at the increased mass loadings, as depicted in Figure C.7. The disparity between the cells is most apparent at 500 mA g^{-1}, where the average capacity over five cycles was 2.09 mA h cm^{-2} for SB25 and 1.46 mA h cm^{-2} for NMC, corresponding to 61% and 44% of their starting rate test capacity. However, as seen for the previous high-energy full cell, both cells can only deliver a very low capacity at the faster discharge current of 1000 mA g^{-1}, where capacities fall to 0.616 mA h cm^{-2} and 0.318 mA h cm^{-2} for SB25 and NMC. At the end of the rate tests, both cells displayed respectable recovery levels similar to that observed earlier in the lower energy (1 mA h cm^{-2}) cells, with SB25 recovering 93% of its initial 3.41 mA h cm^{-2} compared to 91% of the 3.32 mA h cm^{-2} in NMC.

Figure 5.13a shows the electrochemical cycling performance of the N/P = 1.0 cells, which was initially assessed by asymmetric cycling with current densities of 50 and 100 mA g^{-1} for the first 200 charge and discharge cycles. The discharge capacities for NMC and SB25 at the end of the first cycle when normalised by active mass were 146.1 and 158.4 mA h g^{-1}. Despite the lower charging rate used in these cycle tests, which should enable slower intercalation reactions, the capacity in both cells was not stable, with the SB25 full-cell showing a faster rate of capacity fade. After 67 cycles, the capacity retention of SB25 had fallen to 80% where the capacity was 2.29 mA h cm^{-2}, whilst this threshold was extended to the 98th cycle in the NMC cell at a capacity of 2.10 mA h cm^{-2}. The capacity retention in the NMC and SB25 full cells after the 200th cycle was determined as 69% and 57% for corresponding final capacities of 1.84 mA h cm^{-2} and 1.64 mA h cm^{-2}.

Periodic EIS measurements were also taken at the start of the cycle life tests and after every 50 cycles to compare the impedance changes in the high-energy cells. Figure 5.13b-c display the Nyquist plots recorded at the upper voltage limit of 4.3 V, corresponding to the fully charged state of the full cells up to the 100th cycle. The shape of the impedance spectra is consistent with the upper voltage EIS

response seen previously for the lower loading full cells (Figure 5.6), displaying two semi-circles. The ECM displayed alongside the Nyquist plots was used to fit the spectra for the ohmic (R_s), ionic (R_{Ion}), and charge transfer (R_{CT}) components of the impedance, for which the resulting values are collected in

Table . Before cycling, the charge transfer process which are attributed to the larger semi-circle at lower frequency, is considerably larger in NMC than the equivalent semi-circle in SB25. This is consistent with findings by previous researchers who noted a decrease in charge transfer resistances with increasing electrode thickness in porous electrodes, where the thicker electrodes afford a larger reaction surface area.[261]

During the cycling, the R_{CT} components in both cells continue to increase but at slightly different rates. However, the most significant increase for both cells occurs in the first 50 cycles, after which the growth is steadier in NMC, whilst the R_{CT} almost doubles again for SB25 in the next 50 cycles before showing minimal growth between cycles 100 to 150.

There is also a notable increase in the ohmic resistance for NMC between the 1st and 50th cycle from 0.61 Ω to 1.42 Ω, whilst the R_s is smaller in SB25 and remains at around 0.3 Ω over this cycling period. Both cells also show a small increase in R_{ion} during cycling, however the change is fairly minimal in contrast to the higher frequency process and so does not appear to be pivotal to the cell degradation.

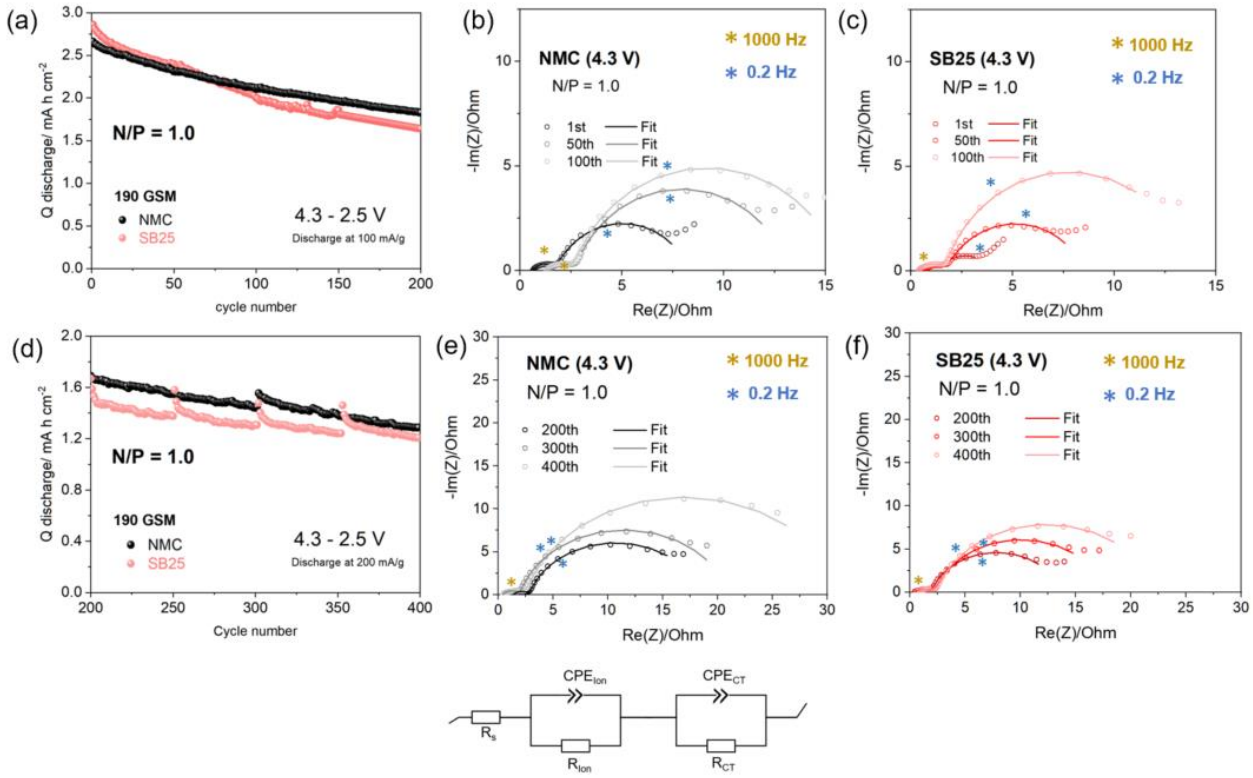

Figure 5.13: Electrochemical testing of full cells assembled at N/P = 1.0 for NMC and SB25 (loadings = 190 GSM); cycle life tests at discharge rates of 100 mA g^{-1} (c), followed by 200 mA g^{-1} (d), and the Nyquist plots from the EIS measurements taken periodically over the first 100 cycles at the lower rate (b – c) and after the 200th cycle at the faster rate cycling (e – f).

In the second part of the cycle stability tests, the specific current applied in the charge and discharge cycles was increased to 50/100 mA g^{-1} to be consistent with the rates used in the lower loading cells discussed earlier. The NMC and SB25 cells show a similar overall cycling stability over this period, as seen in Figure 5.13d, displaying capacity retentions of 76% and 72% with final capacities of 1.29 and 1.21 mA h cm^{-2} after 200 cycles at the faster rate. There is a notable spike in the discharge capacities in SB25 at the start of the cycling regime and every 50 cycles following the EIS measurements and recovery cycles, before shortly decaying back to a similar capacity to that in the preceding cycles.

The increased cycling rate did not change the shape of the Nyquist plot from the EIS responses at 4.3 V for NMC and SB25. However, the larger semi-circle from the charge transfer reactions grew and became more incomplete with increasing cycles, suggesting

the reactions proceeded on timescales slower than the 10 mHz limit. EIS fitting results of these spectra can be found in Table C.4 and show a similar trend to that observed at the slower rate cycling, with SB25 yielding the lower values of R_{CT} throughout the cycle test, whilst the values of R_{ion} are broadly the same across both cells. Interestingly, a decrease in R_s is observed for the NMC cell between the 250th and 300th cycle from 1.67 Ω to 0.41 Ω, which is also accompanied by a small decrease in R_{CT}. The lower impedance displayed here is consistent with the small spike in capacity displayed in the 301st cycle that followed the EIS measurement. This is similar to that observed in each of these cases in the SB25, however, no decrease in impedances was recorded for that cell. To further elucidate the degradation mechanism in the high energy full-cells the spectra from the EIS measurements recorded at mid-discharge (3.5 V) is shown in Figure C.8. As seen in the lower loading cells, the EIS response at 3.5 V shows a smaller charge transfer response relative to that at 4.3 V, whilst the smaller semi-circle begins to split into two more distinct responses in the SB25 full-cell. In contrast to the higher SOC case, the values of R_{CT} are lower in NMC than SB25 at each of the recorded cycle points, however the deviation between these impedances is much smaller than when the cells are in the fully charged state.

5.3.6. Impact of material properties on cell design

The impact of Boron (B) and Boron-Tin (B, Sn) co-doping on $LiNi_{0.9}Mn_{0.5}Co_{0.05}O_2$ (NMC 90-5-5) cathodes is significant on electrochemical performance in high-power and high-energy full cells and their cell design considerations. The key comparisons between the three cathode compositions—undoped NMC90, single-doped B25, and co-doped SB25—highlight kinetics, polarisation, capacity retention, and rate performance differences.

SB25 consistently demonstrated the best rate performance, followed by B25, while undoped NMC90 showed the fastest capacity drop at high rates. In coin cells, at 500 mA g^{-1}, SB25 retained 78.9% of its initial capacity, compared to B25 (72.2%) and NMC90 (69.5%). In pouch cells, B25 showed moderate improvement over NMC90 but did not match SB25 at high discharge rates. The B-doped (B25) cathode demonstrated better lithium diffusion kinetics than NMC90 but higher polarisation than SB25, limiting its overall rate capability.

Electrochemical impedance spectroscopy (EIS) confirmed that B25 exhibited lower R_{CT} than NMC90 at higher SOC, reducing kinetic barriers for lithium transport. However, SB25 had the lowest R_{CT} across all SOC ranges, indicating superior charge transfer efficiency and reduced polarisation. GITT analysis showed that B25 had improved Li diffusion coefficients (D_{Li}) compared to NMC90 but did not reach the higher diffusion rates observed in SB25.

At low SOC, graphite overpotentials were significantly higher in NMC90 cells, leading to a higher risk of lithium plating in lower N/P ratio cells. B25 mitigated some of these overpotentials, but not as effectively as SB25, which allowed for better anode-cathode balancing at high charge/discharge rates. Both B25 and SB25 delayed the H2-H3 phase transition at high SOC, reducing the risk of phase instability in the cathode. B25 exhibited slightly higher polarisation than SB25, leading to a greater tendency for early voltage cut-off, reducing accessible capacity.

In 200-cycle tests at 200 mA g^{-1} for the high-power cells (1 mA h cm^{-2}), B25 exhibited the highest capacity retention, followed by SB25, while NMC90 degraded the fastest. B25 stabilised cycle life compared to NMC90 but the higher polarisation limited long-term high-rate performance. Over time, impedance growth (VIR) was lowest in B25, whereas

SB25 showed moderate impedance increase, and NMC90 exhibited the steepest rise in charge transfer resistance, especially in the high SOC region, contributing to faster degradation.

In pouch cells with high-mass-loading electrodes (~4.5 mA h cm^{-2}), SB25 improved the rate capability and higher initial cycling capacity over NMC90, although both cells showed capacity fading. Under long term cycling at a faster discharge rate, SB25 demonstrated better reversibility and lower impedance build-up, making it more effective at maintaining performance in thick electrodes at practical rates. NMC90 suffered from early voltage cut-offs and greater degradation in high-energy configurations, limiting its suitability for long-term high-capacity applications.

Table 5.4: Summary of Comparisons:

Performance Metric	NMC90 (Undoped)	B25 (B-Doped)	SB25 (B, Sn Co-Doped)
Rate Capability	Poor	Moderate	Best
Charge Transfer Resistance (R_{CT})	Highest	Lower than NMC90	Lowest
Lithium Diffusion (D_{Li})	Moderate	Improved and stable with cycling	Highest pre-cycling
Polarization	High	Moderate	Lowest
Overpotentials at Low SOC	Highest (risk of Li plating)	Lower than NMC90	Lowest (best anode-cathode balance)
High SOC Phase Stability (H2-H3 Transition Delay)	Poor	Delayed above voltage cut-off	Improved reversibility
Cycle Life Stability	Fastest degradation	Best retention	Similar to NMC90 but higher capacity
Impedance Growth Over Cycling	Fast increase	Moderate increase	Slowest increase
High-Energy Electrode Performance	Poor (high polarization)		Best (low polarization, stable performance)

Boron doping (B25) improves lithium transport reduces resistance, and improves cycle life compared to undoped NMC90 but its higher polarisation limits rate performance. However, Boron-Tin co-doping (SB25) optimises kinetics and structural stability, offering superior rate capability, lower overpotentials, and higher long-term cycling

capacity. In high-energy designs (thick electrodes), SB25 outperforms NMC90, showing the best reversibility, lowest impedance growth, and highest long-term capacity retention. SB25 provides the best balance for high-power and high-energy applications, making it the most promising cathode composition.

5.4 Conclusions

This study has investigated the electrochemical performance of Boron (B) and Tin (Sn) co-doped $Li([Ni_{0.9}Mn_{0.05}Co_{0.05}]_{1-x-y}B_xSn_y)O_2$ cathodes in lithium-ion full cells, with a focus on optimising both high-power and high-energy battery designs. The trade-offs between rate capability, polarisation, lithium diffusion, and long-term cycling stability were explored by systematically analysing different cell formats (coin and pouch cells) and negative-to-positive (N/P) ratios.

The cell design is shown to be impacted by the kinetics of the reactions at low and high states of charge, where they are typically slower and result in higher overpotentials. At low SOC, overpotentials are significantly higher on the graphite anode, particularly at lower N/P ratios. This increases the risk of lithium plating and hinders fast charge/discharge kinetics. A higher N/P ratio is required for high-power applications to reduce these overpotentials and improve rate performance. At high SOC, increased polarisation in the cathode limits the accessible lithium stoichiometry, causing the cut off voltage to be reached at a lower lithium extraction level. This reduces the effective capacity and decreases the time spent in the high-voltage region (~4.2V) where the H2-H3 phase transition occurs. The results highlight that the balance between anode and cathode stoichiometry is key to optimisation; higher N/P ratios mitigate kinetic limitations, allowing better rate performance, reduced overpotentials, and improved stability at high cycling rates.

Because of the sloping voltage profile, more significant hysteresis and polarisation in the cathode results in less lithium transfer, preventing it from reaching its full thermodynamic lithium stoichiometry and reducing observed capacities. Higher ohmic resistance systems may exhibit longer cycle life at lower capacity because they spend less time in the H2-H3 transition region, reducing structural degradation. However, added impedance increases capacity fade at high rates as resistance builds up during cycling. This underscores the need for an optimal balance between reducing polarisation and maintaining long-term stability.

The dual B and Sn doping strategy (SB25) demonstrated lower charge transfer resistance and higher lithium diffusion coefficients, resulting in superior rate capability.SB25 outperformed NMC90 in coin cells, retaining 78.9% of its capacity at 500 mA g^{-1}, and maintained higher areal capacities in pouch cells at fast discharge rates. By delaying the H2-H3 phase transition, SB25 reduced structural stress and showed higher capacity retention over 200 cycles at 200 mA g^{-1} in both coin and pouch cells.

High-Energy Electrode Development and Performance

To explore high-energy designs, full cells were assembled with high-mass-loading cathodes (~4.5 mA h cm^{-2}) in a pouch cell format. SB25 exhibited better reversibility and cycling stability than NMC9½½, despite increased polarization in thicker electrodes. Nevertheless, while thicker electrodes enabled higher energy density, they introduced higher ohmic resistance, requiring careful balancing to maintain long-term performance.

These results emphasise the delicate trade-offs in high-power vs. high-energy lithium-ion battery designs. A higher N/P ratio is needed for high-power applications to mitigate overpotentials at low SOC and improve rate performance. For high-energy applications, thick electrodes increase energy density but must be optimised to minimise polarisation

and impedance growth to maintain cycle life. The growth of resistance over cycling dictates long-term performance, highlighting the importance of balancing initial capacity, lithium transport efficiency, and electrode stability.

Overall, this study demonstrates that B, Sn co-doping enhances both high-power and high-energy LIB performance by improving lithium diffusion, reducing charge transfer resistance, and stabilising the cathode structure. However, precise control of N/P ratios, electrode thickness, and polarisation effects is necessary to optimise performance for specific applications fully.

Chapter 6: Conclusions and Outlook

6.1 Conclusions

The high reactivity of Ni-rich cathode materials at the surface and in the bulk is a considerable challenge in the development of high energy density lithium-ion batteries (LIBs). The aim of this thesis was to develop and optimise the preparation and stabilise the structure and electrochemical performance of $LiNi_{0.9}Mn_{0.05}Co_{0.05}O_2$ (NMC 90-5-5) as a prospective cathode material in LIBs. The results presented in this thesis have demonstrated the importance of tailored synthesis conditions, strategic doping, and electrode design in enhancing the reaction kinetics and long-term stability.

In Chapter 3, the use of boron fluxes was investigated to optimise the firing conditions at lower temperatures and shorter residence times. Here, it is intended that the boron acts as a mineralisation aid, in which the extra boron ions are introduced to aid particle growth and modify the surface properties, rather than necessarily lattice substitution. A lower hold temperature of 450°C and a higher hold temperature of 750°C, without the need for an O_2 atmosphere, enabled the optimal balance between low cation mixing and high initial reversible capacity (213 mA h g^{-1}) with the highest first cycle coulombic efficiency (96%). Therefore, providing a route to high performance Ni-rich NMC material under low energy firing conditions, which could provide considerable energy and cost savings at scale.

The particular effect of each of the flux materials, boric acid and borax, was also elucidated through extensive characterisation using XRD, SEM, FTIR, XPS, and EIS. The analysis revealed that boric acid was more effective in limiting the bulk cation disorder and surface lithium residues, yielding the higher initial capacities as well as improved

kinetics. However, the borax flux-treated samples exhibited superior cycle life, with a 74.9% capacity retention over 200 cycles at C/2, attributed to enhanced boron and sodium incorporation, which stabilised the structure by delaying the high voltage phase transition and reducing volumetric changes during cycling in the voltage range of 4.3 – 2.5 V. This work emphasized the need to optimize both bulk and surface properties, as small changes in surface resistance impact the capacity and cycle life through the overpotentials that are observed. Achieving the right balance between surface kinetics, overpotentials, and cycling voltage is crucial for optimizing materials and full-cell performance.

Building on the insights of the flux effects on the cathode structure and performance, targeted bulk doping into the lattice was explored in Chapter 4 with the aim to optimise both cycle stability and transport properties in NMC 90-5-5 by adjusting the stoichiometric composition. Single boron (B25) and dual tin-boron (SB25) doping strategies were both effective in extending the cycle life of the NMC 90-5-5 cathode, whilst SB25 also increased the delivered capacity. The mechanism for the improved cycle stability was also investigated *via* ex-situ analysis, which suggested the dopants act to stabilise transition metal oxidation states and mitigated electrolyte-induced surface degradation. Electrochemical testing at elevated (45°C) and low (−5°C) temperatures also revealed distinct advantages of bulk doping on the transport properties. Both of the doped materials exhibited improved rate capability than the pristine material at 45°C , with SB25 delivering the highest capacities at all discharge rates. The dual tin-boron doping also revealed a superior rate performance at low temperatures, attributed to the enhanced lithium-ion transport and reduced interfacial resistance. The improved performance, particularly at low temperatures, highlights the potential of tailored doping

strategies to advance lithium-ion batteries for electric vehicles and other demanding applications.

Having investigated the structural-performance relationship of the doped cathodes at a materials level, the next objective of the thesis was to demonstrate their practical application in full-cell testing. In Chapter 5, the effect of N/P ratio was evaluated for the pristine and doped cathodes across different full-cell formats based on NMC 90-5-5|| graphite cell chemistry. The full-cells containing the SB25 cathode demonstrated superior rate performance due to lower charge transfer resistance and enhanced lithium diffusion, delivering high capacity across different formats. High-power applications benefited from higher N/P ratios, reducing overpotentials and improving kinetics, whilst thicker electrode designs enabled much higher energy densities but faced higher resistance challenges at faster rate cycling. The interplay between polarisation and lithium transport efficiency dictated long-term performance. While higher ohmic resistance systems exhibited longer cycle life due to reduced time spent in the H2-H3 transition region, excessive impedance growth accelerated capacity fade at high rates. This highlights the importance of optimising electrode design to balance initial capacity, structural stability, and lithium transport efficiency.

6.2 Outlook

The work presented in this thesis has highlighted how modifications during the synthesis of $LiNi_{0.9}Mn_{0.05}Co_{0.05}O_2$ can be applied to help guide large-scale cathode design and improve key performance properties at both the half-cell and full-cell application. It is hoped that the results and insights from this work can also direct further investigations to help accelerate the commercial development of Ni-rich NMC cathodes.

The synthesis process relies on multiple input variables over the course of the coprecipitation and firing steps which all contribute to the resulting structure and morphology of the cathode active material. For the design of higher energy density materials, future work should focus on optimising the synthesis parameters to engineer particle morphologies that promote higher tap densities. In particular, a systematic study of the pH, stirring rate, temperature, and ammonia concentration during the coprecipitation reaction could be employed to target the formation of dense spherical secondary particles to improve packing efficiency during electrode preparation. Whilst the concentration of the boron fluxes could be tailored to encourage increased grain connectivity, thus reducing internal porosity and further densifying the particles.

Given the improved cycle stability of the boron and tin-boron doped materials, which is highest for the former but at lower specific capacities, further studies to systematically vary the boron and tin concentrations would enable the optimal balance between cycle lattice stabilisation and lithium kinetics. Additionally, electrolyte compatibility remains a critical factor in extending cycle life, particularly at higher voltages. Investigating different electrolyte compositions and additives to stabilise high voltages, such as fluorinated solvents like fluoroethylene carbonate (FEC), could help mitigate surface degradation and enhance overall cathode performance. Tailoring electrolyte chemistry to complement the doped cathodes may enable even further improvements in both rate capability and long-term cycling stability.

The promising low temperature kinetics of the tin-boron dual doped NMC 90-5-5 demonstrated in Chapter 4 in half-cell testing, warrant further investigation at the full-cell level to assess their practical impact on long-term cycling performance. Additionally, a comprehensive temperature-dependent study should be conducted, extending beyond

−5°C to ultra-low temperatures (−20°C or lower), to evaluate lithium transport limitations and interfacial resistances in extreme environments. These studies will require comprehensive electrochemical analysis to decouple the limiting contribution to the increased overpotentials arising at low temperature.

Regarding the development of high-energy full-cells, additional research is necessary to improve the long-term cycle performance. Given the increased polarization and ohmic resistance in thicker electrodes, advanced electrode design strategies such as graded porosity structures, optimized binder compositions, and 3D conductive frameworks could be explored to enhance ionic and electronic transport while maintaining mechanical integrity. Furthermore, as lithium-ion battery technology advances, it is essential to assess the compatibility of these cathodes with next-generation anode materials, such as titanium niobium oxide (TNO). High-power full cells integrating these novel anodes could offer improved safety, cycle life, and fast-charging capabilities. These anodes introduce a different operating voltage window when paired with NMC, which may require re-evaluation of the optimal potential limits and N/P ratios to enable the appropriate lithium stoichiometries for the higher rate performance. Exploring the electrochemical interactions between co-doped cathodes and TNO anodes could be highly advantageous in developing high-performance energy storage solutions for future applications.

Appendix A: Supporting Information for Chapter 3

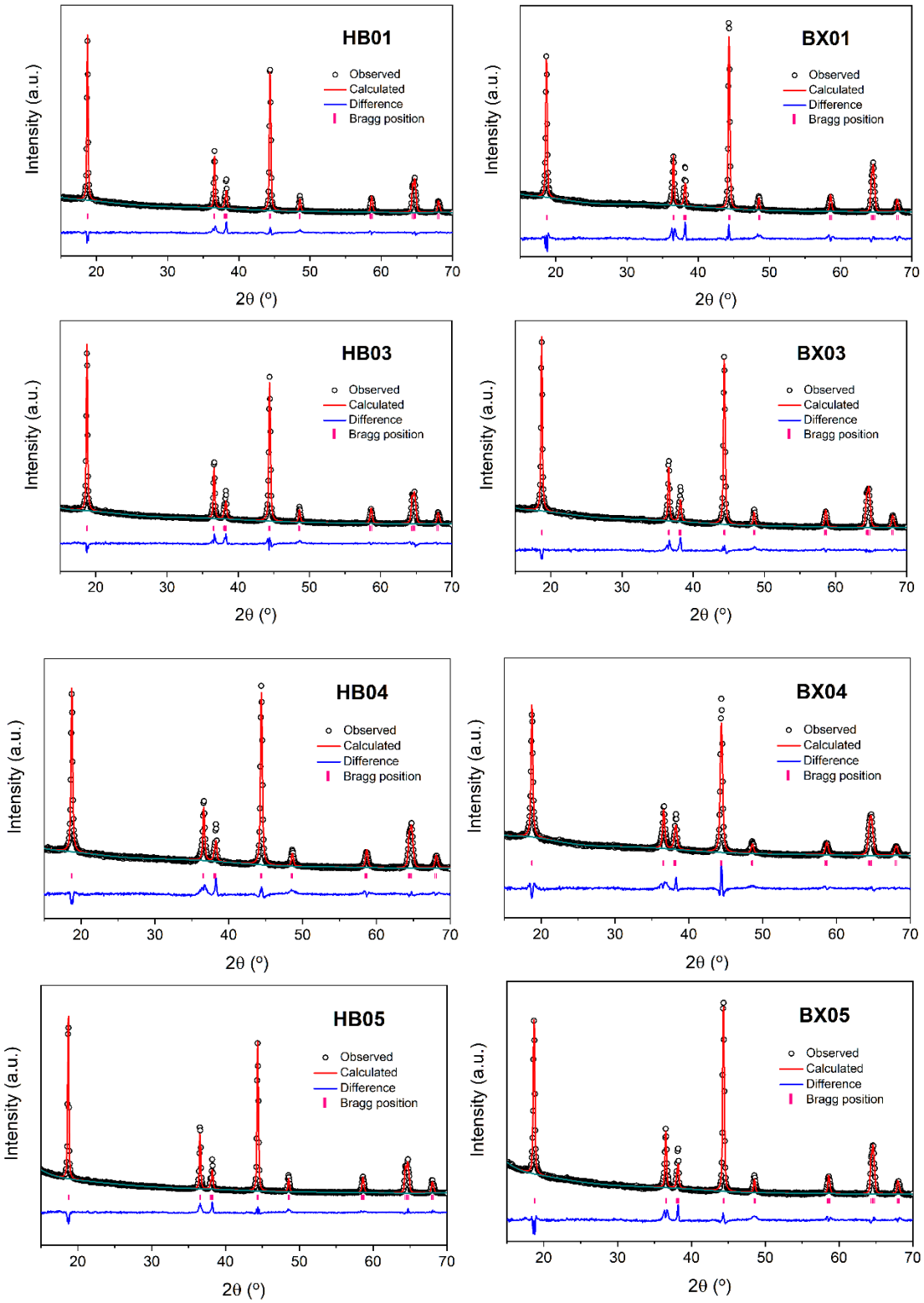

Figure A1: Observed, calculated and difference profiles from Rietveld refinements using powder XRD data for NMC 90-5-5 materials fired with boric acid (HB) and borax (BX) with different firing conditions.

Table A.1: Lattice parameters, cation exchange of Ni^{2+} into the 3a sites, and the 003/104 peak intensity ratio (R) of the NMC 90-5-5 samples synthesised with HB and BX in different firing conditions.

Sample	*a*/ Å	*c*/ Å	Volume/ Å^3	Ni in Li %	Rwp %
HB01	2.87886(6)	14.1947(5)	101.890(5)	7.7	4.98
HB02	2.87851(2)	14.2056(2)	101.936(2)	6.8	3.40
HB03	2.87718(7)	14.1971(5)	101.780(5)	7.5	4.97
HB04	2.8767(1)	14.1909(8)	101.705(8)	9.2	5.24
HB05	2.87956(6)	14.2049(4)	102.004(5)	7.3	5.97
BX01	2.88251(9)	14.2025(7)	102.197(7)	11.8	6.16
BX02	2.88059(5)	14.2058(4)	102.085(4)	11.1	8.70
BX03	2.88014(7)	14.2038(5)	102.039(6)	9.2	4.68
BX04	2.8780(1)	14.1875(9)	101.77(1)	14.5	7.10
BX05	2.88177(8)	14.2021(7)	102.141(7)	11.5	5.68

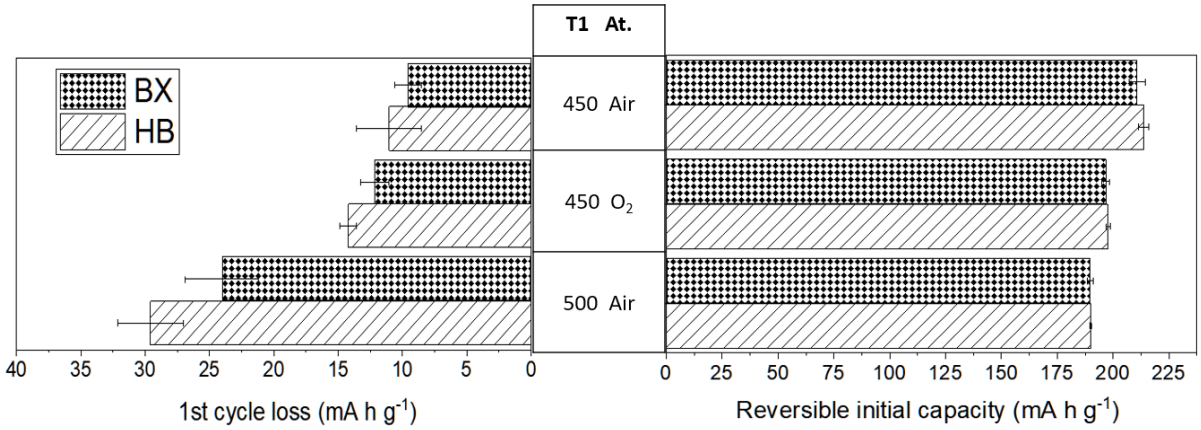

Figure A2: Formation capacity (right) and first cycle loss (left) for the NMC 90.5.5 prepared with boric acid (HB) and borax (BX) in different furnace conditions, recorded at 10 mA g^{-1}.

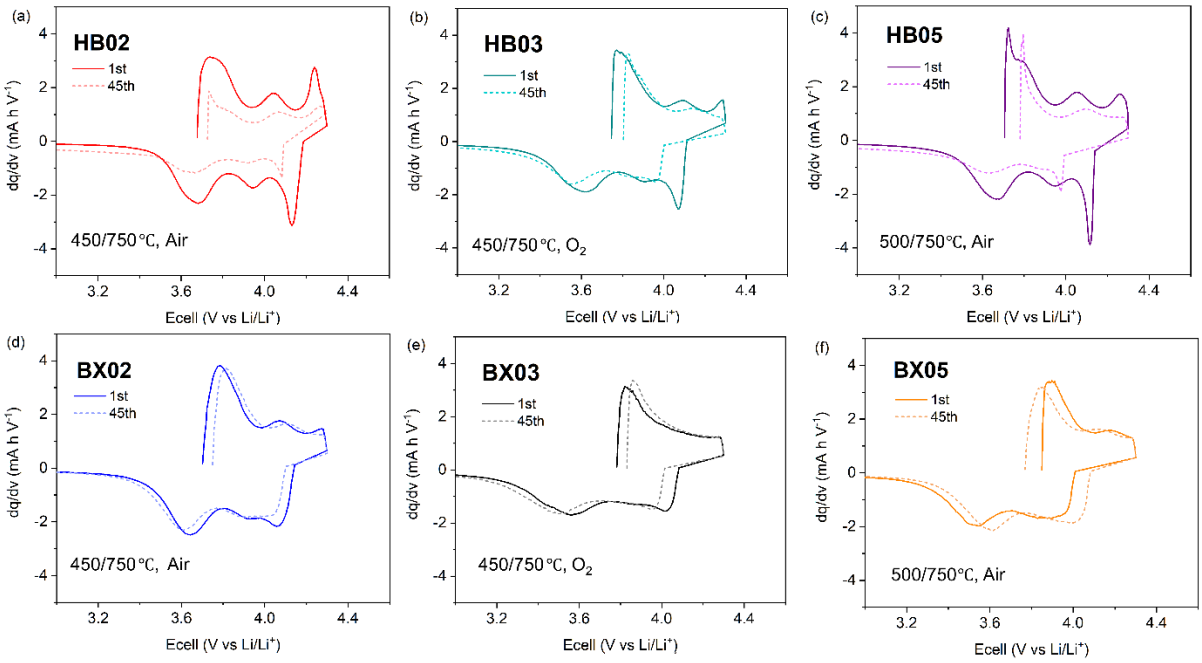

Figure A.3: Differential capacity plots of the 1st and 45th cycle at 1C rate in the post-formation cycling tests for NMC 90-5-5 materials prepared with HB (a – c) and BX (d – f) at different firing conditions.

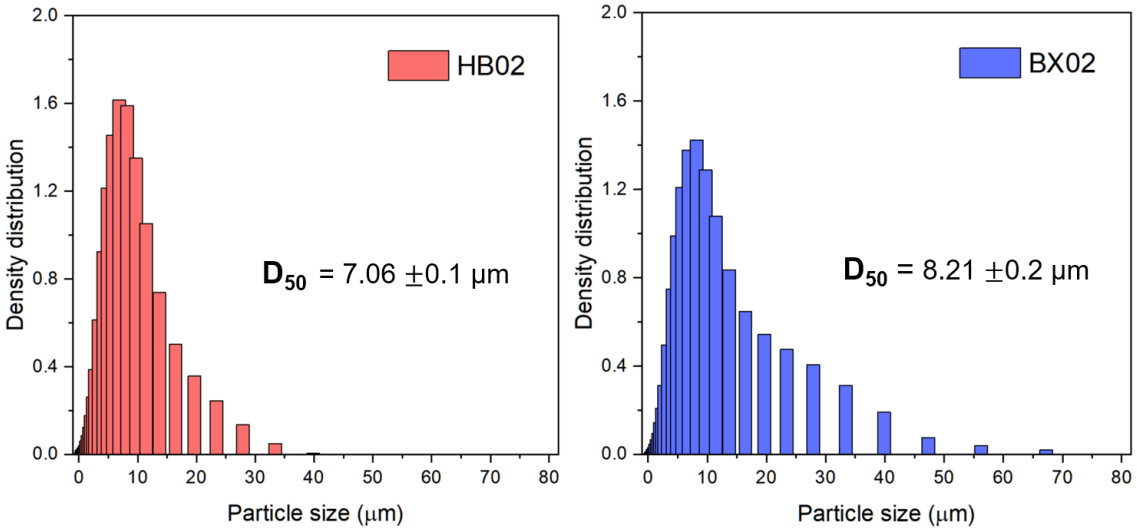

Figure A.4: Particle size distributions of HB02 and BX02 active materials.

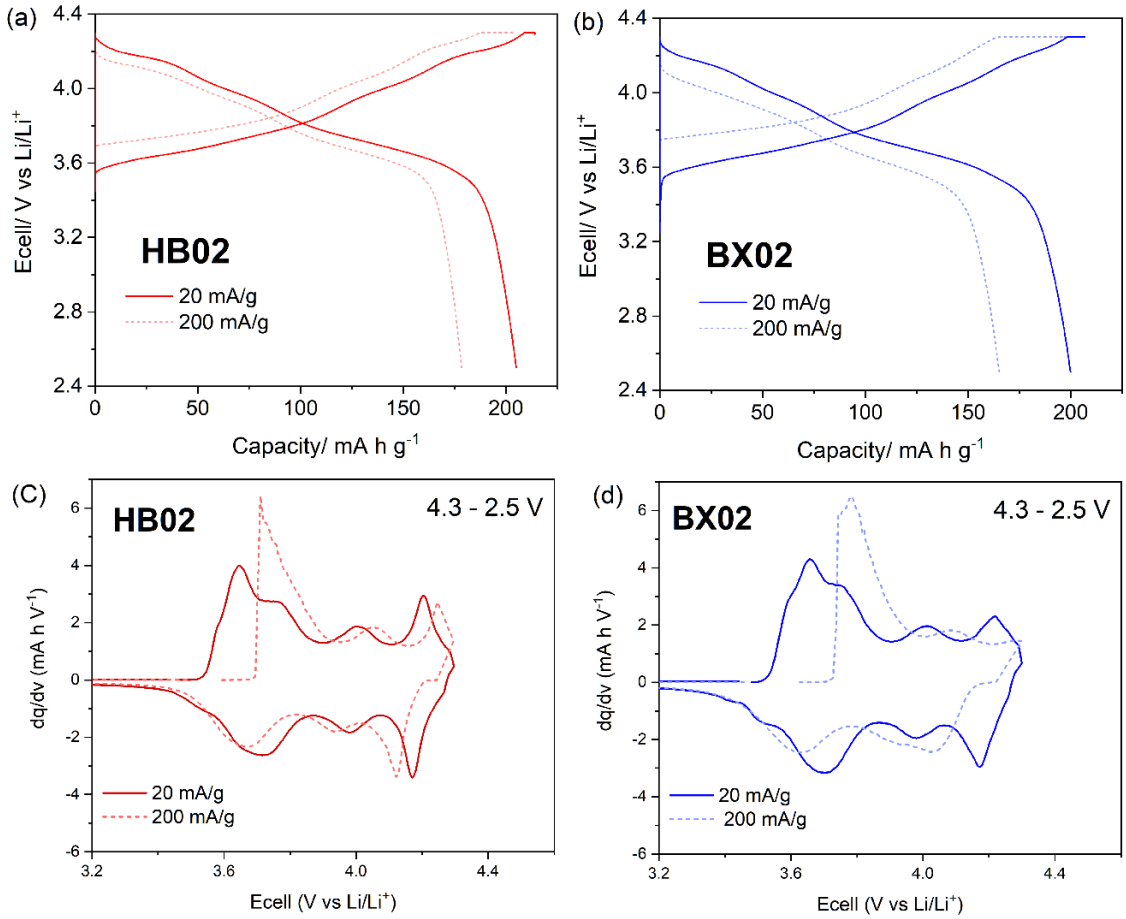

Figure A.5: Charge-discharge curves of a single post-formation cycle recorded at current densities of 20 mA g^{-1} and 200 mA g^{-1} and the resulting differential capacity plots for HB02 (a, c) and BX02 (b, d).

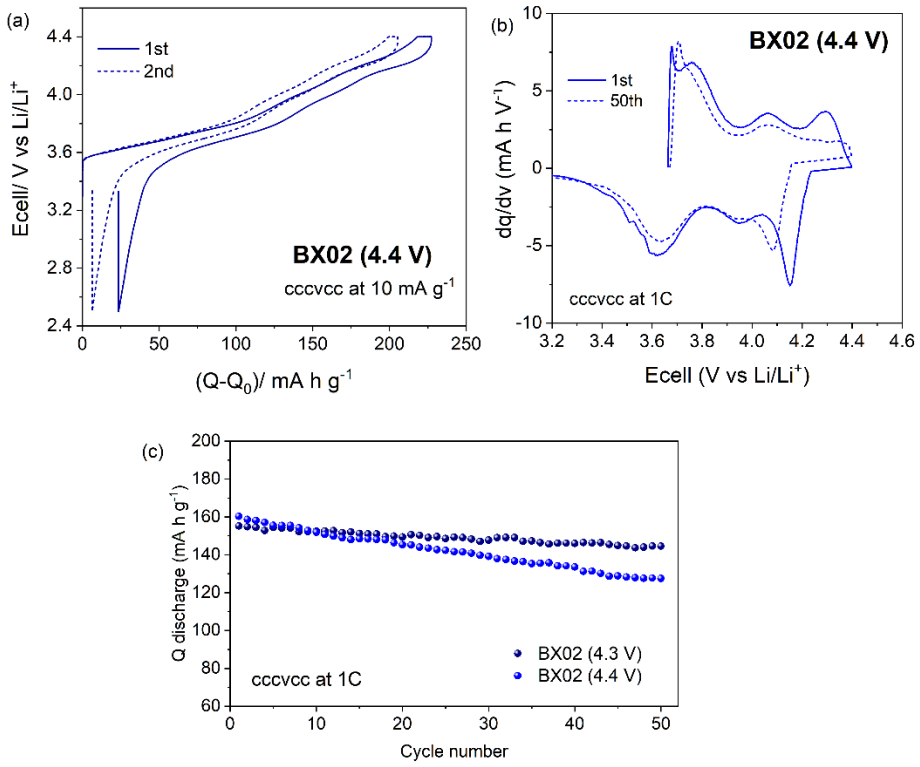

Figure A.6: Charge-discharge formation profiles of BX02 cycled between 4.4 – 2.5 V (a) and the subsequent differential capacity plots of the 1st and 50th cycle from the 1C cycling performance (b), with a comparison of the discharge capacities of BX02 at this rate when charged to 4.4 V or 4.3 V (c).

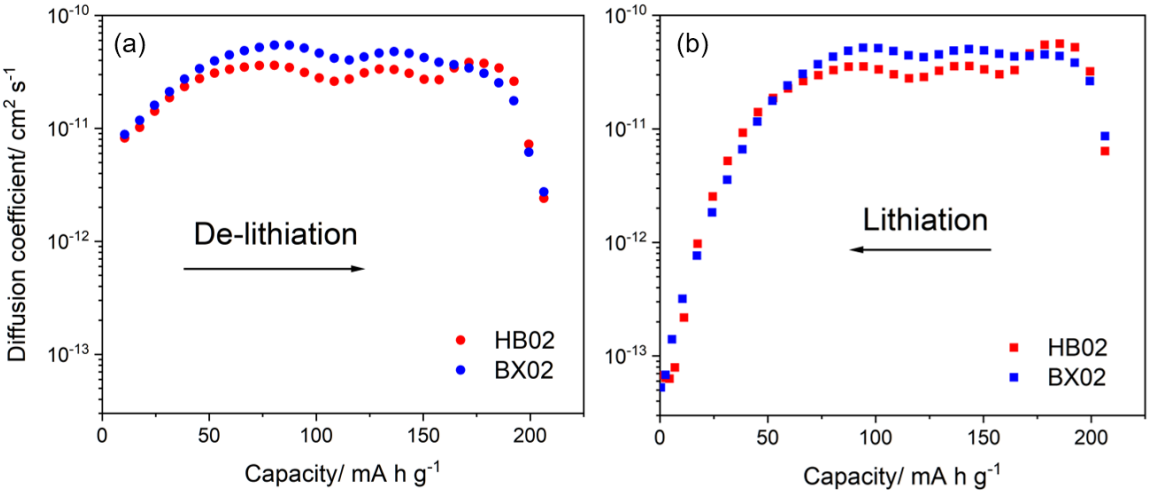

Figure A.7: Lithium-ion diffusivities measured by GITT in the HB02 and BX02 electrodes during de-lithiation (a) and lithiation (b).

Appendix B: Supporting Information for Chapter 5

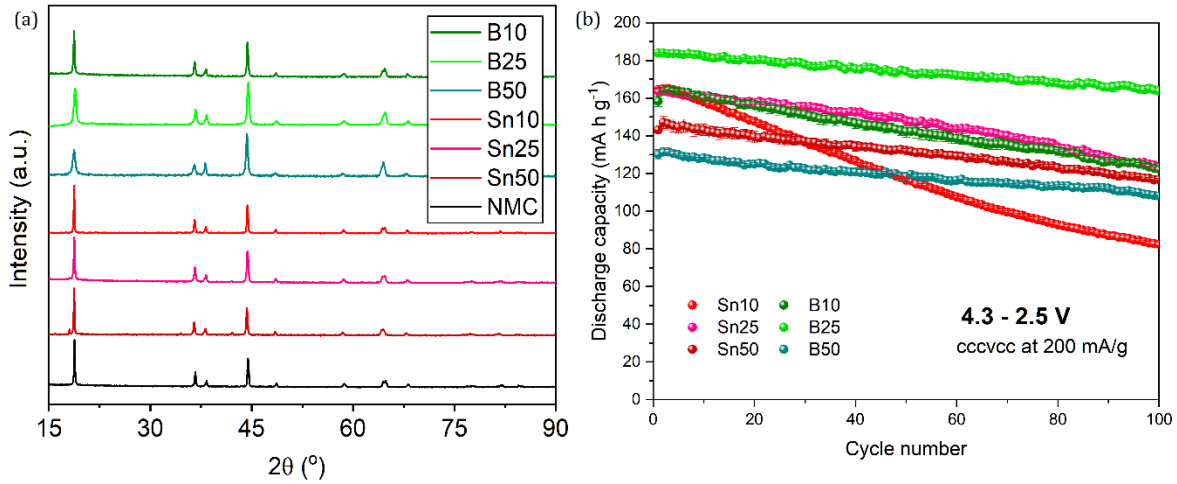

Figure B.1: XRD patterns of single cation doped $Li(Ni_{0.9}Mn_{0.05}Co_{0.05})_{1-x}M_xO_2$ where M = B, Sn, and x = 0.01, 0.025, 0.05 (a), and the discharge capacity cycle performance of the doped samples (b).

Table B1: Discharge capacity and Coulombic efficiency data of Sn and B doped NMC90-5-5 at various mol% concentrations taken from the initial formation cycles between 4.3 - 2.5 V at 10 mA g^{-1}

Sample	1st Qch	1st Qdis	2nd Qch	2nd Qdis	1st CE
Sn10	223.9	202.3	204.3	193.9	90.3%
Sn25	210.3	202.5	203.0	198.5	96.3%
Sn50	207.0	196.6	188.5	185.5	95.0%
B10	222.4	201.6	204.5	190.7	90.7%
B25	232.9	201.6	221.4	198.5	86.6%
B50	188.2	172.8	172.6	167.3	91.9%

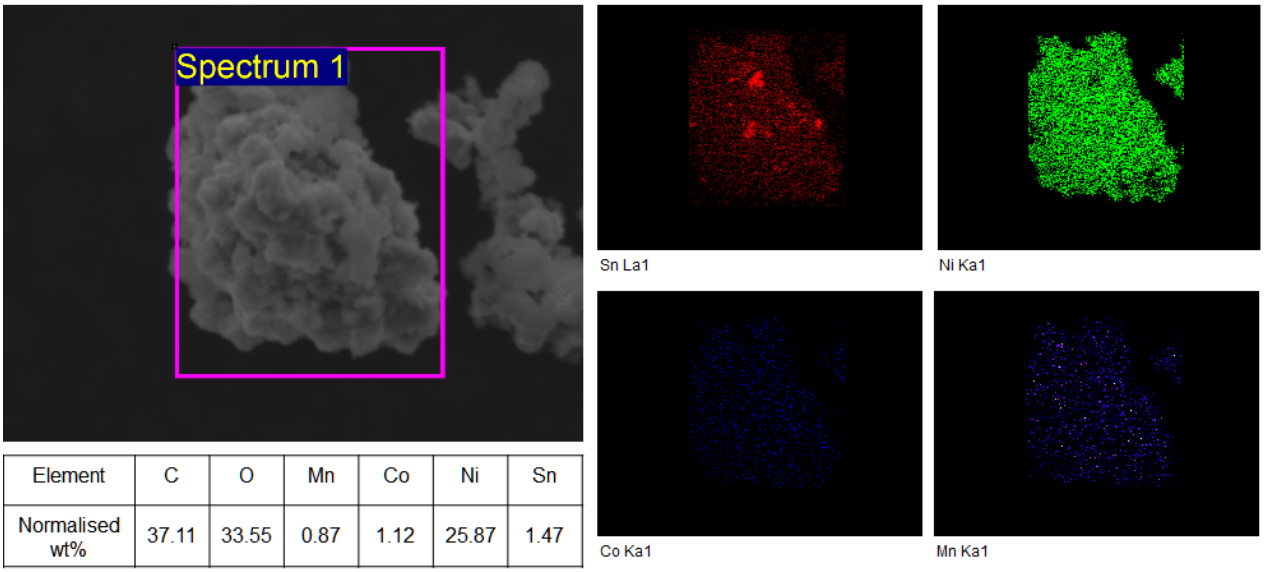

Element	C	O	Mn	Co	Ni	Sn
Normalised wt%	37.11	33.55	0.87	1.12	25.87	1.47

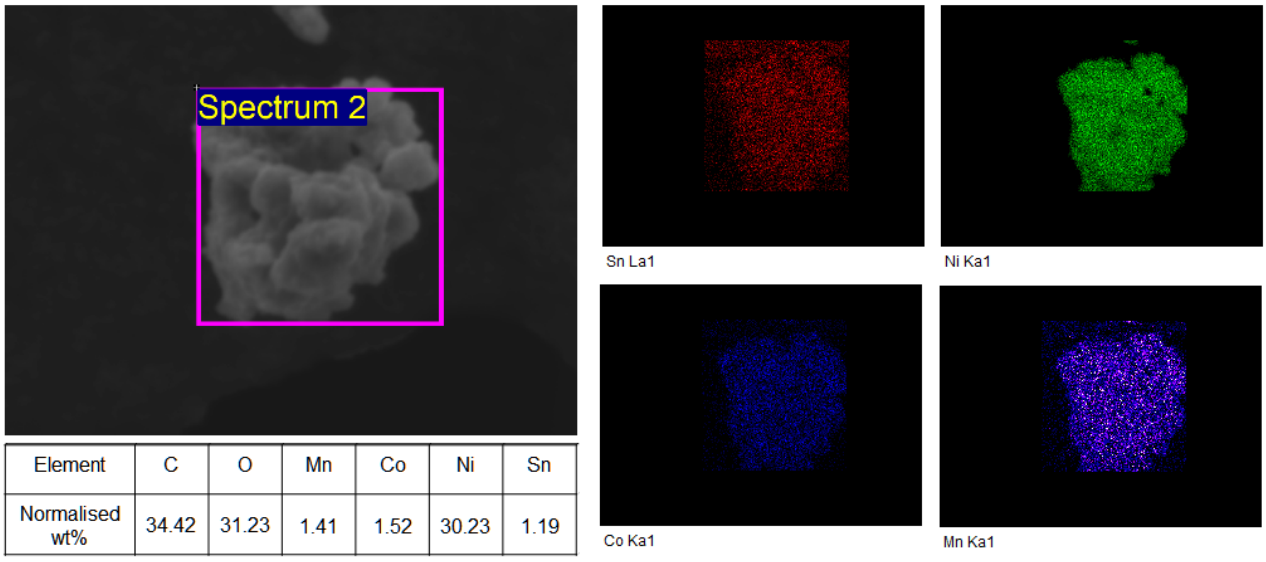

Element	C	O	Mn	Co	Ni	Sn
Normalised wt%	34.42	31.23	1.41	1.52	30.23	1.19

Figure B.2: EDS elemental mapping of SB25 taken across two different particles of the CAM.

Table B2: The threshold energies (E_0) of the main edge of XANES Ni, Mn, and Co K-edge spectra for the powdered cathode and reference samples. [Ac] = $CH_3CO_2^{2-}$

Ni K-edge	**E_0/ eV**	**Mn K-edge**	**E_0/ eV**	**Co K-edge**	**E_0/ eV**
NMC	8347.95	NMC	6556.42	NMC	7726.66
B25	8347.80	B25	6556.37	B25	7726.62
SB25	8347.88	SB25	6556.46	SB25	7726.55
NiO	8345.53	$Mn[Ac]_2$	6547.97	$Co[Ac]_2$	7721.53
$Ni[Ac]_2$	8345.92	Mn_2O_3	6552.56	Co_3O_4	7724.62
		MnO_2	6555.28	$LiCoO_2$	7725.70

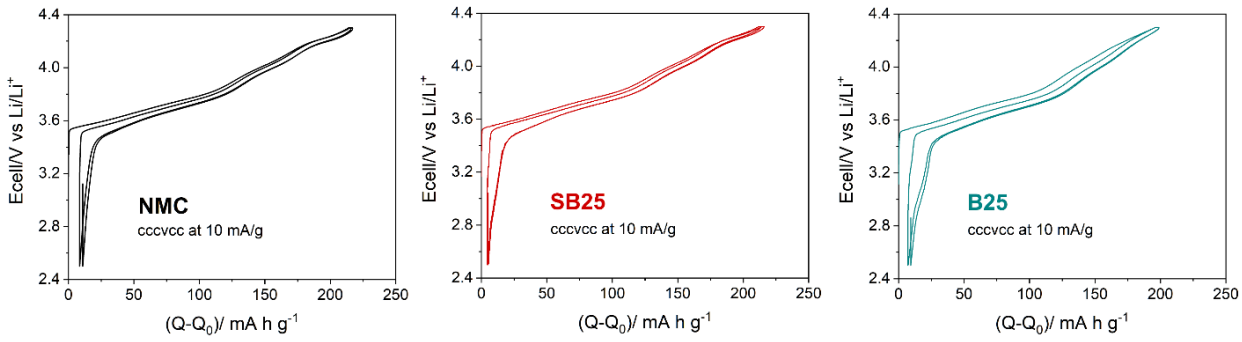

Figure B.3: Formation profiles of the 1st and 2nd charge-discharge cycles of NMC, SB25, and B25 measured at 10 mA g^{-1} between 4.3 – 2.5 V.

Table B3: Equivalent circuit element values taken from the fitted EIS results at different SOC recorded at room temperature.

	NMC				SB25			B25		
SOC %	R_S	R_{SEI}	R_{CT}	R_{CT}	R_S	R_{SEI}	R_{CT}	R_S	R_{SEI}	R_{CT}
0	3.08	7.70	11.0	11.6	1.32	30.42	208	1.16	67.49	274.4
10	4.35	7.71	6.70	27.0	1.62	2.23	19.4	1.37	3.21	19.3
20	3.45	4.30	8.83	9.58	1.55	1.63	14.7	1.38	2.46	15.0
30	3.60	5.77	4.95	7.74	1.60	1.49	13.2	1.50	2.41	12.1
40	4.33	2.23	5.36	9.04	1.05	4.57	8.84	1.48	2.54	9.93
50	3.76	4.48	4.32	7.48	1.13	3.31	8.79	1.42	2.04	10.0
60	4.27	3.19	4.54	8.07	1.67	1.13	9.59	1.48	1.85	9.05
70	3.94	3.18	4.59	9.82	1.10	2.48	8.71	1.41	1.79	8.47
80	3.28	3.90	4.22	17.4	1.17	2.07	8.40	1.45	1.69	7.70
90	3.79	4.16	4.41	53.1	1.58	0.88	8.16	1.46	1.70	7.25
100	3.08	7.70	11.0	11.6	1.36	1.09	10.44	1.40	1.83	6.91

Table B4: Equivalent circuit element values taken from the fitted EIS results at different SOC recorded at 45°C

	NMC			SB25			B25		
SOC %	R_S	R_{SEI}	R_{CT}	R_S	R_{SEI}	R_{CT}	R_S	R_{SEI}	R_{CT}
0	1.42	7.66	17.5	1.34	2.31	8.79	1.433	1.58	12.1
10	1.56	4.47	9.45	1.41	1.74	7.30	1.515	2.77	8.10
20	1.19	3.24	8.76	1.30	1.81	6.54	1.322	0.632	10.4
30	1.18	6.32	7.72	1.30	1.80	5.83	1.310	0.540	9.91
40	1.04	5.60	6.51	1.35	1.34	5.97	1.494	3.86	5.33
50	0.791	5.88	5.94	1.39	1.32	5.50	1.463	3.82	4.51
60	0.833	5.39	5.64	1.34	1.34	5.27	1.556	2.55	5.23
70	0.834	5.38	5.98	1.33	1.44	4.90	1.372	3.54	3.72
80	0.867	5.30	6.06	1.31	1.50	4.81	1.660	1.03	5.81
90	0.963	5.97	6.50	1.32	1.25	5.14	1.522	2.02	4.61
100	1.05	6.23	20.2	1.29	1.23	5.29	1.538	1.27	5.49

Table B5: Equivalent circuit element values taken from the fitted EIS results at different SOC recorded at −5°C.

SOC	NMC				SB25			B25		
%	R_S	R_{SEI}	R_{CT}	R_{CT}	R_S	R_{SEI}	R_{CT}	R_S	R_{SEI}	R_{CT}
0	2.58	12.1	98.8	-	2.72	7.82	1530	3.37	15.4	419
10	2.67	18.3	75.9	346	1.94	11.04	154	3.22	13.1	236
20	2.73	17.3	64.6	132	1.88	8.24	116	3.34	11.6	177
30	2.70	16.8	58.7	100	1.32	8.61	101	3.29	11.8	183
40	2.65	16.5	55.8	115	1.03	8.46	91.5	3.26	11.7	182
50	2.56	16.2	50.7	136	1.19	7.46	86.5	3.23	11.4	172
60	2.51	15.7	51.2	161	1.55	6.20	84.3	3.23	11.7	190
70	2.40	15.5	50.1	305	2.09	4.87	80.0	3.20	11.3	173
80	2.36	15.7	51.2	348	1.06	6.91	74.7	3.28	11.9	216

90	2.36	15.5	50.5	356	1.02	6.98	76.7	3.26	11.8	210
100	2.33	15.4	49.8	717	0.86	7.22	71.4	4.62	7.01	232

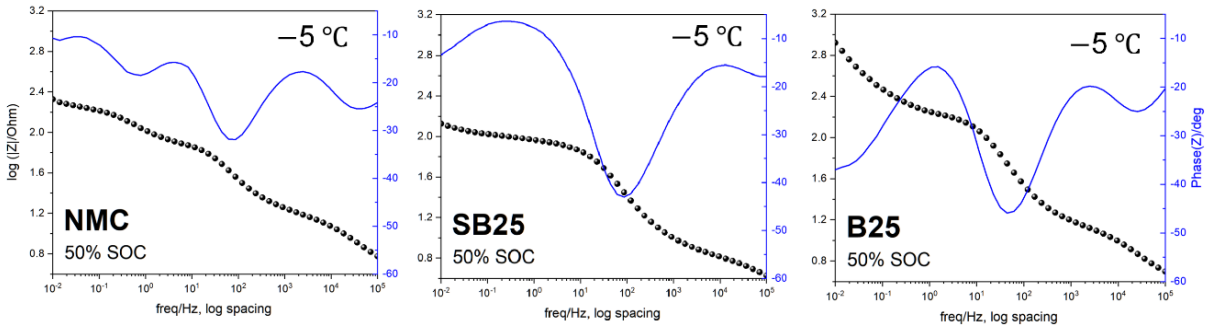

Figure B.4: Bode plots from EIS measurements in cathode half-cells recorded at 50% SOC tested at −5°C.

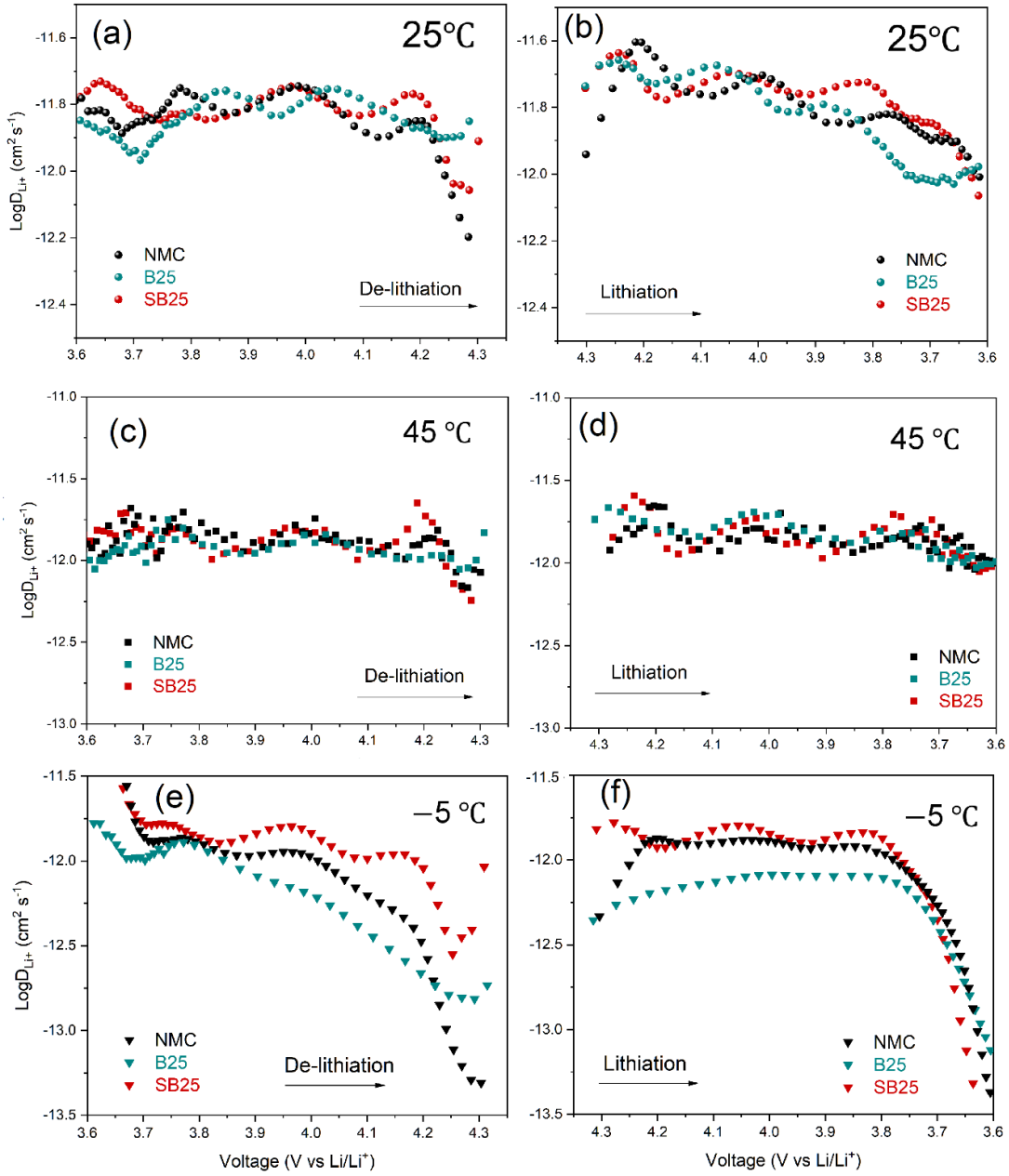

Figure B.5: GITT results showing the log of the diffusion coefficients during charge (a, c, d) and discharge (b, d, f) at room temperature (a, b), 45 °C (c, d), and −5°C (e, f).

Table B6: Peak positions of the (003) reflection in the pristine electrode and electrodes in the charged state during the 1st cycle and after 20 cycles at 500 mA g^{-1}.

Cathode	(003) 2θ position/ °			Δ(003)$_{Pristine - 4.3 V}$	
	Pristine	1st (4.3 V)	Cyc. (4.3 V)	1st	Cyc.
NMC	18.763	18.612	18.631	-0.151	-0.132
B25	18.726	18.593	18.669	-0.133	-0.057
SB25	18.726	18.574	18.555	-0.152	-0.171

Table B7: Lattice parameters calculated from Rietveld refinements of the as made NMC, B25, and SB25 pristine electrodes and ex-situ XRD measurements of these electrodes at the end of charge (4.3 V) and end of discharge (2.5 V) of the 1st formation cycle and after 20 cycles at 500 mA g^{-1}.

Cathode	Sample	a/ Å	c/ Å	Volume/ Å^3	Rwp %
NMC	Pristine	2.877486	14.17593	101.65	12.76
NMC	1st Cha	2.850072	14.27104	100.392	14.00
NMC	1st Dis	2.875671	14.1933	101.646	8.41
NMC	Cyc Cha	2.85847	14.26823	100.964	15.80
NMC	Cyc Dis	2.880743	14.20206	102.068	14.41
B25	Pristine	2.880283	14.19949	102.017	10.90
B25	1st Cha	2.842672	14.27468	99.897	10.15
B25	1st Dis	2.881105	14.20655	102.126	11.04
B25	Cyc Cha	2.866755	14.25965	101.489	10.89
B25	Cyc Dis	2.884258	14.19168	102.243	12.35
SB25	Pristine	2.880686	14.18203	101.92	16.17
SB25	1st Cha	2.834774	14.30991	99.587	10.30
SB25	1st Dis	2.882279	14.2288	102.37	15.09
SB25	Cyc Cha	2.840289	14.27736	99.748	13.79
SB25	Cyc Dis	2.881046	14.21989	102.218	9.80

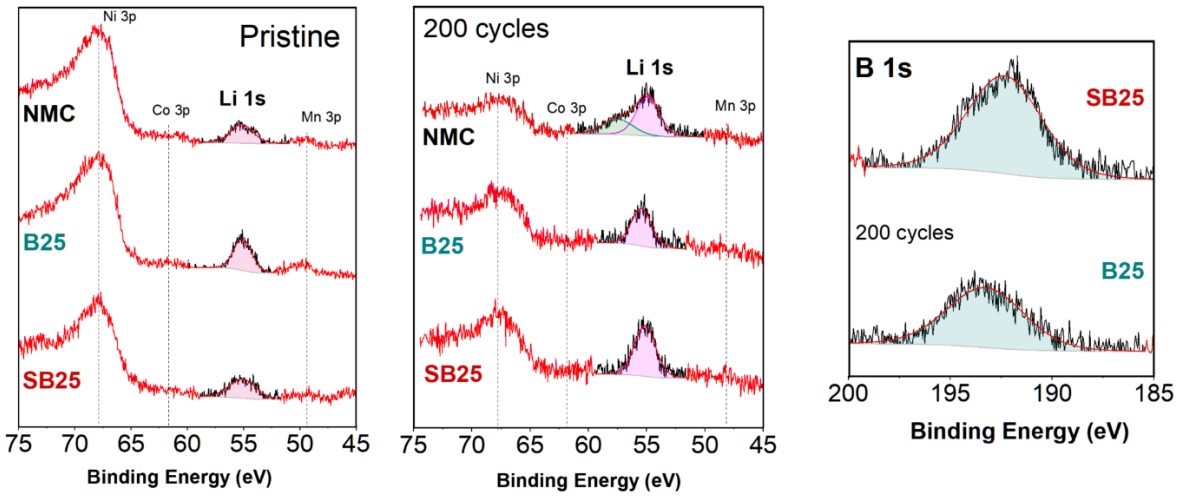

Figure B.6: XPS results showing the Li 1s spectra of the pristine and aged NMC cathode electrodes, and the B 1s spectra of the SB2 and B25 cycled electrodes.

Appendix C: Supporting Information for Chapter 5

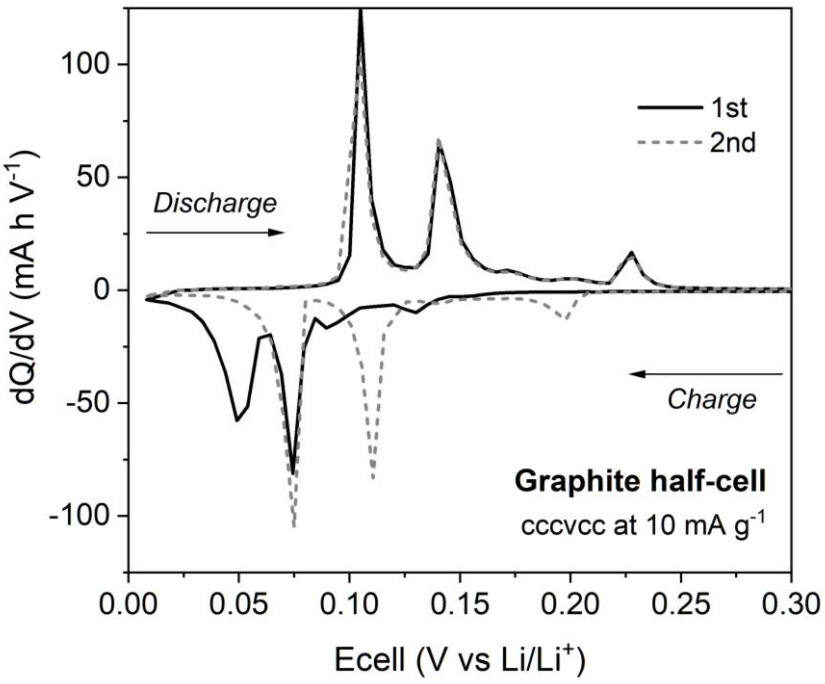

Figure C.1: dQ/dV plot for the formation cycles of the graphite half-cell

Table C.1: Capacities and Coulombic efficiencies (CE) of NMC90-graphite full cell formation cycles at 10 mA/g between 4.2 - 2.5 V prepared at different N/P ratios in coin cells.

N/P	Format	Cathode	Capacity/ mA h cm^{-2}		1st CE/	Capacity/ mA h cm^{-2}		2nd CE/
			1st Cha	1st Dis	%	2nd Cha	2nd Dis	%
1.0	Coin	NMC	1.216	1.067	87.8	1.088	1.072	98.5
1.0	Coin	B25	1.089	0.963	88.4	0.969	0.955	98.5
1.0	Coin	SB25	1.243	1.074	86.4	1.085	1.070	98.7
1.1	Coin	NMC	1.080	0.960	88.9	0.972	0.982	101.1
1.1	Coin	B25	1.044	0.920	88.1	0.914	0.901	98.6
1.1	Coin	SB25	1.222	1.117	91.4	1.113	1.097	98.6
1.2	Coin	NMC	1.122	0.998	89.0	1.012	0.992	98.0
1.2	Coin	B25	0.964	0.821	85.2	0.845	0.843	99.7
1.2	Coin	SB25	1.115	1.004	90.1	1.023	1.023	100.0

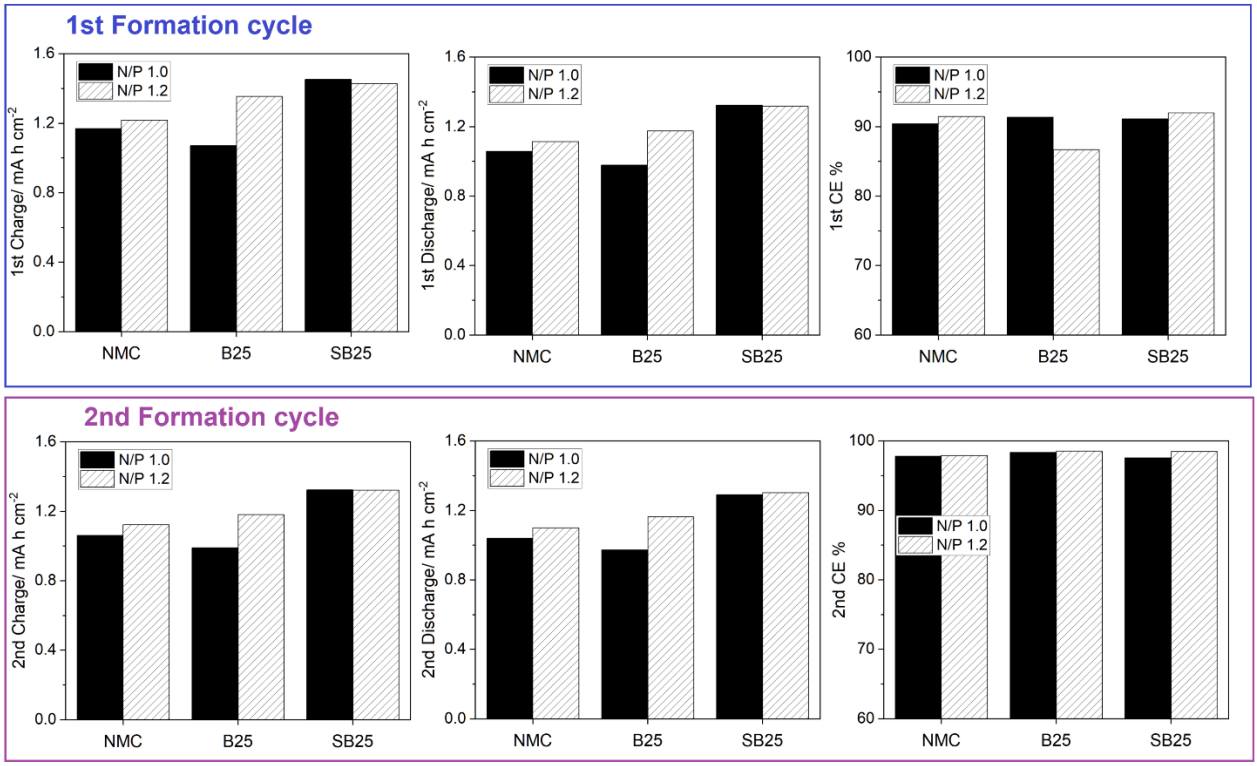

Figure C.2: Formation capacities and Coulombic efficiencies (CE) of graphite-NMC90-5-5 full cells tested in pouch cell format (3x3) for different cathodes and N/P ratios.

Table C8: Terminal Li stoichiometries calculated in the cathode and anode electrodes from the formation cycles at 10 mA g^{-1} in the full coin cells at different N/P ratios.

N/P	Cell	x in Li_xNMC				x in Li_xC_6			
		1st Cha	1st Dis	2nd Cha	2nd Dis	1st Cha	1st Dis	2nd Cha	2nd Dis
1.0	NMC	0.215	0.911	0.207	0.900	0.995	0.113	1.005	0.127
1.0	B25	0.290	0.929	0.287	0.919	0.868	0.087	0.871	0.099
1.0	SB25	0.211	0.924	0.204	0.916	0.990	0.096	1.000	0.105
1.1	NMC	0.260	0.919	0.245	0.919	0.865	0.094	0.882	0.094
1.1	B25	0.308	0.917	0.305	0.904	0.848	0.101	0.851	0.118
1.1	SB25	0.222	0.861	0.215	0.849	0.998	0.179	1.006	0.194
1.2	NMC	0.141	0.914	0.135	0.899	0.917	0.092	0.924	0.108
1.2	B25	0.356	0.924	0.344	0.923	0.720	0.052	0.734	0.053
1.2	SB25	0.282	0.921	0.270	0.925	0.882	0.097	0.897	0.092

Table C.3: Fitting parameters of the Nyquist plots from the EIS measurements of full coin cells with N/P 1.0 at different voltage points along a 20 mA g^{-1} charge cycle between 2.5 and 4.3 V.

Cell	Voltage/ V	R_s/ Ω	R_{ion}/ Ω	R_{SEI}/ Ω	R_{CT}/ Ω
NMC	2.8	2.62	1.01	0.0	49.9
	3.5	2.50	0.78	3.91	26.0
	4.0	2.49	0.94	6.10	19.5
	4.2	2.51	1.38	14.1	22.2
B25	2.8	1.08	1.59	5.92	51.0
	3.5	1.08	1.53	16.7	20.7
	4.0	1.05	0.85	11.8	22.9
	4.2	1.06	0.8	10.6	25.0
SB25	2.8	1.51	1.21	0.09	41.0
	3.5	1.54	1.06	9.14	18.6
	4.0	1.50	0.97	11.6	11.2
	4.2	1.48	0.90	11.0	12.1

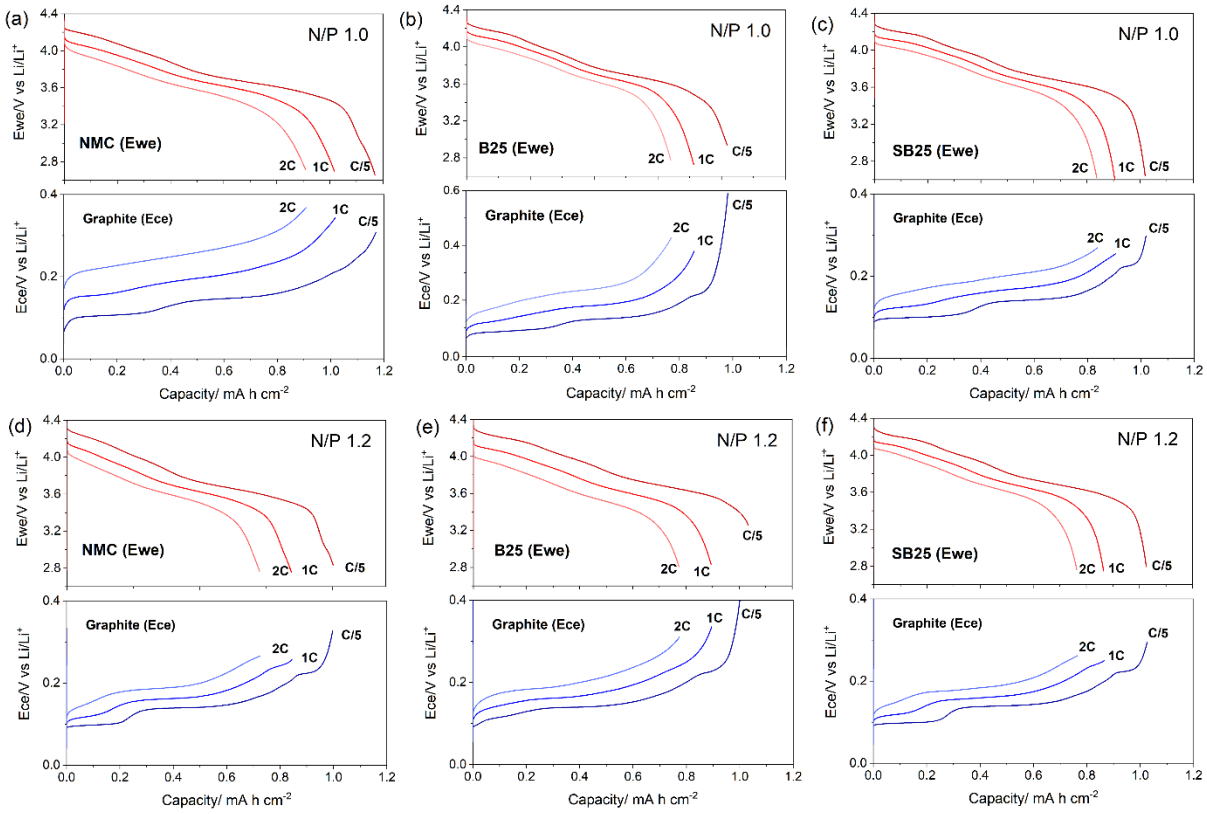

Figure C.3: Discharge profiles of the positive (Ewe) and negative (Ece) electrodes for the three-electrode cells cycled at different C-rates within a controlled voltage window of 4.3 – 2.5 V.

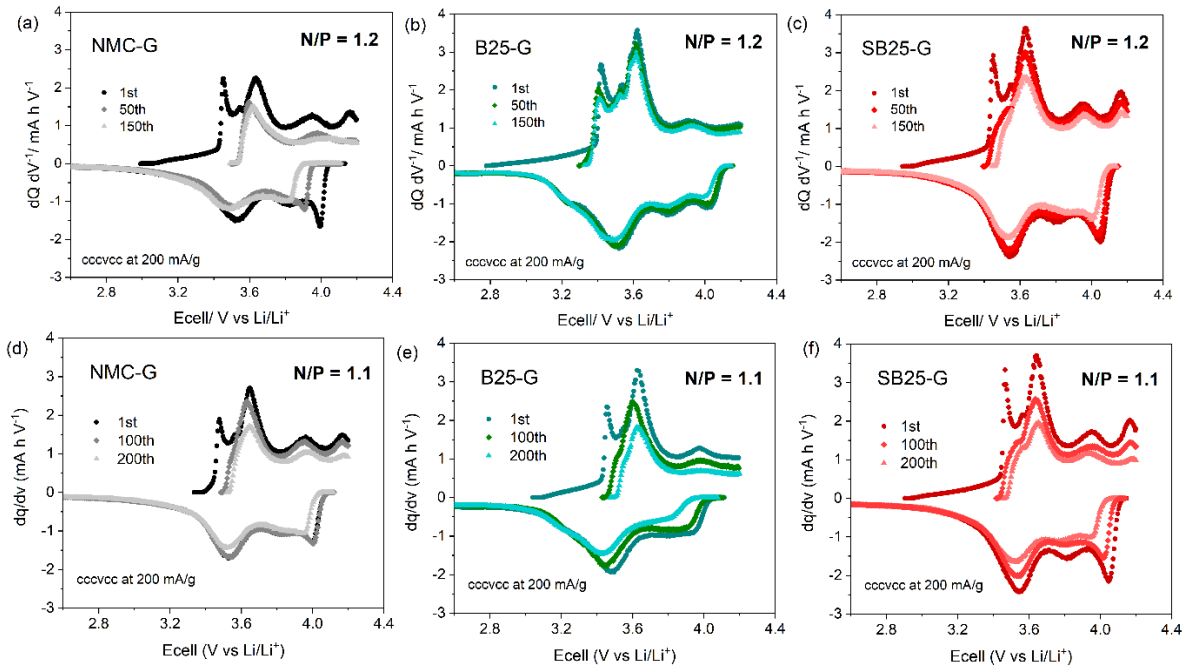

Figure C.4: Differential capacity plots taken from representative cycles of the full cell coin cell cycling tests with a charge-discharge current rate of 200 mA/g between 4.2 - 2.5 V.

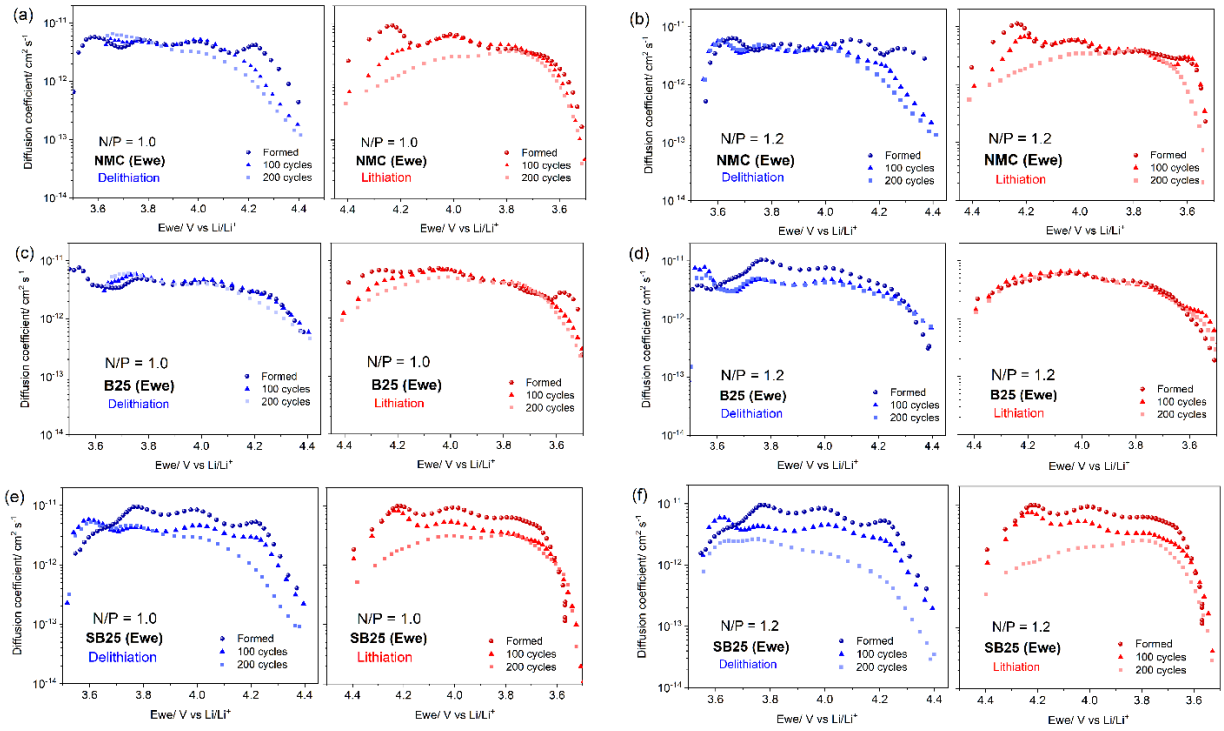

Figure C.5: Positive electrode diffusion coefficients calculated from GITT tests in three-electrode cells at prior to and after 100 and 200 cycles at 2C charge and discharge.

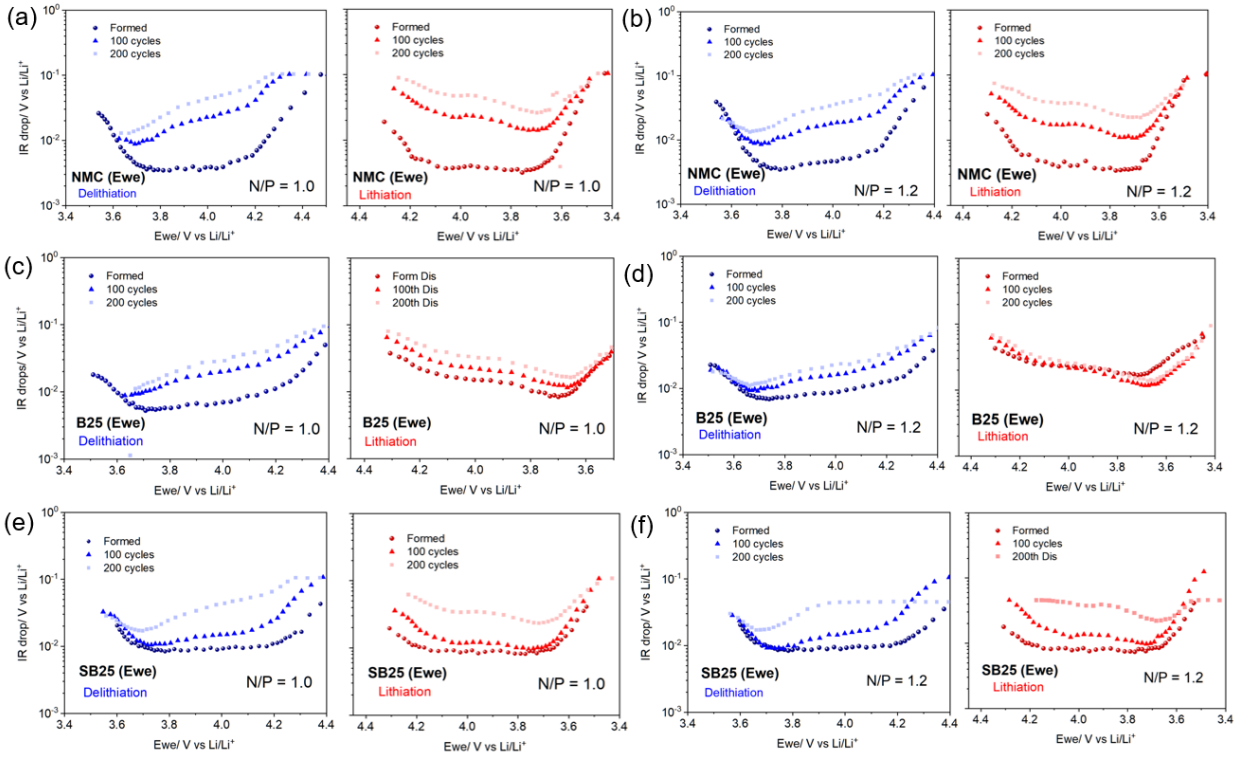

Figure C.6: Calculated overpotentials (VIR) at the positive electrode between each GITT pulse measured in three-electrode full-cells for different cathodes and cell balance in GITT cycles following formation and symmetric cc-cv-cc cycling at 2C.

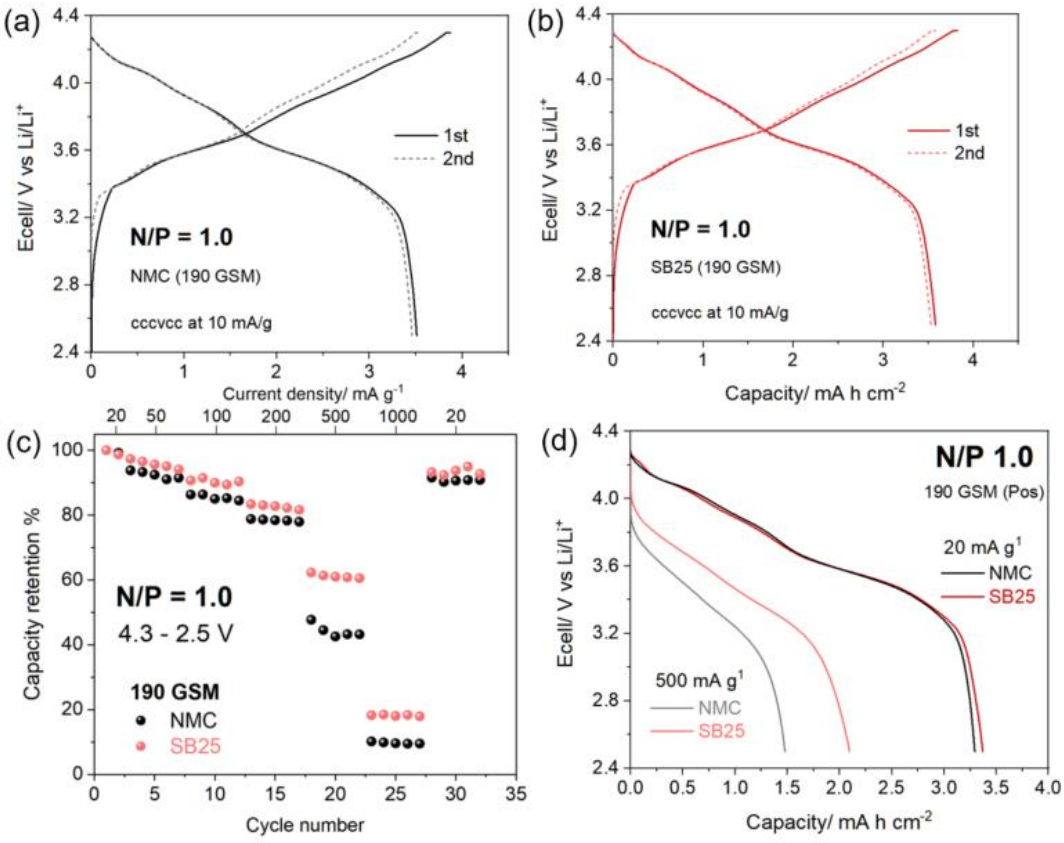

Figure C.7: Electrochemical testing of NMC and SB25 full-cells assembled with cathode loadings of 190 GSM and N/P ratio of 1.0; formation voltage profiles (a – b), rate capability tests at a constant charge rate of 20 mA g^{-1} with increasing discharge current densities between 20 – 1000 (b), and the discharge profiles at 20 mA g^{-1} and 500 mA g^{-1}.

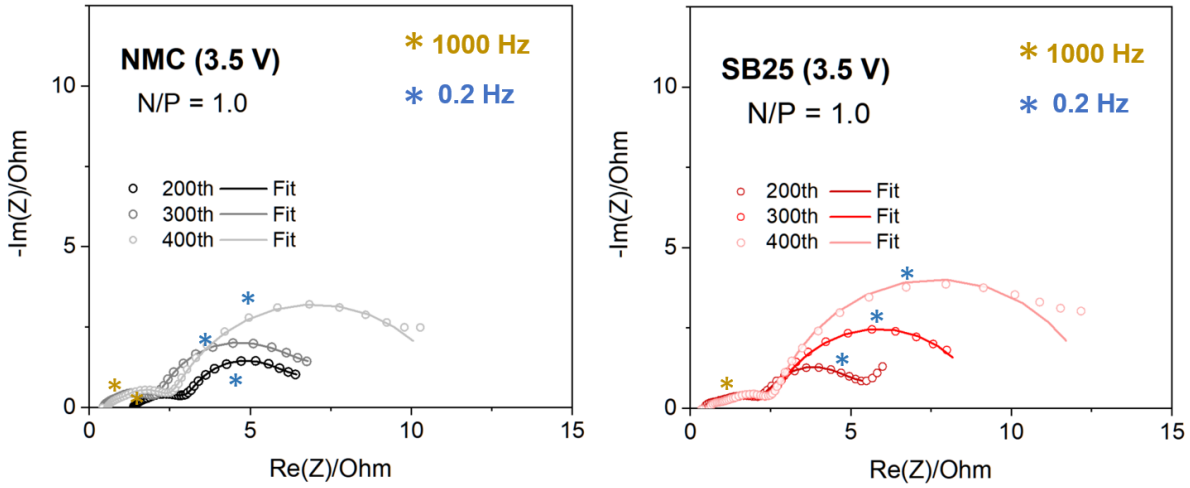

Figure C.8: Nyquist plots from the EIS measurements in NMC and SB25 full cells (190 GSM cathode) at 4.3 V, taken periodically over 200 – 400th cycles at the lower the faster rate cycling with charge-discharge at 100/200 mA g^{-1}

Table C.4: Fitting parameters of the Nyquist plots from the EIS measurements of full pouch cells assembled with cathode loadings of 190 GSM and N/P ratio of 1.0 at various cycles during the extended cycling for the first 200 cycles at 100 mA g^{-1} and following 200 cycles at 200 mA g^{-1}.

Cycle	NMC at 4.3 V			SB25 at 4.3 V		
	R_s/ Ω	R_{ion}/ Ω	R_{CT}/ Ω	R_s/ Ω	R_{ion}/ Ω	R_{CT}/ Ω
0	0.61	1.20	6.47	0.58	0.99	2.35
50	1.42	1.36	10.41	0.68	1.13	6.72
100	1.26	1.43	13.08	0.34	1.43	12.01
150	1.23	1.54	15.61	0.35	1.81	11.90
200	0.61	1.20	6.47	0.58	0.99	2.35
250	1.35	1.56	15.15	0.35	1.81	11.90
300	1.67	1.73	20.19	0.36	1.82	13.93
350	0.41	1.61	19.00	0.52	2.01	15.20
400	0.52	1.89	26.12	0.50	1.92	16.52

References

1 T. Z. Ang, M. Salem, M. Kamarol, H. S. Das, M. A. Nazari and N. Prabaharan, *Energy Strateg. Rev.*, 2022, **43**, 100939.

2 D. O. Akinyele and R. K. Rayudu, *Sustain. Energy Technol. Assessments*, 2014, **8**, 74–91.

3 J. M. Tarascon, *Philos. Trans. R. Soc. A Math. Phys. Eng. Sci.*, 2010, **368**, 3227–3241.

4 B. Ramasubramanian, J. K. Ling, R. Jose and S. Ramakrishna, *Cell Reports Phys. Sci.*, 2024, **5**, 102032.

5 L. Liu, M. Li, L. Chu, B. Jiang, R. Lin, X. Zhu and G. Cao, *Prog. Mater. Sci.*, 2020, 111.

6 C. Liu, Z. G. Neale and G. Cao, *Mater. Today*, 2016, **19**, 109–123.

7 A. K. Koech, G. Mwandila, F. Mulolani and P. Mwaanga, *South African J. Chem. Eng.*, 2024, **50**, 321–339.

8 S. H. Finkelstein, M. Ricci, T. Bötticher and K. Schmidt-Rohr, *Phys. Chem. Chem. Phys.*, 2024, 24157–24171.

9 J. L. Shi, D. D. Xiao, M. Ge, X. Yu, Y. Chu, X. Huang, X. D. Zhang, Y. X. Yin, X. Q. Yang, Y. G. Guo, L. Gu and L. J. Wan, *Adv. Mater.*, 2018, **30**, 1–8.

10 J. B. Goodenough and Y. Kim, *Chem. Mater.*, 2010, **22**, 587–603.

11 M. Park, X. Zhang, M. Chung, G. B. Less and A. M. Sastry, *J. Power Sources*, 2010, **195**, 7904–7929.

12 T. Zhao, H. Mahandra, R. Marthi, X. Ji, W. Zhao, S. Chae, M. Traversy, W. Li, F. Yu, L. Li, Y. Choi, A. Ghahreman, Z. Zhao, C. Zhang, Y. Kang, Y. Lei and Y. Song, *Chem. Eng. J.*, 2024, **485**, 149923.

13 M. Bianchini, M. Roca-Ayats, P. Hartmann, T. Brezesinski and J. Janek, *Angew. Chemie - Int. Ed.*, 2019, **58**, 10434–10458.

14 H. H. Ryu, G. T. Park, C. S. Yoon and Y. K. Sun, *J. Mater. Chem. A*, 2019, **7**, 18580–18588.

15 B. Chu, Y. J. Guo, J. L. Shi, Y. X. Yin, T. Huang, H. Su, A. Yu, Y. G. Guo and Y. Li, *J. Power Sources*, 2022, **544**, 231873.

16 T. Liu, L. Yu, J. Liu, J. Lu, X. Bi, A. Dai, M. Li, M. Li, Z. Hu, L. Ma, D. Luo, J. Zheng, T. Wu, Y. Ren, J. Wen, F. Pan and K. Amine, *Nat. Energy*, 2021, **6**, 277–286.

17 S. Aryal, J. L. Durham, A. L. Lipson, K. Z. Pupek and O. Kahvecioglu, *Electrochim. Acta*, 2021, **391**, 138929.

18 Q. Liu, Z. Wu, J. Sun, R. Xu, X. Li, X. Yu and Y. Liu, *Electrochim. Acta*, 2023, **437**, 141473.

19 Y. S. Chen, R. Dominko, M. Marczewski and W. Wieczorek, *Appl. Phys. A Mater. Sci. Process.*, , DOI:10.1007/s00339-024-07897-7.

20 J. Zheng, W. H. Kan and A. Manthiram, *ACS Appl. Mater. Interfaces*, 2015, **7**, 6926–6934.

21 W. Liu, P. Oh, X. Liu, M. J. Lee, W. Cho, S. Chae, Y. Kim and J. Cho, *Angew. Chemie - Int. Ed.*, 2015, **54**, 4440–4457.

22 P. Kumari and R. Kundu, *Energy and Fuels*, 2025, **39**, 10933–10966.

23 P. Hou, J. Yin, M. Ding, J. Huang and X. Xu, *Small*, 2017, **13**, 1–29.

24 Z. Luo, G. Hu, W. Wang, K. Du and Z. Peng, *J. Power Sources*, 2022, **548**, 232092.

25 J. J. Marie, R. A. House, G. J. Rees, A. W. Robertson, M. Jenkins, J. Chen, S. Agrestini, M. Garcia-Fernandez, K. J. Zhou and P. G. Bruce, *Nat. Mater.*, 2024, **23**, 818–825.

26 H. Y. Jang, D. Eum, J. Cho, J. Lim, Y. Lee, J. H. Song, H. Park, B. Kim, D. H. Kim, S. P. Cho, S. Jo, J. H. Heo, S. Lee, J. Lim and K. Kang, *Nat. Commun.*, , DOI:10.1038/s41467-024-45490-x.

27 H. Zheng, X. Han, W. Guo, L. Lin, Q. Xie, P. Liu, W. He, L. Wang and D. L. Peng, *Mater. Today Energy*, 2020, 18.

28 C. Cui, X. Fan, X. Zhou, J. Chen, Q. Wang, L. Ma, C. Yang, E. Hu, X.-Q. Yang and C. Wang, *J. Am. Chem. Soc.*, 2020, **142**, 8918–8927.

29 J. Ahn, D. Chen and G. Chen, *Adv. Energy Mater.*, 2020, **10**, 1–9.

30 Z. Yu, X. Qu, A. Dou, Y. Zhou, M. Su and Y. Liu, *Ceram. Int.*, 2021, **47**, 1758–1765.

31 N. Mohamed and N. K. Allam, *RSC Adv.*, 2020, **10**, 21662–21685.

32 K. K. Surthi, K. K. Kar and R. Janakarajan, *Chem. Eng. J.*, 2020, **399**, 125858.

33 Y. Lei, J. Ai, S. Yang, H. Jiang, C. Lai and Q. Xu, *J. Alloys Compd.*, 2019, **797**, 421–431.

34 J. Zhu, J. Zheng, G. Cao, Y. Li, Y. Zhou, S. Deng and C. Hai, *J. Power Sources*, 2020, **464**, 228207.

35 Y. Han, X. Shan, G. Zhu, Y. Wang, Q. Qu and H. Zheng, *Electrochim. Acta*, 2020, **329**, 135057.

36 Z. Chang, Z. Chen, F. Wu, H. Tang, Z. Zhu, X. Zi and H. Wang, *Solid State Ionics*, 2008, **179**, 2274–2277.

37 Z. Chang, X. Yu, H. Tang, X. Yuan and H. Wang, *Powder Technol.*, 2011, **207**, 396–400.

38 V. Pimenta, M. Sathiya, D. Batuk, A. M. Abakumov, D. Giaume, S. Cassaignon, D. Larcher, J. Tarascon, U. De Picardie and J. Verne, *Chem. Mater.*, 2020, **29**, 9923–9936.

39 L. Zhu, C. Bao, L. Xie, X. Yang and X. Cao, *J. Alloys Compd.*, 2020, **831**, 154864.

40 Y. Xia, J. Zheng, C. Wang and M. Gu, *Nano Energy*, 2018, 49, 434–452.

41 US Pat., US20180019464A1, 2018

42 W. Li, E. M. Erickson and A. Manthiram, *Nat. Energy*, 2020, **5**, 26–34.

43 B. E. Murdock, K. E. Toghill and N. Tapia-Ruiz, *Adv. Energy Mater.,* 2021, **11**, 2102028

44 T. Song, L. Chen, D. Gastol, B. Dong, J. F. Marco, F. Berry, P. Slater, D. Reed and E. Kendrick, *Chem. Mater.*, 2022, **34,** 4153 - 4165

45 P. Guan, Y. Zhu, M. Li, T. Zeng, X. Li, R. Tian, N. Sharma, Z. Xu, T. Wan, L. Hu, Y. Liu, C. Cazorla and D. Chu, *J. Colloid Interface Sci.*, 2022, **628**, 407–418.

46 W. Zhang, C. Yuan, J. Zhu, T. Jin, C. Shen and K. Xie, *Adv. Energy Mater.*, 2023, **13**, 1–21.

47 K. Min, C. Jung, D. S. Ko, K. Kim, J. Jang, K. Park and E. Cho, *ACS Appl. Mater. Interfaces*, 2018, **10**, 20599–20610.

48 W. B. Hawley and J. Li, *J. Energy Storage*, 2019, **26**, 100994.

49 Z. Wu, C. Zhang, F. Yuan, M. Lyu, P. Yang, L. Zhang, M. Zhou, L. Wang, S. Zhang and L. Wang, *Nano Energy*, 2024, **126**, 109620.

50 T. Shi, F. Liu, W. Liu, H. Wang, K. Han, C. Yang, J. Wu, J. Meng, C. Niu, C. Han and X. Wang, *Nano Energy*, 2024, **123**, 109410.

51 D. Wang, C. Xin, M. Zhang, J. Bai, J. Zheng, R. Kou, J. Y. Peter Ko, A. Huq, G. Zhong, C. J. Sun, Y. Yang, Z. Chen, Y. Xiao, K. Amine, F. Pan and F. Wang, *Chem. Mater.*, 2019, **31**, 2731–2740.

52 J. Zheng, G. Teng, C. Xin, Z. Zhuo, J. Liu, Q. Li, Z. Hu, M. Xu, S. Yan, W. Yang and F. Pan, *J. Phys. Chem. Lett.*, 2017, **8**, 5537–5542.

53 H. xin Wei, L. bo Tang, Y. de Huang, Z. yu Wang, Y. hong Luo, Z. jiang He, C. Yan, J. Mao, K. hua Dai and J. chao Zheng, *Mater. Today*, 2021, **51**, 365–392.

54 J. Li, G. Liang, W. Zheng, S. Zhang, K. Davey, W. K. Pang and Z. Guo, *Nano Mater. Sci.*, 2023, **5**, 404–420.

55 Q. Lin, W. Guan, J. Meng, W. Huang, X. Wei, Y. Zeng, J. Li and Z. Zhang, *Nano Energy*, 2018, **54**, 313–321.

56 S. S. Zhang, *Energy Storage Mater.*, 2020, **24**, 247–254.

57 C. Xu, P. J. Reeves, Q. Jacquet and C. P. Grey, *Adv. Energy Mater.*, 2021, **11**, 2003404.

58 L. Croguennec, C. Pouillerie, A. N. Mansour and C. Delmas, *J. Mater. Chem.*, 2001, **11**, 131–141.

59 J. Chen, H. Yang, T. Li, C. Liu, H. Tong, J. Chen, Z. Liu, L. Xia, Z. Chen, J. Duan and L. Li, *Front. Chem.*, 2019, **7**, 1–10.

60 S. Jamil, G. Wang, L. Yang, X. Xie, S. Cao, H. Liu, B. Chang and X. Wang, *J. Mater. Chem. A*, 2020, **8**, 21306–21316.

61 H. Sun and A. Manthiram, *Chem. Mater.*, 2017, **29**, 8486–8493.

62 H. H. Ryu, G. T. Park, C. S. Yoon and Y. K. Sun, *Small*, 2018, **14**, 1–8.

63 T. Kim, *Mater. Today Sustain.*, 2023, **21**, 100326.

64 H. Li, P. Zhou, F. Liu, H. Li, F. Cheng and J. Chen, *Chem. Sci.*, 2019, **10**, 1374–1379.

65 D. Kumar and K. Ramesha, *ChemPhysChem*, 2024, **25**, 1–14.

66 S. Takamori, T. Doi and M. Inaba, *J. Electrochem. Soc.*, 2023, 2–9.

67 H. Yu, Y. Cao, L. Chen, Y. Hu, X. Duan, S. Dai, C. Li and H. Jiang, *Nat. Commun.*, 2021, **12**, 1–9.

68 J. R. Croy, D. C. O'Hanlon, S. Sharifi-Asl, M. Murphy, A. Mane, C. W. Lee, S. E. Trask, R. Shahbazian-Yassar and M. Balasubramanian, *Chem. Mater.*, 2019, **31**, 3891–3899.

69 H. Huang, L. Qiao, H. Zhou, Y. Tang, M. J. Wahila, H. Liu, P. Liu, G. Zhou, M. Smeu and H. Liu, *Sci. Rep.*, 2024, **14**, 1–15.

70 T. Sattar, S. Lee, S. Sim, B. Jin and H. Kim, *Electrochim. Acta*, 2021, **399**, 139417.

71 K. Park, J. H. Park, S. G. Hong, B. Choi, S. W. Seo, J. H. Park and K. Min, *Phys. Chem. Chem. Phys.*, 2016, **18**, 29076–29085.

72 H. Zhao, W. Li, J. Li, H. Xu, C. Zhang, J. Li, C. Han, Z. Li, M. Chu and X. Qiu, *Nano Energy*,

2022, **92**, 106760.

73 F. Reissig, M. A. Lange, L. Haneke, T. Placke, W. G. Zeier, M. Winter, R. Schmuch and A. Gomez-Martin, *ChemSusChem*, 2022, **15**, e202102220.

74 O. Ni, R. Amin, N. Muralidharan, R. K. Petla, H. Ben, S. Ahmad, J. Al-hail, R. Essehli, C. Daniel, M. A. Khaleel and I. Belharouak, *J. Power Sources*, 2020, **467**, 228318.

75 Y. Qian, S. Hu, X. Zou, Z. Deng, Y. Xu and Z. Cao, *Energy Storage Mater.*, 2018, 1–8.

76 K. Park, S. Yu, C. Lee and H. Lee, *J. Power Sources*, 2015, **296**, 197–203.

77 Z. Liu, J. Chai, G. Xu, Q. Wang and G. Cui, *Coord. Chem. Rev.*, 2015, **292**, 56–73.

78 A. Kazzazi, D. Bresser, M. Kuenzel, M. Hekmatfar, J. Schnaidt, Z. Jusys, T. Diemant, R. J. Behm, M. Copley, K. Maranski, J. Cookson, I. de Meatza, P. Axmann, M. Wohlfahrt-Mehrens and S. Passerini, *J. Power Sources*, 2021, **482**, 228975.

79 H. Oka, Y. Makimura, T. Uyama, T. Nonaka, Y. Kondo and C. Okuda, *J. Power Sources*, 2021, **482**, 228926.

80 W. Mei, L. Jiang, C. Liang, J. Sun and Q. Wang, *Energy Storage Mater.*, 2021, **41**, 209–221.

81 S. Wang, K. Rafiz, J. Liu, Y. Jin and J. Y. S. Lin, *Sustain. Energy Fuels*, 2020, **4**, 2342–2351.

82 Y. Ma, B. Ding, G. Ji and J. Yang Lee, *ACS Nano*, 2013, **7**, 10870–10878.

83 E. J. Moon, J. K. Hong, S. K. Mohanty, M. Yang, K. Ihm, H. Lee and H. D. Yoo, *J. Power Sources*, 2023, **559**, 232657.

84 K. Yuan, Y. Lin, X. Li, Y. Ding, P. Yu, J. Peng, J. Wang, H. K. Liu and S. Dou, *Energy Environ. Mater.*, 2024, **7**, 1–19.

85 A. Kozlova, N. Uvarov and A. Ulihin, *Materials (Basel).*, 2022, **15**, 6079.

86 P. Tsai, W.-D. Hsu and S. Lin, *J. Electrochem. Soc.*, 2014, **161**, A439–A444.

87 D. Young, A. Ransil, R. Amin, Z. Li and Y. M. Chiang, *Adv. Energy Mater.*, 2013, **3**, 1125–1129.

88 C. H. Chen, J. T. Vaughey, A. N. Jansen, D. W. Dees, A. J. Kahaian, T. Goacher and M. M. Thackeray, *J. Electrochem. Soc.*, 2009, **148**, A102.

89 K. Yoshimatsu, M. Niwa, H. Mashiko, T. Oshima and A. Ohtomo, *Sci. Rep.*, 2015, **5**, 16325.

90 D. C. Johnston, H. Prakash, W. H. Zachariasen and R. Viswanathan, *Mater. Res. Bull.*, 1973,

8, 777–784.

91 Y. Luo, Y. Chen, N. Koratkar and W. Liu, *Adv. Sci.*, 2024, **2403530**, 1–16.

92 P. U. Nzereogu, A. D. Omah, F. I. Ezema, E. I. Iwuoha and A. C. Nwanya, *Appl. Surf. Sci. Adv.*, 2022, **9**, 100233.

93 A. M. Li, Z. Wang, T. Lee, N. Zhang, T. Li, W. Zhang, C. Jayawardana, M. Yeddala, B. L. Lucht and C. Wang, *Nat. Energy*, , DOI:10.1038/s41560-024-01619-2.

94 K. Pardikar, J. Entwistle, R. Ge, D. Cumming and R. Smith, *JPhys Energy*, , DOI:10.1088/2515-7655/acc139.

95 S. Ahmed, P. A. Nelson, K. G. Gallagher, N. Susarla and D. W. Dees, *J. Power Sources*, 2017, **342**, 733–740.

96 P. Barai, Z. Feng, H. Kondo and V. Srinivasan, *J. Phys. Chem. B*, 2019, **123**, 3291–3303.

97 V. Pimenta, M. Sathiya, D. Batuk, A. M. Abakumov, D. Giaume, S. Cassaignon, D. Larcher, V. Pimenta, M. Sathiya, D. Batuk, A. M. Abakumov and D. Giaume, *Chem. Mater.*, 2017, **29**, 9923–9936.

98 H. Dong and G. M. Koenig, *CrystEngComm*, 2020, **22**, 1514–1530.

99 T. Dagger, J. Kasnatscheew, B. Vortmann-Westhoven, T. Schwieters, S. Nowak, M. Winter and F. M. Schappacher, *J. Power Sources*, 2018, **396**, 519–526.

100 R. Drees, J. Herdegen, F. Lienesch and M. Kurrat, *J. Power Sources*, 2024, **594**, 233986.

101 R. D. Minter, D. Juarez-Robles, C. Fear, Y. Barsukov and P. P. Mukherjee, *J. Vis. Exp.*, 2018, **2018**, 1–11.

102 A. Ikezawa, G. Fukunishi, T. Okajima, F. Kitamura, K. Suzuki, M. Hirayama, R. Kanno and H. Arai, *Electrochem. commun.*, 2020, **116**, 106743.

103 J. Costard, M. Ender, M. Weiss and E. Ivers-Tiffée, *J. Electrochem. Soc.*, 2017, **164**, A80–A87.

104 W. H. Bragg and W. L. Bragg, *Proc. R. Soc. A Math. Phys. Eng. Sci.*, 1913, **88**, 428–438.

105 B. H. Toby, *J. Appl. Crystallogr.*, 2001, **34**, 210–213.

106 A. C. Larson and R. B. Von Dreele, *Los Alamos Natl. Lab. Rep.*, 2004, 86.

107 L. J. Li, X. H. Li, Z. X. Wang, H. J. Guo, P. Yue, W. Chen and L. Wu, *J. Alloys Compd.*, 2010, **507**, 172–177.

108 F. A. Stevie and C. L. Donley, *J. Vac. Sci. Technol. A*, , DOI:10.1116/6.0000412.

109 C. Moore, J. Moon and D. Chidambaram, *Appl. Surf. Sci.*, 2024, **659**, 159876.

110 B. Ravel and M. Newville, *J. Synchrotron Radiat.*, 2005, **12**, 537–541.

111 J. Z. Olson, M. L. Carmen and E. J. F. Dickinson, *Chem. Mater.*, 2023, **35**, 1487–1513.

112 A. Fly and R. Chen, *J. Energy Storage*, 2020, **29**, 101329.

113 A. C. Lazanas and M. I. Prodromidis, *ACS Meas. Sci. Au*, 2023, **3**, 162–193.

114 A. A. Wang, S. E. J. O'Kane and F. B. Planella, *Prog. Energy*, 2022, **4**, 032004.

115 P. Iurilli, C. Brivio and V. Wood, *J. Power Sources*, 2021, **505**, 229860.

116 N. Meddings, M. Heinrich, J. Lee, V. Ruiz, E. Napolitano, S. Seitz, G. Hinds, R. Raccichini, M. Gaber and J. Park, *J. Power Sources*, 2020, **480**, 228742.

117 W. Choi, H. C. Shin, J. M. Kim, J. Y. Choi and W. S. Yoon, *J. Electrochem. Sci. Technol.*, 2020, **11**, 1–13.

118 W. Weppner and R. A. Huggins, *Ann. Rev. Mater. Sci*, 1978, **8**, 269–311.

119 A. Barai, K. Uddin, W. D. Widanage, A. McGordon and P. Jennings, *Sci. Rep.*, 2018, **8**, 1–14.

120 Z. Geng, Y. C. Chien, M. J. Lacey, T. Thiringer and D. Brandell, *Electrochim. Acta*, 2022, **404**, 139727.

121 Y. Chen, J. Key, K. O. Regan, T. Song, Y. Han and E. Kendrick, *Chem. Eng. J.*, 2022, **450**, 138275.

122 D. Perry and M. Mamlouk, *J. Power Sources*, 2021, **514**, 230577.

123 F. M. N. U. Khan, M. G. Rasul, A. S. M. Sayem and N. Mandal, *Energy Reports*, 2023, **9**, 11–21.

124 R. Jung, R. Morasch, P. Karayaylali, K. Phillips, F. Maglia, C. Stinner, Y. Shao-horn and H. A. Gasteiger, *J. Electrochem. Soc.*, 2018, **165**, A132–A141.

125 A. Chen, K. Wang, J. Li, Q. Mao, Z. Xiao and D. Zhu, *Front. Energy Res.*, 2020, **8**, 1–16.

126 J. Zheng, J. Xiao and J. Zhang, *Nano Today*, 2016, **11**, 678–694.

127 L. Li, J. Chen, H. Huang, L. Tan, L. Song, H. H. Wu, C. Wang, Z. Zhao, H. Yi, J. Duan and T. Dong, *ACS Appl. Mater. Interfaces*, 2021, **13**, 42554–42563.

128 B. M. Goltsman and E. A. Yatsenko, *Open Ceram.*, 2024, **17**, 100540.

129 V. L. Paula, M. S. Conconi and M. F. Hern, *Open Ceram.*, 2022, **9**, 100227.

130 M. B. Sedel and V. M. Pogrebenkov, *Glas. Ceram.*, 2006, **63**, 22–25.

131 M. A. Violini, M. F. S. M. S. Conconi, G. Suarez and N. M. Rendtorff, *J. Therm. Anal. Calorim.*, 2020, **139**, 1717–1729.

132 J. Shi, H. Sheng, X. Meng, X. Zhang, D. Lei, X. Sun, H. Pan, J. Wang, X. Yu and C. Wang, *Natl. Sci. Rev.*, 2023, **10**, nwac226.

133 H. Dong and G. M. Koenig, *CrystEngComm*, 2020, **22**, 1514–1530.

134 J. Langdon and A. Manthiram, *Energy Storage Mater.*, 2021, **37**, 143–160.

135 A. Mesnier and A. Manthiram, *ACS Appl. Mater. Interfaces*, 2023, **15**, 12895–12907.

136 R. Liang, Z. Wu, W. Yang, Z. Tang, G. Xiong, Y. Cao and S. Hu, *Ionics (Kiel).*, 2020, **26**, 1635–1643.

137 Z. Zhong, L. Chen and S. Huang, *J. Mater. Sci.*, 2020, **55**, 2913–2922.

138 L. Mn, C. O. Cathode, Y. Liu, Z. Ma and L. Li, *J. Electrochem. Soc.*, 2021, **168**, 010534.

139 P. Dai, X. Kong, H. Yang, J. Li, J. Zeng and J. Zhao, *ACS Sustain. Chem. Eng.*, 2022, **10**, 4381–4390.

140 F. Chen, C. Zeng, C. Huang, J. Lin, Y. Chen, B. Dong, C. Yin, S. Tian, D. Sun, Z. Zhang, H. Li and C. Li, *Chinese Phys. B*, 2022, **31**, 078101.

141 S. Lee, B. Jin and H. Kim, *Sci. Rep.*, 2019, **9**, 17541.

142 K. Park, H. Jung, L. Kuo, P. Kaghazchi and C. S. Yoon, *Adv. Energy Mater.*, 2018, **1801202**, 1–9.

143 I. A. Skvortsova, E. D. Orlova, A. O. Boev, D. A. Aksyonov, I. Moiseev, E. M. Pazhetnov, A. A. Savina and A. M. Abakumov, *J. Power Sources*, 2023, **583**, 233571.

144 H. Zhu, Q. Li, X. Gong, K. Cao and Z. Chen, *Crystals*, 2018, **8**, 1–12.

145 F. Wu, N. Liu, L. Chen, N. Li, J. Dong, Y. Lu, G. Tan, M. Xu, D. Cao, Y. Liu, Y. Chen and Y. Su, *J. Energy Chem.*, 2021, **62**, 351–358.

146 M. Wood, J. Li, R. E. Ruther, Z. Du, E. C. Self, H. M. Meyer, C. Daniel, I. Belharouak and D. L. Wood, *Energy Storage Mater.*, 2019, **24**, 188–197.

147 T. He, L. Chen, Y. Su, Y. Lu, L. Bao, G. Chen, Q. Zhang, S. Chen and F. Wu, *J. Power Sources*,

2019, **441**, 227195.

148 B. Ying, J. R. Fitzpatrick, Z. Teng, T. Chen, T. Woon, B. Lo, V. Siozios, C. A. Murray, H. E. A. Brand, S. Day, C. C. Tang, R. S. Weatherup, M. Merz, P. Nagel, S. Schuppler, M. Winter and K. Kleiner, *Chem. Mater.*, 2023, 1514–1526.

149 R. K. B. Gover, R. Kanno, B. J. Mitchell, M. Yonemura and Y. Kawamoto, *J. Electrochem. Soc.*, 2000, **147**, 4045.

150 H. Zhou, F. Xin, B. Pei and S. Whittingham, *ACS Energy Lett.*, 2019, **4**, 1902–1906.

151 F. Xin, A. Goel, X. Chen, H. Zhou, J. Bai, S. Liu, F. Wang, G. Zhou and M. S. Whittingham, , DOI:10.1021/acs.chemmater.2c01461.

152 J. Zhao, W. Zhang, A. Huq, S. T. Misture, B. Zhang, S. Guo, L. Wu, Y. Zhu, Z. Chen, K. Amine, F. Pan, J. Bai and F. Wang, *Adv. Energy Mater.*, 2017, **7**, 1–13.

153 C. Julien, A. Mauger, K. Zaghib and H. Groult, *Materials (Basel).*, 2016, **9**, 595.

154 E. D. Orlova, A. A. Savina, S. A. Abakumov, A. V Morozov and M. Abakumov, *Symmetry (Basel).*, 2021, **13**, 1628.

155 Y. Shen, X. Yao, J. Zhang, S. Wang, D. Zhang, D. Yin, L. Wang, Y. Zhang, J. Hu, Y. Cheng and X. Li, *Nano Energy*, 2022, **94**, 106900.

156 Y. S. Kim, J. H. Kim, Y. Sun and C. S. Yoon, *Appl. Mater. Interfaces*, 2022, **14**, 17500–17508.

157 N. Sofyan, F. Angellinnov, D. P. Arsadini, Z. D. Afriandi, A. Subhan and A. Zulfia, *Discov. Mater.*

158 X. Zheng, X. Li, Z. Wang, H. Guo, Z. Huang, G. Yan and D. Wang, *Electrochim. Acta*, 2016, **191**, 832–840.

159 E. Bjorklund, D. Brandell, M. Hahlin and K. Edstrom, *J. Electrochem. Soc.*, 2017, **164**, A3054–A3059.

160 M. Li, L. Cheng, B. Zhang, P. Deng, Z. Xiao, L. Ming, Y. Zhao, B. Xu and X. Ou, *J. Alloys Compd.*, 2022, **907**, 164489.

161 A. T. S. Freiberg, J. Sicklinger, S. Solchenbach and H. A. Gasteiger, *Electrochim. Acta*, 2020, **346**, 136271.

162 Y. Ding, B. Deng, H. Wang, X. Li, T. Chen, X. Yan, Q. Wan, M. Qu and G. Peng, *J. Alloys Compd.*, 2019, **774**, 451–460.

163 B. You, Z. Wang, Y. Chang, W. Yin, Z. Xu and Y. Zeng, *Fundam. Res.*, 2023, **3**, 618–626.

164 O. Bondarchuk, A. P. Lagrow, A. Kvasha, T. Thieu and E. Ayerbe, *Appl. Surf. Sci.*, 2021, **535**, 147699.

165 J. Ma, J. Wang, K. Jia, Z. Liang, G. Ji, H. Ji, Y. Zhu, W. Chen, H. M. Cheng and G. Zhou, *Nat. Commun.*, 2024, **15**, 1–10.

166 I. Källquist, R. Le Ruyet, H. Liu, R. Mogensen, M. T. Lee, K. Edström and A. J. Naylor, *J. Mater. Chem. A*, 2022, **10**, 19466–19505.

167 G. Hu, M. Zhang, L. Liang, Z. Peng, K. Du and Y. Cao, *Electrochim. Acta*, 2016, **190**, 264–275.

168 L. You, B. Chu, G. Li, T. Huang and A. Yu, *J. Power Sources*, 2021, **482**, 228940.

169 F. Wu, J. Dong, L. Chen, G. Chen, Q. Shi, Y. Nie, Y. Lu, L. Bao, N. Li, T. Song, S. Chen and Y. Su, *Energy Mater. Adv.*, 2023, **4**, 1–11.

170 P. Vanaphuti, J. Bai, L. Ma, S. Ehrlich, K. Kisslinger, F. Wang and Y. Wang, *Energy Storage Mater.*, 2020, **31**, 459–469.

171 W. Xiang, C. Zhu, J. Zhang, H. Shi, Y. Liang and M. Yu, *J. Alloys Compd.*, 2019, **786**, 56–64.

172 F. Fan, R. Zheng, T. Zeng, H. Xu, X. Wen, X. Wang, G. Tian, S. Wang, C. Zeng, W. Xiang and C. Shu, *Chem. Eng. J.*, 2023, **477**, 147181.

173 M. Ball, E. Zsoldos, M. Cormier, E. Zsoldos, I. Haman, S. Yu, N. Zhang, N. Phattharasupakun, M. B. Johnson, M. Metzger, C. Yang and J. Dahn, *J. Electrochem. Soc.*, 2024, **120535**, 020552.

174 A. A. Savina and A. M. Abakumov, *Heliyon*, 2023, **9**, e21881.

175 R. Essehli, A. Parejiya, N. Muralidharan, C. J. Jafta, R. Amin, M. B. Dixit, Y. Bai, J. Liu and I. Belharouak, *J. Power Sources*, 2022, **545**, 231938.

176 J. Kim, H. Lee, H. Cha, M. Yoon and M. Park, *Adv. Energy Mater.*, 2018, **8**, 1702028.

177 J. Hu, L. Li, Y. Bi, J. Tao, J. Lochala, D. Liu, B. Wu, X. Cao, S. Chae, C. Wang and J. Xiao, *Energy Storage Mater.*, 2022, **47**, 195–202.

178 J. Xu, E. Hu, D. Nordlund, A. Mehta, S. N. Ehrlich, X. Yang and W. Tong, *ACS Appl. Mater. Interfaces*, 2016, **8**, 31677–31683.

179 W. M. Seong, Y. Kim and A. Manthiram, *Chem. Mater.*, 2020, **32**, 9479–9489.

180 B. L. D. Rinkel, J. P. Vivek, N. Garcia-Araez and C. P. Grey, *Energy Environ. Sci.*, 2022, **15**, 3416–3438.

181 S. Prempluem, T. Sangsanit, K. Santiyuk, K. Homlamai, W. Tejangkura, R. Songthan, N. Anansuksawat and M. Sawangphruk, *J. Power Sources*, 2024, **606**, 234538.

182 G. T. Park, H. H. Ryu, N. Y. Park, C. S. Yoon and Y. K. Sun, *J. Power Sources*, 2019, **442**, 227242.

183 M. Yi, A. Dolocan and A. Manthiram, *Adv. Funct. Mater.*, 2023, **2213164**, 1–14.

184 J. Molenda, A. Milewska, M. Rybski, L. Lu, W. Zajac, S. Gerasin and J. Tobola, *Phys. Status Solidi Appl. Mater. Sci.*, , DOI:10.1002/pssa.201900951.

185 F. Xin, H. Zhou, Y. Zong, M. Zuba, Y. Chen, N. A. Chernova, J. Bai, B. Pei, A. Goel, J. Rana, F. Wang, K. An, L. F. J. Piper, G. Zhou and M. S. Whittingham, *ACS Energy Lett.*, 2021, **6**, 1377–1382.

186 W. M. Dose, J. K. Morzy, A. Mahadevegowda, C. Ducati, C. P. Grey and M. F. L. De Volder, *J. Mater. Chem. A*, 2021, **9**, 23582–23596.

187 H. Dai, L. Gomes, D. Maxwell, S. Zamani, K. Yang, D. Atienza, N. Dale and S. Mukerjee, *ACS Appl. Mater. Interfaces*, 2024, **16**, 8639–8654.

188 N. Phattharasupakun, J. Wutthiprom, S. Duangdangchote, S. Sarawutanukul, C. Tomon, F. Duriyasart, S. Tubtimkuna, C. Aphirakaramwong and M. Sawangphruk, *Energy Storage Mater.*, 2021, **36**, 485–495.

189 A. L. Lipson, B. J. Ross, J. L. Durham, D. Liu, M. Leresche, T. T. Fister, L. Liu and K. Kim, *Appl. Energy Mater.*, 2021, **4**, 1972–1977.

190 I. A. Skvortsova, E. D. Orlova, A. O. Boev, D. A. Aksyonov, I. Moiseev, E. M. Pazhetnov, A. A. Savina and A. M. Abakumov, *J. Power Sources*, 2023, **583**, 233571.

191 Q. Q. Qiao, L. Qin, G. R. Li, Y. L. Wang and X. P. Gao, *J. Mater. Chem. A*, 2015, **3**, 17627–17634.

192 A. Paulus, M. Hendrickx, M. Bercx, O. M. Karakulina, M. A. Kirsanova, D. Lamoen, J. Hadermann, A. M. Abakumov, M. K. Van Bael and A. Hardy, *Dalt. Trans.*, 2020, **49**, 10486–10497.

193 M. Eilers-Rethwisch, S. Hildebrand, M. Evertz, L. Ibing, T. Dagger, M. Winter and F. M. Schappacher, *J. Power Sources*, 2018, **397**, 68–78.

194 T. Taskovic, A. Eldesoky, W. Song, M. Bauer and J. R. Dahn, *J. Electrochem. Soc.*, 2022, **169**, 040538.

195 M. Alipour, C. Ziebert, F. V. Conte and R. Kizilel, *Batteries*, 2020, **6**, 1–32.

196 P. Lyu, Y. Huo, Z. Qu and Z. Rao, *Appl. Therm. Eng.*, 2020, **166**, 114749.

197 J. E. Harlow, X. Ma, J. Li, E. Logan, Y. Liu, N. Zhang, L. Ma, S. L. Glazier, M. M. E. Cormier, M. Genovese, S. Buteau, A. Cameron, J. E. Stark and J. R. Dahn, *J. Electrochem. Soc.*, 2019, **166**, A3031–A3044.

198 L. M. Thompson, J. E. Harlow, A. Eldesoky, M. K. G. Bauer, J. H. Cheng, W. S. Stone, T. Taskovic, C. R. M. McFarlane and J. R. Dahn, *J. Electrochem. Soc.*, 2021, **168**, 020532.

199 Z. Dai, Y. Liu, X. Lu, H. Zhao and Y. Bai, *Adv. Mater.*, 2024, **36**, 1–11.

200 L. Xu, F. Zhou, J. Kong, H. Zhou and Q. Zhang, *J. Alloys Compd.*, 2019, **804**, 353–363.

201 J. Ren, Z. Liu, Y. Tang, Z. Yin, T. Yang, Z. Huang, W. Wang, W. Cui, C. Zhang, Z. Shen, Y. Liu, Y. Ren and Q. Liu, *J. Power Sources*, 2024, **606**, 234522.

202 A. J. Dent, G. Cibin, S. Ramos, A. D. Smith, S. M. Scott, L. Varandas, M. R. Pearson, N. A. Krumpa, C. P. Jones and P. E. Robbins, *J. Phys. Conf. Ser.*, 2009, **190**, 0–4.

203 C. Chen, F. B. Planella, K. O. Regan, W. D. Widanage and E. Kendrick, *J. Electrochem. Soc.*, 2020, **167**, 080534. DOI:10.1149/1945-7111/ab9050.

204 H. Zhu, R. Shen, Y. Tang, X. Yan, J. Liu, L. Song and Z. Fan, *Nanomaterials*, 2020, **10**, 1–11.

205 N. Zaker, C. Geng, D. Rathore, I. Hamam, N. Chen, P. Xiao, C. Yang, J. R. Dahn and G. A. Botton, *Adv. Funct. Mater.*, 2023, **33**, 2211178. DOI:10.1002/adfm.202211178.

206 H. N. Pollen, J. R. Tolchard, A. M. Svensson and N. P. Wagner, *ChemElectroChem*, 2022, **9**, e202200859.

207 L. Zhou, J. Liu, L. Huang, N. Jiang, Q. Zheng and D. Lin, *J Solid State Electrochem*, 2017, **21**, 3467–3477.

208 L. Ni, M. O. Li-rich, Y. Zhao, M. Xia, X. Hu, Z. Zhao, Y. Wang and Z. Lv, *Electrochim. Acta*, 2015, **174**, 1167–1174.

209 Z. Xie, Y. Zhang, A. Yuan and J. Xu, *J. Alloys Compd.*, 2019, **787**, 429–439.

210 S. H. Jung, K. Oh, Y. J. Nam, D. Y. Oh, K. Kang and Y. S. Jung, *Chem. Mater.*, 2018, **30**, 8190–8200.

211 J. Cen, B. Zhu and D. O. Scanlon, *J. Phys. Energy*, 2023, **5**, 035005.

212 D. P. Abraham, R. D. Twesten, M. Balasubramanian, J. Kropf and D. Fischer, *J. Electrochem. Soc.*, 2003, **150**, A1450–A1456.

213 A. EL Aouam, N. Sabi, H. Aziam, O. Touag, O. Dolotko, M. Mansori, S. Dsoke, M. Dollé and I. Saadoune, *J. Power Sources*, 2024, **606**, 234551.

214 M. J. Zuba, A. Grenier, Z. Lebens-higgins, G. J. P. Fajardo, Y. Li, Y. Ha, H. Zhou, M. S. Whittingham, W. Yang, Y. S. Meng, K. W. Chapman and L. F. J. Piper, *ACS Energy Lett.*, 2021, **6**, 1055–1064.

215 T. Ohnuma and T. Kobayashi, *RSC Adv.*, 2019, **9**, 35655–35661.

216 J. Guo, Y. Xu, M. Exner, X. Huang, Y. Li, Y. Liu, H. Wang, J. Kowal, Q. Zhang, P. K. Kristensen, D. Wang, K. Pedersen, L. Gurevich, D. I. Stroe and P. Adelhelm, *Adv. Energy Mater.*, 2024, **14**, 1–14.

217 J. Li, Z. Du, R. E. Ruther, S. J. An, L. A. David, K. Hays, M. Wood, N. D. Phillip, Y. Sheng, C. Mao, S. Kalnaus, C. Daniel and D. L. Wood, *Jom*, 2017, **69**, 1484–1496.

218 A. Belgibayeva, A. Rakhmetova, M. Rakhatkyzy and M. Kairova, *J. Power Sources*, 2023, **557**, 232550.

219 A. Nickol, C. Heubner, M. Schneider and A. Michaelis, *J. Electrochem. Soc.*, 2022, **169**, 050511.

220 K. O. Regan, F. Brosa, W. D. Widanage, E. Kendrick, G. H. Road and C. Cv, *Electrochim. Acta*, 2022, **425**, 140700.

221 C. Roitzheim, L. Y. Kuo, Y. J. Sohn, M. Finsterbusch, S. Möller, D. Sebold, H. Valencia, M. Meledina, J. Mayer, U. Breuer, P. Kaghazchi, O. Guillon and D. Fattakhova-Rohlfing, *ACS Appl. Energy Mater.*, 2022, **5**, 524–538.

222 Z. Li, X. Yu, Y. Lv, L. Qi, Y. Ma, H. zhang, D. Song, X. Shi and L. Zhang, *Electrochim. Acta*, , DOI:10.1016/j.electacta.2021.139468.

223 T. Thien Nguyen, U. H. Kim, C. S. Yoon and Y. K. Sun, *Chem. Eng. J.*, 2021, **405**, 126887.

224 F. A. Susai, A. Bano, S. Maiti, J. Grinblat, A. Chakraborty, H. Sclar, T. Kravchuk, A. Kondrakov, M. Tkachev, M. Talianker, D. T. Major, B. Markovsky and D. Aurbach, *J. Mater. Chem. A*, 2023, **11**, 12958–12972.

225 G. Nuroldayeva, D. Adair, Z. Bakenov and B. Uzakbaiuly, *ACS Omega*, 2023, **8**, 37899–

37907.

226 D. Mohanty, A. S. Sefat, J. Li, R. A. Meisner, A. J. Rondinone, E. A. Payzant, D. P. Abraham, D. L. Wood and C. Daniel, *Phys. Chem. Chem. Phys.*, 2013, **15**, 19496–19509.

227 A. E. Abdel-Ghany, A. M. Hashem, A. Mauger and C. M. Julien, *J. Solid State Electrochem.*, 2020, **24**, 3157–3172.

228 A. Gomez-martin, F. Reissig, L. Frankenstein, M. Heidbüchel, M. Winter, T. Placke and R. Schmuch, *Adv. Energy Mater.*, 2022, **12**, 2103045.

229 C. Ghanty, B. Markovsky, E. M. Erickson, M. Talianker, O. Haik, Y. Tal-Yossef, A. Mor, D. Aurbach, J. Lampert, A. Volkov, J. Y. Shin, A. Garsuch, F. F. Chesneau and C. Erk, *ChemElectroChem*, 2015, **2**, 1479–1486.

230 S. R. Daemi, C. Tan, A. Vamvakeros, T. M. M. Heenan, D. P. Finegan, M. Di Michiel, A. M. Beale, J. Cookson, E. Petrucco, J. S. Weaving, S. Jacques, R. Jervis, D. J. L. Brett and P. R. Shearing, *Phys. Chem. Chem. Phys.*, 2020, **22**, 17814–17823.

231 B. Fu, A. Kulka, B. Wang, M. Moździerz, A. Brzoza-Kos, P. Czaja and K. Świerczek, *Electrochim. Acta*, 2024, **494**, 14455. DOI:10.1016/j.electacta.2024.144455.

232 H. Liu, A. J. Naylor, A. S. Menon, W. R. Brant, K. Edström and R. Younesi, *Adv. Mater. Interfaces*, 2020, **7**, 2000277.

233 K. R. Tallman, G. P. Wheeler, C. J. Kern, E. Stavitski, X. Tong, K. J. Takeuchi, A. C. Marschilok, D. C. Bock and E. S. Takeuchi, *J. Phys. Chem. C*, 2021, **125**, 58–73.

234 Y. Chen, W. Zhao, Q. Zhang, G. Yang, J. Zheng, W. Tang, Q. Xu, C. Lai, J. Yang and C. Peng, *Adv. Funct. Mater.*, 2020, **30**, 1–12.

235 W. S. Yoon, M. Balasubramanian, K. Y. Chung, X. Q. Yang, J. McBreen, C. P. Grey and D. A. Fischer, *J. Am. Chem. Soc.*, 2005, **127**, 17479–17487.

236 S. Suttison, K. Pengpat, U. Intatha, J. Fan, W. Zhang and S. Eitssayeam, *Mater. Today Proc.*, 2022, **65**, 2347–2350.

237 Y. Lakhdar, Y. Chen, H. Geary, M. E. Houck, A. S. Groombridge, P. R. Slater and E. Kendrick, *J. Power Sources*, 2023, **588**, 233710.

238 E. Hüger, L. Riedel, J. Zhu, J. Stahn, P. Heitjans and H. Schmidt, *Batteries*, , DOI:10.3390/batteries9050244.

239 M. J. Lain, J. Brandon and E. Kendrick, *Batteries*, 2019, **5**, DOI:10.3390/batteries5040064.

240 F. Ghani, K. An and D. Lee, *Batteries*, 2024, **10**, DOI:10.3390/batteries10100340.

241 B. F. Song, A. Dhanabalan and S. L. Biswal, *J. Energy Storage*, 2020, **28**, 101268. , DOI:10.1016/j.est.2020.101268.

242 L. Yang, T. Meng, W. Zheng, J. Zhong, H. Cheng, Y. Tong and D. Shu, *Energy Storage Mater.*, 2024, **72**, 103766.

243 M. Li, S. Li, D. Yan, Y. Ma, X. Niu and L. Wang, *Chem. Sci.*, 2025, 2609–2618.

244 Y. Chen, Y. Lakhdar, L. Chen, B. Kishore, J. Choi, E. Williams, D. Spathara, R. Jackowska and E. Kendrick, *Next Energy*, 2024, **5**, 100166.

245 A. Smith, P. Stüble, L. Leuthner, A. Hofmann and F. Jeschull, *Batter. Supercaps*, 2023, **6**, 202300080.

246 J. Asenbauer, T. Eisenmann, M. Kuenzel, A. Kazzazi, Z. Chen and D. Bresser, *Sustain. Energy Fuels*, 2020, **4**, 5363–5870.

247 Z. Chen, L. Zhang, X. Wu, K. Song, B. Ren, T. Li and S. Zhang, *J. Power Sources*, 2019, **439**, 227056.

248 C. Hogrefe, T. Waldmann, M. Hölzle and M. Wohlfahrt-Mehrens, *J. Power Sources*, 2023, **556**, 232391.

249 P. Yan, J. Zheng, M. Gu, J. Xiao, J. G. Zhang and C. M. Wang, *Nat. Commun.*, 2017, **8**, 1–9.

250 G. Sun, T. Sui, B. Song, H. Zheng, L. Lu and A. M. Korsunsky, *Extrem. Mech. Lett.*, 2016, **9**, 449–458.

251 N. Lin, Z. Jia, Z. Wang, H. Zhao, G. Ai, X. Song, Y. Bai, V. Battaglia, C. Sun, J. Qiao, K. Wu and G. Liu, *J. Power Sources*, 2017, **365**, 235–239.

252 K. Dai, Z. Wang, G. Ai, H. Zhao, W. Yuan, X. Song, V. Battaglia, C. Sun, K. Wu and G. Liu, *J. Power Sources*, 2015, **298**, 349–354.

253 S. H. Lee, H. G. You, K. S. Han, J. Kim, I. H. Jung and J. H. Song, *J. Power Sources*, 2014, **247**, 307–313.

254 Y. Kim, M. Kim, T. Lee, E. Kim, M. An, J. Park, J. Cho and Y. Son, *Electrochem. commun.*, 2023, **147**, 107437.

255 H. Zheng, J. Li, X. Song, G. Liu and V. S. Battaglia, *Electrochim. Acta*, 2012, **71**, 258–265.

256 G. Bridgewater, M. J. Capener, J. Brandon, M. J. Lain, M. Copley and E. Kendrick, *Batteries*,

2021, **7**, 1–14.

257 T. M. M. Heenan, A. Wade, C. Tan, J. E. Parker, D. Matras, A. S. Leach, J. B. Robinson, A. Llewellyn, A. Dimitrijevic, R. Jervis, P. D. Quinn, D. J. L. Brett and P. R. Shearing, *Adv. Energy Mater.*, 2020, **10**, 2002655.

258 J. Kumberg, M. Müller, R. Diehm, S. Spiegel, C. Wachsmann, W. Bauer, P. Scharfer and W. Schabel, *Energy Technol.*, 2019, **7**, 1900722.

259 M. Strobl, M. E. Baur, S. Samothrakitis, F. Malamud, X. Zhang, P. K. M. Tung, S. Schmidt, R. Woracek, J. Lee, R. Kiyanagi, L. T. Kuhn, I. Gavish Segev and Y. Ein-Eli, *Adv. Energy Mater.*, 2025, **2405238**, 1–9.

260 H. Gao, Q. Wu, Y. Hu, J. P. Zheng, K. Amine and Z. Chen, *J. Phys. Chem. Lett.*, 2018, **9**, 5100–5104.

261 N. Ogihara, Y. Itou, T. Sasaki and Y. Takeuchi, *J. Phys. Chem. C*, 2015, **119**, 4612–4619.